ABSTRACT

Title of Dissertation: GAS AND STAR FORMATION AT THE PEAK OF COSMIC STAR FORMING ACTIVITY

Laura Lenkić
Doctor of Philosophy, 2021

Dissertation Directed by: Professor Alberto D. Bolatto
Department of Astronomy

Gas and star formation in galaxies are intimately linked to one another. Molecular hydrogen gas is the material out of which stars form, while the process of forming stars, in turn, depletes the reservoirs of gas in galaxies and builds up their stellar mass. Observations of star formation in galaxies over time indicate that they must form stars for timescales longer than would be expected from their gas content and star formation rates, indicating that processes that replenish the star forming fuel must be present. The focus of this thesis is on two components of this qualitative picture: the molecular hydrogen gas content of galaxies over time, and the link between gas and star formation in galaxies resembling those observed at the epoch of most active star formation.

First, I present a systematic search for serendipitous carbon monoxide emitting sources in the second Plateau de Bure High-z Blue-Sequence Survey (PHIBSS2). These observations presented an opportunity to quantify the mass density of molecular gas in galaxies as a function of time, and to link this to the star formation

history of the Universe. I use a match-filter technique to systematically detect 67 serendipitous sources, after which I characterize their properties, creating a catalog of their redshifts, line widths, fluxes, estimations of the detection reliability, and completeness of the detection algorithm. I find that these serendipitous sources are unrelated to the primary sources that were targeted by PHIBSS2, and use the catalog to construct luminosity functions spanning a redshift range from $\sim 0.3 - 5$. From these luminosity functions, I place constraints on the molecular hydrogen content in galaxies over cosmic time. My work presents one of the first attempts to use existing observations for this measurement and yields results that are consistent with previous studies, while demonstrating the scientific power of large, targeted surveys.

Next, I study a sample of rare, nearby galaxies that are most similar to those we observe at the peak of cosmic star forming activity that occured $\sim$ 10 billion years ago. These galaxies are drawn from the DYnamics of Newly Assembled Massive Objects (DYNAMO) survey, and their proximity to us allows for very detailed studies of their massive star forming clumps. I use observations from the Hubble Space Telescope (HST) to measure colors that are sensitive to stellar population age and extinction. From these measurements, I find that clumps in DYNAMO galaxies have colors that are most consistent with very young centers and outskirts that appear systematically older, by as much as 150 Myr in some cases. I attribute this age difference to the presence of ongoing star formation in the centers of clumps that maintains the population of massive, short-lived stars and gives rise to colors consistent with young ages. Furthermore, I find that within the disks of their host

galaxies, younger clumps are preferentially located far from galaxy centers, while older clumps are preferentially located closer to the centers. These results are consistent with hydrodynamic simulations of high-redshift clumpy galaxies that predict clumps form in the outskirts of galaxies via a violent disk instability, and as they age, migrate to the centers of galaxies where they merge and contribute to the growth of galactic bulges.

Building on this study, I combine observations of DYNAMO galaxies from the HST and the Atacama Large Millimeter/sub-millimeter Array (ALMA) to trace molecular hydrogen gas and star formation. I link these observations to measurements of the molecular gas velocity dispersions to test theories of star formation. I find that compared to local samples of "normal" star forming galaxies, DYNAMO systems have consistently high velocity dispersions, molecular gas surface densities, and star formation rate surface densities. Indeed, throughout their disks, DYNAMO galaxies are comparable to the centers of local star forming galaxies. Stellar bar driven gas flows into the centers of galaxies in these local samples may give rise to the high observed velocity dispersions, and gas and star formation rate surface densities. For DYNAMO galaxies, the widespread elevated values of these parameters may be driven by galactic-scale gas inflows, which is predicted by theories. Finally, current theories of star formation, such as the feedback regulated model, assume that turbulence dissipates on timescales proportional to the angular velocity of a galaxy (eddy or crossing time). Yet, I find such models have difficulty reproducing the DYNAMO measurements, and thus conclude that the turbulent dissipation timescale in DYNAMO galaxies must scale with galactocentric radius.

GAS AND STAR FORMATION AT THE PEAK OF COSMIC STAR FORMING ACTIVITY

by

Laura Lenkić

Dissertation submitted to the Faculty of the Graduate School of the
University of Maryland, College Park in partial fulfillment
of the requirements for the degree of
Doctor of Philosophy
2021

Advisory Committee:
Professor Alberto D. Bolatto, Chair/Advisor
Professor Andrew Harris
Professor Sylvain Veilleux
Dr. Deanne B. Fisher, External Examiner
Professor Peter Shawhan, Dean's Representative

Preface

This thesis focuses on two aspects of star–forming galaxies: the availability of fuel for star formation across cosmic time and star formation in clumpy, gas–rich, turbulent galaxies that are nearby analogues of star forming galaxies at the peak of cosmic star forming activity. Parts of this thesis have been published in peer-reviewed journals and presented at several conferences.

Chapter 2 has been published in the Astronomy Journal as *"Plateau de Bure High-z Blue Sequence Survey 2 (PHIBSS2): Search for Secondary Sources, CO Luminosity Functions in the Field, and the Evolution of Molecular Gas Density through Cosmic Time"* and appears in this thesis with minimal changes (Lenkić et al., 2020). Chapter 3 has been published in the Monthly Notices of the Royal Astronomical Society as "Giant Star Forming Complexes in High-z Main Sequence Galaxy Analogues: The Internal Structure of Clumps in DYNAMO Galaxies" and also appears in this thesis with minimal changes (Lenkić et al., 2021). Chapter 4 is currently in preparation for submission to the Astrophysical Journal.

Dedication

To my parents,

Zdravka Lenkić and Franko Lenkić,

who nurtured and encouraged in me

a curiosity in all aspects of life.

Acknowledgments

This thesis would not have been possible without my advisor, Alberto Bolatto. Thank you so much for believing in me and seeing this thesis through to the end. It's been a real team effort and I appreciate all our discussions and everything you have taught me. I also thank the rest of my committee: Andy Harris for all our conversations and the great instrumentation class you taught, Sylvain Veilleux for your insights and help with observing proposals like JWST, Deanne Fisher for all the early Friday mornings in Australia that you spent meeting with me and Alberto, sharing with me your incredible knowledge of DYNAMO, and Peter Shawhan for taking on the role of Dean's Representative of my committe. Thank you all.

I thank the rest of our research group: Stuart Vogel for always being an advocate for grad students, Peter Teuben for your endless help with all things radio, and especially the grad students Becca, Liz, Jialu, Vicente, and Rye for making this group really feel like being a part of something bigger. You are all amazing people, scientists, and friends.

Amy, I cherish our friendship; it is one of the best things that happened to me at UMD. Thank you for your support, for always listening, and for being unapologetically you. You make the world a better place and I admire and respect you. Derek, thank you for caring about grad students and always being understanding

and compassionate. Thank you for introducing me to birding, and most of all thank you for your friendship. The memories of all our birding trips are some of the best I have from my time here. I hope there will be many more! Sara, thank you for your mentorship, friendship, and sharing your time and experiences with me as we were both navigating career options and trying to sort out and piece together the next steps of our lives. Milena, thank you for being a shining light in the department. Thank you for your friendship, for our swims, book club discussions, attempts to make burek, and everything in between.

To all the grads I had the pleasure of sharing an office with: Milena, Tomás, Pradip, Joe, Jialu, Guangwei, Ramsey, Zeeve, Thomas, Jegug, Sara, ChongChong, Ginny, Jongwon, Charlotte, thank you for bringing the offices to life with your personalities. To all grads in the department: I am grateful for, and appreciate all of you, you make the department a very special place. To everyone on the eclipse roadtrip of 2017: Zeeve, Thomas, Bernadette, Jialu, Jiali, Liz, Matt, and Pradip: thank you for one of the most incredible grad school experiences. To Dana and Jeff, thank you for everything you have done to make College Park feel like home.

To all the administrative and front office staff: Olivia, Susan, Dorinda, Mona, Barbara, the department would not function without you! Thank you for all your kindness and patience as I figured out how things worked, messed up my TARs, and crumbled under the pressure of paperwork in the last few weeks of my thesis. You are all amazing!

My friends near and far: Julie, Alex, Mladen, Robin, Nathalie; thank you for your everlasting presence that made me feel like I was never alone or too far from

home, even when the world otherwise seemed to be caving in on me.

To my sister, Elizabeth, thank you for always being there for me, for all your love, for all that you have taught me about life and perseverance. To my brother Stefan, you've listened to all my rants about physics and astronomy for as long as I can remember and have always supported me in this pursuit. Thank you.

To my parents Zdravka and Franko Lenkić, words don't quite seem enough to express the gratitude I have for you. You uprooted your lives, left behind everyone and everything you know, learned two new languages, and worked harder than anyone I have ever known, so that we could have opportunities you didn't. Mama, you went to college with three unruly kids running around, became a respiratory therapist, and over the last 18 months have fought tirelessly to save people's lives throughout the pandemic. You are a fierce and inspiring woman who has shown me that anything is possible. Tata, I know you once dreamed of being an astronomer too. Thank you for everything you have done to make it possible for me to chase that dream instead. Thank you both for the values you have taught me and the infinite support you provide; you are the reason I am here today.

Finally, to Petr, my partner, I know you would rather I write some joke or something ridiculous, but I want the world to know of the infinite well of love and support that lives inside your heart. You weren't just there to see me through these last five years, you lived every single moment of this time with me, as if you were going through the PhD yourself. Your unparalleled wit and humour have kept a smile on my face even at times when I felt like I would just break down. Thank you for all the big and small ways you have supported me, from fixing my glasses on

my face, to going through homework assignments with me, passing on to me some of your jedi coding skills, talking through research problems, reading my thesis, accepting with curiosity and enthusiasm every wild travel/nutrition/exercise ideas I propose (like driving with me through the desert of Namibia!), and everything in between. Thank you for everything, I love you beyond words!

Table of Contents

List of Tables

List of Figures

List of Abbreviations

Acronyms:

ACS	Advanced Camera for Surveys (onboard the HST)
ALMA	Atacama Large Millimeter/submillimeter Array
CASA	Common Astronomy Software Application
CDF	Cumulative Distribution Function
DYNAMO	DYnamics of Newly Assembled Massive Objects
FIFI-LS	Far Infrared Field-Imaging Line Spectrometer (onboard SOFIA)
FIR	Far-Infrared
FWHM	Full Width at Half Maximum
GBT	Green Bank Telescope
HAWC+	High-resolution Airborne Wideband Camera Plus (onboard SOFIA)
HIM	Hot Ionized Medium
HST	Hubble Space Telescope
IFU	Integral Field Unit
IMF	Initial Mass Function
IR	Infrared
IRAC	Infrared ARray Camera (onboard the Spitzer Space Telescope)
ISM	Interstellar Medium
JWST	James Webb Space Telescope
KDE	Kernel Density Estimate
LIRG	Luminous Infrared Galaxy
ngVLA	Next Generation Very Large Array

NIRSpec	Near Infrared Spectrograph
NOEMA	NOrthern Extended Millimeter Array
PdBI	Plateau de Bure Interferometer
PDF	Probability Density Function
PHIBSS	Plateau de Bure High$-z$ Blue Sequence Survey
PI	Principal Investigator
PSF	Point Spread Function
SDSS	Sloan Digital Sky Survey
SED	Spectral Energy Distribution
SFR	Star Formation Rate
SLED	Spectral Line Energy Distribution
SMG	Submillimeter Galaxy
SOFIA	Stratospheric Observatory For Infrared Astronomy
ULIRG	Ultra Luminous Infrared Galaxy
UV	Ultraviolet
VLA	Very Large Array
WCS	World Coordinate System
WFC3	Wide Field Camera 3 (onboard the HST)
WNM	Warm Neutral Medium

Atoms, Molecules, and Line Transitions:

C	Carbon
[CII]	Fine-structure line emission of singly ionized carbon at 158 μm
CO	Carbon Monoxide
H	Hydrogen
HI	Neutral atomic hydrogen
HII	Ionized hydrogen
H_2	Molecular hydrogen
Hα	Spectral line in the Balmer series of hydrogen corresponding to the n$= 3-2$ electronic transition at 6562.8 Å
Paα	Spectral line in the Paschen series of hydrogen corresponding to the n$= 4-3$ electronic transition at 1.875 μm
He	Helium
O	Oxygen

Symbols:

$M_\odot$	Solar Mass equal to 1.988×10^{30} kg
M_*	Stellar Mass
n_H	Hydrogen volume density

Chapter 1: Introduction

"The cosmos is within us. We are made of star-stuff.

We are a way for the universe to know itself."

– Dr. Carl Sagan

Galaxies are the largest individual structures in the Universe that we can observe. They contain planets, stars, stellar remnants, dust, interstellar gas, dark matter, have supermassive black holes in their centers, and at least one galaxy that we know of, the Milky Way, hosts intelligent life: us. We study galaxies, namely their formation and evolution, to ultimately learn about the formation and evolution of the Universe itself.

To this end, we observe galaxies across cosmic time and morphological properties, which give us snapshots at different epochs in the history of the Universe of the characteristics of galaxies, and the physical processes that shape them, as is illustrated in Figure 1.1 (from Schawinski et al., 2014). This figure plots the $u - r$ color on the y-axis and stellar mass on the x-axis. It illustrates in the top left panel that galaxies occupy two distinct regions in this parameter space, based on their "color" (see also Salim et al., 2007).

Late-type galaxies, or spirals, occupy the "blue cloud" (bottom right panel

of Figure 1.1) and are characterized by spiral-like morphologies with blue optical colors, higher rates of star formation, higher cold molecular gas fractions (which is the fuel for star formation), and motions largely dominated by rotation. As a result of existing molecular gas reservoirs, these galaxies are able to sustain star formation, which in turn maintains the population of the short-lived ($<$ 10 million years), massive O and B stars, whose spectra peak in the UV, giving rise to the blue colors of spiral galaxies. In contrast, early-type galaxies, or ellipticals[1], occupy the "red sequence" (top right panel of Figure 1.1). These galaxies present elliptical-like morphologies and are characterized by random motions, red optical colors, low rates of star formation, and small cold molecular gas fractions. Because these galaxies do not have large reservoirs of cold molecular gas, their star formation winds down and shuts off. As the lives of the last massive O and B stars in these galaxies end, the low-mass stars whose spectra peak at longer (redder) wavelengths remain, transitioning the colors of these galaxies from blue to red.

As star formation becomes quenched in galaxies, they progress from the blue cloud to the red sequence through the "green valley" (indicated by the parallel green lines in Figure 1.1). This transition must occur rapidly, because if it were a slow process, galaxies would spend more time in the green valley and we would observe more of them in that region. Processes that can quench star formation in galaxies can include a shut down of gas accretion onto disks (a process needed to replenish gas reservoirs as star formation consumes existing ones), galaxy mergers that strip

[1]Late-type galaxies are what we commonly refer to today as spiral galaxies, while early-type galaxies are often referred to as elliptical galaxies. I will preferentially use the spiral/elliptical terminology, except where for the sake of clarity, the late-/early-type terminology makes more sense.

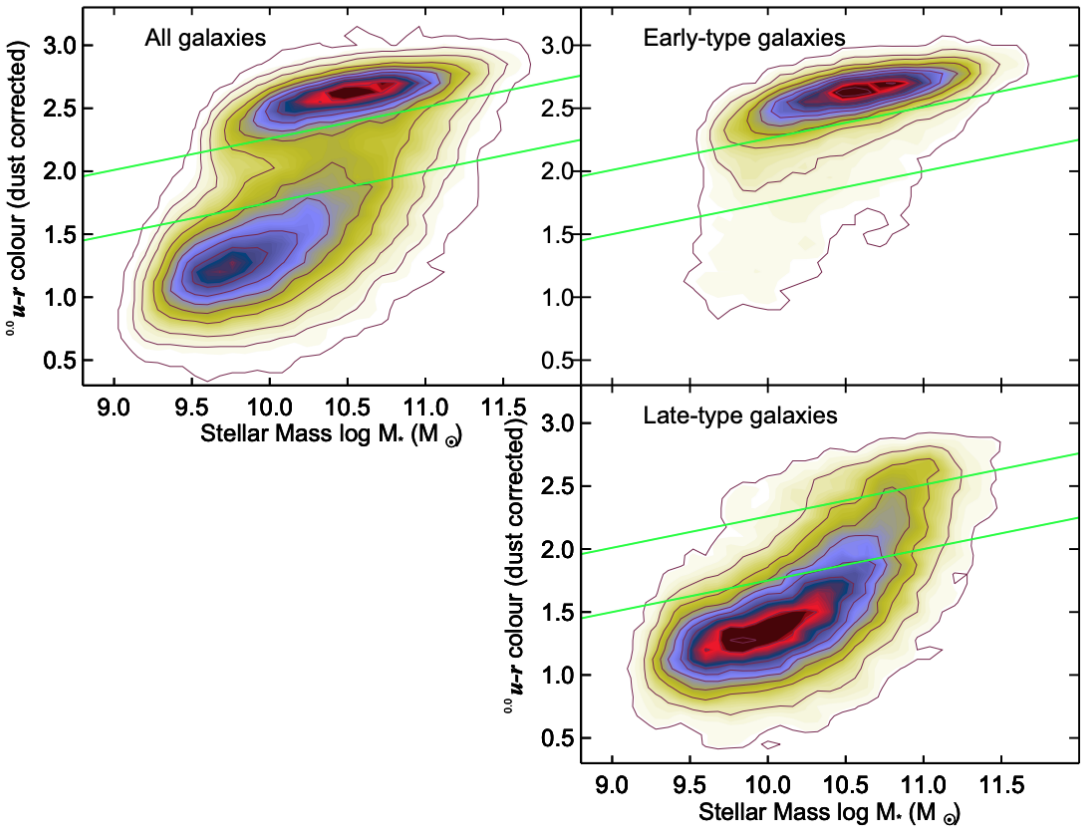

Figure 1.1: A $u-r$ versus stellar mass plot from Schawinski et al. (2014), where higher values of $u-r$ on the y-axis indicate redder colors. This illustrates that early-type (elliptical) galaxies and late-type (spiral) galaxies generally occupy distinct regions in this parameter space, with some overlap in between (top left panel). Elliptical galaxies preferentially occupy the "red sequence" where star formation has shut down (top right panel), while spiral galaxies preferentially occupy the "blue cloud" where star formation is actively ongoing (bottom right panel). The intermediate region, indicated by the set of two green lines, is dubbed the "green valley" and represents a region of quenching or rapid transition between the red sequence and the blue cloud.

galaxies of their gas, and high energy processes such as jets from supermassive black holes that can drive the gas out of galaxies through outflows. However, as is shown in Figure 1.1, there are red late-type galaxies and blue early-type galaxies, indicating that galaxies cannot be neatly separated into these two categories, and the processes that cause galaxies to move around in this parameter space are complex.

Observations of galaxies not only reveal differences in the properties between ellipticals and spirals, but they also show that star forming galaxies are very different in the early Universe when compared to today's galaxies, like our Milky Way. Figure 1.2 (from Pearson et al., 2018) plots galaxy star formation rates (SFRs) on the y-axis and stellar mass (M_*) on the x-axis. Star forming galaxies, which reside in the blue cloud, form a fairly tight correlation in this parameter space, that is referred to as the "main sequence (MS) of star formation" (Brinchmann et al., 2004). Most notably, observations reveal that the main sequence of star formation evolves with redshift, as shown by the evolution of the colored lines in Figure 1.2. Galaxies in the early Universe had more star formation per unit mass than galaxies today, indicating that as the Universe has aged, star formation activity has decreased. Furthermore, red sequence galaxies lie below the main sequence of star formation at their respective redshifts, indicating that they have less star formation per unit stellar mass. On the other side, galaxies that lie much higher above the main sequence of star formation at their respective redshifts are considered "starbursts", and have much higher star forming activity than "normal" main sequence galaxies.

The focus of this thesis is primarily on main sequence galaxies over a large range of redshifts. Specifically, Chapter 2 will focus on a population of serendipi-

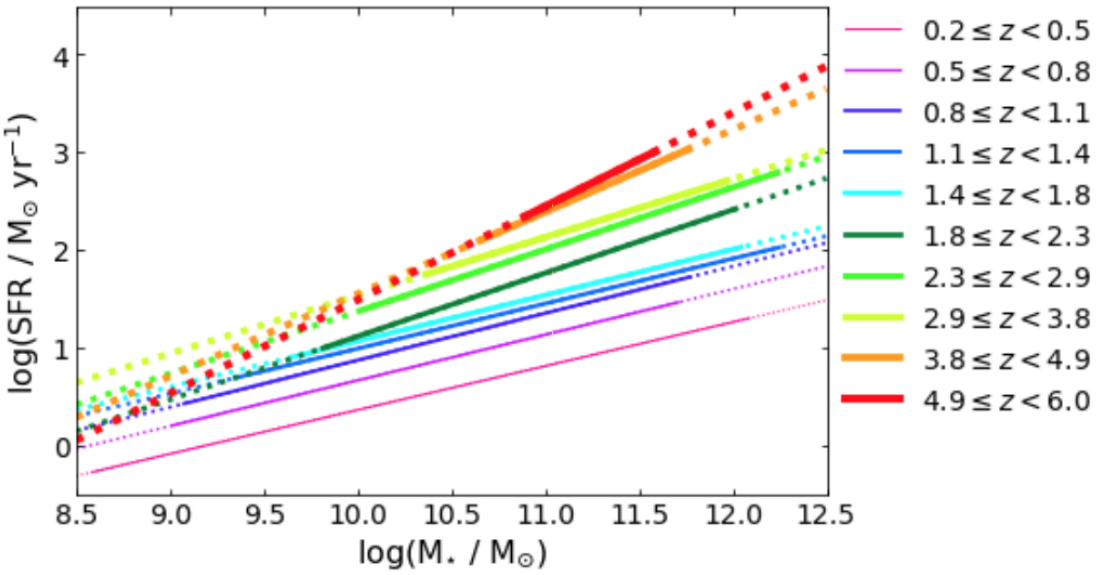

Figure 1.2: A star formation rate (SFR) versus stellar mass (M_*) plot form Pearson et al. (2018). Star forming galaxies at similar redshifts form a tight correlation in this parameter space called the "main sequence of star formation". It represents the level of star formation per unit mass present in galaxies, and shows that in the early Universe, galaxies were forming stars at a greater rate than they are today.

tously detected galaxies that span redshifts from $z \sim 0.5$ to $z \sim 5$, corresponding to $\sim 5 - 12$ billion years ago. Chapters 3 and 4 will focus on a population of nearby ($z \sim 0.1$) galaxies whose properties are much more similar to the very actively star forming galaxies that populated the Universe when it was just about $2 - 6$ billion years old ($z \sim 1 - 3$). These galaxies lie above the MS of star formation at $z \sim 0.1$ and fall on the MS of star formation at $z \sim 2$, indicating they are starbursts in the local Universe and are more similar to MS galaxies at $z \sim 2$.

The following sections will introduce the interstellar medium and star formation and how we trace these with observations; the star formation history of the Universe and galaxies at the epoch of peak star forming activity; and radio interferometry. Finally, I will give an overview of each chapter in this thesis.

1.1 The Interstellar Medium and Star Formation

The interstellar medium (ISM) of galaxies is composed of dust and hydrogen (H) gas that exists in multiple phases, distinguished by the temperature and density at which that gas is found. I will summarize these phases here and the typical physical conditions that are found in each, and refer readers to Draine (2011) for more detailed information.

The hottest phase of the ISM is the hot ionized medium (HIM); it is a diffuse plasma, with proton number densities of $n \sim 10^{-3}$ cm^{-3}, heated by shock-waves from supernova explosions to temperatures of T $\gtrsim 10^{5.5}$ K. The next hottest phase is found around massive hot O-type stars whose ultraviolet (UV) photons photoionize hydrogen and create HII regions. This gas has temperatures of $\sim 10^4$ K and densities up to $n_{\rm H} \sim 10^4$ cm^{-3}. The warm neutral medium (WNM) consists of atomic hydrogen (HI) gas heated by photoelectrons from dust to temperatures of $\sim 10^{3.7}$ K and has densities of $n_{\rm H} \sim 10^{-1}$ cm^{-3}. Similarly, there is a cold neutral medium (CNM) component also consisting of atomic hydrogen, with cooler temperatures (T $\sim 10^2$ K) and higher densities ($n_{\rm H} \sim 30$ cm^{-3}). The subsequent phases become cold and dense enough for molecular hydrogen (H_2) to form. Diffuse H_2 regions are found at temperatures of T ~ 50 K and densities of $n_{\rm H} \sim 10^2$ cm^{-3}, while the densest and coldest regions of the ISM form gravitationally bound structures of H_2 called giant molecular clouds (GMCs), where star formation occurs. The conditions in GMCs range from T $= 10 - 50$ K and $n_{\rm H} \sim 10^3 - 10^6$ cm^{-3}.

While the ISM consists of multiple phases, it is not static; gas transitions

between these phases depending on the physical processes that are acting within it, including photoionization, radiative cooling, and recombination (see e.g., Heiles et al., 1999, for a multi-wavelength view of these phases in the Eridanus superbubble). In this thesis, I will focus on the molecular phase of the ISM and how it relates to the process of star formation.

1.1.1 Dense Molecular Gas and its Tracers

Star formation in galaxies can take place when gas in the ISM cools to sufficiently low temperatures to transition to the molecular hydrogen gas phase: this is the fuel for star formation (Leroy et al., 2008, Schruba et al., 2011). Studies in our own Milky Way and nearby galaxies reveal that star formation specifically takes place in GMCs (McKee and Ostriker, 2007, Kennicutt and Evans, 2012). The outer edges of these clouds consist of mainly HI; however, H_2 begins to form deeper within a cloud (see for e.g., Figure 1(a) in Bolatto et al., 2013) and is protected from dissociation by UV radiation through self-shielding and shielding by dust (Tielens, 2005).

We can observe phases of the ISM by detecting emission of photons from atoms and molecules through their transitions from higher to lower electronic, vibrational, and rotational energy states. However, molecular hydrogen, despite being the most abundant molecule in the Universe, has no observable emission lines in the very cold conditions found in GMCs. Molecular hydrogen is a symmetric molecule composed of two bound hydrogen atoms. The consequence of this is that H_2 has no permanent

dipole moment, and thus can emit no photons through dipolar rotational transitions (Kennicutt and Evans, 2012, Bolatto et al., 2013). The lowest energy rotational quadrupole transition of H_2 has a high upper level energy of $E/k \sim 510$ K; therefore, it is only excited in conditions where the gas is at temperatures of $T \gtrsim 100$ K. The energy of the vibrational transition of H_2 has an even higher upper level energy of $E/k \sim 6741$ K. This means that H_2 is effectively invisible in emission in the very cold and dense GMC conditions.

After hydrogen and helium (He), the most abundant atoms in the Universe are carbon (C) and oxygen (O) at the level of $\sim 10^{-4}$ atoms per hydrogen nucleon (see for e.g., Table 1.4 in Draine, 2011). Within dense molecular clouds, C and O combine to form the next most abundant molecule: carbon monoxide, $^{12}C^{16}O$ (hereafter I will refer to $^{12}C^{16}O$, the most common isotopologue of carbon monoxide, as CO). The ground rotational transition of CO ($J = 1-0$) at a rest frequency of 115.27 GHz (2.6 mm) has an excitation energy of $E/k \sim 5.53$ K, and is thus easily excited within molecular clouds. Higher rotational transitions of CO are spaced at energy levels of $E/k \sim 5.53 \times J\,(J+1)/2$ K and frequencies increasing by ~ 115 GHz. Therefore, the low- and mid-J transitions of CO occur in the submillimeter wavelength regime of the electromagnetic spectrum and are observable from the ground with instruments such as the Very Large Array (VLA) and the Atacama Large Millimeter/submillimeter Array (ALMA). Since CO was first observed (Wilson et al., 1970) and established to be widespread within the inner Milky Way (Solomon et al., 1972, Wilson et al., 1974, Burton et al., 1975), it has become the primary tracer of H_2 in galaxies (Carilli and Walter, 2013).

To extract the molecular gas mass in a galaxy from observations of the ground CO transition, it is necessary to scale the integrated luminosity of the emission line with a "CO-to-H_2" conversion factor, α_{CO}. The CO-to-H_2 conversion factor depends on environmental factors such as metallicity, temperature, density, and column density (Leroy et al., 2011, Feldmann et al., 2012, Genzel et al., 2012, Narayanan et al., 2012); therefore, there is uncertainty when choosing a value to adopt. The CO-to-H_2 conversion factor ranges from $\alpha_{CO} = 3.6 - 4.3\ M_\odot\,pc^{-2}\,(K\,km\,s^{-1})^{-1}$ in Milky Way type galaxies, to $\alpha_{CO} = 0.6 - 0.8\ M_\odot\,pc^{-2}\,(K\,km\,s^{-1})^{-1}$ for starbursts (Downes and Solomon, 1998, Papadopoulos et al., 2012).

In addition to environmental factors that may impact the value of α_{CO} and introduce uncertainty in deriving molecular gas masses, the uncertainty in the CO spectral line energy distribution (SLED) in different galaxy populations at different redshifts also poses a challenge, where the CO SLED quantifies the excitation of higher-J CO transitions with respect to the ground, CO(J = 1 − 0), transition. A difficulty with attempting to quantify the molecular gas content of high-redshift galaxies is that the CO-to-H_2 conversion factor depends upon the luminosity of the CO(J = 1 − 0) transition. However, this is only observable up to redshifts of $z \sim 0.5$ with ALMA, at redshifts of $z > 2$ with the VLA for the brightest sources, and is observable for example with the Green Bank Telescope and the Effelsberg 100 m Radio Telescope with the proper receiver bands. Therefore, to observe CO in normal star forming galaxies across a large range in redshift, one must resort to observing higher-J transitions of CO and then assume a line ratio between the observed line and the ground transition.

In Chapter 2, I will use observations of CO(2−1) to CO(6−5) to constrain the evolution of molecular gas content in galaxies over time, while in Chapter 4, I will use observations of CO(3−2) and CO(4−3) to study the relation between star formation and gas, and help constrain theories of star formation.

1.1.2 Star Formation and its Tracers

While observations of CO allow us to characterize the molecular gas reservoirs of galaxies, it is also necessary to quantify the rate of star formation itself. There are several tracers of star formation that can be used to determine how rapidly galaxies are forming stars; I summarize a few of these here and refer readers to Kennicutt (1998b) and Mo et al. (2010) for more details.

The ISM around massive, young stars is ionized by the UV photons they produce, creating HII regions. The recombination of hydrogen nuclei and electrons to atomic hydrogen produces a cascade of emission lines as electrons transition from excited energy states to the ground state, including Hα, Hβ, Paα, Paβ, Brα, and Brγ. The flux of these emission lines is thus proportional to the ionizing flux from the young, massive stars, and can be used as a probe of star formation activity; i.e., because massive stars are short-lived, the amount of emission in these lines is related to recent star formation. Specifically, because hydrogen is ionized at an energy of 13.6 eV and only stars with $M_* \gtrsim 10$ $M_\odot$ and lifetimes shorter than ~ 20 Myr contribute significantly to the ionizing photon flux, these emission lines are a nearly instantaneous measure of star formation. The most commonly used

line to measure SFRs is Hα; there are, however, two caveats associated with this: (1) dust absorption of Hα flux may not necessarily be negligible; this reduces the observed flux and underestimates the true SFR, and (2) the calibration between Hα flux and SFR depends on the initial mass function (IMF) of stars which is an empirical description of the distribution of stellar masses in a population of stars. Typically, there are fewer massive stars and many more lower mass stars that form in a given population of stars. A related tracer of star formation is the UV luminosity of a galaxy, optimally over the wavelength range $1250 - 2500$ Å. Because the UV light from galaxies is dominated by stars with $M_* \gtrsim 5\ M_\odot$, the UV luminosity can be related to the SFR. However, using UV luminosity as a tracer of star formation suffers from the same caveats as using Hα as a tracer.

A significant fraction ($35 \pm 3\%$; Driver et al., 2012) of the total luminosity of a galaxy is absorbed by dust and re-radiated in the far-infrared (FIR) regime of the electromagnetic spectrum, because much of the star formation in the Universe takes place in regions that are deeply embedded in dust. The absorption cross-section of dust peaks in the UV, which means that young, massive stars are in principle the dominant heating source of dust, and the FIR emission of a galaxy can then be used to trace its star formation. There are of course caveats with this method as well. The FIR emission is not only attributable to the reprocessed UV radiation of young stars by dust around star forming regions, but also to more extended dust regions heated by the general stellar radiation field, including radiation from older stars. Therefore, using the FIR luminosity as a SFR tracer is ideal in starburst galaxies which can form stars at rates of $100 - 1000\ M_\odot\,\mathrm{yr}^{-1}$.

The FIR emission of a galaxy is observed to correlate with fine-structure forbidden emission lines of atoms like carbon and as a result, these can also be used as SFR tracers. For example, the singly ionized carbon fine-structure line at 158 μm, [CII], has an excitation energy of ~ 91 K and is one of the dominant coolants of the neutral ISM. It arises from the photodissociation regions (PDRs) of molecular gas in massive star-forming regions, where the UV radiation of young stars is absorbed by dust and re-radiated at longer wavelengths, giving rise to the FIR continuum, as discussed above (though it may also arise from HII regions and neutral atomic hydrogen gas). These same UV photons eject electrons from dust grains and polycyclic aromatic hydrocarbons, which heat the gas and collisionally excite the [CII] line, allowing the gas to cool through emission of [CII] photons. Because the excitation of the [CII] is closely linked to the UV radiation field, it can also be used as a tracer of star formation (see e.g., Herrera-Camus et al., 2015). Similarly, the [OIII] fine-structure line at 88μm, which has an excitation temperature of T ~ 163 K and an ionization energy of ~ 35 eV, originates from the vicinity of a very hard ionizing source like HII regions hosting massive stars. Since the most massive stars spend $\sim 3-10$ million years on the main sequence, [OIII] line emission can also be related to recent star formation (see e.g., De Looze et al., 2014).

Finally, additional SFR tracers include emission at radio wavelengths which correlate linearly with IR emission (Bell, 2003) and X-ray emission of galaxies originating from high-mass X-ray binaries (Mineo et al., 2012). In Chapter 4, I will use observations of Hα to measure the SFRs of nearby galaxies and study the relation between gas and star formation.

1.2 Star Formation and Gas Content History of the Universe

Galaxies consume their molecular gas reservoirs through star formation, and in doing so build up their stellar mass. Yet, to fuel ongoing star formation, gas must be replenished. The gas content, star formation, and stellar mass of galaxies are properties that we can quantify with observations across cosmic time. Measuring the combination of these properties across the history of the Universe enables astronomers to build an understanding of how these processes act together to produce the galaxies that we observe today (see e.g., Walter et al., 2020).

Employing UV and IR observations in galaxies across time has enabled astronomers to trace how the magnitude of star formation has evolved in galaxies; this is the star formation history of the Universe. It is measured as the total amount of star formation in galaxies per unit of comoving volume of the Universe, which corresponds to a SFR volume density ($M_\odot\,yr^{-1}\,Mpc^{-3}$). These observations reveal that the process of star formation in galaxies peaked about 10 billion years ago. Figure 1.3 shows the SFR density evolution over more than 12 billion years. We can see that from very early times, star formation in galaxies was increasing until it reached its peak roughly 10 billion years ago, $z \sim 1-2$, and it has since then been steadily decreasing up until the present day (see Lilly et al., 1995, Madau et al., 1996, Hopkins and Beacom, 2006, Madau and Dickinson, 2014, Bouwens et al., 2016, 2020, Loiacono et al., 2021). It is during this period of peak cosmic star forming activity that roughly half of the stars in the Universe formed. There are several fundamental physical processes that can shape this evolution: (1) if high-redshift

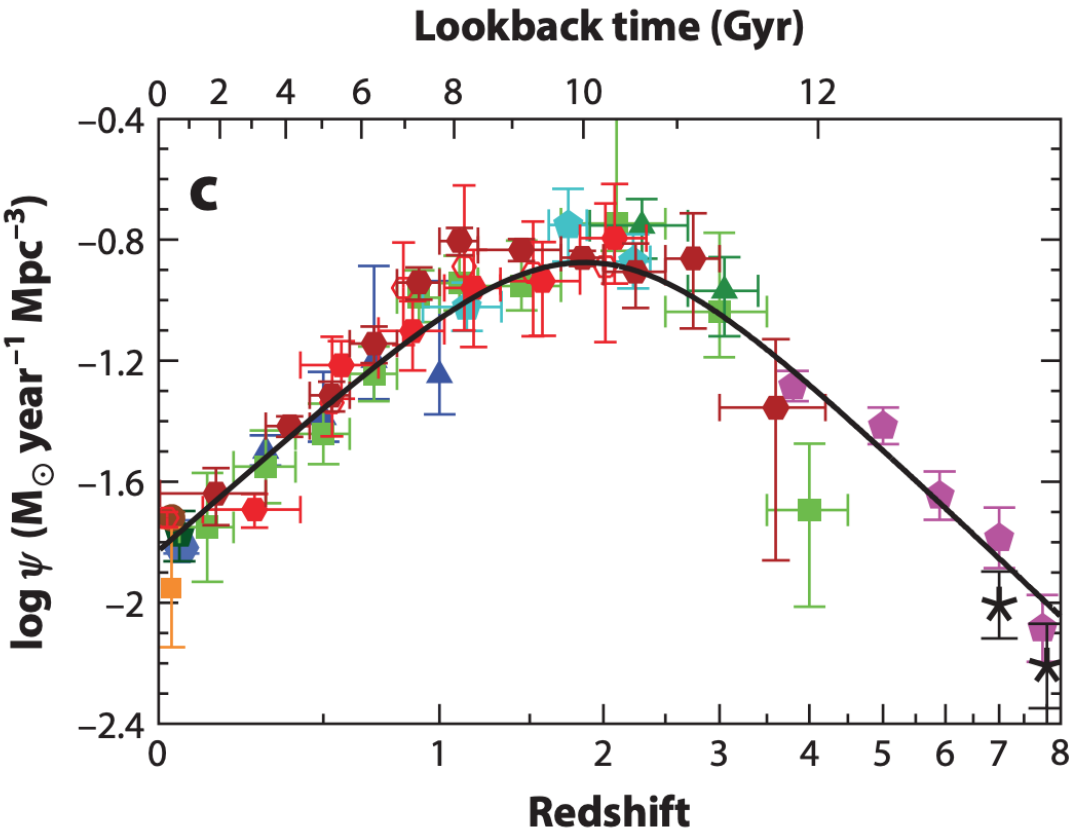

Figure 1.3: The total SFR in galaxies per unit comoving volume of the Universe as a function of redshift (or lookback time), derived from UV and IR observations (from Madau and Dickinson, 2014, see their Table 1 for a description of the symbols). Star formation in galaxies peaked about 10 billion years ago ($z \sim 1-2$), and has been steadily decreasing to the present day. Studying the neutral and molecular gas content of galaxies over time can build our understanding of how galaxies consume and replenish their star forming fuel, and build up their stellar mass (Walter et al., 2020).

galaxies have larger reservoir of molecular gas, then this can fuel more vigorous star formation, (2) if high-redshift galaxies convert their molecular gas into stars with a higher efficiency, then this could also translate into a higher stellar mass build up in the past, and (3) the growth rate of dark matter halos dropped by an order of magnitude from $z = 2$ to $z = 0$ (Griffen et al., 2016), which can impact the ability of galaxies to replenish their supply of gas.

The HI content in galaxies over time can be constrained by observing Lyα absorption in the spectra of distant quasars (see e.g., Crighton et al., 2015, Neeleman et al., 2016). These studies show the mass density of HI in galaxies from $z \sim 0.3 - 5$ decreases very gradually, unlike the cosmic SFR density evolution. This indicates that HI is a transitory phase between ionized gas accreted from the intergalactic medium and recycled gas from galactic outflows, and the H_2 that actually fuels star formation. Beyond the local Universe, however, studies of the H_2 content in galaxies over time have been limited, and have only recently begun to emerge. Therefore, to fully understand the evolution of the cosmic star formation history, it is imperative to constrain the mass density of molecular gas in galaxies over cosmic time.

The very first attempts to constrain this density involved the use of galaxies targeted and observed in carbon monoxide (CO), the most common tracer of H_2 (see §1.1.1). As part of her thesis work, Verter (1987) observed 19 galaxies in CO with the 7 m diameter offset Cassegrain antenna of Bell Laboratories at Crawford Hill. Combining these observations with 56 CO detections and 189 upper limits from the literature, Verter (1987) derived average CO luminosity values and discovered a trend of increasing number density of CO-emitting galaxies with decreasing galaxy

CO luminosity.

Owing to the large number of upper limits, it was not until a few years later when surveys like the Five College Radio Astronomy Observatory (FCRAO) Extragalactic Survey (Young et al., 1995) became available, that the CO luminosity function could be constrained (Verter, 1991, Keres et al., 2003). These studies selected galaxies based on optical magnitudes or infrared (IR) fluxes and constrained the CO$(1-0)$ luminosity function in the local universe (see e.g., Figure 4 in Keres et al., 2003). While these studies mark the first important steps in addressing the question of how molecular gas content in galaxies over time relates to the star formation history of the universe, they are subject to selection biases. For example, the correlation between IR luminosity and CO luminosity favours luminous galaxies if they are selected based on an infrared flux cutoff (see e.g., Figure 2 in Tacconi and Young, 1987).

More recently, galaxies detected in CO at higher redshifts were initially selected from rest-frame far-infrared continuum surveys as sub-millimeter galaxies (Blain et al., 2002, Casey et al., 2014). These studies have shaped our understanding of the relation between molecular gas content and star formation in known populations of galaxies. For example, targeted CO studies find that $z \sim 2$ galaxies have much larger molecular gas reservoirs than local galaxies and that the changes in growth history are largely driven by the cold molecular gas mass properties of galaxies (Greve et al., 2005, Daddi et al., 2010a, Genzel et al., 2010, 2015, Tacconi et al., 2010, 2013, 2018, Freundlich et al., 2019). While these types of studies allow us to understand the properties of galaxy samples, they are also subject to systematic

biases through selection effects (see for example Strandet et al., 2016).

These selection effects are the reason that studies whose goal it is to constrain the cosmic evolution of molecular gas mass density have shifted to "blind" CO surveys where galaxies are selected solely on their CO luminosity. The observing strategy is to perform spectral scans on specific deep fields, targeting rotational transitions of CO over wide frequency and redshift ranges, and carrying out blind searches for CO-emitting galaxies in the data. The detections are then used to measure the CO luminosity function at different epochs in the history of the universe, resulting in a measurement of the molecular gas mass density over the range of redshifts sampled by the observations (Carilli and Walter, 2013). The first efforts that have implemented this strategy (see Decarli et al., 2014, Walter et al., 2016, for survey descriptions) provide some of the first constraints on the cosmic molecular gas mass density evolution, and suggest that the molecular gas mass density of the universe follows a similar pattern of evolution as the cosmic star formation density, but are limited by the small comoving volume of space sampled and the small number of sources detected (Walter et al., 2014, Decarli et al., 2016).

To address this, more recent studies have devoted several hundred hours of VLA and ALMA time (Pavesi et al., 2018, González-López et al., 2019) and have made significant improvements in terms of survey size; yet the number of sources detected (Riechers et al., 2019, Decarli et al., 2019) continues to be a large source of uncertainty, and the time required to observe large fields (100s of hours) is expensive for current facilities (the next generation VLA[2] will be able to address this within

[2]See also https://public.nrao.edu/news/nsf-awards-funding-ngvla-antenna/

the next decade; Walter et al., 2019). To remedy this, in the first chapter of my thesis, I explore the feasibility of using existing observations of targeted galaxies to perform a "blind" search for serendipitous CO sources (see also Klitsch et al., 2019). Re-using existing data for this purpose provides an alternative way to build up a large co-moving volume of space for exploration, as long as there is existing ancillary data that can be used to find counterparts to CO sources and constrain their redshifts (and hence CO transitions). The second Plateau de Bure High-z Blue Sequence Survey (PHIBSS2; Freundlich et al., 2019) data set is very well suited to this purpose.

Finally, galaxies in the era of peak mass assembly are characterized by massive ($10^7 - 10^9$ $M_\odot$), kpc-sized, star forming clumps (Genzel et al., 2008, 2011, Förster Schreiber et al., 2011, Tacconi et al., 2013, Guo et al., 2012, 2015, Huertas-Company et al., 2020). This mode of star formation is very different from what is observed in the local Universe. Therefore, to understand star formation in the time when a significant fraction of stars in the Universe formed, we need to understand star formation at the peak of cosmic star forming activity. Studies of high-redshift, lensed, clumpy systems (Livermore et al., 2015) and nearby analogues (Fisher et al., 2017b) reveal that the physical size of clumps may be smaller than originally inferred from high-redshift observations, and that this is a result of limitations in angular resolution which cause multiple smaller clumps to blend and appear as one massive clump. The size and mass of clumps are important parameters, because these relate to their ability to withstand stellar feedback and remain intact, and determine their lifetime. Hydrodynamic simulation studies are actively seeking to characterize the

properties of star forming clumps (see e.g., Oklopčić et al., 2017, Buck et al., 2017, Dekel et al., 2021, Ginzburg et al., 2021); however, observations are ultimately required to place constraints on the real observed properties of clumps. For this reason, in Chapters 3 and 4, I turn my attention to a sample of nearby galaxies drawn from the DYnamics of Newly Assembled Massive Objects (DYNAMO; Green et al., 2014). These are clumpy, gas-rich systems that are much more similar to clumpy high-redshift galaxies than they are to local ones. The benefit of using them as proxies to understanding high-redshift galaxies is that we can obtain much higher resolution observations that can probe their properties on the scale of individual clumps.

1.3 Radio Interferometry and Synthesis Imaging

The angular resolution (θ) of a telescope determines the smallest sized object on the sky that the telescope can resolve. This depends on the wavelength of the observed light (λ), and the diameter of the telescope light collecting area (D) through the relation: $\theta \sim \lambda/D$. This means that in order for a telescope operating at long wavelengths to have the same angular resolution as a telescope operating at short wavelengths, a bigger telescope is required. To illustrate, a 100 m diameter telescope observing at 7 mm will have an angular resolution of $\sim 17''$ (where 1 arcsecond is equal to $1^\circ/3600$ Thompson et al., 2017). In contrast, the *Hubble Space Telescope* (HST) observations I present in Chapters 3 and 4 have angular resolution of $\sim 0.1''$.

The largest radio telescopes, the Five-hundred-meter Aperture Spherical Tele-

scope (FAST) in China and the now decommissioned Arecibo Telescope (305 m) in Puerto Rico, are placed within natural depressions in the landscapes, and are thus unable to observe portions of the sky. The Effelsberg 100 m diameter radio telescope, and Green Bank Telescope in West Virginia with a 100 m diameter (the largest steerable radio telescope), are still not enough to reach the sub-arcsecond resolution of telescopes like the HST. To achieve better angular resolution at long wavelengths, it is necessary to employ a different approach. Interferometry is one such approach and will be discussed in the remainder of this section (see Condon and Ransom, 2016, Thompson et al., 2017, for more detailed discussions).

1.3.1 Interferometry Basics

The simplest radio interferometer consists of two antennas separated by some baseline distance, B, as illustrated in Figure 1.4. In this illustration, two antennas (i and j) are separated by a distance $\vec{B}_{ij}$. A plane parallel wavefront (an electric field with some amplitude and phase) from a distant point source in the direction $\vec{d}$ reaches the antenna on the right first, then after a geometric time delay of $\tau_{ij} = \vec{B}_{ij} \cdot \vec{d}/c$, the wavefront reaches the second antenna. We can write the time dependent voltage output of each antenna as:

$$V_i = V \times \cos(2\pi\nu(t + \tau_{ij})) \quad \text{and} \quad V_j = V \times \cos(2\pi\nu t) \tag{1.1}$$

for the left and right antennas respectively, where V is an amplitude and ν is the observing frequency. If we assume that the interferometer operates over a very

narrow range of frequencies, then the voltage output of each antenna has the same amplitude, and they are only offset in phase by τ_{ij}. The correlator multiplies the two voltages, V_i and V_j, and after integrating (time averaging) it outputs a response, R_c:

$$R_c = \frac{V^2}{2} \times \cos(2\pi\nu\tau_{ij}). \tag{1.2}$$

The interferometer, therefore, produces an interference pattern, called fringes, which depends only on the power received ($P = V^2/2$), the time delay (therefore the baseline orientation and source direction), and the observing frequency.

Because the geometric time delay depends on the separation between the two antennas, the fringe spacing then also depends on this distance; moving the antennas farther apart moves the fringes closer, and vice versa. However, for an extended source, the antenna is unable to see the components of the source that fall between the fringes. This can be addressed by the use of a complex correlator, which consists of two correlators 90° out of phase, so that one produces a cosine fringe pattern, and the other a sine fringe pattern. The second correlator in this case produces a response like equation 1.2, but with a sine function:

$$R_s = \frac{V^2}{2} \times \sin(2\pi\nu\tau_{ij}). \tag{1.3}$$

The response of the complex correlator is then the combination of these two responses:

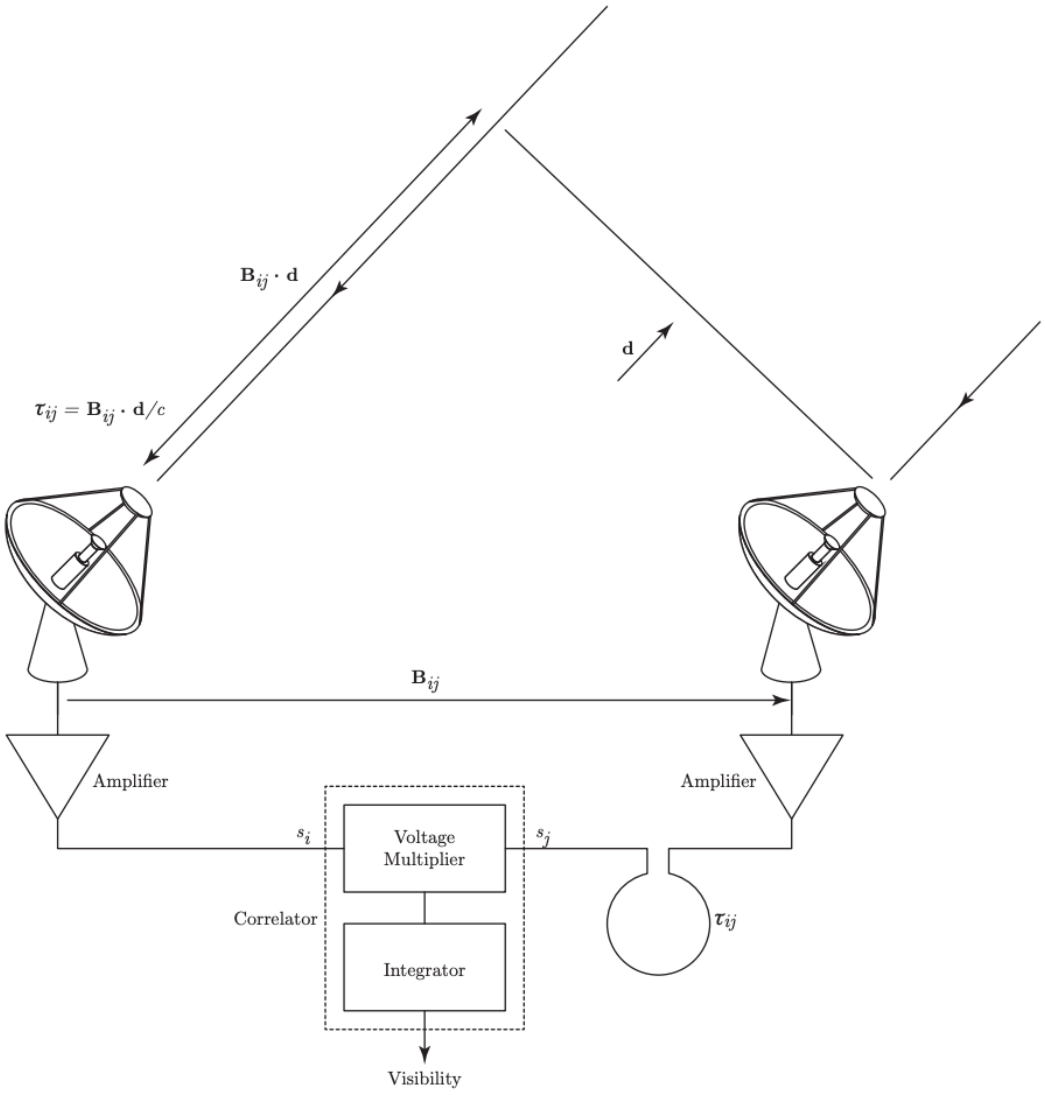

Figure 1.4: Illustration of a two element interferometer, separated by a baseline distance D, observing a source in the direction θ. The source is assumed to be distant enough that the incident wavefront can be assumed to be a plane. Thus, the incident wave reaches the antenna on the right before it reaches the one on the left; this introduces a geometric time delay. The signal from each antenna is then amplified, a instrumental time lag equal to the geometric time lag is introduced in the signal from the right antenna, then the signals of both antennas are multiplied and time-averaged by the correlator (adopted from Figure 1 in Mahmoud et al., 2011).

$$V = R_c - iR_s = A\, e^{-i2\pi\nu\tau_{ij}} = A\, e^{-i2\pi(\vec{B}_{ij}\cdot\vec{d}/\lambda)} \tag{1.4}$$

where in the final equality, we replace the geometric time delay with its dependence on the baseline and source direction vectors, and replace ν/c with $1/\lambda$ to define the baseline in units of wavelength. We can define a coordinate system (u,v,w) to describe the baseline vector in units of wavelength, where u is the component of $\vec{B}_{ij}/\lambda$ along the east-west direction, v is its component along the north-south direction, and w is the vertical (up-down) component. Similarly, we can define the source direction vector, $\vec{d}$, in (l, m) coordinates where l is the east-west direction cosing and m is the north-south direction cosine on the sky. If we assume that w is parallel to $\vec{d}$, then we can expand the dot product in equation 1.4 and integrate over the whole source on the sky to obtain:

$$V(u,v) = \int\int P(l,m)\, I(l,m)\, e^{-i2\pi(ul+vm)}\, dl\, dm \tag{1.5}$$

where $P(l,m)$ is a function that describes the "primary beam" of the telescope, $I(l,m)$ is the source brightness distribution on the sky, and $V(u,v)$ is the response of the complex correlator, called the "visibility". The primary beam for an array of antennas of equal diameter, D, observing at a wavelength λ, is equal to a Gaussian function with a full width at half maximum of $\sim \lambda/D$. The sky is always seen through the filter of the telescope primary beam; therefore $P(l,m)\, I(l,m)$ is the source brightness perceived by the telescope. We can recognize the expression in equation 1.5 as a Fourier Transform of the sky, which means that to obtain the

source intensity, $I(l, m)$, we can perform an inverse Fourier Transform:

$$A(l, m)\, I(l, m) = \int \int V(u, v)\, e^{-i2\pi(ul+vm)}\, du\, dv. \tag{1.6}$$

However, a single baseline defines only one point in the $uv-$plane, and thus measures the source on a spatial scale and direction determined by the antenna separation – the telescope cannot "see" any emission from the source on other scales. Therefore, to properly observe a source that has emission on multiple scales, like a galaxy, we need to sample many more points in the $uv-$plane. This is done by increasing the number of antenna pairs. For N number of antennas, there will be $N(N-1)/2$ antenna pairs, and therefore $N(N-1)$ baselines, each of which corresponds to an additional point in the $uv-$plane. Each pair of antennas will produce a different fringe spacing and direction, depending on the length of the baseline distance and orientation relative to the source. This fills in the sampling of the source in the Fourier domain and allows for better recovery. By observing for longer periods of time, we can also take advantage of the Earth's rotation. As the Earth rotates, the orientation of each baseline with respect to the sky changes, which further fills in the $uv-$plane. This is illustrated in Figure 1.5, which shows the sampling of the $uv-$plane by the Atacama Large Millimeter/sub-millimeter Array (ALMA), which has 66 antennas, after observing a source at a declination of $\delta = -23°$ for one minute (left panel) and one hour (right panel).

Because the visibilities measured by an interferometer are related to the source intensity via a Fourier Transform, an interferometer is essentially a spatial filter,

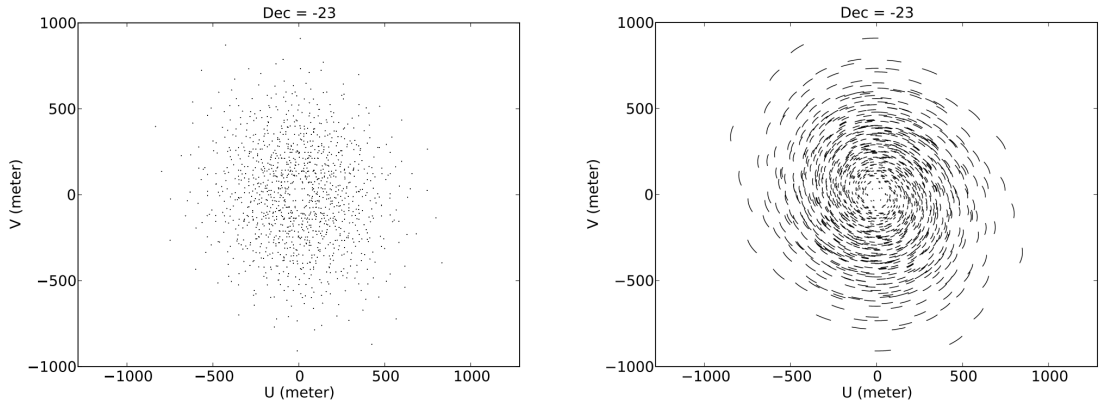

Figure 1.5: An example of the $uv-$ plane sampling for a model ALMA observation of a source at declination $\delta = -23°$ after one minute of observing (left panel) and one hour of observing (right panel). The Earth rotates over the course of the longer observation, and thus each point in the $uv-$plane "stretches out" as the orientation of each baseline changes with respect to the sky. However, the hole at $(u, v) = 0$ can never be filled because the spacing between antennas can never be zero. (adopted from Figure 7.10 in the ALMA Technical Handbook).

where the filtering is set by the separation between antenna pairs. The smallest angular scale at which an interferometer can detect emission is determined by the largest antenna separation, while the largest scale emission is determined by the smallest antenna separation. This means that because the separation between antennas can never be zero, an interferometer cannot measure the total flux of a source, and the measured source flux will always be less than the true source flux. This also means that the angular resolution (θ) of an interferometer is set by the largest distance between any two antennas: $\theta \sim \lambda/B$, where λ is the observing wavelength and B is the length of the longest baseline. Interferometry allows us to "synthesize" a telescope whose aperture diameter is the longest baseline, baselines much longer than would be possible in a single aperture. This is the strength of interferometry, and what allows astronomers to study objects in the Universe at sub-millimeter and radio wavelengths in incredible detail.

1.3.2 Deconvolution

As with any telescope, the image obtained is a convolution of the true source brightness distribution (enveloped by the primary beam for an interferometer) and the point spread function (PSF; the Fourier Transform of the interferometer's measurements in the $uv-$plane), or "dirty beam", and is often called the "dirty map". We can, therefore, modify equation 1.6 to reflect this:

$$P(l,m)\, I(l,m) \circledast G(l,m) = \int\int g(u,v)\, V(u,v)\, e^{-i2\pi(ul+vm)}\, du\, dv. \tag{1.7}$$

where $G(l,m)$ is the dirty beam, which for an interferometer is determined by the Fourier Transform of the $uv-$plane sampling by the antenna array, and $g(u,v)$ is the weighting function of the sampled $uv-$plane points (e.g., natural, uniform, Briggs weighting). As a result of this convolution, the dirty map will have the pattern of the dirty beam imprinted in it. This can make interpretation of the dirty map difficult, because the dirty beam causes flux from the source to be distributed in "sidelobes" and other artefacts that do not represent real structure. It is, therefore, desirable to remove the dirty beam pattern from the image or to deconvolve it from the image.

There are several deconvolution procedures; however, the CLEAN method forms the basis of many deconvolution algorithms that are used in radio interferometry today. The Högbom CLEAN, which I will use in Chapter 4, assumes that the

sky brightness distribution can be modeled by a collection of point sources, and it operates in the image domain (the Fourier Transform of the visibilities). Figure 1.6 illustrates the basic idea for a one-dimensional case[3]. Panels A and B of Figure 1.6 show the dirty map and dirty beam, respectively, of this mock observation, where the oscillations beyond the main lobe of the dirty beam are visible in the dirty map as well.

The algorithm operates iteratively where in each step it: (1) finds the peak amplitude in the dirty map and stores that as a "clean component" (panel E), (2) it then scales the dirty beam by a "loopgain" factor $\gamma \ll 1$, (3) it shifts the scaled beam to the position of peak amplitude in the dirty map (panel C), (4) the scaled and shifted dirty beam is then subtracted from the entire dirty map which produces the residual map (panel H), (5) steps (1)$-$(4) are then repeated until a specified threshold is reached; this can be when the root-mean-square (rms) of the residual map reaches some level (panel D), or until a defined limit on the number of iterations is reached, (6) finally once the threshold is reached, the procedure convolves the clean components with the clean beam (panel F) to produce a "clean signal" (panel G), and adds the final residuals to this clean signal to produce the final "clean map" (panel I). We can see that the final clean map recovers the two signals that we see in the original dirty map, but the pattern of the dirty beam has been removed.

The clean beam in step (6) is a Gaussian function fit to the main lobe of the dirty beam. For two-dimensional maps, this will generally be an elliptical Gaussian.

[3]This is thanks to Andy Harris' instrumentation class where we had to write code to do this for an assignment!

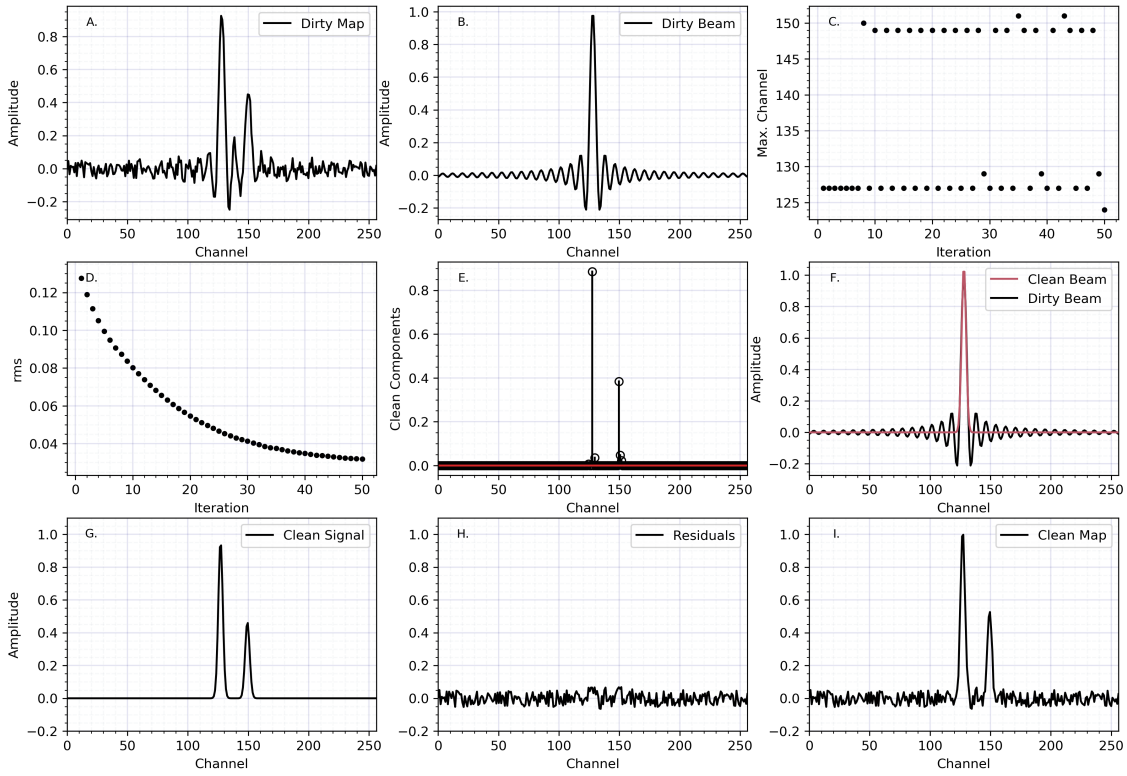

Figure 1.6: A one-dimensional illustration of the Högbom CLEAN algorithm with a loopgain $\gamma = 0.1$, after 50 iterations. In each iteration, the algorithm subtracts a scaled down version of the dirty beam (panel B) from the dirty map (panel A) at the location of the peak amplitude (panel C) in the dirty map. This subtracted map is the residual (panel H) and the peak is saved as a "clean component" (panel E). This process continues until a threshold is reached: for example when the root-mean-square of the residual map reaches a specified threshold (panel D). Once the threshold is reached, the clean components are convolved with the clean beam (panel F) to produce the clean signal (panel G). Adding the residuals to the clean signal produces the final clean map (panel I).

The beam size is defined by the major (θ_{maj}) and minor (θ_{min}) axes of the ellipse at the FWHM of the Gaussian, and its area (Ω) is defined by:

$$\Omega = \frac{\theta_{maj}\,\theta_{min}}{4\ln 2}. \tag{1.8}$$

In reality, programs such as the Common Astronomy Software Application (CASA; McMullin et al., 2007) employ a major/minor cycle approach to deconvolution where the minor cycles perform multiple iterations of CLEAN in the image domain, and the major cycles subtract the model image from the visibilities in the $uv-$domain to produce a new residual map. Beside the Högbom algorithm, there are additional versions of CLEAN such as the Clark CLEAN (Clark, 1980) and the Cornwell-Holdaway Multi-Scale CLEAN (Cornwell, 2008). Besides CLEAN, there are additional deconvolution methods such as the Maximum Entropy method (Cornwell and Evans, 1985, Narayan and Nityananda, 1986) and Adaptive Scale Pixel method (Bhatnagar and Cornwell, 2004).

Regardless of the deconvolution procedure adopted, the final data products from an interferometer are three-dimensional "data cubes", where the x and y directions are the spatial dimensions corresponding to the position on the sky, and the z direction is the spectral dimension, where every "channel" is a measurement of the sky at a particular frequency (or equivalently a particular wavelength or velocity). As a result, every pixel in a data cube (referred to as a "voxel") contains a spectrum of the source at a particular (x, y) location. These are the data products that I will use in Chapters 2 and 4.

1.4 Thesis Overview

This thesis consists of multi-wavelength studies, spanning from the UV/optical to the sub-millimeter, that characterize the gas content of galaxies across cosmic time, and links the gas content of nearby, high-redshift analogue galaxies to their star formation.

In Chapter 2, I explore and test the feasibility of using existing large survey data to constrain the molecular gas content in galaxies over cosmic time. PHIBSS2 observed ~ 100 galaxies in CO at the peak of cosmic star forming activity. Additional "sources" were noted in several resulting data cubes. Therefore, I devised a systematic approach to detect these serendipitous sources, identify potential counterparts and constrain their redshifts, and characterize their properties, including the reliability of each detection. With a final catalog of sources, I constructed CO luminosity functions and derived the evolution of the molecular gas mass density of galaxies up to redshifts of ~ 5. These results probe a comoving volume of space larger than any previous survey dedicated to this evolution, and found that the results obtained in this way are consistent with existing measurements.

In Chapter 3, I use HST observations of star forming clumps in DYNAMO galaxies to constrain their lifetimes. Hydrodynamic simulations of star formation in clumpy galaxies at $z \sim 1-3$ are very sensitive to the feedback prescription implementations, resulting in clumps that are disrupted on very short timescales and have no impact on the evolution of these galaxies, to clumps that remain bound for timescales $\gtrsim 100$ Myr and are able to migrate and coalesce at the centers of galaxies,

thus contributing to the growth of bulges. I conclude that clumps in DYNAMO galaxies have colours most consistent with age spreads predicted by simulations of long-lived clump scenarios, which challenges the predictions that clumps disrupt on very short timescales.

In Chapter 4, I combine HST and ALMA observations to measure the SFR and molecular gas mass surface densities, and velocity dispersions of DYNAMO galaxies on $\sim 1-2$ kpc scales to test theories of star formation. I find that throughout their disks, DYNAMO galaxies have velocity dispersions, gas and SFR surface densities comparable to the centers of nearby galaxies. This suggests that large-scale turbulent mechanisms, such as gas accretions and inflows, may be responsible for the higher velocity dispersions and higher gas densities in DYNAMO galaxies. In addition, I find that current theoretical models relating velocity dispersion to gas and SFR surface densities are unable to predict the velocity dispersions in our DYNAMO sample due to the inclusion of the angular velocity as a representation that turbulence dissipates on eddy timescales. This suggests that an alternative timescales for turbulent dissipation for galaxies in our sample is required to explain our observations.

Finally, I summarize a few upcoming and planned research directions that build upon this thesis and that I will pursue as a post-doctoral researcher at NASA Ames, in Chapter 5.

Chapter 2: Cosmic Evolution of Molecular Hydrogen Gas Mass Density

2.1 Overview

We report on the results of a search for serendipitous sources in CO emission in 110 cubes targeting CO $(2-1)$, CO $(3-2)$, and CO $(6-5)$ at $z \sim 1-2$ from the second Plateau de Bure High-z Blue-Sequence Survey (PHIBSS2). The PHIBSS2 observations were part of a 4-year legacy program at the IRAM Plateau de Bure Interferometer aimed at studying early galaxy evolution from the perspective of molecular gas reservoirs. We present a catalog of 67 candidate secondary sources from this search, with 45 out of the 110 data cubes showing sources in addition to the primary target that appear to be field detections, unrelated to the central sources. This catalog includes the redshifts, line widths, fluxes, as well as an estimation of their reliability based on their false positive probability. We perform a search in the 3D-HST/CANDELS catalogs for the secondary CO detections and tentatively find that $\sim 64\%$ of these have optical counterparts, which we use to constrain their redshifts. Finally, we use our catalog of candidate CO detections to derive the CO $(2-1)$, CO $(3-2)$, CO $(4-3)$, CO $(5-4)$, and CO $(6-5)$ luminosity functions

over a range of redshifts, as well as the molecular gas mass density evolution. Despite the different methodology, these results are in very good agreement with previous observational constraints derived from blind searches in deep fields. They provide an example of the type of "deep field" science that can be carried out with targeted observations.

2.2 Introduction

Detailed measurements of the star formation history of the universe reveal that the process of galaxy assembly peaked about 10 billion years ago. The star formation rate (SFR) density in galaxies (i.e., total SFR in galaxies in a comoving volume of the universe) across cosmic time is observed to gradually increase to redshifts of $z \gtrsim 2$, peak at $z \sim 1-2$, and then decrease from redshifts of $z \sim 1$ to the present day by almost an order of magnitude (see e.g., Madau and Dickinson, 2014). The fundamental physical processes that shape this evolution, however, are still uncertain. This evolution may be driven by the availability of larger reservoirs of cold dense molecular gas (the immediate fuel for star formation) in high-z galaxies, by higher efficiencies for converting molecular gas into stars, or by a combination of both. Therefore, it is interesting to constrain the molecular gas content of galaxies over cosmic time (measured as total gas mass per co-moving volume) in order to understand the evolution of the cosmic star formation history.

Most studies of the cold molecular gas in galaxies have used CO observations, the most common molecular gas mass tracer (Bolatto et al., 2013), of galaxies that

were pre-selected based on optical or near-infrared surveys. Other galaxies detected in CO at higher redshifts were initially selected from rest-frame far-infrared continuum surveys as sub-mm galaxies (Blain et al., 2002, Casey et al., 2014). These studies have shaped our understanding of the relation between molecular gas content and star formation in known populations of galaxies. Targeted CO studies find that $z \sim 2$ galaxies have much larger molecular gas reservoirs than local galaxies (Greve et al., 2005, Daddi et al., 2010a, Genzel et al., 2010, 2015, Tacconi et al., 2010, 2013, 2018, Freundlich et al., 2019) and that the changes in growth history are largely driven by the cold molecular gas mass properties of galaxies. While these types of studies allow us to understand the properties of galaxy samples, they can potentially introduce unknown systematic biases through selection effects. It is therefore beneficial to complement them with blind searches for CO-emitting galaxies.

Spectral scans on specific deep fields have been used to carry out blind searches targeting rotational transitions of CO over wide frequency and redshift ranges, measuring the CO luminosity function at different epochs in the history of the universe. The CO luminosity function so obtained gives a measurement of the molecular gas mass density over the range of redshifts sampled by the observations (Carilli and Walter, 2013). Initial efforts that have followed this strategy are the IRAM Plateau de Bure Interferometer (PdBI) observations in the *Hubble* Deep Field North, and the Atacama Large Millimeter Array (ALMA) observations in the *Hubble* Ultra Deep Field (the ASPECS-Pilot program). These spectral scans were conducted at 3 mm and 1 mm wavelengths, covering areas of ~ 0.5 and ~ 1 arcmin^2 in size, respectively (see Decarli et al., 2014, Walter et al., 2016, for survey descriptions). Walter

et al. (2014) and Decarli et al. (2016) present luminosity function measurements for CO $(3-2)$ and higher-J transitions at $z \sim 2-3$, and CO $(5-4)$ and higher-J transitions at $z \sim 5-7$. These studies provided some of the first constraints on the cosmological CO luminosity function, and the cosmic molecular gas mass density evolution, but they are limited by the small areas covered.

More recently, the COLDz project (> 300 hours of observations on the JVLA) covered a ~ 48 armin^2 area in GOODS-N and a ~ 8 arcmin^2 area in COSMOS in the $30-38$ GHz frequency range, targeting CO $(1-0)$ at $z \sim 2-2.8$ and CO $(2-1)$ at $z \sim 4.9-6.7$ (Pavesi et al., 2018). This survey provides constraints for the CO luminosity function at $z > 2$ (Riechers et al., 2019). The ASPECS Large Program (LP; 150 hours of observations on ALMA) covers most of the *Hubble* eXtremely Deep Field (~ 4.6 arcmin^2) at 3 mm and 1.2 mm wavelengths (González-López et al., 2019). Decarli et al. (2019) use it to measure the CO luminosity function and find that the cosmic molecular gas mass density peaks at $z \sim 1.5$ and decreases by a factor of $\sim 6.5^{+1.8}_{-1.4}$ to the present day.

In this paper, we present CO luminosity function and cosmic molecular gas mass density evolution measurements we make from repurposed data which takes advantage of independent deep observations of targeted galaxies. Specifically, we present the results from a "blind" CO search in the second Plateau de Bure High-z Blue-Sequence Survey (PHIBSS2) observations, the follow up to PHIBSS. PHIBSS and PHIBSS2 have been productive surveys with key results on their main objective, characterizing normal $z \sim 1-2$ galaxies. Among other results, PHIBSS and PHIBSS2 have yielded scaling relations for main sequence galaxies at those red-

shifts, depletion times and molecular fractions (Genzel et al., 2015, Tacconi et al., 2018), and characterized molecular reservoirs for $z < 1$ galaxies (Freundlich et al., 2019). However, these observations also have the potential to yield impactful "deep field" science. Since each PHIBSS2 observation targeted a galaxy selected from the 3D-HST CANDELS fields, characterization of serendipitous detections benefits from the extensive multi-wavelength coverage available in these legacy fields.

This paper is structured as follows: Section 2.3 summarizes the observations used, Section 2.4 describes the blind search algorithm, the optical counterpart search, and our statistical methods for assessing the likelihood that each candidate is real as well as the completeness of the search algorithm. Section 2.5 presents the results of the line search, the CO luminosity functions we derive, and the molecular gas mass density evolution constraints. Sections 2.6 compares to previous works and Section 2.7 summarizes the work done. The properties of the candidate sources, their spectra, and optical counterparts are presented in the Appendices.

Throughout the paper, we assume ΛCDM cosmology with $H_0 = 70\,\mathrm{km\,s^{-1}\,Mpc^{-1}}$, $\Omega_m = 0.3$, and $\Omega_\Lambda = 0.7$, consistent with the *Wilkinson Microwave Anisotropy Probe* measurements (Komatsu et al., 2011).

2.3 Observations

2.3.1 The "Plateau de Bure High-z Blue-Sequence Survey" (PHIBSS)

The PHIBSS2 survey is an IRAM Plateau de Bure Interferometer (PdbI; Guilloteau et al., 1992) 4-year legacy program aimed at studying early galaxy evolution

from the perspective of molecular gas reservoirs, while exploiting the capabilities of the NOrthern Extended Millimeter Array (NOEMA; Schuster, 2014) as they came online. Observations of ^{12}CO $(2-1)$, ^{12}CO $(3-2)$, and ^{12}CO $(6-5)$ transitions took place between October 2013 and June 2017. Observation times per target range from 0.6 to 30.3 hours, with a total of $\sim 1,100$ hours of 6-antenna equivalent on source integration time, and were mostly taken in C configuration to ensure that the galaxies are not spatially resolved (see Freundlich et al., 2019, for more details on the data reduction process). Given the integration times and configurations, the synthesized beams range from $1''$ to $5''$. At the redshifts targeted by PHIBSS, the typical scales are $6-8.5$ kpc per arcsec.

The survey consists of 110 individual observations of main sequence galaxies, exploring the CO $(2-1)$, CO $(3-2)$, and CO $(6-5)$ line emission, covering a total area of ~ 130 arcmin^2 and sampling a total co-moving volume of ~ 200000 Mpc^3 (see Table 2.1).

2.3.2 Ancillary Data

We use the 3D-HST/CANDELS survey catalogs (Brammer et al., 2012, Skelton et al., 2014, Momcheva et al., 2016) for the COSMOS, GOODS-N, and EGS/AEGIS fields to search for optical counterparts. We present cutouts from the HST Advanced Camera for Surveys (ACS) for filter F814W for each field (where possible) corresponding to the PHIBSS2 observations in Appendix B (see §2.5.1.1). For targets lying outside the area covered by the HST ACS optical or WFC3 near-IR mosaics,

we show cutouts of Spitzer IRAC 3.6 μm images.

2.4 Methods

2.4.1 Line Search

The goal of the line search is to systematically select candidate sources from noisy data, and assess their significance in terms of their corresponding signal-to-noise ratio (SNR). For our sample of observations, we expect sources to be unresolved and to mostly have FWHM in the range of $\sim 50 - 500$ km s^{-1}, and at most ~ 1000 km s^{-1}. Rubin et al. (1985) shows massive galaxies have maximum rotation velocities that span from $\sim 100 - 400$ km s^{-1}, while small irregular galaxies have minimum rotation speeds of $\sim 50 - 100$ km s^{-1}, and Carilli and Walter (2013) show that hyper-starburst quasar hosts and sub-millimeter galaxies can have line widths up to ~ 1000 km s^{-1}.

Our line search method is a 1D matched filter technique where we select a Hanning kernel as our template. We Hanning-smooth and decimate each observation five times, where each iteration of the smoothing increases the width of a channel by a factor of two while removing one every two channels (that is, decimating the highly correlated channels). This creates cubes with velocity resolutions spanning from ~ 7 to ~ 1000 km s^{-1}, depending on the observation (the original data cubes have channel widths ranging from 7 to 88 km s^{-1}). The purpose of this matching is to maximize the signal-to-noise for signals of a given line-width. Hence our choice of smoothing allows us to attempt to match the velocity resolution of the data

cube with that of the potential sources in the data. Each data cube generates five additional smoothed cubes corresponding to the different velocity resolution templates.

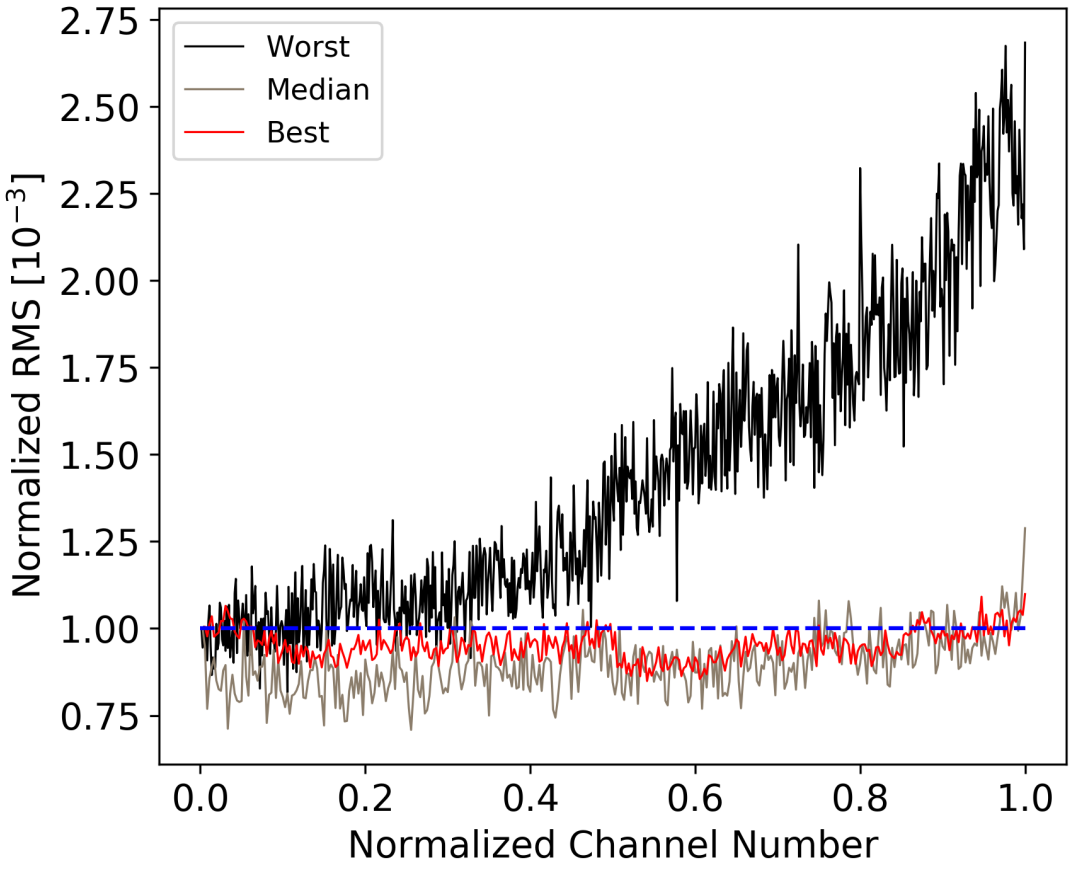

Figure 2.1: RMS as a function of channel number (both normalized to unity), showing a typical best case scenario (red line) where the RMS is approximately flat across all channels, a typical worst case scenario (black line) where the RMS varies quite significantly across the channels, and a median case (beige line). This illustrates the need to properly model the RMS variations across the passband in order to correctly estimate the SNR of every pixel. We do this by modeling the RMS variations as a function of frequency with a seventh order polynomial for each data cube.

For each of these cubes (original and smoothed), we compute a significance (SNR) map by taking the peak value at each pixel along the spectral axis and

dividing it by the RMS (taken to be the standard deviation) of the spectral channel. The RMS as a function of channel number (frequency) is usually fairly flat, but occasionally it can vary quite substantially across the passband. We illustrate this in Figure 2.1, where we show three examples of how the noise varies across channels in three different data cubes. For the purpose of comparing the RMS channel variations in different data cubes, we normalize the axes. The channel RMS values vary from one data cube to another, therefore we normalize the y-axis to 1×10^{-3}. The number of channels in the three data cubes that we compare here also varies, thus we also normalize the x-axis to unity (the bandwidth is about 3 GHz). We plot a typical best case scenario in red, a typical worst case scenario in black, and a median example in beige, while the dashed blue line serves as a reference point for a straight horizontal line. It is therefore important to properly account for this when calculating the SNR in order to not over or underestimate the SNR of a given pixel. To characterize this variation, we fit the distribution of the channel RMS as a function of channel number for each data cube with a polynomial, in order to have a smooth representation of the large-scale noise variation to properly calculate SNR. We then divide each peak pixel by the corresponding channel RMS from our fit. The order of the polynomial chosen to obtain our smooth representation of the noise is not particularly important, and a value of seven was found to produce very reasonable results.

In order to obtain the distribution of the noise, we repeat this process for the negative peaks, that is dividing the largest negative peak at each pixel by the channel RMS, thus creating SNR maps of "negative emission". Positive emission

corresponds to real astrophysical sources as well as noise peaks, while "negative emission" corresponds only to noise. The most significant negative peak therefore provides an estimate of what is the boundary between likely noise and likely signal. From these SNR maps, we build a list of candidate sources by selecting pixels with a positive SNR value that is greater than the absolute value of the largest negative peak SNR. We save a list of all pixels that satisfy this condition, sort it by decreasing SNR, and filter out all pixels that lie within one beam of the highest SNR pixels to arrive at a list of independent possible sources. We perform this search and filtering on all smoothed cubes and then combine the lists into one list, where we filter out candidate sources that satisfy our detection threshold in multiple cubes for a given field (original and/or smoothed cubes), but with lower SNR. This leaves us with a final list of candidate sources for each field in our sample, where the position of each source corresponds to the position of the most significant pixel for the velocity smoothing parameter that provides the highest SNR. Figure 2.2 shows an example SNR map for one of our fields (eg016; see Table A.1) at a velocity resolution of 352 $\mathrm{km\,s^{-1}}$, with the black contour showing the threshold of the most significant negative peak in that cube, our chosen boundary between "likely noise" and "likely signal". In what follows we estimate the probability of this candidate source being real.

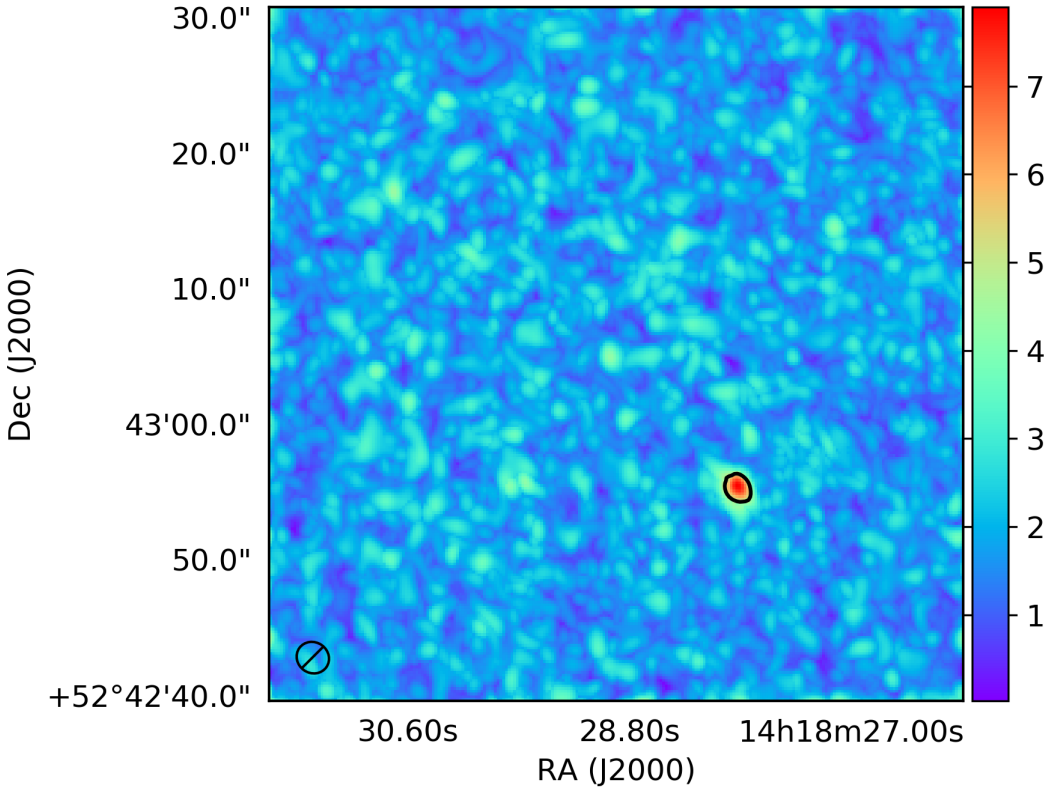

Figure 2.2: Hanning-smoothed SNR map for the eg016 data cube, at a velocity resolution of 352 $\mathrm{km\,s^{-1}}$. The black contour corresponds to the SNR level of the largest negative peak in this cube, which is our detection threshold and in this case corresponds to a SNR of 4.93. A single source appears in this map with SNR above the detection threshold we impose (see eg016-1 in Table A.1 for physical properties). The central targeted source in the eg016 data cube has a SNR of 3.1 (see Table 3 in Freundlich et al., 2019), which is below our detection threshold and is therefore not visible in this SNR map.

2.4.1.1 False Positives

The purpose of the false positive analysis is to assign to each candidate source a probability of it being a real astrophysical source, which we will call reliability (also called fidelity or purity). To address this question, we use the statistics of the negative emission, which consists of only noise, to determine the likelihood that noise could produce a SNR as large as that of each candidate source.

In order to estimate this we would ideally consider the statistics of independent points in the map. In our significance maps, in principle all pixels within one beam of a strong emission pixel will be correlated. To remove from our distribution of peak SNR values pixels that are correlated, we perform a "cleaning" of the map. We do that by taking the most significant value in a given map, subtracting a beam-like Gaussian from that pixel position, and then repeating the process until no values above 3× the RMS level of the map remain, leaving us with a list of independent "sources" in terms of SNR. As a comparison, we do the same thing with the SNR map distribution of positive peaks.

The distributions of independent positive and negative peaks in a given map overlap very well, and are well approximated by a Gaussian with an exponential tail toward high significance (Figure 2.3). However, the tail of the distribution is the region that we are interested in characterizing because this is where the candidate sources we detect lie. To achieve this goal, we begin by normalizing the distribution of independent positive and negative peaks so that their integrals equal unity. We then treat the normalized independent negative distribution as our

probability density function, which we fit with an exponentially modified Gaussian distribution of the form:

$$h(x) = \frac{\lambda}{2} e^{\frac{\lambda}{2}(2\mu+\lambda\sigma^2-2x)} \text{erfc}\left(\frac{\mu+\lambda\sigma^2-x}{\sqrt{2}\sigma}\right) \tag{2.1}$$

where x corresponds to the peak SNR values of the inverted cube, μ and σ are the mean and standard deviation of the Gaussian, λ is the rate of the exponential, and erfc is the complementary error function which is equal to $1-\text{erf}(x)$. This function describes a Gaussian distribution with a positive skew due to an exponential component. An example of this fit is shown in Figure 2.3, where the orange histogram corresponds to the SNR distribution of the negative emission, the blue histogram is the SNR distribution of the positive emission, and the black line is the exponentially modified Gaussian; the bottom panel shows the residuals. Figure 2.3 corresponds to the data cube eg016 (Table A.1), where one candidate source is identified as possible emission through the line search procedure described above. While the y-axis in Figure 2.3 is plotted on a log-scale, the fitting procedure is done in linear space. As such the resulting parameters are not sensitive to the high-SNR "outliers". Therefore the reliability parameters we derive from this method are robust with respect to the inclusion or exclusion of these data points.

To estimate the probability that the observed significance could be produced by noise fluctuations, we use the cumulative distribution of the exponentially modified Gaussian distribution, which has the form:

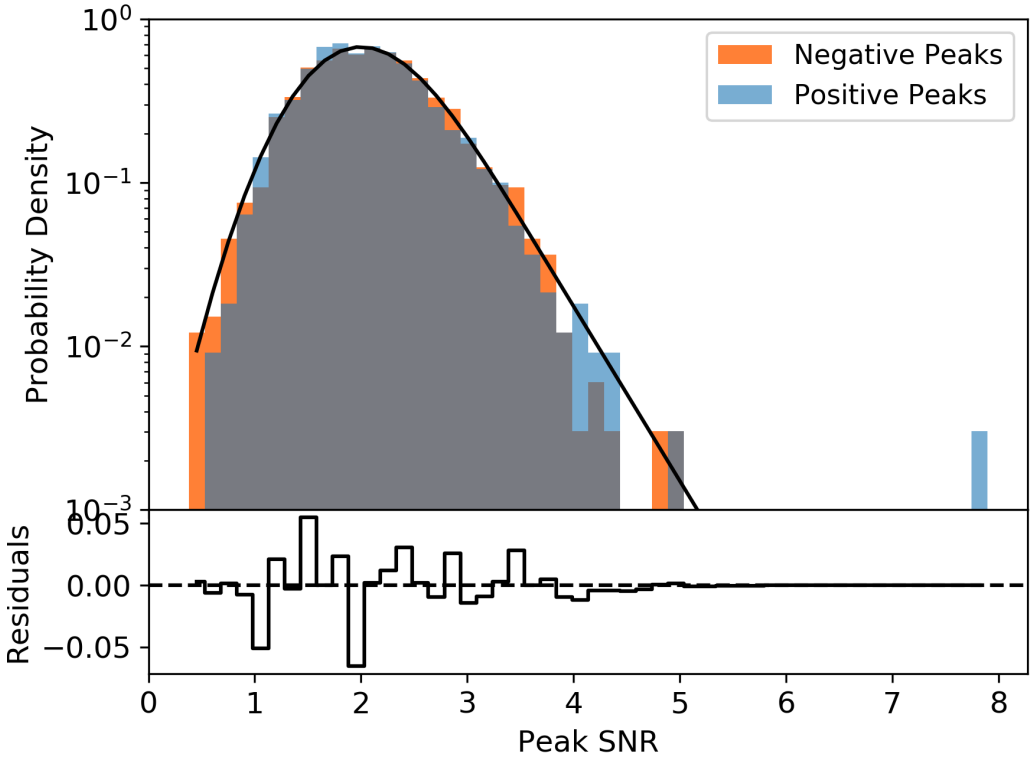

Figure 2.3: The top panel shows the distribution of positive (blue) and negative (orange) peak SNRs per beam of the eg016 data cube, at a velocity resolution of 352 $\mathrm{km\,s^{-1}}$ (the gray histogram is the overlap of the blue and orange histograms). The black line is the exponentially modified Gaussian fit to the negative peaks distribution. We see one object with positive peak SNR much greater than the largest negative peak SNR (in absolute values); this corresponds to the candidate sources. The bottom panel shows the residuals from fitting with an exponentially modified Gaussian function, which we find represents that data reasonably well.

$$H(x) = \Phi(u, 0, \sigma) - e^{-u+v^2/2+\log(\Phi(u,v^2,v))} \tag{2.2}$$

where $u = \lambda(x - \mu)$ and $v = \lambda\sigma$, and $\Phi(x, \mu, \sigma)$ is the cumulative distribution function of a Gaussian distribution with mean μ and standard deviation σ.

For a given candidate source, the probability that a random fluctuation produces a source with SNR greater than or equal to that of the candidate source, (i.e.,

falls in the range $x \in [\mathrm{SNR_{src}}, \infty)$), is:

$$\mathrm{P}(x > \mathrm{SNR_{src}}) = 1 - H(\mathrm{SNR_{src}}). \tag{2.3}$$

For each candidate source, this gives an estimate of the probability that a given independent measurement (a beam) in the map could have a peak SNR greater than or equal to that of the candidate source itself. To assess the significance of these values, we compare them to the number of independent beams sampled by each SNR map. We do this by taking the inverse of the false positive probability we calculate from equation 2.3 as a measure of how many random measurements it would take to observe the given candidate source SNR value once (i.e., one in every N number of measurements will have an SNR equal to or greater than what is observed for the candidate source given only noise; we call this $\mathrm{N_{expected}}$). Then the ratio of $\mathrm{N_{expected}}$ to the number of independent beams sampled ($\mathrm{N_{beams}}$) by each SNR map is the total number of measurements with a given SNR we would expect to make due to noise only. As an example, if we measure a probability of 10^{-3} for a candidate source of some SNR, but then find that we sample 1000 beams in that map, then we would expect to find one such "source" in our map from just noise, so this candidate source would be considered unreliable. For very strong candidate sources this number is very small, and for weaker sources it becomes larger and can become on the order of unity. The reliability parameter (R) we assign to each source is one minus this ratio:

$$R = 1 - \frac{\mathrm{N_{expected}}}{\mathrm{N_{beams}}} \tag{2.4}$$

Our reliability measurements range from $0.01-1$ (i.e., $1-100\%$ reliability), and we include in our sample candidate sources with $R > 5\%$ since this is the threshold adopted by Riechers et al. (2019). We show these values in Table A.1. Note that we do not attempt to further filter our list of candidate sources by choosing a higher reliability cutoff. Note also that this definition of reliability is more conservative than the "fidelity" parameter employed by Decarli et al. (2016), for example, as per our definition there are no candidate sources with lower flux than the absolute value of the largest negative peak in a map. There is a strong correlation between integrated flux and reliability, where fainter sources with lower SNR naturally tend to show lower R (see §2.5.2, Figure 2.8). The derivation of the luminosity function (§2.5.3) properly takes into account the statistics by weighting by reliability, and artificially inserting a high reliability cutoff would cause us to preferentially remove the contribution from fainter sources. Note also that computation of R for the central sources, all known to be real, shows a large spread driven by SNR. So it is clear that real sources can have low reliability when they are faint in relation to the noise of the observation.

2.4.1.2 Completeness

To assess the completeness of our search algorithm, we perform an analysis of the chance of detecting sources we artificially inject into each data cube. The

purpose of this analysis is to relate the fraction of recovered simulated sources to the line flux. Since we do not expect resolved sources in the PHIBSS2 data, we do not account for varying sources sizes.

To simulate sources, we assume a Gaussian line profile along the spectral axis, and generate sources with five free parameters: the spatial position, the peak flux density of the line, its velocity width as FWHM, and the velocity of the peak by drawing random numbers from a uniform distribution. The x and y coordinates are limited to between 1 and 256, since the cubes are 256×256 pixels in size. We test the effect of source position on the completeness by simulating sources at the edges of pixels and at the centers of pixels, and find that this has a negligible impact on the completeness correction factors. The peak flux density of each artificial source ranges between the maximum value in the data and 1% of the maximum. Because completeness is also a function of line width, we simulate sources with FWHM values ranging from $50 - 1000$ km s^{-1}, to reflect the range of line widths spanned by the data.

We then assume that each source will be "beam-like", so we take the flux density at each velocity channel that the source appears in to be the peak of a two-dimensional Gaussian which has the same position angle and size as the synthesized beam for each data cube. However, since power is lost in the side lobes of the full synthesized beam, we take this into account by correcting the flux of each simulated source by the ratio of power in the primary lobe of the beam and its side lobes. We generate 2500 artificial sources for each data cube in this way, add them to the data cube 5 sources at a time to avoid crowding, run the search algorithm, and check

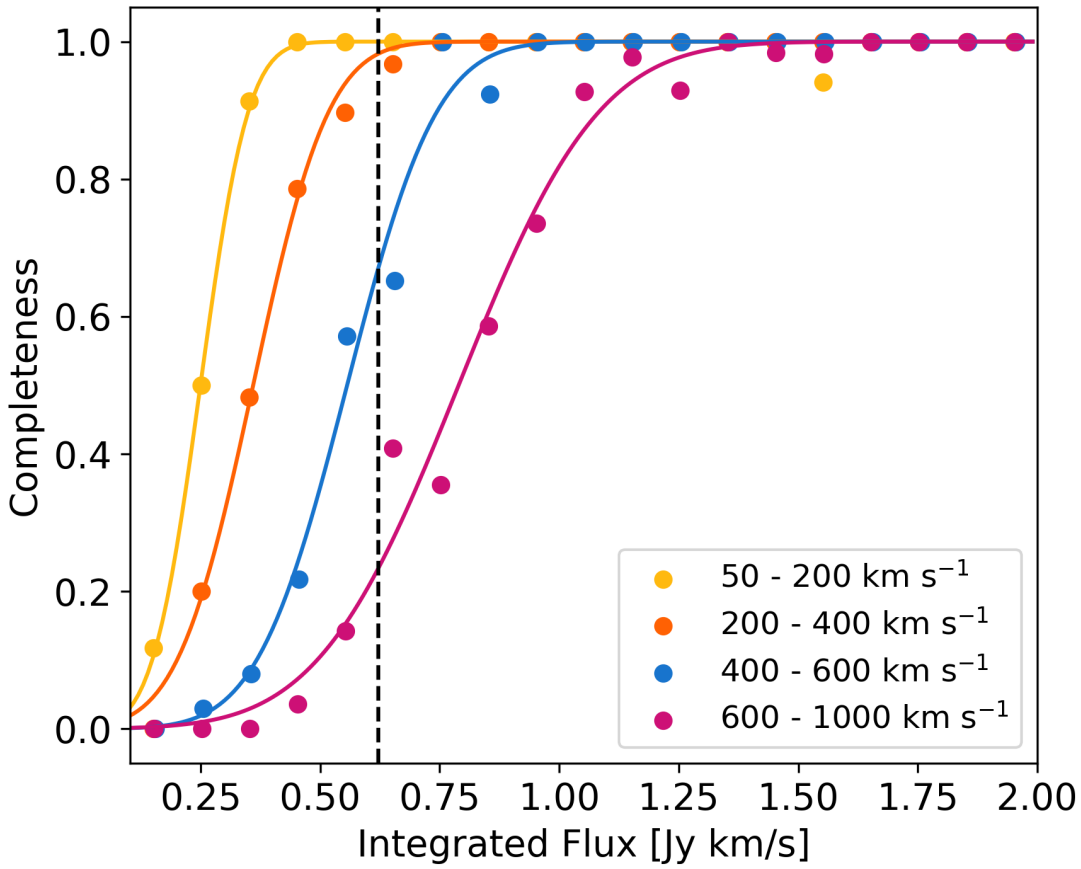

Figure 2.4: The fractions of recovered sources to artificial sources injected as a function of integrated flux and FWHM for the eg016 field, from our analysis of 2500 simulated sources. The colored data points correspond to the fraction of recovered sources for four velocity bins. The colored lines are fits to the four distributions using a cumulative Gaussian distribution. The vertical dashed lines correspond to the integrated flux of the candidate source. As we would expect, the recovery of sources decreases with decreasing integrated flux indicating that fainter sources are harder to detect than brighter ones. We also see that the recovery of sources at a given integrated flux decreases with increasing FWHM. This analysis allows us to correct our CO luminosity functions for the incompleteness of our search algorithm, particularly at the faint end where this becomes a larger effect (see §2.5.3).

the fraction of sources recovered. Figure 2.4 plots the fraction of recovered artificial sources as a function of integrated flux (blue circles), for the eg016 data cube. The recovered fraction is fit with a Gaussian cumulative distribution function (solid blue line). The vertical dashed black lines correspond to the integrated flux of the candidate sources for this data cube. We can see that the recovery fraction decreases with decreasing integrated flux, which is known for each simulated source. We correct for completeness on a source-by-source basis using the cumulative Gaussian distribution fit for each data cube. Given the integrated flux of each candidate source, x, the corresponding completion correction is

$$C(x) = \frac{1}{2}\left[1 + \mathrm{erf}\left(\frac{x-\mu}{\sigma\sqrt{2}}\right)\right], \tag{2.5}$$

where μ and σ are the mean and standard deviation derived from our Gaussian cumulative distribution function fit for a given cube. Primary beam attenuation, the sensitivity drop off as a function of distance from the pointing center, will decrease the chances of detecting weaker sources closer to the edges of each data cube. We take this effect into account in our comoving volume calculations, which results in a smaller effective volume sampled by each cube.

2.5 Results of Line Search

2.5.1 Line Properties

We extract the spectrum of each candidate source at the position of the peak SNR pixel, given that the sources in PHIBSS2 are unresolved, in each field at all velocity resolutions, and apply a primary beam correction. These spectra are fit with a Gaussian profile using Python's `scipy.optimize.curve_fit`. Example spectra of the three brightest candidate sources detected in the COSMOS, EGS/AEGIS, and GOODS-N fields are shown in Figure 2.5, while the remaining figures are shown in Appendix A.

The redshift of each candidate source is calculated from the central frequency of the line, assuming that the emission detected corresponds to a CO transition from CO $(1-0)$ to CO $(6-5)$. CO emission represents usually the brightest line in galaxy spectra at wavelengths between 400 and 2600 μm. Rotational transitions of CO are spaced by intervals of 115.27 GHz, so with a single transition by itself it is impossible to determine the redshift of the source. The optical counterpart search discussed in the next section allows us to, in some cases, determine which CO transitions a candidate source may correspond to, and in other cases, to constrain the range of possible CO transitions.

The flux and full-width-half-maximum of each candidate source are calculated from the best fit standard deviation and amplitude of the Gaussian profile fit. These results are presented in Table A.1 in Appendix A.

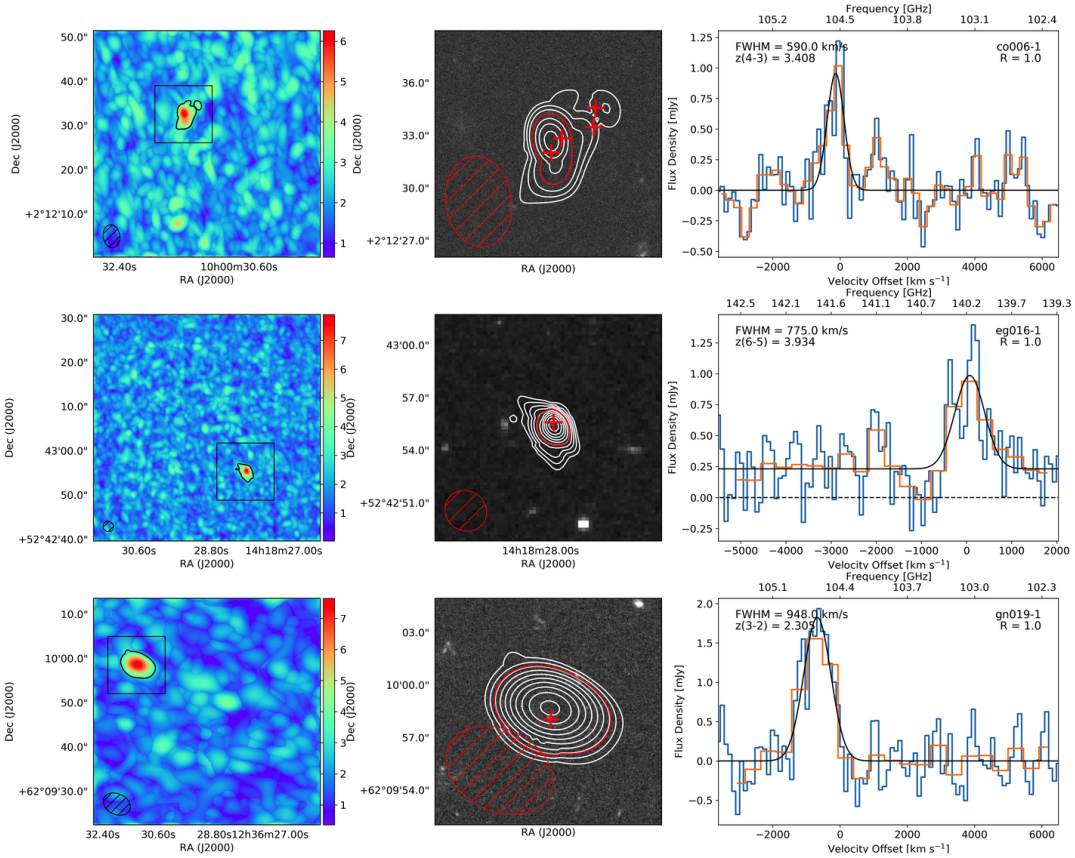

Figure 2.5: The brightest serendipitous CO sources in the COSMOS (top), EGS/AEGIS (middle), and GOODS-N (bottom) fields. The complete set of figures is available in Appendix A.

2.5.1.1 Optical Counterparts

The purpose of identifying counterparts (CPs) for the candidate sources is to constrain their likely redshift and CO transition, as well as properties like their stellar masses and SFRs. We search for all optical sources in the 3D-HST/CANDELS catalogs (Brammer et al., 2012, Skelton et al., 2014, Momcheva et al., 2016) that lie within one beam FWHM radius of the peak SNR position of each candidate source we identify in PHIBSS2, while leaving the redshifts unconstrained. The objects in these catalogs have a distribution of redshifts determined from HST and ground-based spectral energy distribution (SED) fitting using the EAZY code (Brammer et al., 2008). To match the redshifts, we then consider all transitions from CO $(1-0)$ to CO $(6-5)$ and check which, if any, CO transitions are plausible given the posterior likelihood distributions of the redshift determination from the SED fitting. In several cases the redshifts of the optical counterparts are poorly constrained by the SED fitting, allowing a range of possible CO transitions. When grism or spectroscopic redshifts are available, we compare our redshifts to those because they are much better constrained than the photometric redshifts. For the purpose of constructing the CO luminosity functions, we assign a "redshift probability" to each source based on the posterior likelihood distribution. We also assign an "association probability" for candidate CO sources where multiple optical counterpart candidates lie within the synthesized beam of the CO data cube (which changes from cube to cube). This "association probability" is defined as $P_a = 1 - (\Delta r^2/\theta)$, where Δr is the projected angular separation between the CO source and potential counterpart, and

θ is the synthesized beam area. In this way, optical sources that lie outside of the synthesized beam area are assigned an association probability of zero, and the probability of association increases as the projected angular separation decreases.

From this spatial matching, and CO transition/redshift association, we find that $\sim 64\%$ (43 out of 67) of source candidates in our catalog have at least a tentative optical counterpart. The lack of an optical counterpart in the 3D-HST/CANDELS catalog (rest frame optical/UV counterparts) could imply that the candidate source is spurious, though based on our reliability calculations, we would not expect more than 25% of sources to be spurious. Thus, this could also be physically caused by heavy extinction associated with the molecular gas (in which case there may be infrared counterparts). Whitaker et al. (2017) investigate the relation between dust obscured star formation and stellar mass as a function of redshift ($z = 0 - 2.5$). They find that for $\log(M/M_{\odot}) > 10.5$, more than 90% of star formation is obscured by dust at all redshifts, and that at $z > 1$, there is a tail of heavily obscured low-mass star-forming galaxies. This highlights the importance of infrared data, and future work may involve carrying out a systematic infrared counterpart search beyond existing catalogs (e.g., *Spitzer* IRAC 3.6 and 4.5 μm).

The results of our search are presented in the middle panel of the figures in Appendix A. These are for the most part HST ACS F814W images where the red crosses mark the positions of the candidate optical counterparts for candidate CO sources where one could be tentatively identified. For candidate sources where no ACS optical and/or WFC3 near-IR data was available, we present *Spitzer* IRAC 3.6 μm images. In the left panel, the redshifts reported correspond to the CO transition

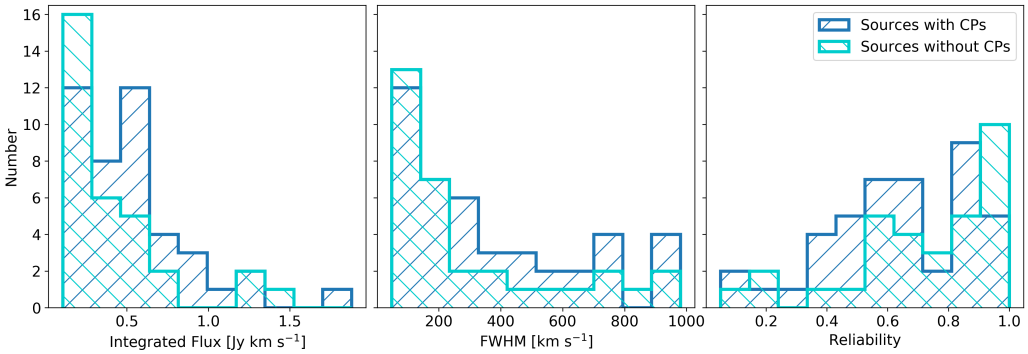

Figure 2.6: Comparing the properties of the candidate sources with optical counterparts (dark blue, right-hatched histogram) to those without (cyan, left-hatched histogram). *Left*: comparing the integrated flux, *Middle*: comparing the line width (FWHM), *Right*: comparing the reliability. The K-S test results indicate that the distributions are similar in terms of all three properties.

that most closely matches the "best" redshift reported in the 3D-HST/CANDELS catalogs. In the computation of the CO luminosity functions, we however use the range of possible CO transitions/redshifts allowed by the potential counterparts to derive CO luminosities, weighted by their respective probabilities (see §2.5.3 for details). Finally, these results are also summarized in Table A.1 where we give the right ascension, declination, and "best" redshift reported in the 3D-HST/CANDELS catalogs of each optical counterpart. We also provide the CO based redshifts for the range of possible CO transitions as determined from the EAZY SED fitting posterior likelihood distributions. Finally, we provide the angular separation between the candidate source and potential optical counterpart, with a probability of association in cases where more than one possible counterpart exists within the synthesized beam.

In Figure 2.6 we compare the integrated flux, line width, and reliability of candidate sources with potential optical counterparts (dark blue, right-hatched his-

togram), and those without (lighter blue, left-hatched histogram). In all three cases, both populations of candidate sources span the same parameter space. Both populations contain many fainter objects and fewer bright objects, so while some of those may be spurious detections, the reliability distribution shows that there are several high-reliability objects with no optical counterpart identified. In terms of line width, both populations span essentially the same range of line widths probed.

To quantify this we perform the Kolmogorov-Smirnov test and find a K-S statistic of $D_{n,m} = 0.21$, 0.25, and 0.36 for the integrated flux, FWHM, and reliability distributions respectively (where n and m are the lengths of the two samples). The K-S statistic is the maximum distance between the cumulative distributions of the two compared populations, so a small enough K-S statistic indicates that the hypothesis that two samples are drawn from the same distribution cannot be rejected. Specifically, the two samples can be said to come from different distributions at a confidence level α if

$$D_{n,m} > c(\alpha)\sqrt{\frac{n+m}{nm}} \tag{2.6}$$

where

$$c(\alpha) = \sqrt{-\frac{1}{2}\ln\alpha}. \tag{2.7}$$

From the K-S statistics for these three distributions, we find that the hypothesis that both samples are drawn from the same distribution can be rejected at the 74.4%, 86.1%, and 98.1% confidence level for the integrated flux, FWHM, and reliability respectively. These confidence levels are usually not considered significant

enough to reject the hypothesis. We conclude from this that we lack evidence to say that the two populations are different and note only that the candidate sources without counterparts tend to be fainter and consequently less reliable that the candidate sources with counterparts.

For candidate sources where we identify possible counterparts (and hence for which we have a redshift z), we compare the molecular gas mass from the CO luminosity to the molecular gas inferred from the potential counterpart SFR, using the depletion time scale scaling relation of Tacconi et al. (2018):

$$\log(t_{dep}) = A_t + B_t \log(1+z) + C_t \log(\delta\text{MS}) \tag{2.8}$$

where $A_t = 0.09$, $B_t = -0.62$, $C_t = -0.44$ (for details see Tacconi et al., 2018), and δMS is the offset from the main sequence of a source. Using the redshift and main sequence offset of the potential counterpart, we calculate their depletion timescales and then infer the molecular gas mass based on their SFR (since $t_{dep} = M_{gas}/\text{SFR}$).

We plot this comparison in Figure 2.7, omitting candidate sources with multiple possible counterparts identified within one synthesized beam and sources where the product of the CO source reliability (R) times the counterpart probability of association (P_a) is less than 50%, as we consider these sources and/or counterparts not highly reliable. The size of the data points is scaled according to the product of the reliability and the probability of association (higher $R \times P_a$ correspond to larger symbols), and colored according to redshift. The black solid line is the one-to-one relation and the black stars are primary PHIBSS2 targets plotted as a comparison.

These all lie on the one-to-one line, except for one target, which has a large offset from the main sequence of star formation ($\log \delta\mathrm{MS} = +2.41$, corresponding to a target over the main sequence) and therefore a very short depletion timescale. In contrast, the majority of potential counterparts lie systematically below the one-to-one relation, which would imply molecular gas reservoirs larger than would be inferred from the measured star formation.

The SFRs reported in the 3D-HST/CANDELS catalog for these objects are derived from SED modeling. We have used the catalog by Momcheva et al. (2016), but with SFR values recomputed according to the Herschel-calibrated ladder of indicators in Wuyts et al. (2011) (see also Tacconi et al., 2018, and references therein). The SEDs for all objects contain optical to $8\,\mu$m photometry, and some objects have photometry at longer wavelengths. At the redshifts of these objects, 8 μm corresponds to rest-frame wavelengths of $\lambda \sim 1.5 - 4$ μm. For six data points the photometry also includes 24 μm to 160 μm measurements. These are indicated by vertical dashed lines, which join the SFR obtained from fitting the $\lambda \leq 8\,\mu$m photometry to the SFR computed including the longer wavelengths (which corresponds to the square symbols in Figure 2.7). When the SED modeling includes only the shorter wavelengths, it results in SFRs one to two orders of magnitude lower than is estimated when longer wavelength data are included. The agreement between molecular masses estimated from the optical counterpart star formation activity, and those directly measured in the PHIBSS2 observations, is very good when the SFR estimate includes $\lambda \geq 24\,\mu$m information.

Our identification process naturally selects objects that are bright in CO, and

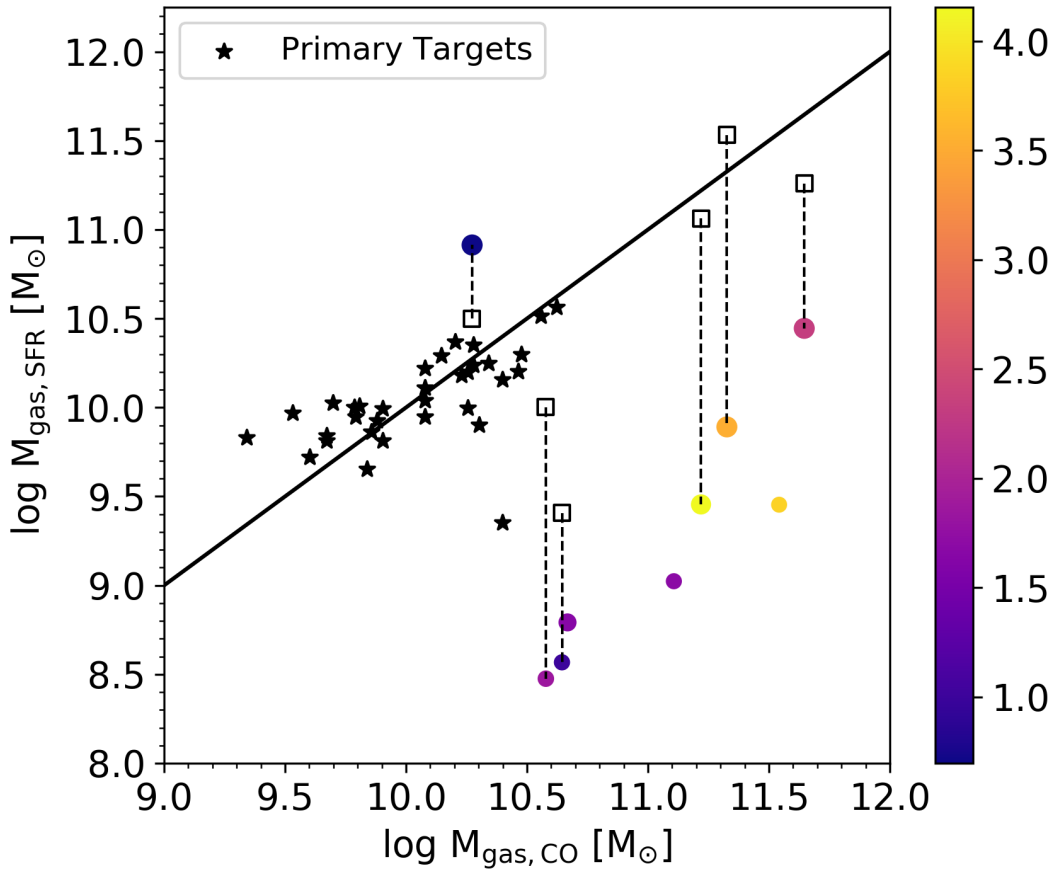

Figure 2.7: Comparison of the molecular gas mass measured from the candidate source CO luminosities to the molecular gas mass inferred from the potential optical counterpart SFR and the depletion timescale scaling relation of Tacconi et al. (2018). The size of the colored points is scaled according to the product of reliability and association probability of the detection, and they are colored according to redshift. The diagonal black solid line is the one-to-one relation. All colored symbols correspond to SFR measurements from SED modeling of optical to 8 μm photometry; the black square symbols show the effect of including longer wavelength photometry (24 or 160 μm) on the SFR calculation for the sources where that is available.

indeed they all have very large molecular masses as inferred from their flux. Therefore they are likely dust-rich, and their star formation activity is highly extincted. It appears likely that the dust-obscured component of star formation is not properly accounted for when the longest rest-frame wavelength included in the SED is $\lambda \sim 1.5 - 4$ μm. We believe this is the main cause for the majority of the large discrepancies between the two estimates of molecular gas mass. It is also possible, particularly for sources with low reliability or probability of association, that some of them are not real or that some counterparts are misidentified. The agreement between the CO luminosity function we derive from these data (§2.5.3) and other measurements in the literature, however, suggests that this is not the case for the majority of our objects.

2.5.2 Comparing Serendipitous Detections to Central Sources

The goal of PHIBSS2 is to study galaxy evolution from the perspective of molecular gas reservoirs. Surveys such as PHIBSS2 that target specific galaxies selected based on their stellar mass, SFR, and availability of ancillary data have complex selection functions. The blind search we have performed here, and our catalog of serendipitous detections provide a sample of objects that are mostly free of selection biases, other than the selection function imposed by the redshift ranges surveyed in any given observation and the flux which makes brighter objects easier to detect. We can therefore compare these two samples to get an idea of their respective biases.

In the left panel of Figure 2.8, we compare the integrated fluxes of all 67 candidate sources to those of the central sources targeted by PHIBSS2. In the right panel of Figure 2.8, we compare the molecular gas masses of the candidate sources with tentative optical counterpart identifications to that of the central sources. The central sources are plotted as the blue hatched histogram and the candidate sources are separated into histograms corresponding to likelihood levels: the hatched magenta histogram corresponds to sources with reliabilities between 5 and 50%, the orange filled histogram corresponds to sources with reliabilities between 50 and 90%, and the yellow histogram corresponds to sources with reliabilities greater than 90%.

We see in the flux comparison that the sample of central sources and the sample of secondary candidate detections seem to generally probe objects with similar properties. To quantify this observation and determine if candidate sources with lower reliabilities have systematically different integrated flux properties, we perform a K-S test. We find that $D_{n,m} = 0.13, 0.19, 0.34$, which results in rejecting at the 54.0%, 73.3%, and 95.4% confidence level the hypothesis that the candidate source distributions come from the same distribution of central sources for the $5-50\%$, $50-90\%$, and $>90\%$ reliability ranges respectively. These are not strong rejections, suggesting that regardless of the reliability, the candidate secondary sources have properties that are very similar to those of the central targeted sources. In terms of molecular mass, our higher reliability candidate sources seem to correspond to slightly more massive objects not well represented in the original PHIBSS2 sample, selected to represent the main sequence at the redshifts of interest. In both panels we see that the fainter/less massive candidate sources tend to have lower reliabil-

ities than the brighter/more massive objects. This is not surprising, since these candidates will have lower SNRs.

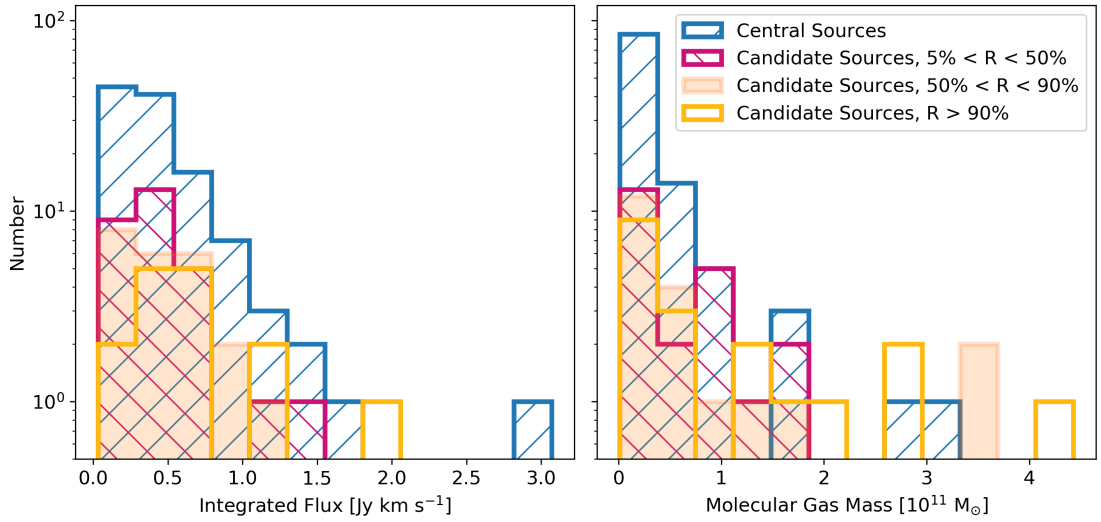

Figure 2.8: *Left*: Comparison of the integrated flux measurements of the central galaxies that were specifically targeted by PHIBSS2 (blue hatched histograms) to the additional serendipitous CO detections. The candidate sources are divided according to their likelihood parameter. The candidate sources generally seem to follow a similar distribution of fluxes as the targeted central sources. A K-S test reveals that at the 48.2%, 94%, and 96.6% confidence level, the candidate source distributions do not come from the same distribution as the central sources (for the $5-50\%$, $50-90\%$, and $>90\%$ reliability ranges). These weak rejections suggest that the samples are representative of the same parent population of objects. *Right*: The same as the left panel, but now comparing the molecular gas masses. The highest reliability objects tend to have the higher molecular gas masses.

We observe across our sample of candidate detections and tentative optical counterpart identifications that some candidate sources lie at redshifts similar to that of the central target source. This raises the question of whether constructing a CO luminosity function from data targeted at particular objects introduces biases due to possible clustering of sources around the targeted object. To evaluate whether this is the case, we compare in Figure 2.9 the difference between the frequency of

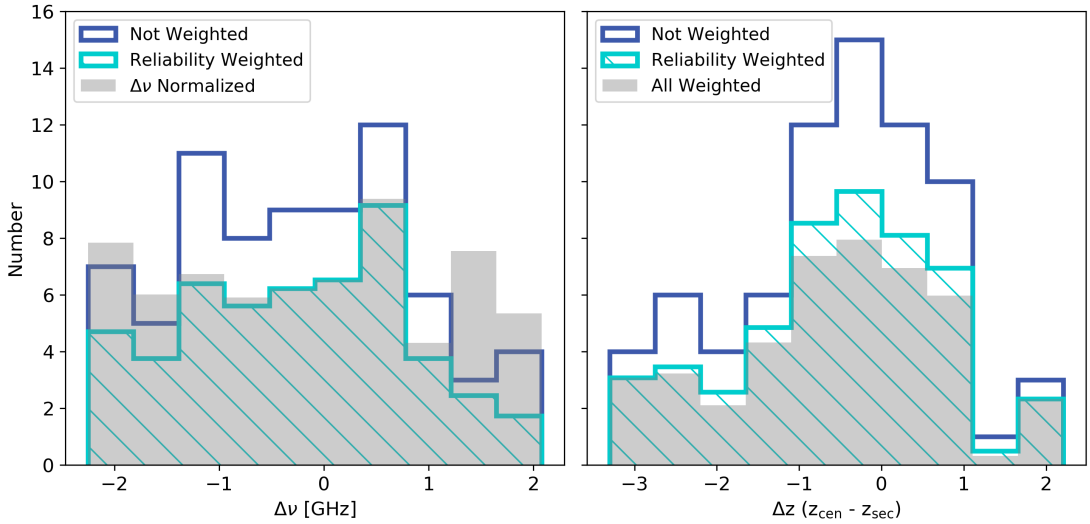

Figure 2.9: *Left*: Difference between the central frequency of each candidate source and the reference frequency of the observation, $\Delta\nu$. The dark blue empty histogram is unweighted by reliability, while the cyan left hatched histogram is weighted by reliability. The grey shaded histogram is the reliability weighted distribution normalized to the number of data cubes that cover a large enough frequency range to reach a given $\Delta\nu$ value. For randomly distributed objects, we would expect a flat distribution and this is what we observe. *Right*: Difference between the redshift of the central source and candidate source (only for cases where a tentative optical counterpart is identified), Δz. The dark blue empty histogram is the unweighted data, the cyan hatched histogram is weighted by reliability, and the grey shaded histogram is weighted by reliability, the probability of association, and the redshift probability. There is a tendency here for objects to cluster around $\Delta z \pm 1$, however this is too large of a redshift separation to form physical associations. We conclude the candidate sources we detect are not biased by clustering around the central source.

each candidate source and the frequency of the central source in each data cube ($\Delta\nu$; left panel). We also show the difference between the redshift of the central source and candidate source, for candidates with identified counterparts (Δz; right panel). In both cases we also compare the distribution of $\Delta\nu$ and Δz when weighting the data by reliability, probability of association, and redshift probability.

The left panel of Figure 2.9 shows in both the unweighted and weighted cases that the candidate sources are approximately uniformly distributed in $\Delta\nu$ with a

slight decrease for $\Delta\nu \gtrsim 1$ and a bit of a central bump for completely unweighted sources. However, the data cubes do not all cover the same frequency range and therefore the chance of a source to show at a particular $\Delta\nu$ has to be weighted accordingly. To account for this, we normalize the reliability weighted histogram by the number of data cubes that span the different possible $\Delta\nu$ ranges. This is shown in the gray histogram, where we see that the recovered distribution is very consistent with a uniform distribution across the spectral range. This shows that our secondary detections are uniformly distributed in $\Delta\nu$, and therefore there is no signature of a bias introduced by clustering around the targeted central sources. In physical terms, $\Delta\nu = 1$ GHz for a source at $z \sim 1.5$ in a $\lambda \simeq 3\,\mathrm{mm}$ observation represents a physical velocity difference of over 3,000 $\mathrm{km\,s^{-1}}$, larger than the central velocity dispersion of a massive galaxy cluster like Coma ($\sigma_V \sim 1200\ \mathrm{km\,s^{-1}}$, Kent and Gunn, 1982). Therefore we would expect a relatively narrow peak in the corrected histogram if most sources were physically related to the central source, independent of our ability to identify counterparts.

The right panel of Figure 2.9 shows the distribution in Δz for only those candidate sources for which we find tentative optical counterparts. The unweighted case shows a wide peak in the distribution of objects at $z \pm 1$ from the central sources. When weighting by reliability, probability of association, and redshift probability this peak is significantly smoothed but still present. The existence of a broad peak is to be expected: most of our observations target the $2-1$ and $3-2$ CO transitions at $z \sim 1-2$, and the most likely bright transitions for field objects will be $2-1$ to $4-3$, which would place them in the $\Delta z \sim \pm 1$ range for most observations. Note

also that if this were an indication of true physical clustering we would expect the peak to be much narrower, $\Delta z \lesssim \pm 0.1$.

2.5.3 CO Luminosity Functions

We construct the CO luminosity functions using equation 2.9:

$$\Phi(\log L_i) = \frac{1}{V} \sum_{j=1}^{N_i} \frac{R_j}{C_j} P_{a,j} P_{z,j} \,. \tag{2.9}$$

Here N_i is the number of galaxies that fall within the luminosity bin i defined by $\log L_i - 0.25$ and $\log L_i + 0.25$ ($\log L_i - 0.5$ and $\log L_i + 0.5$ for cases where we only have a small number of sources), V is the total volume of the Universe that is sampled by a given transition across all of our data cubes, R_j is the reliability of the j^{th} line and C_j is its completeness, $P_{a,j}$ is the probability that the candidate source is associated with a particular optical counterpart, and $P_{z,j}$ is the probability that a given candidate optical counterpart corresponds to a particular CO transition (and hence redshift). Each CO line is down-weighted by its likelihood probability calculated in §2.4, probability of association, and redshift probability, and then up-scaled by its completeness fraction. The CO luminosities are calculated from equation 3 of Solomon et al. (1997):

$$L'_{CO} = 3.25 \times 10^7 \frac{S_{\rm CO} \Delta V D_L^2}{\nu_{obs}^2 (1+z)^3} \quad [\text{K km s}^{-1} \text{ pc}^2] \tag{2.10}$$

where $S_{CO}\Delta V$ is the integrated flux density in units of Jansky kilometers per second, D_L is the luminosity distance of the source in megaparsecs, ν_{obs} is the observed

Survey	Transition	$\nu_{\rm rest}$ [GHz]	$z_{\rm min}$	$z_{\rm max}$	Volume [Mpc^3]	CV [%]
PHIBSS2	CO $(2-1)$	230.538	0.017	1.562	11250	18.2
	CO $(3-2)$	345.538	0.492	2.843	26136	15.9
	CO $(4-3)$	461.041	0.989	4.124	36144	14.9
	CO $(5-4)$	576.268	1.486	5.405	42380	13.3
	CO $(6-5)$	691.473	1.983	6.685	46288	15.6
COLDz COSMOS	CO $(1-0)$	115.271	1.953	2.723	20189	36.9
	CO $(2-1)$	230.538	4.906	6.445	30398	37.8
COLDz GOODS-N	CO $(1-0)$	115.271	2.032	2.847	131042	25.5
	CO $(2-1)$	230.538	5.064	6.695	193286	25.6
ASPECS LP	CO $(1-0)$	115.271	0.003	0.369	338	59.4
	CO $(2-1)$	230.538	1.006	1.738	8198	36.9
	CO $(3-2)$	345.538	2.008	3.107	14931	35.0
	CO $(4-3)$	461.041	3.011	4.475	18242	35.2

Table 2.1: Comoving Volume Sampled by each CO Transition. The sensitivity drop off due to the primary beam is accounted for in the volume calculations.

frequency of the line in GHz, and z is its redshift. The volume of the Universe that is sampled by a given PHIBSS2 data cube is calculated as a three-dimensional slab of space defined by the field-of-view of the given observation, and frequency range that is observable by the instrument, for each CO transition we consider in our counterpart search. These values are summarized in Table 2.1.

We exclude from our CO luminosity functions all central sources since these were targeted objects and are therefore not the result of our blind search. We also exclude objects with no optical counterpart identification, because we have no information on their corresponding redshift or CO transition. We note that because we choose to not include sources for which we identify no counterpart, that care should be taken when comparing our results to previous blind survey results in subsequent sections and figures. The constraints we derive should be considered

lower limits since the catalogs we draw counterparts from may be incomplete.

2.5.3.1 PHIBSS2 CO Luminosity Functions

Figure 2.10 plots the PHIBSS2 CO luminosity function for a range of CO transitions and median redshifts in gray shaded boxes. Our results are plotted as a moving average, by displacing each luminosity bin by 0.1 dex and recalculating the CO luminosity function according to equation 2.9. In each panel, we give the number of candidate sources used to derive the given CO luminosity function and their median redshift. We are able to constrain CO $(2-1)$ at $\langle z \rangle \sim 0.7$ and 1.2, CO $(3-2)$ at $\langle z \rangle \sim 1.5$ and 2.2, CO $(4-3)$ at $\langle z \rangle \sim 1.9$, 2.2 and 3.3, CO $(5-4)$ at $\langle z \rangle \sim 3.4$ and 4.4, and CO $(6-5)$ at $\langle z \rangle \sim 3.7$. We compare each of these to existing theoretical predictions from Popping et al. (2019)[1], Popping et al. (2016), Vallini et al. (2016), and Lagos et al. (2012) and where possible, to existing observational constraints. To be able to consistently compare with the work of Walter et al. (2014) and Decarli et al. (2016, 2019), we calculate our uncertainties on the CO luminosity function in the same way. Thus the error bars along the y-axis correspond to Poissonian errors on N_i, the number of sources within a luminosity bin i, at the 1σ level according to Tables 1 and 2 of Gehrels (1986), while the "error bars" along the x-axis simply reflect the width of the luminosity bin.

We fit our observed CO luminosity functions with a Schechter function (Schechter, 1976) in the logarithmic form used by Riechers et al. (2019) and Decarli et al. (2019):

[1]We convert the molecular hydrogen mass functions to CO luminosity functions assuming an $\alpha_{\rm CO} = 3.6\ {\rm M}_\odot\ ({\rm K\,km\,s^{-1}\,pc^2})^{-1}$ and temperature ratios of $r_{\rm J1} = 0.76 \pm 0.09$, 0.42 ± 0.07 for J = 2, 3 respectively (Daddi et al., 2015).

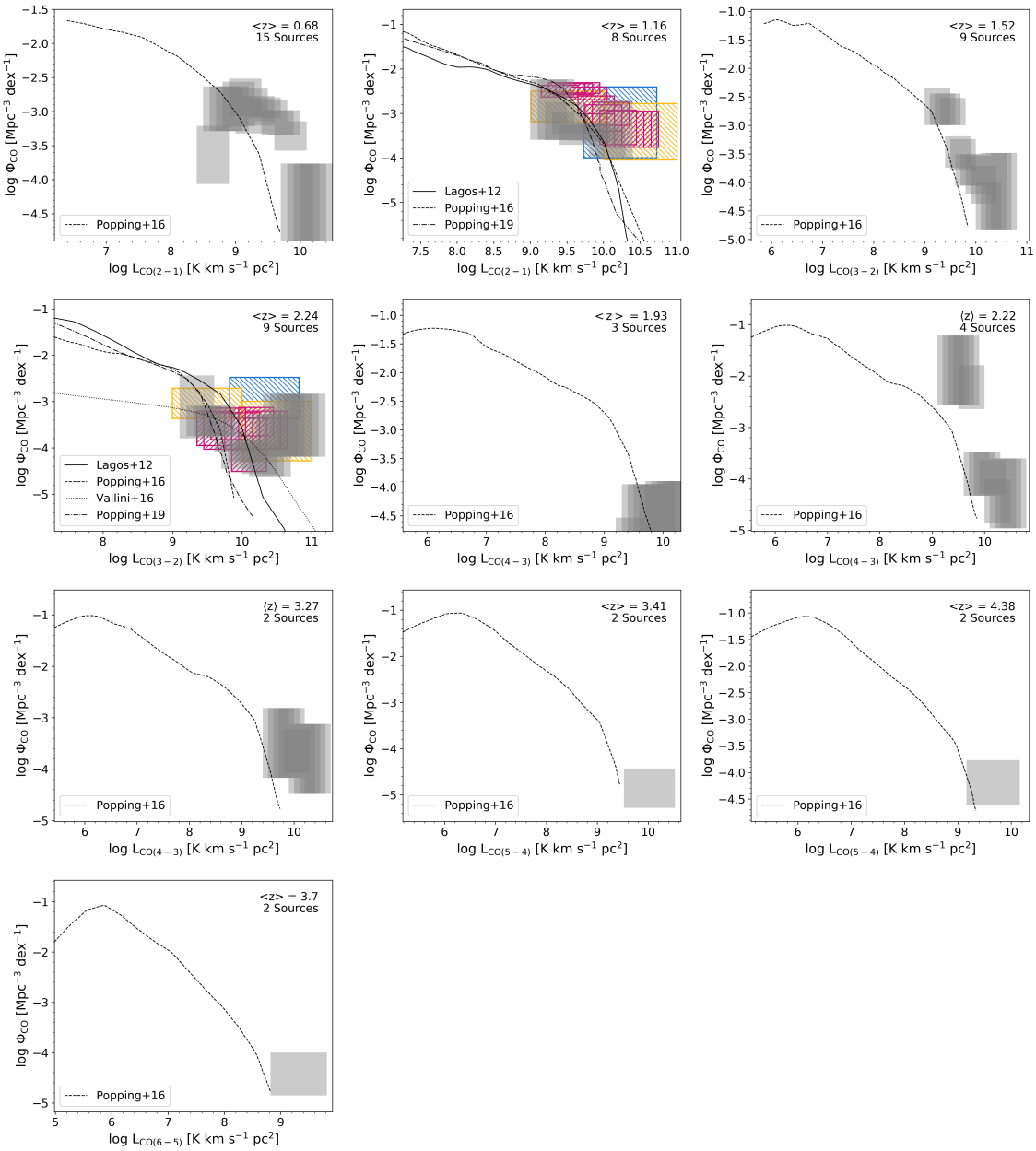

Figure 2.10: The PHIBSS2 CO luminosity functions observed here (shaded gray boxes, with sizes corresponding to 1σ uncertainties), compared to the PdBI HDF-N work (blue left-hatched boxes; Walter et al., 2014), the ASPECS pilot work (yellow left-hatched boxes; Decarli et al., 2016), the ASPECS LP work (magenta right-hatched boxes; Decarli et al., 2019), the predicted CO luminosity function of Vallini et al. (2016) based on the *Herschel* IR luminosity function, and the theoretical predictions of Lagos et al. (2012) and Popping et al. (2016). Our derived CO luminostiy functions are consistent with constraints from previous work, but are in tension with the semi-analytic model predictions, particularly at the higher-J CO transitions where we observe larger number densities at higher CO luminosities than is predicted by these models.

$$\log \Phi(L') = \log \Phi^* + \alpha \log \left(\frac{L'}{L'^*} \right) - \frac{1}{\ln 10} \frac{L'}{L'^*} + \log(\ln(10)) \tag{2.11}$$

where Φ^* is the scale number of galaxies per unit volume, L'^* is the scale line luminosity and the parameter that sets the "knee" of the luminosity function, and α is the slope of the faint end.

To obtain estimates of the allowed range of Schechter parameters, we fit the characteristic parameters described above to our CO $(2-1)$ at $\langle z \rangle = 0.68$ luminosity function due to the small numbers of sources in all other cases. To account for the uncertainties of each luminosity bin, we draw points from normal distributions centered in each luminosity bin, with standard deviation corresponding to the size of the luminosity bin. We fit a Schechter function to that set of points while assuming unconstrained priors on the characteristic Schechter parameters. We then repeat the process with a new set of randomly drawn points from each luminosity bin and do this until enough points have been drawn to determine the posterior likelihood distributions of each Schechter parameter.

We show the results of this fitting in Figure 2.11, where we also include the posterior likelihood distribution of each parameter along with the 5th, 50th, and 95th percentiles. In Figure 2.12, we show the density of Schechter function fits to each sample of points drawn from the data. This Figure shows that the uncertainties are dominated by the faint end, below the "knee" of the luminosity functions. However, the three parameters $L'^*_{\rm CO}$, $\Phi^*_{\rm CO}$, α are fairly reliably constrained by the data. We

Line	Redshift	log $L'^{*}_{\rm CO}$	log $\Phi^{*}_{\rm CO}$	α
CO $(2-1)$	$0.33-0.99$	$9.76^{+0.41}_{-0.31}$	$-3.31^{+0.38}_{-0.58}$	$-0.07^{+0.55}_{-0.45}$

Table 2.2: Schechter Function Fit Parameter Constraints from PHIBSS2

summarize the constraints on the Schechter model parameters for each fit in Table 2.2, including the 5th and 95th percentiles.

2.5.4 Molecular Gas Mass Density Evolution

To derive constraints on the evolution of co-moving molecular gas mass, we need to convert our high-J CO luminosities to CO $(1-0)$ luminosities. We assume Rayleigh-Jeans brightness temperature ratios of $r_{\rm J1} = 0.76 \pm 0.09$, 0.42 ± 0.07, 0.31 ± 0.06, and 0.23 ± 0.04 for J = 2, 3, 4, and 5 respectively (Daddi et al., 2015). We then convert these CO $(1-0)$ luminosities to molecular gas masses, using an $\alpha_{\rm CO}$ value of 3.6 $\rm M_{\odot}$ (K km s^{-1} pc^2)$^{-1}$ for the sake of consistency with previous work using

$$M_{\rm H_2} = \alpha_{\rm CO} L'_{(\rm CO\,(1-0))}. \tag{2.12}$$

The PHIBSS project has consistently used a 20% larger value of $\alpha_{\rm CO}$ (Tacconi et al., 2018). Carleton et al. (2017) investigate the dependence of the conversion factor $\alpha_{\rm CO}$ on total mass surface density for $z > 1.7$ in the PHIBSS sample of galaxies and find that $92-100\%$ of $\alpha_{\rm CO}$ measurements are similar to the Milky Way value of 4.36 $\rm M_{\odot}$ (K km s^{-1} pc^2)$^{-1}$ adopted by PHIBSS. Here we use a value of 3.6 to compare consistently to other results in the literature who have adopted this value (Riechers et al., 2019, Decarli et al., 2019). Adopting a different constant

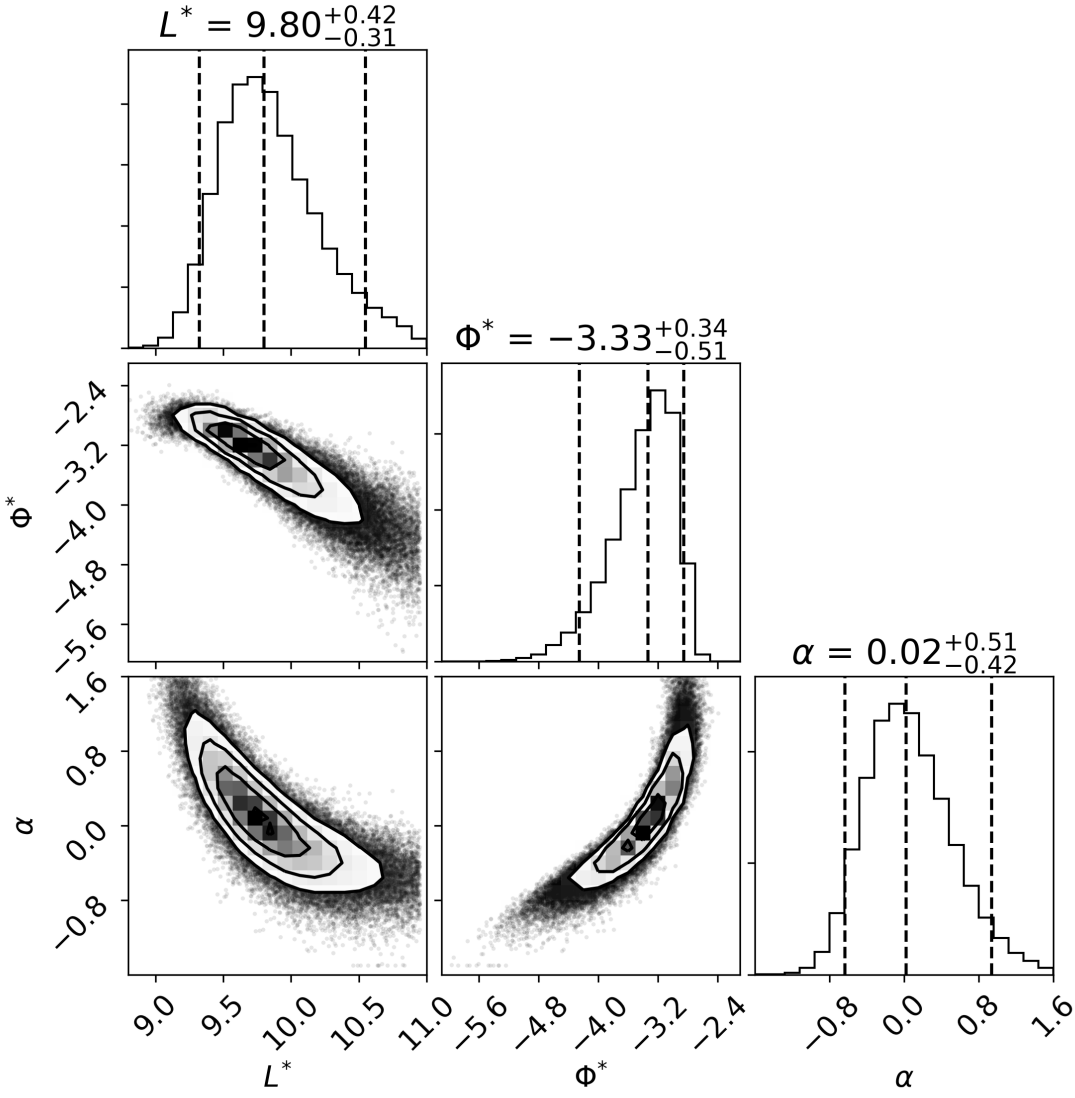

Figure 2.11: Corner plot of the Schechter model parameters posterior distribution from fitting the CO $(2-1)$ luminosity function. The parameters are reasonably well constrained by the data.

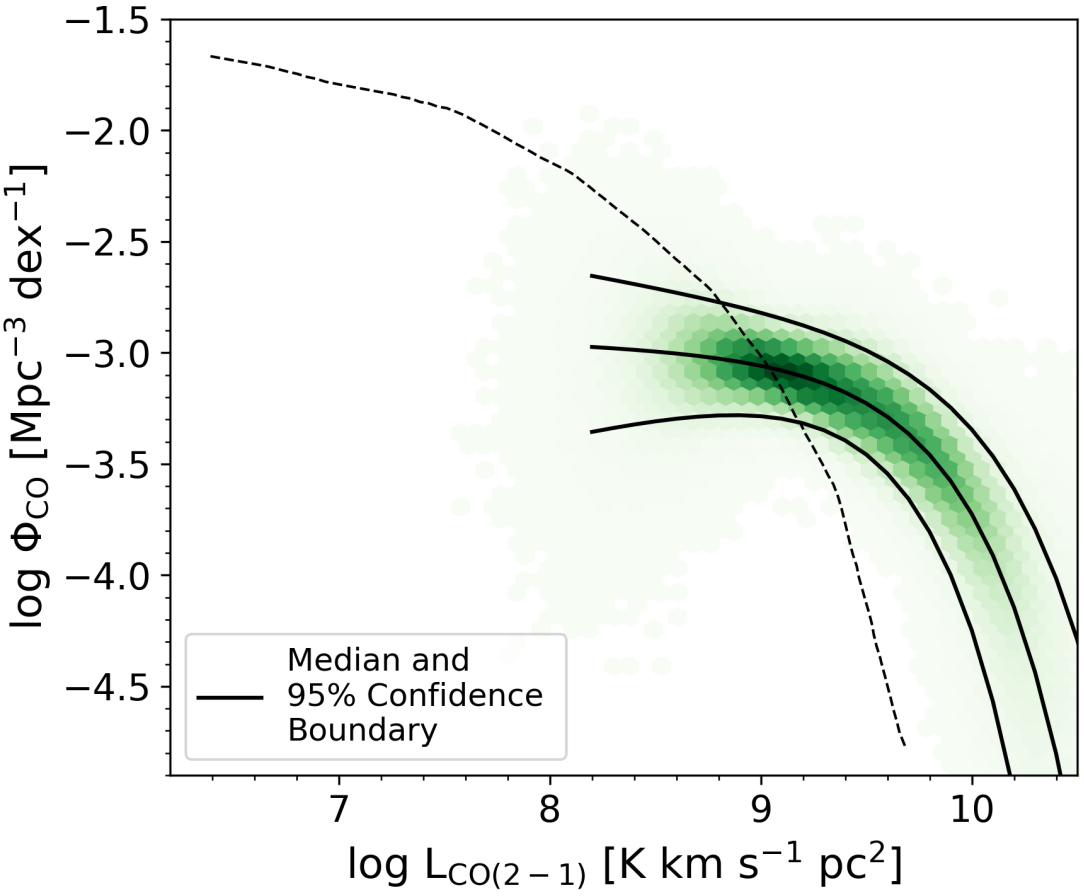

Figure 2.12: Density of Schechter fits for the CO $(2-1)$ $z \sim 0.7$ luminosity function. The black lines correspond to the median points and the boundary where 95% of the fits lie. For reference, the Popping et al. (2016) prediction is plotted as the dashed black line. We see from this that the "knee" of the CO luminosity function is well constrained by the data, while there is more uncertainty in constraining the slope of the faint end.

value of α_{CO} will result in a straightforward linear scaling of our M_{H_2} and $\rho(H_2)$ measurements.

As in Walter et al. (2014), Decarli et al. (2016), Riechers et al. (2019), and Decarli et al. (2019), we do not extrapolate to the undetected faint end of the luminosity functions and only use actual candidate sources. We should note that this conversion from high-J CO transitions to molecular mass is increasingly uncertain as J increases: this is unavoidable as the excitation requirements become increasingly stringent, and so a diminishing fraction of the gas emits brightly in these transitions. The only way around this constraint is to directly observe the J=1 − 0 or 2 − 1 transitions at high redshift, but that requires more powerful facilities than those in existence (such as the ngVLA, Decarli et al., 2018). Our results are shown as black boxes in Figure 2.13, where each box corresponds to the combination of candidate sources observed at any transition in the given redshift range.

2.6 Discussion

2.6.1 Comparison to Previous Blind CO Surveys

2.6.1.1 Luminosity Functions

The CO $(2-1)$ at $\langle z \rangle \sim 1.2$ and the CO $(3-2)$ at $\langle z \rangle \sim 2.3$ were previously constrained by Walter et al. (2014), Decarli et al. (2016), and Decarli et al. (2019). The observational constraints from Walter et al. (2014) are the result of a blind CO survey in part of the *Hubble* Deep Field North. Decarli et al. (2016) observed a

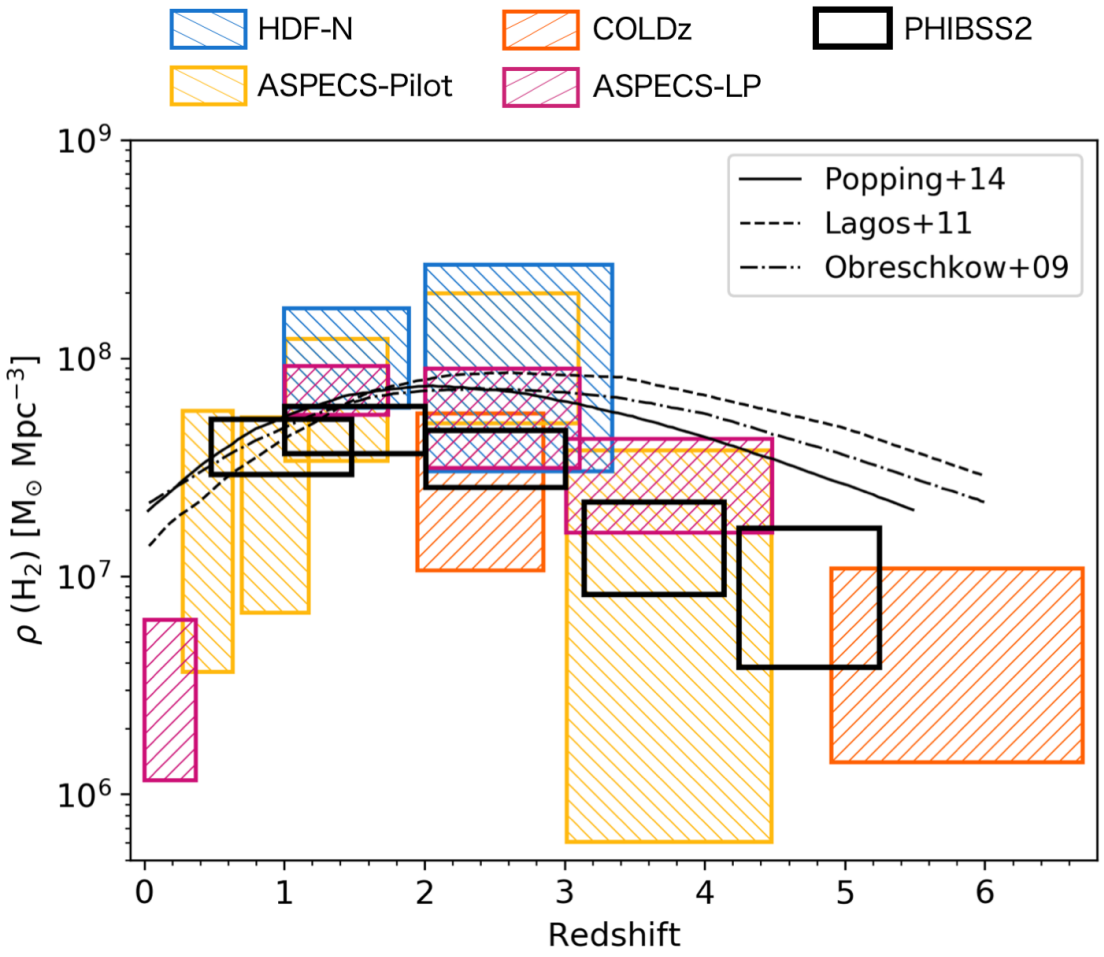

Figure 2.13: The evolution of the molecular gas mass density with redshift, where the black boxes represent the constraints from the PHIBSS2 data. Orange right hatched boxes correspond to the constraints derived from the VLA COLDz measurements of Riechers et al. (2019), purple right hatched boxes correspond to the constraints of ASPECS LP measurements of Decarli et al. (2019), yellow left hatched boxes correspond to the work of Decarli et al. (2016), and the blue left hatched boxes correspond to the constraints from the work of Walter et al. (2014). The dashed lines correspond to model predictions for the evolution of the molecular gas mass density, as derived by Obreschkow et al. (2009), Lagos et al. (2011), and Popping et al. (2014b), Popping et al. (2014a). The constraints derived from serendipitous detections of CO in the PHIBSS2 fields are consistent with those of previous blind surveys.

$\sim$ 1 arcmin region of the *Hubble* Ultra Deep Field (UDF) with ALMA (the ASPECS pilot program), while Decarli et al. (2019) derive their constraints from the ASPECS

Large Program. The redshift ranges for which we derive constraints from CO $(2-1)$ and CO $(3-2)$ are very similar to these previous works, so we directly compare our measurements to them. We see from Figure 2.10 that our results correspond to approximately the same luminosity bins as Decarli et al. (2016), and are in agreement with their results. Decarli et al. (2016) report an excess of CO-bright galaxies in the UDF with respect to theoretical predictions, and our results confirm this for the galaxies we observe in the 3D-HST/CANDELS fields sampled by our PHIBSS2 data. This implies that galaxies in this redshift bin are more gas-rich than is currently predicted by theoretical models.

Riechers et al. (2019) derive the CO $(1-0)$ luminosity function for a median redshift of $z = 2.4$ in the COLDz program. Our CO $(3-2)$ luminosity function is derived for a median redshift of $z \sim 2.3$. We consider this difference in redshift to be negligible and therefore compare to the COLDz measurements without any modifications. To compare these results then, it is only necessary to assume a line ratio between these two transitions. To convert our CO $(3-2)$ luminosities to CO $(1-0)$ we use $r_{31} = 0.42 \pm 0.07$ from Daddi et al. (2015).

We show the comparison between our derivation and that of the COLDz results of Riechers et al. (2019) in Figure 2.14. Overall we find that our measurements are consistent with those of Riechers et al. (2019) within the uncertainties, although there is a hint that our results may point to higher number densities than those measured in COLDz. This could be due to cosmic variance (CV), or it could also be evidence that higher-J observations or surveys tend to preferentially select higher gas excitation galaxies. This would then mean that our temperature ratio is too low.

Bolatto et al. (2015) find for two CO $(3-2)$ bright $z \sim 2.2-2.3$ galaxies r_{31} ratios of order unity, while samples of nearby galaxies, luminous infrared galaxies, and ultra luminous infrared galaxies show mean values of $r_{31} \sim 0.66$. We convert our CO $(3-2)$ luminosities to CO $(1-0)$ using this higher temperature ratio and show the result in Figure 2.14 (dashed black boxes). The change in assumed excitation produces a moderate shift toward lower luminosities, which brings the data into somewhat better agreement but does not completely eliminate the tension between both sets of measurement.

2.6.1.2 Molecular Gas Mass Density Evolution

In Figure 2.13, we compare our results to all previous observational constraints: those from Walter et al. (2014), the ASPECS pilot work of Decarli et al. (2016), the COLDz measurements of Riechers et al. (2019), and the ASPECS LP measurements of Decarli et al. (2019). Within the uncertainties, our results are consistent with all previous observational constraints. Between redshifts of $z \sim 2-3$, our result is most consistent with the measurement of Walter et al. (2014) and the ASPECS pilot, and hints at maybe a higher molecular gas mass density than that obtained by COLDz. From redshifts of $z \sim 3-5$, our measurements are consistent with the ASPECS pilot measurements, and hints at a lower molecular gas mass density than derived in the ASPECS-LP. Given the present state of the art in the uncertainties it is unclear if these discrepancies are real, but their magnitude is easily explained by cosmic variance.

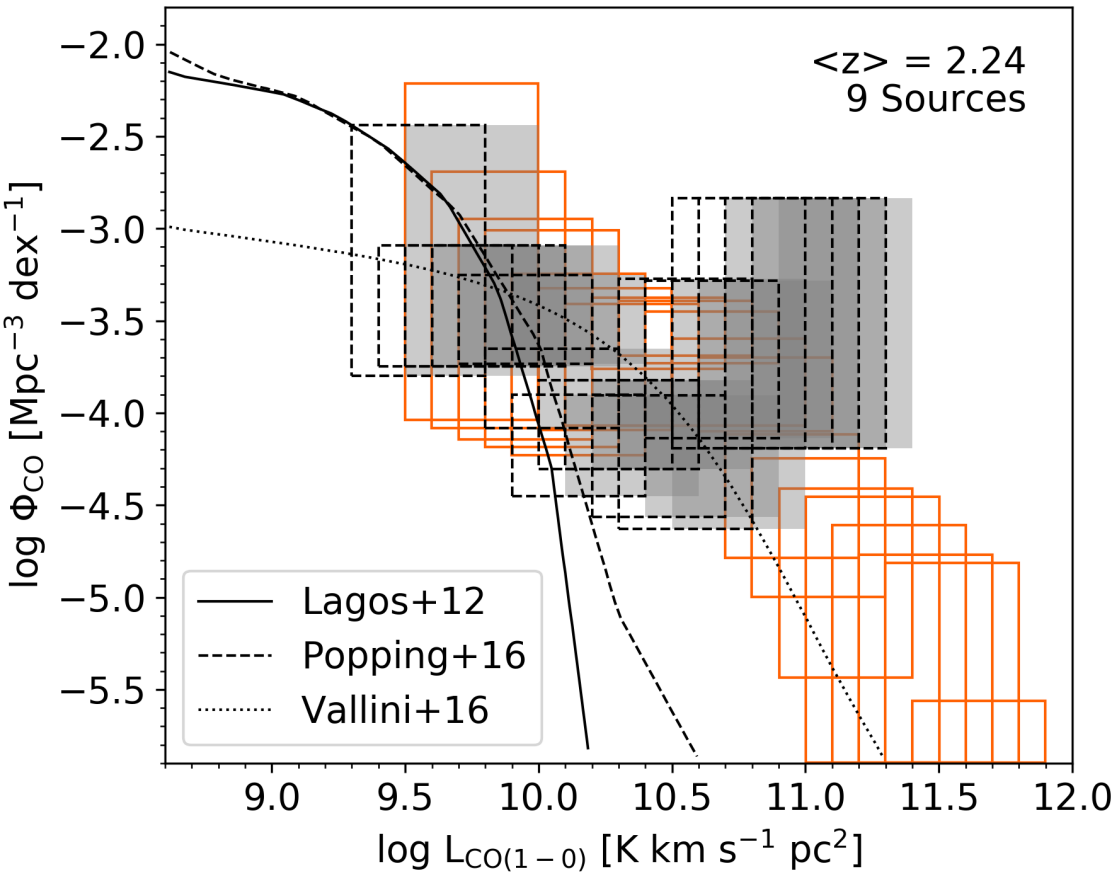

Figure 2.14: The comparison of our CO $(3-2)$ luminosity function, converted to CO $(1-0)$ assuming a brightness temperature ratio of $r_{31} = 0.42$ (gray boxes) to the results of Riechers et al. (2019) (orange boxes). Within the uncertainties, our measurements are consistent with those of Riechers et al. (2019). As an additional comparison, we convert out CO $(3-2)$ luminosities with a $r_{31} = 0.66$ (Bolatto et al., 2015, black dashed boxes). This shifts our measurements to lower CO luminosities but our results stay in agreement with Riechers et al. (2019). We plot the predictions of Lagos et al. (2012), Vallini et al. (2016), Popping et al. (2016) as a reference.

2.6.2 Cosmic Variance

To address the question of cosmic variance, we use the results of Driver and Robotham (2010) to quantify the cosmic variance of the PHIBSS2 data. The authors repeatedly extract galaxy counts in cells of fixed size at random locations in the Sloan Digital Sky Survey (SDSS) Data Release 7. They explore the variance of the SDSS data in square cells from 1 to 2048 square degrees and in rectangular cells with aspect ratios ranging from 1:1 to 1:128. They find that cosmic variance depends on total survey volume, the survey aspect ratio, and whether the survey area is contiguous or composed on independent lines of sight, with cosmic variance decreasing for higher aspect ratios and non-contiguous survey areas (which essentially help sample a larger range of environments). Driver and Robotham (2010) provide a general equation that can be used at any redshift to estimate the cosmic variance of a survey (eq. 4 in Driver and Robotham, 2010):

$$\begin{aligned}\zeta_{\mathrm{Cos.Var.}}(\%) = (1.00 - 0.03\sqrt{(A/B)-}) \\ \times [219.7 - 52.4\log_{10}(AB \times 291.0) \\ + 3.21[\log_{10}(AB \times 291.0)]^2]/\sqrt{NC/291.0} \quad (2.13)\end{aligned}$$

where A and B are the transverse lengths at the median redshift, C is the radial depth all expressed in units of $h_{0.7}^{-1}$ Mpc, and N is the number of independent sight-lines. This empirical expression for estimating the cosmic variance is implemented as a function in the `R` library `celestial`, as `cosvarsph`. We input into `cosvarsph`

the RA, Dec, and redshift limits that correspond to those values of the PHIBSS2 data cube with the median volume (since not all data cubes have the same size), and finally take N to be the total number of data cubes. With this estimate, we derive cosmic variances in the range $\sim 13\% - 18\%$; these values are summarized in the last column of Table 2.1.

For comparison, we perform a crude estimate of the cosmic variance in the COLDz survey. The COLDz survey covers an area of 8.9 arcmin^2 at 31 GHz and 7.0 arcmin^2 at 39 GHz for COSMOS and an area of 50.9 arcmin^2 at 30 GHz and 46.4 arcmin^2 at 38 GHz. Using the average area and the redshift limits reported in their Figure 1 for both the CO $(1-0)$ and CO $(2-1)$ transitions as inputs into `cosvararea`, we estimate a cosmic variance of $\sim 34\%$ and $\sim 24\%$ for COSMOS and GOODS-N respectively. Performing the same estimate for the ASPECS-LP using the redshift limits from Table 1 of Decarli et al. (2019), we find that the cosmic variance is in the range $\sim 59\%$ to $\sim 35\%$ for CO $(1-0)$ to CO $(4-3)$. These estimates are for a square survey area with aspect ratio 1:1, which is only approximate for either the COLDz or the ASPECS-LP surveys, and are therefore likely upper limits on their cosmic variance. However, this still shows that cosmic variance may be less of an issue in surveys that are composed of multiple independent lines of sight rather than one contiguous area.

2.7 Conclusions

We present a catalog of 67 candidate secondary sources observed in 110 observations of PHIBSS2, where the primary target is a known optical high-z galaxy, which includes spectra, redshifts, line widths, integrated fluxes, CO luminosities, and molecular gas masses. We perform an analysis of the false positive probabilities for each candidate secondary source, characterizing them with a reliability parameter R, and assess the completeness of the search algorithm. We perform a search for optical counterparts corresponding to each candidate source, taking into account the redshift uncertainty for the optical sources in the 3D-HST/CANDELS catalogs. We find that $\sim 64\%$ of these secondary detections have optical counterparts (in some cases more than one) and include these together with an estimate of the probability of association in our catalog. Finally, we use the catalog of candidate sources to build the CO $(2-1)$, CO $(3-2)$, CO $(4-3)$, CO $(5-4)$, and CO $(6-5)$ luminosity functions for a range of median redshifts, spanning $z \sim 0.6-4.4$ and a volume sampled of $\sim 13500-57000$ Mpc^3 depending on the CO transition. We find broad agreement between our results and those of Walter et al. (2014), Decarli et al. (2016), Riechers et al. (2019), and Decarli et al. (2019). We also demonstrate that a blind CO search across many independent fields in observations of targeted objects can be successfully combined to establish constraints on the luminosity functions of different CO transitions in different redshift bins. We show that, in the case of CO, there appears to be little or no bias towards physically associated neighbors of the primary target down to the luminosities probed. We use an estimate of the

cosmic variance to show that an approach which combines multiple independent fields mitigates the impact of cosmic variance. This is because for a contiguous survey area, the volume sampled needs to be very large in order to cut across many different environments; on the order of 10^7 $h_{0.7}^{-3}$ Mpc^3 (for an aspect ratio of 1:1) to decrease cosmic variance to a 10% level according to the formalism by Driver and Robotham (2010). This approach also exploits existing data which can significantly expand blind survey samples. The caveat is that one must deal with non-uniform sensitivity, which can however be handled through a good SNR characterization of the data sets.

We have derived the molecular gas mass density evolution from converting our high-J CO luminosity functions to CO $(1-0)$, assuming a CO luminosity to molecular gas mass conversion factor of $\alpha_{CO} = 3.6$ $M_\odot$ (K km s^{-1} $pc^2)^{-1}$ for consistency with previous studies, and find our results to be largely consistent with previous constraints on the evolution of the cosmic cold gas mass density.

Chapter 3: The Nature and Fate of Star Forming Clumps in Gas-Rich, Turbulent Galaxies

3.1 Overview

To indirectly study the internal structure of giant clumps in main sequence galaxies at $z \sim 1-3$, we target very turbulent and gas-rich local analogues from the DYNAMO sample with the *Hubble Space Telescope*, over a wavelength range of $\sim 200-480$ nm. We present a catalog of 58 clumps identified in six DYNAMO galaxies, including the WFC3/UVIS F225W, F336W, and F467M photometry where the $(225-336)$ and $(336-467)$ colours are sensitive to extinction and stellar population age respectively. We measure the internal colour gradients of clumps themselves to study their age and extinction properties. We find a marked colour trend within individual clumps, where the resolved colour distributions show that clumps generally have bluer $(336-467)$ colours (denoting very young ages) in their centers than at their edges, with little variation in the $(225-336)$ colour associated with extinction. Furthermore, we find that clumps whose colours suggest they are older, are preferentially located closer toward the centers of their galaxies, and we find no young clumps at small galactocentric distances. Both results are consistent with

simulations of high–redshift star forming systems that show clumps form via violent disc instability, and through dynamic processes migrate to the centers of their galaxies to contribute to bulge growth on timescales of a few 100 Myr, while continually forming stars in their centers. When we compare the DYNAMO clumps to those in these simulations, we find the best agreement with the long-lived clumps.

3.2 Introduction

The morphologies of massive star-forming galaxies at $z \sim 1-3$ are irregular compared to local star-forming galaxies of similar mass. Rest-frame UV and optical images of these galaxies reveal giant, $\sim 0.1-1$ kpc sized clumps with masses ranging from 10^7-10^9 $M_\odot$ (Förster Schreiber et al., 2011, Guo et al., 2012, Huertas-Company et al., 2020) that are the sites of active star formation, accounting for up to $10-20\%$ of the total integrated star forming activity of galaxies at this epoch (Wuyts et al., 2012, 2013). These giant clumps are also observed in resolved molecular gas maps (Tacconi et al., 2013) and rest-frame optical line emission spectra (Genzel et al., 2008, 2011), but are less prominent in stellar mass distribution maps (Wuyts et al., 2012). Galaxies at this epoch are also observed to have high gas-fractions, defined as $f_{gas} = M_{H_2}/(M_{H_2} + M_*)$ ($f_{gas} \sim 0.3-0.8$, Daddi et al., 2010a, Tacconi et al., 2010, 2013, Genzel et al., 2015), high star formation rates (Genzel et al., 2008), and high velocity dispersions (Förster Schreiber et al., 2006).

There is an ongoing debate as to the nature of these clumps and their eventual fate. Cosmological simulations (e.g., Dekel et al., 2009, Bournaud et al., 2014, Man-

delker et al., 2017) produce clumpy galaxies via cold gas accretion and gravitational disc instabilities. These clumps survive long enough in some simulations to migrate to the centers of galaxies through orbit decay by loss of orbital angular momentum, on timescales of $\lessapprox$ 500 Myr and thus contribute to galaxy bulge growth (Noguchi, 1999, Immeli et al., 2004, Bournaud et al., 2007, Ceverino et al., 2010). Ceverino et al. (2012) show in their cosmological simulations that this migration results in a clump age gradient that is much steeper than the disc age gradients (see also Mandelker et al., 2017). Observational measurements of clump colours also provide evidence for this inward migration: redder clumps are found closer to the centers of galaxies, while bluer clumps are found preferentially at larger galactocentric distances. These galaxy-wide colour gradients are interpreted as an age gradient, where the redder clumps are thought to be older (Förster Schreiber et al., 2011, Guo et al., 2012, Shibuya et al., 2016, Soto et al., 2017, Guo et al., 2018).

This scenario however, requires that clumps survive for timescales of $\sim$ 150 Myr. Yet other numerical simulations (such as Feedback in Realistic Environments, FIRE; Hopkins et al. 2014, and NIHAO; Wang et al. 2015) find that clumps dissolve on timescales of $\sim$ 100 Myr or less and thus do not survive long enough to contribute significantly to galaxy bulge growth (Buck et al., 2017, Oklopčić et al., 2017), even though these simulated galaxies show the same clump colour gradients as observed. Furthermore, other simulations show that increasing clump ages at small distances can be produced by inside-out formation of the disc, rather than clump migration, and that clumps disrupt on timescales of $\sim$50 Myr (Genel et al., 2012).

Buck et al. (2017) propose that the colour gradient found by observers may be

the result of contamination from disc light. The density of disc stars is lower in the outskirts of a galaxy and higher in the center, thus the authors argue that redder stellar light in the centers of galaxies can artificially produce colour gradients such as the ones observed. Contrary to this idea, Guo et al. (2018) find that regardless of the chosen disc subtraction method used (ranging from no disc subtraction to very strict disc subtraction), the clump colour gradients in their sample of 1270 galaxies at $0.5 \leq z < 3.0$ are still present and only the amplitude of the gradients are affected.

Nonetheless, in agreement with observations, the NIHAO galaxies of Buck et al. (2017) show clumps in light maps but not in stellar mass maps. The authors use this to argue that the clumps detected in the simulated galaxies are not long-lived gravitationally bound systems that have any dynamical influence on the evolution of the disc. Rather they are simply localized (clumpy) regions of star formation. The authors furthermore postulate that dust attenuation can affect the observed structure of a galaxy by enhancing intrinsically dim clumps, and suppressing intrinsically bright ones, suggesting that clumps are simply the result of variations in extinction.

Fortunately, the existence of nearby galaxies with properties similar to those at high redshift, allows us to study the light and extinction distributions in clumpy galaxies on a resolved scale. The DYnamics of Newly Assembled Massive Objects (DYNAMO; Green et al., 2014) sample consists of very rare local ($z \sim 0.1$) galaxies whose properties are very well matched to those of main-sequence galaxies at $z \sim 1 - 3$. Green et al. (2014) derive Hα rotation curves for DYNAMO galaxies and find that the mean ionized gas velocity dispersion is ~ 50 km s^{-1}, reflecting much

larger turbulent motions than in normal local galaxies, and infer gas fractions as high as $f_{gas} \sim 0.8$, and star formation rates in the $0.1 - 100$ $M_{\odot}\,yr^{-1}$ range. The properties of DYNAMO galaxies place them on the main sequence of star formation of $z \sim 1 - 2$ galaxies (e.g., see Figure 1 in Fisher et al., 2019); as a result, we have the opportunity to investigate clump properties on resolved scales, where we can learn more about their true nature and evolutionary fate.

In this work, we investigate the internal radial variation of age and extinction of individual clumps in six DYNAMO galaxies through colour measurements, as well as galaxy-wide radial trends in colour and age evolution. The paper is structured as follows: §3.3 describes the targets and their HST observations, §3.4 describes our clump identification process, point-spread-function matching procedure and other data analysis, in §3.5 we present and discuss our photometry results, finally we summarize and conclude our work in §3.6.

We assume ΛCDM cosmology with $H_0 = 70$ $km\,s^{-1}\,Mpc^{-1}$, $\Omega_m = 0.3$, and $\Omega_\Lambda = 0.7$, and a Kroupa initial mass function (IMF; Kroupa, 2001) throughout this paper. All magnitudes we report are AB magnitudes. The physical scale corresponding to the typical redshift of our sources ($z \sim 0.1$) is 1.844 kpc per arcsecond (Wright, 2006).

3.3 Observations

3.3.1 Sample

The DYnamics of Newly Assembled Massive Objects (DYNAMO; Green et al., 2014) sample consists of 67 galaxies selected from the Sloan Digital Sky Survey DR4 (SDSS; Adelman-McCarthy et al., 2006) to cover a range of Hα luminosities up to $L_{H_\alpha} > 10^{42}$ erg s^{-1}, in the SDSS 3.0″ diameter fiber, and to lie in two redshift windows to avoid atmospheric absorption of H_α (centered at $z \sim 0.075$ and $z \sim 0.13$). DYNAMO galaxies span stellar masses from $10^9 - 10^{11}$ $M_\odot$ and SFRs from $\sim 0.1 - 100$ $M_\odot$ yr^{-1}.

In this work, we consider a sub-sample of six DYNAMO galaxies selected to build on a multi-wavelength study of these objects: DYNAMO D13-5, D15-3, G04-1, G08-5, G14-1, and G20-2, which are classified as rotating discs based on Hα kinematics. Galaxies G04-1, G14-1, and G20-2 are furthermore classified as "compact" rotating discs (Green et al., 2014). These galaxies are ones for whom the SDSS $r-$band exponential scale lengths are less than 3 kpc. Since the resolution for these objects is poorer, their kinematic classifications are less reliable. All six of these objects have molecular gas measurements from CO$(1-0)$ observations with the Plateau de Bure Interferometer (PdBI), and have gas fractions of $20-30\%$ and depletion timescales of $t_{dep} \sim 0.5$ Gyr (Fisher et al., 2014, White et al., 2017). Using HST Hα observations and Keck/OSIRIS Paα observations, Bassett et al. (2017) created spatially resolved ($\sim 0.8 - 1$ kpc) Hα extinction maps for galaxies

D13-5, G04-1, and G20-2, showing that there is only mild spatial variability in the amount of extinction within a given galaxy, and finding no evidence for highly attenuated star-forming clumps. Finally, the MPA-JHU Value Added Catalog[1] provides gas-phase metallicity measurements for $\sim$53,000 star forming galaxies, including the six DYNAMO galaxies we study here, derived from comparing several strong emission lines ([OII]λ3727, H$\beta\lambda$4861, [OIII]λ5007, Hα, [NII]λ6584, [SII]λ6717, and [SII]λ6731) to photoionization models (see Tremonti et al., 2004). These properties are summarized in Table 3.1.

3.3.2 HST Observations

The six DYNAMO galaxies in our sub-sample were observed with the *Hubble Space Telescope* (HST) Wide Field Camera 3 (WFC3) UVIS channel in three filters: F225W (UV wide), F336W (U), and F467M (Strömgren b). Observations were taken between February and November 2018. The full-width-half-maximum (FWHM) of the point-spread-function (PSF) of each filter is: $\sim$0.092″ for F225W, $\sim$0.080″ for F336W and F467M. We note that the observations are not diffraction limited until longward of 500 nm, thus the broader F225W PSF at shorter wavelengths. We present these data in Figures 3.1 and 3.2.

[1] https://wwwmpa.mpa-garching.mpg.de/SDSS/DR4/

Galaxy	z	M_* ($M_\odot$)	M_{gas} (10^9 $M_\odot$)	f_{gas}	SFR_{H_α} (10^9 $M_\odot$)	$< A_{H_\alpha} >$ (mag)	$< r_{clump} >$ (pc)	12 + log(O/H)
D13-5	0.07535	53.84	20.17	0.36 ± 0.02	21.20	1.80 ± 0.52	400	$9.10^{+9.11}_{-9.09}$
D15-3	0.06712	54.15	14.74	0.17 ± 0.02	13.70	...	394	$9.18^{+9.19}_{-9.17}$
G04-1	0.12981	64.64	43.68	0.33 ± 0.04	41.61	1.52 ± 0.26	451	$9.15^{+9.16}_{-9.12}$
G08-5	0.13964	9.65	16.29	0.30 ± 0.05	11.05	...	521	$9.00^{+9.02}_{-8.98}$
G14-1	0.13233	8.30	9.72	0.77 ± 0.08	22.33	...	353	$9.10^{+9.11}_{-9.06}$
G20-2	0.14113	17.27	19.12	0.21 ± 0.05	21.56	0.89 ± 0.14	449	$8.98^{+8.99}_{-8.96}$

Table 3.1: Properties of HST-DYNAMO Galaxies

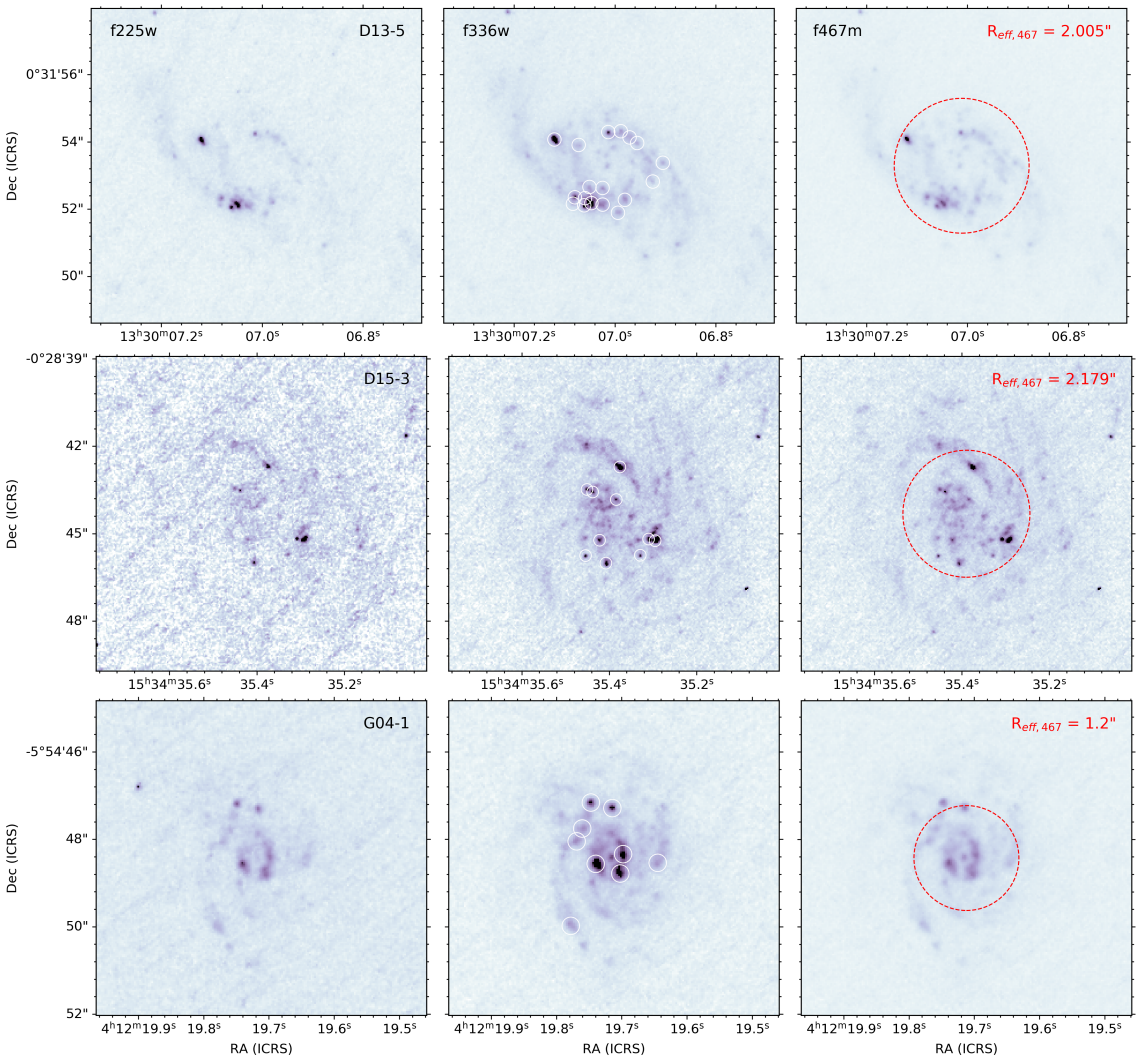

Figure 3.1: HST observations of galaxies D13-5, D15-3, and G04-1: F225W (left), F336W (middle), F467M (right). The F467M measured effective radius of each galaxy is shown in the right panels (dashed red circle). The middle panels outline in white each detected clump, as described in §3.4. Galaxy G04-1 is classified as a "compact" rotating disc (Green et al., 2014).

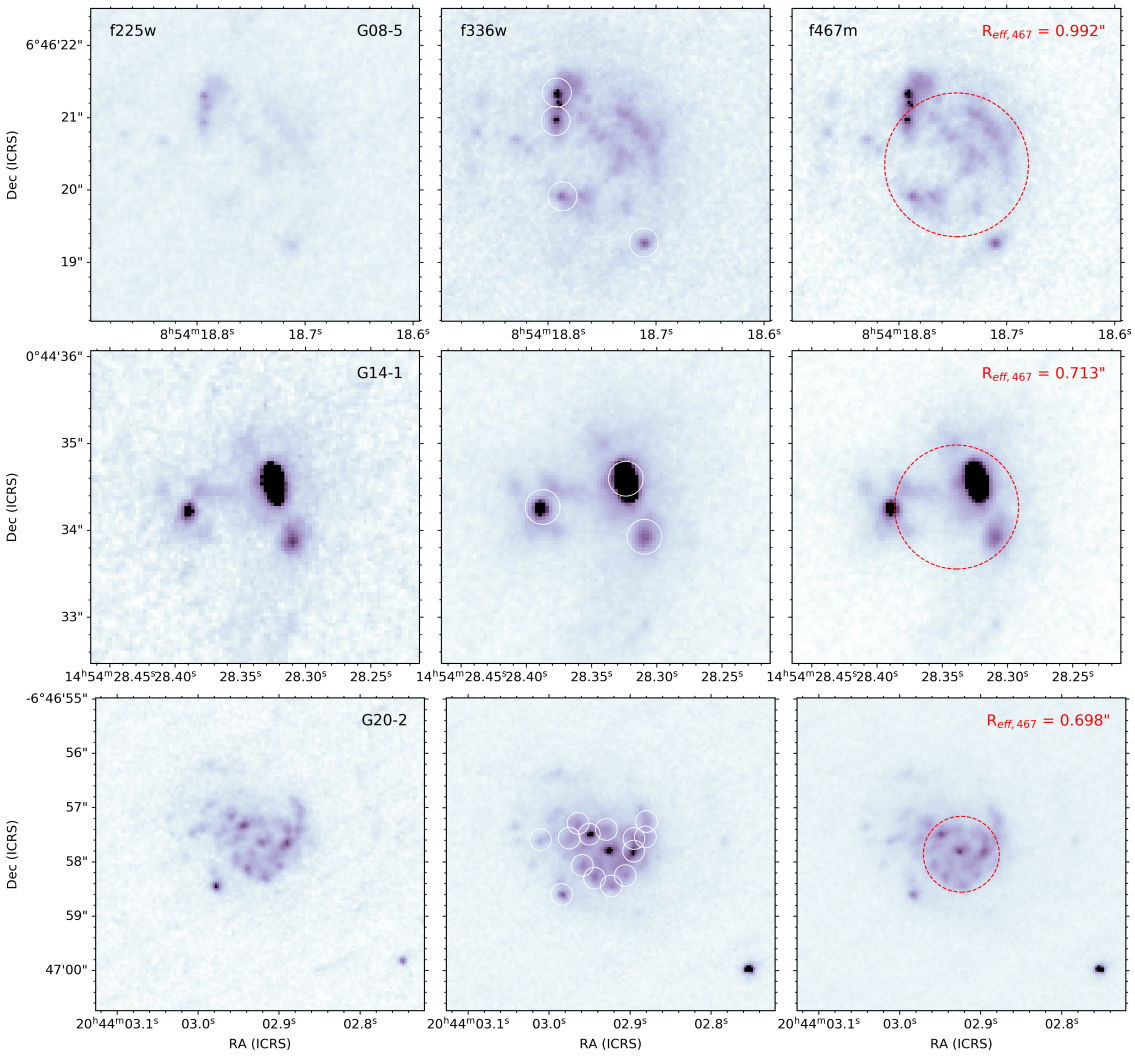

Figure 3.2: Same as Figure 3.1, but now showing galaxies G08-5, G14-1, and G20-2. Galaxies G14-1 and G20-2 are classified as "compact" rotating discs; therefore, their classification may be less reliable (Green et al., 2014).

3.4 Data Analysis

3.4.1 Kernel Generation for PSF Matching

The goal of this work is to measure the internal colours of clumps in DYNAMO galaxies, taking full advantage of the HST resolution. To do this, it is necessary to transform images from different filters to a common point spread function (PSF). Since the HST filters we use here do not have the same PSFs, the variation of structure on different spatial scales will result in unphysical colours when directly comparing images with different PSFs (see e.g., Gordon et al., 2008, Aniano et al., 2011). To transform images to a common PSF, we need to generate a convolution kernel, such that when the PSF of one filter (F336W or F467M) is convolved with this kernel, it will resemble the broader PSF of the second filter (F225W):

$$\Psi_{225} = \Psi_{336} \circledast K\{336 \rightarrow 225\} \tag{3.1}$$

where Ψ represents the filter PSFs, and K represents the convolution kernel. The convolution kernel that will satisfy this equation can be generated by taking the Fourier Transform (FT) of the same equation:

$$\mathrm{FT}(\Psi_{225}) = \mathrm{FT}(\Psi_{336} \circledast K\{336 \rightarrow 225\}) \tag{3.2}$$

$$= \mathrm{FT}(\Psi_{336}) \times \mathrm{FT}(K\{336 \rightarrow 225\}), \tag{3.3}$$

solving for the kernel, and taking an inverse Fourier Transform, we find that:

$$K\{336 \rightarrow 225\} = \mathrm{FT}^{-1}\left[\mathrm{FT}(\Psi_{225}) \times \frac{1}{\mathrm{FT}(\Psi_{336})}\right]. \tag{3.4}$$

In reality, computing the convolution kernel numerically requires additional steps to ensure that it is stable and performs well. We follow the steps to do this as outlined in detail in Aniano et al. (2011) and summarize them here for completeness.

3.4.1.1 HST PSFs

We obtained the PSFs for the F225W, F336W, F467M filters from the `Tiny Tim`[2] tool, version 7.5, by downloading and installing the source code available on `GitHub`. The three PSFs are 89×89 pixels and have a pixel scale of $0.04''$, matching the pixel scale of the HST images; therefore, we perform no gridding, padding or centering of the PSFs.

3.4.1.2 Circularizing the PSFs

The PSFs modeled by `Tiny Tim` are not rotationally symmetric; therefore, the first step we take is to circularize them. Following Aniano et al. (2011), we circularize the PSFs by performing 14 rotations of the PSF, and averaging after each rotation, such that the final PSF is invariant for any rotation that is a multiple of $360^\circ/2^{14} = 0.022^\circ$. We begin by rotating the original PSF, Ψ, by the smallest angle first: $\theta_1 = 0.022^\circ$ to produce a new PSF image, Ψ', and then compute the

[2]https://www.stsci.edu/hst/instrumentation/focus-and-pointing/focus/tiny-tim-hst-psf-modeling

average of the two: $\overline{\Psi} = \frac{1}{2} \times (\Psi + \Psi')$. We then rotate $\overline{\Psi}$ by $\theta_2 = 360°/2^{13}$ and repeat the process until $\theta_{14} = 360°/2^1$.

3.4.1.3 Compute the Kernels

We compute the Fourier Transform of each circularized PSF using the `Python` `numpy` two-dimensional Fast Fourier Transform (FFT) function `fft.fft2`. We compute the $K\{336 \rightarrow 225\}$ and $K\{467 \rightarrow 225\}$ kernels according to equation 3.4, by evaluating the $1/FT(\Psi_{336})$ and $1/FT(\Psi_{467})$ terms where they are not equal to zero. After taking the inverse Fourier Transform of the kernel, we normalize the integral of the kernels to unity to ensure flux conservation (see also `photutils.psf.matching`[3]).

3.4.1.4 Kernel Testing

We test our kernels according to the two metrics defined by Aniano et al. (2011): measuring how accurately the kernel redistributes flux (D, their equation 20), and studying the negative values in each kernel (W_-, their equation 21), and by comparing the encircled energy of the target PSF (F225W) and the convolved source PSFs (F336W and F467M). We show the latter in Figure 3.3, where the black line is the encircled energy of the F225W PSF, the dashed line is the original source PSF, and red is the convolved source PSF (left: F336W, right: F467M). We see from this that our PSF-matching reproduces well the target F225W PSF. The integral of the absolute value of the difference between the target PSF and the PSF derived from the convolution kernel is the definition of D, and $D = 0$ for

[3]https://photutils.readthedocs.io/en/stable/psf_matching.html

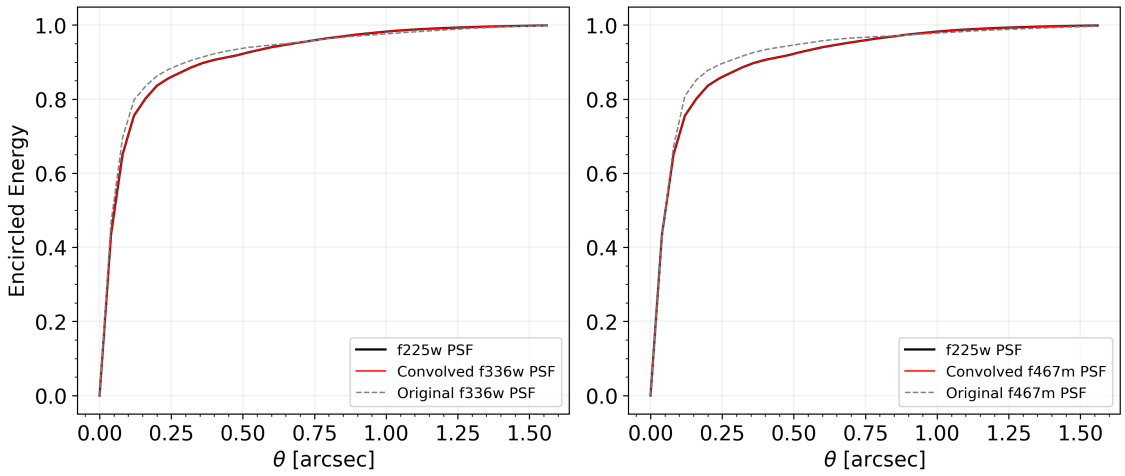

Figure 3.3: A comparison of the encircled energy (energy with an aperture of radius θ divided by the total energy) of the target PSF, F225W, and the source PSFs: F336W and F467M. The solid black lines are the encircled energy of the F225W PSF, while the dashed gray lines and and solid red lines are the original and convolved F336W (left) and F467M (right) PSFs. Our convolution kernels perform well and are capable of matching the target PSF.

perfect kernel performance. For the $K\{336 \rightarrow 225\}$ and $K\{467 \rightarrow 225\}$ kernels we derive, $D_{336} = 0.0.00015$ and $D_{467} = 0.00016$ respectively, which indicate very good agreement between the PSFs. The W_- value is defined as the integral of the negative values in the kernel, and a kernel with a large value of W_- may amplify image artifacts. Aniano et al. find from experimenting with several kernels that a value of $W_- \sim 0.3$ corresponds to a kernel that is very safe to use. Our kernels have $W_{-,336} = 0.01$ and $W_{-,467} = 0.21$, thus we conclude that they are safe to use.

3.4.2 Clump Selection

To systematically select clumps in our sample of galaxies, we use the unsharp masking technique, after which we run a source detection algorithm to identify clumps. The unsharp masking technique is a filter that removes low-frequency

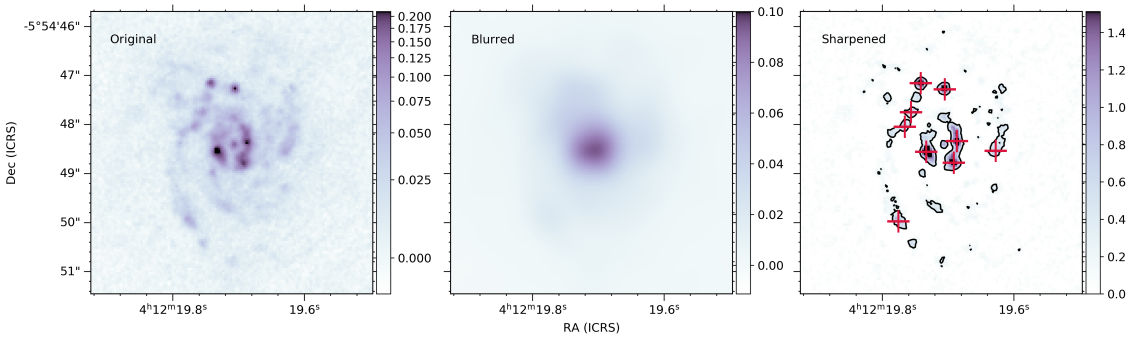

Figure 3.4: Outline of the unsharp masking technique for identifying clumps in DYNAMO galaxies: original F336W image of the galaxy G04-1 (left), the F336W image smoothed by convolving with a Gaussian kernel with a 15 pixel (0.6″) FWHM (middle), the contrast image that is created by "blending" the original and smoothed image (right). The black contours outline regions that are at 5× the standard deviation of the image, while the crimson coloured crosses mark the central positions of the clumps that are identified in this galaxy and are selected to be brighter than 5× the standard deviation of the image and to have a minimum diameter of 5 pixels (0.2″).

components of an image, thereby sharpening said image. Here we describe our procedure, and refer to Figure 3.4 where we use galaxy G04-1 as an example to illustrate this. We identify clumps from the F336W images (left panel of Figure 3.4) by first convolving each image with a Gaussian kernel whose full-width-half-maximum (FWHM) is 15 pixels, which at the pixel scale of the image (0.04″/pixel) corresponds to 0.6″, or 7.5× the size of the PSF for this filter. The result of this convolution is a smoothed version of the F336W image, shown in the middle panel of Figure 3.4. Finally a sharpened (contrast) image is produced by blending the original image with the smoothed image (right panel of Figure 3.4):

$$\text{sharpened} = \text{original} + (\text{original} - \text{blurred}) \times C \tag{3.5}$$

where C is a constant that controls how much lighter and darker edge borders

become; we use a value of 15 for all galaxies in our sample. We then use these sharpened images to identify clumps in each of the six galaxies.

To detect clumps, we use the blob detection algorithm based on the Laplacian of a Gaussian implemented in the `Python` package `scikit-image` (see `skimage.feature.blob_log`; van der Walt et al., 2014). This algorithm works by convolving the image with a Gaussian kernel of a given size, then applying the Laplacian operator to the convolved image, which results in a strong response for clumps ("blobs") on a given background. The response of the operator is however sensitive to the relation between the size of the smoothing kernel, and the size of the clump. For this reason, the `scikit-image` implementation of this algorithm, the `blob_log` function, takes as input the minimum and maximum standard deviation to use for the convolution kernels, and the number of kernels to test between the minimum and maximum.

We impose the criterion that clumps must have a minimum diameter of 2.5× the size of the F336W PSF. The F336W PSF has a size of 2 pixels, thus all our clumps are required to have a minimum diameter of 5 pixels. We therefore input into the blob detector function a minimum standard deviation of $2.5/\sqrt{2}$, and test smoothing kernels that increase in units of 0.05, up to a maximum of a 9 pixel diameter. The clump finder also takes as input a threshold parameter which controls the required intensity a clump needs to have to be detected. We set our detection limit such that clumps are regions that are 5× the standard deviation of the sharpened image (see black contours in the right panel of Figure 3.4). The clumps that meet all these requirements are indicated by crimson coloured crosses in the right panel of Figure 3.4.

Fisher et al. (2017b) finds that DYNAMO clumps have a median diameter of $\sim$450 pc in HST Hα images, in two ways: (1) by fitting 2D Gaussian functions to each clump, then defining the clump size as the geometric mean of the major (a) and minor (b) axes resulting from the 2D Gaussian fit: $2 \times \sqrt{a \times b}$, and (2) by fitting a 1D Gaussian to the light profile of each clump, then defining the clump size as $2 \times \sigma$ from the 1D Gaussian fits. We adopt the latter technique: for each clump, we mask neighboring clumps, extract the clump light profile, fit a 1D Gaussian, then define the clump size as $r_{clump} = 2 \times \sigma$, which encompasses 95% of the clump light. We report these sizes in Table B.1 in Appendix B.1. From this, we find a median clump diameter of $\sim$400 pc, similar to the Fisher et al. (2017b) results.

3.4.3 Photometry

The motivation for the filter choice to observe the six DYNAMO galaxies in our sample was the fact that they provide colours that are sensitive to stellar population age and extinction. At the DYNAMO redshifts, the F225W and F336W filters bracket the UV slope, thus the $225-336$ colour is sensitive to changes in dust extinction. Conversely, the F336W and F467M filters measure the 4000Å break, thus they bracket stellar emission and the $336-467$ colour is sensitive to changes in the age of the underlying stellar population. With these two colour combinations, we are able to establish constraints on how much extinction and age each contribute to the evolution of the clump colours. To this end, we modified `Starburst99` (Leitherer et al., 1999) to use the *HST* filter transmission curves for determining colours, and

to blueshift by $1+z$ the transmission curves of the standard HST filters to derive the colours at the rest wavelengths of interest. We then derive models for a single burst of star formation at solar metallicity to track how the two colours we measure here evolve with time, in steps of 0.1 Myr. As we perform our photometry and derive results from them, we will compare our colours to those of `Starburst99` to infer the age and extinction structures within clumps.

3.4.3.1 Aperture Photometry

We perform aperture photometry for each clump identified by the procedure described in the previous section. We center a circular aperture on every clump with radius equal to r_{clump}, and define a circular annulus whose inner radius is $4\times r_{clump}$, and whose outer radius is $5\times r_{clump}$, for disc subtraction. We mask from this annulus any pixels that are contaminated by other nearby clumps. We then calculate the clumps flux as:

$$F = \sum_{i=1}^{n_A} F_i - n_A \overline{B} \tag{3.6}$$

where F is the total flux in electrons per second, n_A is the total number of pixels in the clump aperture, and $\overline{B}$ is the median disc light measured in the disc annulus. We perform the above calculation with and without disc subtraction for comparison.

We estimate the uncertainties on all of our measurements by calculating the aperture signal−to−noise ratio (S/N) using the CCD equation (see for e.g., Howell, 2006):

$$\frac{\mathrm{S}}{\mathrm{N}} = \frac{N_* t}{\sqrt{N_* t + n_A(1 + \frac{n_A}{n_B})(N_S t + N_D t + N_R^2 + G^2\sigma_f^2)}} \tag{3.7}$$

where $N_* t$ is the total aperture counts (i.e., counts $\mathrm{s}^{-1}\times$ exposure time), n_A is the total number of pixels in the clump aperture, n_B is the total number of pixels in the background annulus, $N_S t$ is the total counts per pixel from the background, $N_D t$ is the total number of counts due to the dark current, N_R^2 is the total number of counts per pixel from the read noise, and $G^2\sigma_f^2$ accounts for the error introduced by the digitization noise within the A/D converter. These terms are obtained in the following way: (1) $N_* t$ and $N_S t$ are what we measure, (2) we use a value of $\sim$8e$^-$/hr/pixel for the WFC3 CCD dark current to calculate $N_D t$ (late-2017 value from the WFC3 Data Handbook, version 4.0 – May 2018[4]), and (3) we obtain the read noise and gain terms from the images headers. Since we report results in magnitudes, the final uncertainties are:

$$\sigma_{magnitudes} = \frac{1.0857}{\mathrm{S/N}}. \tag{3.8}$$

We perform the above calculations with and without disc-subtraction, and record the non-disc-subtracted integrated measurements along with their uncertainties in Appendix B.1, Table B.1. We choose to exclude disc subtraction, because as we will show in §3.5.1, the disc colour distributions are relatively flat, thus including disc subtraction will only increase the uncertainties of our measurements.

We plot the non-disc-subtracted integrated colours in Figure 3.5, where each

[4]https://hst-docs.stsci.edu/wfc3dhb

set of coloured points corresponds to one of the six galaxies in our sample. The solid and dashed coloured grid overlaid in the background represent the change of the $225-336$ and $336-467$ colours, as derived by `Starburst99` for a single burst of star formation and solar metallicity, and for varying degrees of extinction. We use the Cardelli et al. (1989) extinction law to derive a relation between the $225-336$ and $336-467$ colours and A_v, the extinction at rest-frame V-band. We then begin with the `Starburst99` model with an $A_v = 0$ magnitudes and then redden the model by increasing A_v in steps of 0.2 magnitudes, until we reach $A_v = 2$ magnitudes. Thus, each individual coloured line represents the evolution of the $225-336$ and $336-467$ colours at a fixed value of A_v, for ages ranging from 5 Myr to 500 Myr.

We can see from this that dust extinction primarily moves the colours horizontally while age primarily moves the colours vertically. Though there is some diagonal evolution with increasing extinction and age, indicating that both affect the colours, it is clear that (by experimental design) a change in extinction has a much larger effect on the $225-336$ colour, while a change in age has a much larger effect on the $336-467$ colour. The integrated colours of the clumps in our DYNAMO galaxies all lie within ages of $10-250$ Myr with A_v extinction ranging from 0.6 to 2.0 magnitudes. To assess the impact of our choice of metallicity on the ages we infer, we compare the model we adopt here (single burst of star formation and solar metallicity), to a model with the same star formation history and 40% solar metallicity in Figure B.1 in Appendix B.2. This changes the ages we infer from our current adopted model by a factor of ~ 1.4; namely clumps appear older by a factor of ~ 1.4 in the lower metallicity model. Assuming a continuous star formation his-

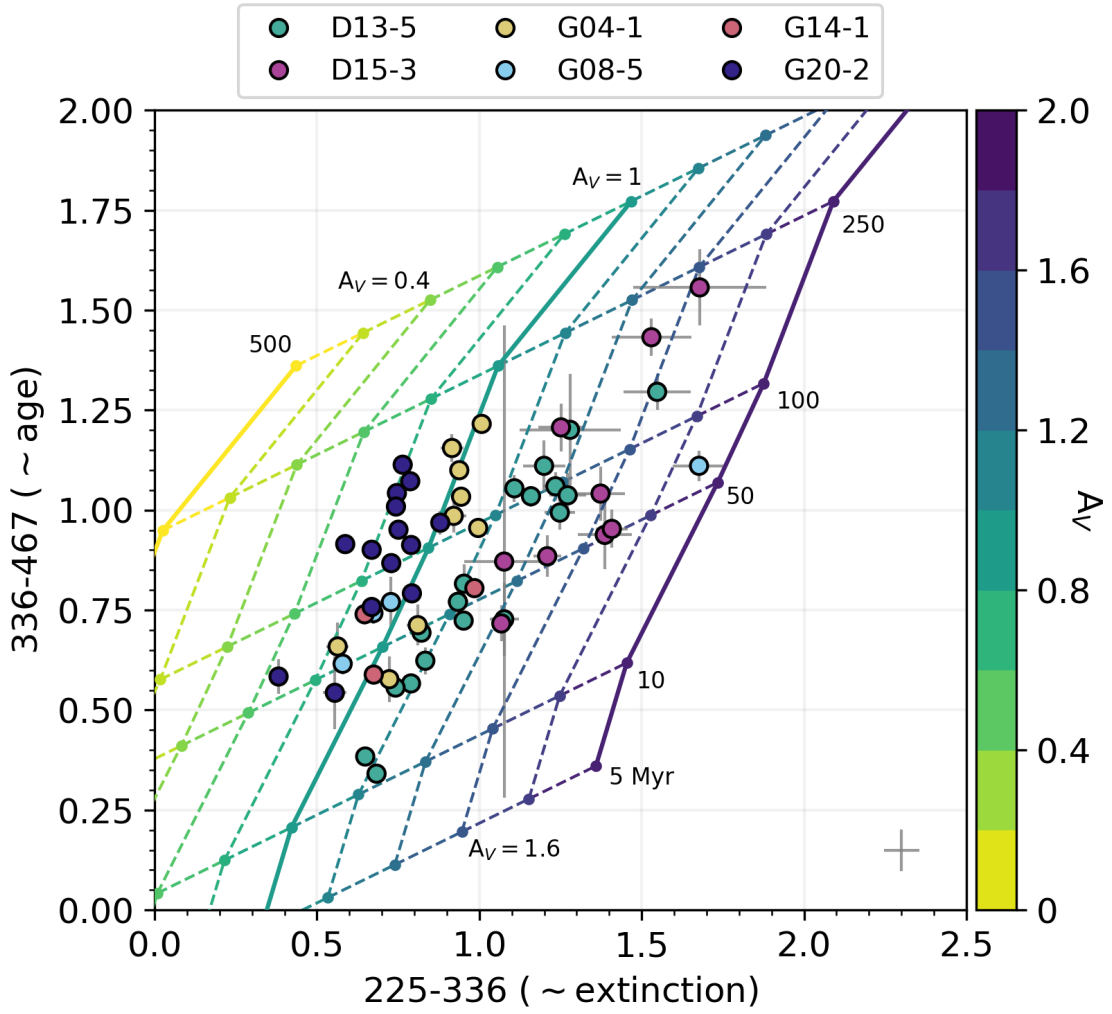

Figure 3.5: Colour-colour diagram of the $336-467$ colour (proxy for age) versus the $225-336$ colour (proxy for extinction), showing the integrated colours of each clump in our sample. The grey error bars are the photometric uncertainties, and we show the median errors bars in the bottom right corner. The coloured lines represent the evolution of these two colours as modeled by `Starburst99`, with extinction applied ranging from $A_V = 0$ to $A_V = 2$: the solid coloured lines are $A_V = 0, 1, 2$, while the dashed lines increase A_V in steps of 0.2 ($A_V = 0.4, 1, 1.6$ are labeled). The points on each line correspond to specific times after a single burst of star formation: 5, 10, 50, 100, 250, 500 Myr (labeled). These colours suggest clump ages as young as 10 Myr, and no older than 250 Myr, consistent with the ages derived in high$-z$ simulations of clumpy star forming galaxies (Bournaud et al., 2014). They also suggest visual band extinction values in the range $A_V \sim 0.6 - 2.0$, while for any one given galaxy, extinction does not vary drastically from clump-to-clump. This is consistent with the findings of Bassett et al. (2017); in addition, we derive A_V clump values that are in agreement with theirs for our overlapping galaxies (D13-5, G04-1, G20-2).

tory rather than a burst of star formation has a much larger impact on the inferred ages; in this case the inferred ages increase by several factors of 10, with clump ages $\sim$2 Gyr in some cases, for both the solar metallicity and 40% solar metallicity scenarios. We note, however, that these models likely represent a simplified scenario, and that the true star formation history of these clumps may be a combination of both bursty and continuous star formation.

3.4.3.2 Surface Brightness Profiles

In addition to measuring integrated fluxes and colours for each clump in our sample, we also derive surface brightness profiles as a means of investigating clump properties as a function of distance from the clump center. We use a set of concentric circular annuli, centered on each clump, where each annulus is two pixels wide ($0.08''$, or approximately 150 pc for $z \sim 0.1$), and overlaps with the previous annulus by one pixel (therefore the central radius of the annulus moves by $0.04''$for each measurement). We do this to smooth the surface brightness profiles because each clump is only a few pixels across, and we are therefore working with small numbers of pixels. We sum the signal within the annulus, determine its area, and then calculate the surface brightness according to:

$$\mu\,[\mathrm{mag\,arcsec^{-2}}] = m_{HST} + 2.5\log_{10}(A) \tag{3.9}$$

where m_{HST} is the total signal of the annulus, in AB magnitudes, and A is the area of the annulus in arcsec^2.

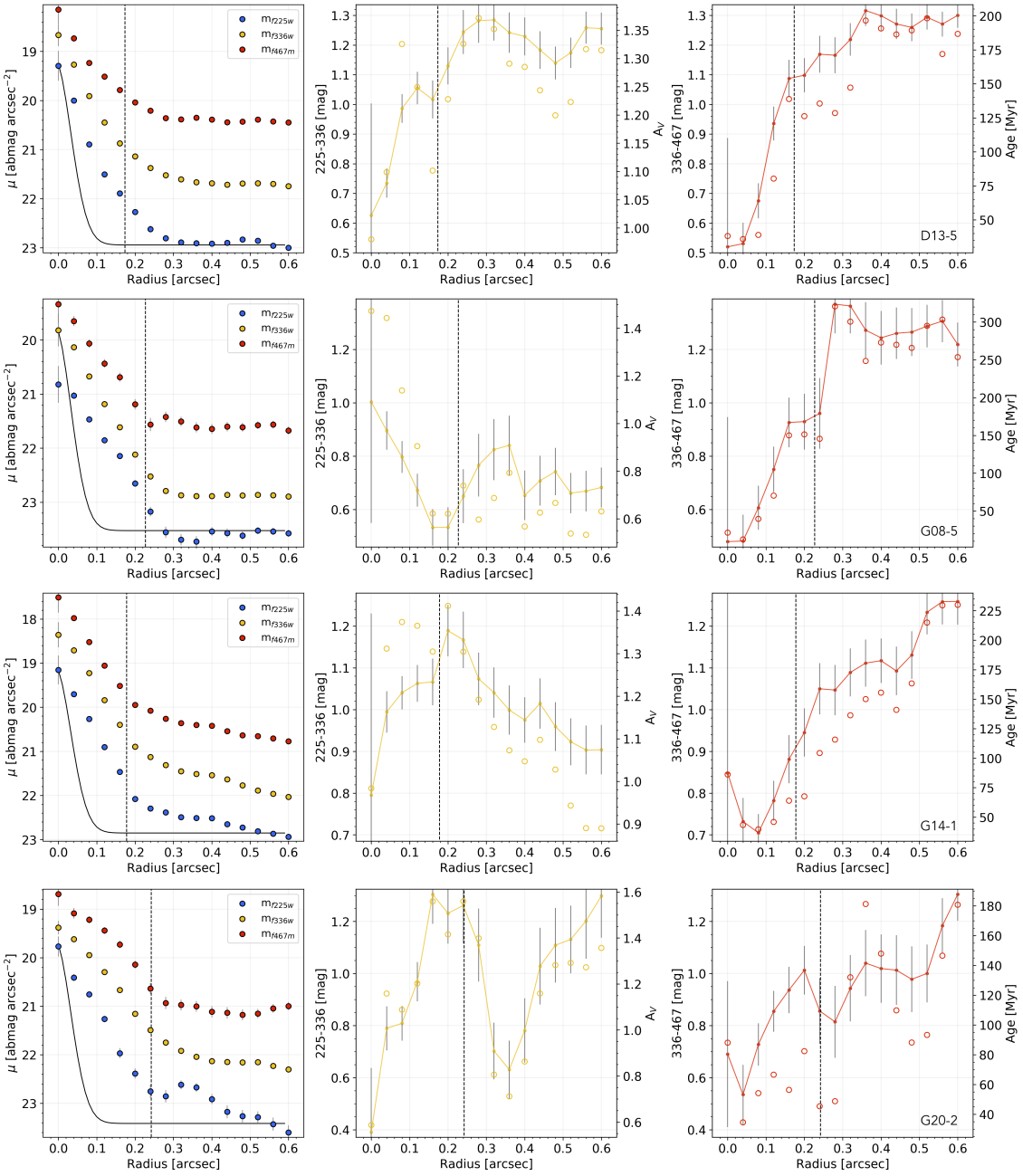

Figure 3.6: *Left:* The μ_{f225w} (blue circles), μ_{f336w} (yellow circles), and μ_{f467m} (red circles) surface brightness profiles as a function of distance from the clump center, for clumps in galaxies D13-5 (clump 4), G08-5 (clump 3), G14-1 (clump 3), and G20-2 (clump 9). *Middle:* The $225 - 336$ colour profile (yellow filled circles) and the conversion of these colours to A_V extinction (open yellow circles). *Right:* The $336 - 467$ colour profile (red filled circles) and the conversion to age (open red circles). We plot the uncertainties as gray lines, the dashed vertical lines indicate r_{clump}, and the solid black curve is the F225W PSF. When we map these colours to age and extinction, we see that there are clumps that show clear increase in age from the center and outward, such as we show in galaxy D13-5 and G08-5, while other clumps show a large increase in extinction rather than age, such as we show in galaxy G14-1 and G20-2.

We perform background subtraction in the same manner as we do in our aperture photometry, but now we apply it to each annulus. Furthermore, we mask nearby clumps that may contaminate the surface brightness profile of a given clump, by excluding those pixels from our calculations. Finally, we are also able to derive colour profiles from the surface brightness profiles.

In Figure 3.6, we show examples of the surface brightness (left panel) and colour profiles (middle and right panel) for clumps in galaxies D13-5 (clump 4), G08-5 (clump 3), G14-1 (clump 3), and G20-2 (clump 9). We chose these four examples to illustrate two typical trends we observe in the clump colour profiles. We measure the lowest S/N and largest uncertainties in the F225W images, thus the $225-336$ colour profiles generally have larger uncertainties than the $336-467$ colour profiles. The filled coloured symbols in the middle and right panels correspond to the actual colour measurements, while the open symbols show the conversion of these colours into A_V extinction and age.

To map our colours to age and extinction, we first note that:

$$\frac{A_{225}}{A_V} = 2.667089, \frac{A_{336}}{A_V} = 1.634535, \frac{A_{467}}{A_V} = 1.2229745 \tag{3.10}$$

assuming the Cardelli et al. (1989) extinction law. Combining these relations, we obtain:

$$A_{225} - A_{336} = C_1 \times A_V = (225 - 336)_o - (225 - 336)_i \tag{3.11}$$

$$A_{336} - A_{467} = C_2 \times A_V = (336 - 467)_o - (336 - 467)_i \tag{3.12}$$

where the subscript "o" corresponds to observed colours and the subscript "i" corresponds to intrinsic colours, and $C_1 = 1.032554$ and $C_2 = 0.411561$. Then, multiplying equation 3.11 by C_2 and equation 3.12 by C_1, and subtracting the two equations from each other, we obtain an equation independent of A_V:

$$C_2[(225 - 336)_o - (225 - 336)_i] - C_1[(336 - 467)_o - (336 - 467)_i] = 0. \tag{3.13}$$

We use our observed colours from the HST observations and the colours generated by `Starburst99` with 0.1 Myr time steps to solve equation 3.13 and infer an age. We then use the results to solve for A_V from equations 3.11 and 3.12. Those are the numbers that we present on the right y-axis in both of these panels. We match to extinction and age in this way because these two parameters are not entirely independent of one another; i.e., changes in extinction have a small effect on the $336-467$ colour, while changes in age also have a small effect on the $225-336$ colour (the model grid lines are not parallel to the x− and y− axes). A significant fraction of the clumps in our sample show colour (age/extinction) profiles such as the ones we show for galaxies D13-5 and G08-5 in Figure 3.6, where there is a strong increase in age, while fewer clumps show profiles such as the ones we show for galaxies G14-1 and G20-2, where there is no strong change in age but a strong change in extinction

across the clump. This will be discussed further in §3.5.2.

3.5 Results and Discussion

3.5.1 Galactocentric Variations of Global Clump Properties

We begin by first inspecting the evolution of clump colours as a function of their position within their galaxy, and compare clump colours to the disc colours. In Figure 3.7 and 3.8, we plot for all six galaxies, the integrated $336-467$ and $225-336$ colours respectively, of each clump as a function of galactocentric radius, normalized to the galaxy F467M half-light radius (effective radius: $R_{eff,467}$). To assess the impact of disc light on the clump colours we measure, we show the non-disc subtracted (filled symbols) and disc subtracted clump colours (empty symbols). We include the photometric uncertainties (section 3.4.3.1) as gray error bars on the non-disc subtracted colour. The solid black line in each panel shows the disc light evolution. To measure the disc light, we first mask all pixels that we identify as clump pixels. We then place a series of annuli at the galaxy center, which we define as the pixel of peak emission in existing *HST* F125W images (wide J). We finally integrate the light in each annulus, out to $4''$.

In our clump light to disc light comparison, we notice two things: (1) the $336-467$ clump colours are generally bluer than the disc light, within the uncertainties, independently of whether we subtract the disc background light from our clump measurements or not, and (2) the disc light is much flatter as a function of radius, than the clump colours (these trends were also observed for $0.5 \leq z < 3.0$ galaxies by

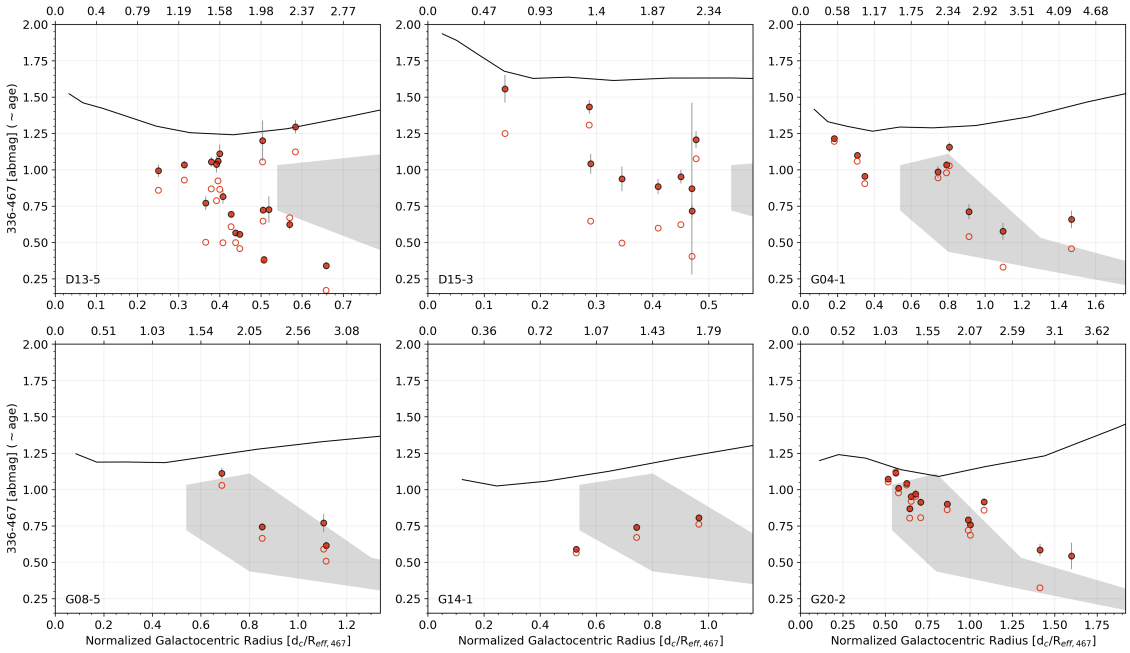

Figure 3.7: Clump integrated $336-467$ colour without (red filled circles) and with disc subtraction (red open circles) as a function of galactocentric radius (the upper x-axis scale gives the galactocentric radii equivalents in kpc). Photometric uncertainties appear as gray error bars. The gray-shaded regions are the $u-b$ results of Guo et al. (2018) at redshifts of $0.5 \leq z < 3.0$, for comparison. The $336-467$ colour, a proxy for age, is redder for clumps closer to the center of their galaxy and bluer for those on the outskirts, with the exception of galaxy G14-1 for which the opposite is true. However, the disc colours are relatively flat in comparison (black solid line). Furthermore, we see that clumps are on average bluer than the disc, and this is true whether or not we subtract the disc light. This suggests clumps are older closer to the centers of their galaxies and that this is not an effect of contamination from disc stars.

Guo et al., 2018). With respect to the first point, it is perhaps not surprising that the clumps exhibit bluer colours than the disc, because we select them as bright regions in the F336W (U band) images. This does however suggest that clumps are a structure separate from and embedded within the disc of the galaxy. This is further supported by our second observation: that the clump colour gradient is much steeper than the disc light suggests that clumps are structures that exist and evolve within the discs.

We see in all cases except for G14-1 that the $336-467$ colours of clumps tend to be redder closer to the galactic centers, and bluer farther in the outskirts. This trend has been previously observed in the $u-b$ colours of high$-z$ galaxies (e.g., Förster Schreiber et al., 2011, Soto et al., 2017, Guo et al., 2018). We reproduce here the results presented in Figure 8 of Guo et al. (2018) as the gray shaded area in each panel of Figure 3.7, to illustrate the trends measured by these authors. The authors normalize their clump distances to the HST F160W effective radius along the galaxy major axis. At redshifts of $0.5 \leq z < 3.0$, they are unable to distinguish clumps from galaxy bulges at normalized galactocentric radii < 0.5, which is where we find many of our clumps. This shaded region covers the median $u-b$ values in the $0.5 < z < 1.0$ and $1.0 < z < 2.0$ redshift bins, for all three mass ranges the authors present. Such a colour gradient suggests that since the $336-467$ colour is age-sensitive, the clumps that are closer to the centers of their galaxies are older than their bluer counterparts in the outskirts. We will discuss this further in §3.5.3.

It is important to note that our observations remain true whether we apply disc subtraction or not. In fact, we can see that when we subtract the disc light, the

effects are generally the greatest on the clumps that are farther from the centers of their respective galaxies: the colours of these clumps become even bluer than the uncertainties, while the clumps closer to the center do not change so drastically. This has the effect of steepening the colour gradients we observe when we perform disc subtraction and is in disagreement with the hypothesis that colour gradients observed in galaxies are the result of contamination of clump colours by older disc stars, whose densities are larger closer to the centers of galaxies (Buck et al., 2017, Oklopčić et al., 2017).

Other authors suggest that negative colour gradients, in which the clumps deviate from the galaxy gradient, are interpreted as supporting theories in which clumps migrate to the centers of galaxies and contribute to bulge growth. Dekel et al. (2009) predict migration timescales on the order of $\sim 10\times$ the dynamical timescale, or about 0.5 Gyr, from their theoretical framework, while Ceverino et al. (2010) perform the first cosmological simulation of high-z clumpy discs and show that their simulated clumps migrate to the centers of their hosts in $\sim 8\times$ the dynamical timescale. From the clump ages suggested by the integrated colours in Figure 3.5 of $\sim 50 - 250$ Myr, and the colour gradient observed here, we find that this scenario remains plausible given these observations and our measurements.

In Figure 3.8, we show the behavior of the $225 - 336$ colour and compare the clumps to the discs (as in Figure 3.7). We see that the disc colour gradient varies from galaxy-to-galaxy: a flat profile in this colour suggests little variation in extinction across the disc of the galaxy, while a downward (upward) turn in the colour would suggest a decrease (increase) in extinction. When inspecting the clump

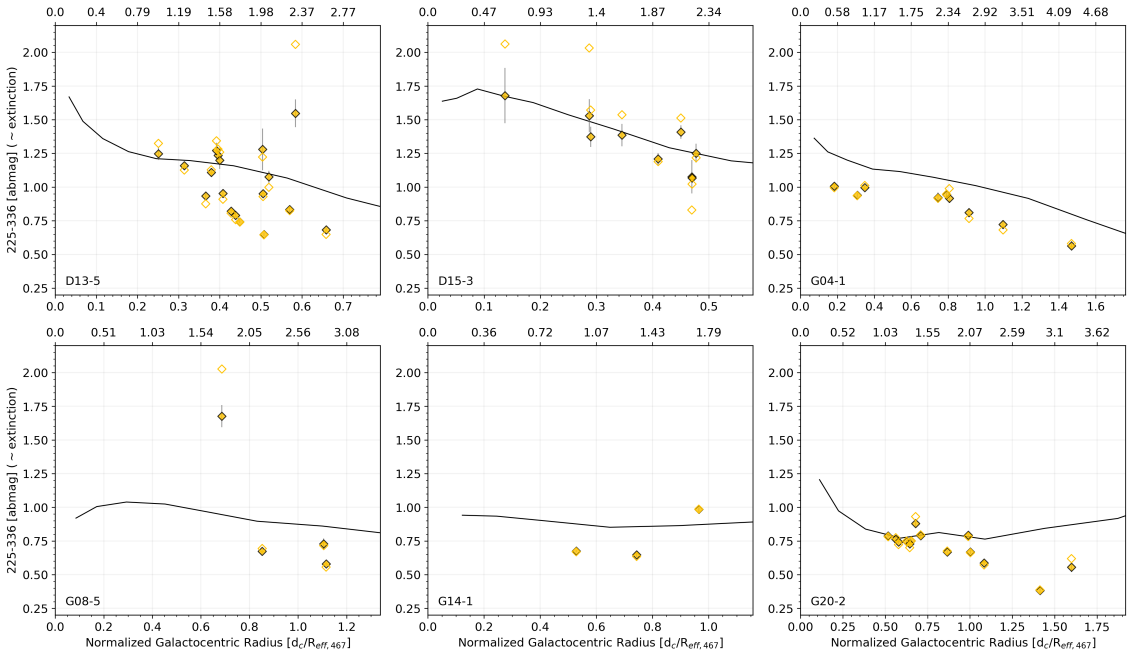

Figure 3.8: Same as Figure 3.7, but now showing the integrated $225 - 336$ colour without (filled yellow diamonds) and with (empty yellow diamonds) disc subtraction. The gray solid line shows how the $225 - 336$ colour evolves across each galaxy when we mask clumps. The $225 - 336$ colours of clumps are generally flatter than the $336 - 467$ and track the disc colour more closely, suggesting clump extinction does not differ strongly from the disc extinction.

colours, we do not find a very strong preference for clumps to appear much bluer than the discs, as we do in the $336-467$ colour. Clumps are generally either slightly bluer than the discs or scatter around the disc colours. It may not be surprising to measure bluer colours for clumps, because they are F336W-bright regions, and thus are likely to have less dust. In fact, previous works have observed this trend as well; for example Wuyts et al. (2013) find that the rest-UV-selected clumps in their sample of 473 CANDELS galaxies exhibit lower H_α/UV ratios than the underlying disc, which they interpret as an indication that these clumps are viewed through a smaller column of obscuring material. Conversely, Bassett et al. (2017) find little spatial variation in extinction across a subset of DYNAMO galaxies, thus it may also not be surprising to find clumps with $225-336$ colours similar to the discs within which they reside.

However, the gradient of $225-336$ colour with galactocentric radius seems to in general have a similar sign gradient for the clumps as the disc light, and in some cases the clumps follows the disc colour gradient closely. This is well illustrated in G04-1, where the disc colour decreases from the center, flattens, then decreases again. This same trend is seen in the clumps and is in contrast to what we observe in the $336-467$ colour, where the trends with galactocentric radius of clumps is not observed in the disc light, indicating that disc contamination is not the source of the colour gradient.

Our observations of the $225-336$ clump colours remain true when we apply disc subtraction. The effect of disc subtraction on the $225-336$ colour is less severe than on the $336-467$ colour and shows that dust extinction is not a contributing

factor to the observed colour gradient in the $336-467$ colour. In summary, clumps are similar to their host galaxy's disc in extinction, but are very different in age.

3.5.2 Internal colour Gradients of Clumps

The $0.092''$ resolution of the F225W HST observations allows us to go beyond investigating integrated clump colour trends with galactocentric radius, and to inspect how these colours vary across the extent of each individual clump ("colour track"). At the average DYNAMO redshift of $z \sim 0.1$, this angular resolution corresponds to ~ 170 pc; thus, it is not possible to do this analysis in clumps at $z \sim 1$. To derive the internal colour gradient of each clump, we use the surface brightness profile measurements of Section §3.4.3.2 to calculate colours in concentric circular annuli, centered on each clump (essentially combining the two colour profiles in Figure 3.6 into a two-dimensional representation, which we call a "colour track"). We illustrate one example of such a colour track for galaxy DYNAMO D13-5, clump 4, in Figure 3.9. The axes and the coloured grid are the same as in Figure 3.5; however, the data points now represent the colour change of one clump from its center (white point), to its edge (black point). In this particular case, we see that the colour track suggests a large change in age with fairly constant extinction across the clump. This is because as we move outward from the center of the clump, the colours track along the line of a single extinction model (in this case $A_V \sim 1.2$), indicating constant extinction and varying age. In the bottom panel of Figure 3.9, we illustrate another colour track for clump 9 in DYNAMO G20-2. In this case, the colour track is nearly

parallel to a line of constant age ($\sim$ 50 Myr), and crosses many lines of extinction, indicating that extinction varies strongly across this clump, while age does not. For ease of visualization, we fit this colour track with a line that minimizes the distance between the points and itself. The red line in Figure 3.9 is this fit. We fit the colour track of all 58 clumps in our sample in this way.

In Figure 3.10 we show the fitted lines of the colour tracks for all clumps. The axes and coloured grid are exactly the same as in Figures 3.5 and 3.9. We have added an additional colour bar in the second row to show how A_V translates into A_{336} when we assume the extinction law of Cardelli et al. (1989). The solid red shaded lines show the fitted colour track of each clump in our sample. Thus, they represent the general change of the $225-336$ and $336-467$ colours across the extent of each clump. We shade the lines to represent the clump S/N in the F336W images: darker (lighter) shaded lines have higher (lower) S/N. The single data points found at one end of each colour track correspond to the central region of each clump, thus indicating the direction in which the distance from the clump center increases. The length of each colour track is such that the end point corresponds to the colours of the outermost annulus of each clump, defined as the "edge" of the clump as described in Section 3.4.2 (r_{clump}).

We identify from this collection of colour tracks three scenarios (in increasing order of occurrence frequency): (1) clumps with colour tracks that suggest little to no change in age and large changes in extinction across the clump; these are indicated by shallow positive (increasing extinction) or shallow negative (decreasing extinction) slopes (i.e., colour tracks that cut across many lines of A_V but follow

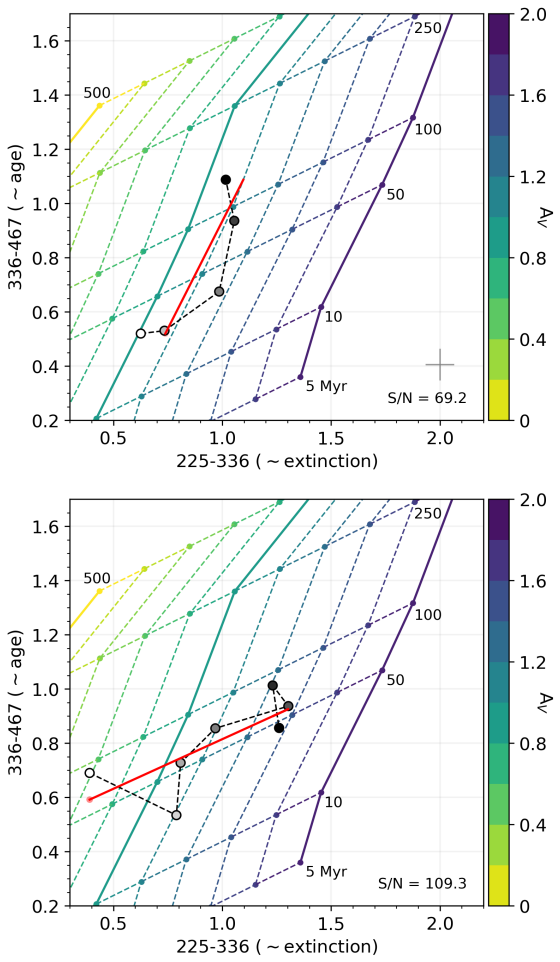

Figure 3.9: The same colour− colour space as we show in Figure 3.5. The data points now represent the colour track of a two clumps: DYNAMO D13-5 clump 4 (top panel) and DYNAMO G20-2 clump 9 (bottom panel), with colours measured in concentric circular annuli centered on the clump, showing their internal age and extinction structure. The shading of the data points corresponds to the distance from the center of the clump in steps of 0.04″(∼ 60 pc) as described in §3.4.3.2: white represents the colour at the center, black represents the colour farthest from the center. The red solid lines shows the linear fits to these colour track. The internal colour gradient of the first clump indicates that it has a constant A_V of $\sim$1.2 and that the age is a few 10 Myr at the center and increases to $>$ 100 Myr at the clump edge, while the colour track of the second clump indicates it has a constant age of $\sim$50 Myr and a large change in extinction (from $A_V \sim 0.8-1.6$). Median error bars on the colour track points are shown in the bottom right corner of the top panel.

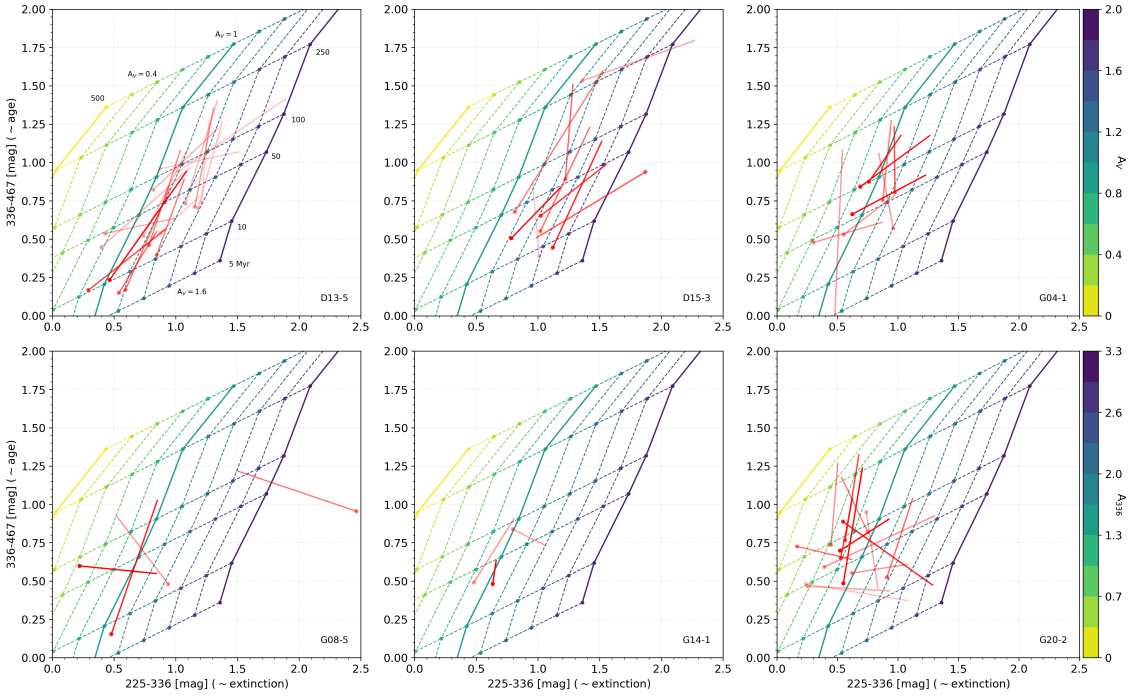

Figure 3.10: For each clump in our sample we plot a colour track which represents how the colour of the clump itself evolves from its center to its edge, in the $225-336$ vs $336-467$ parameter space. The coloured lines represent $V-$ band extinction, as in Figure 3.5. The red lines show the linear fit to the colours of each clump measured in concentric annuli as a function of distance from the clump center with the dot indicating the value at the center, and are shaded based on the F336W S/N (these range from $\sim 10-150$). Thus, lighter shaded lines have lower S/N, while darker ones have a higher S/N and are more certain. We can see that for high S/N clumps the colours typically change primarily along the vertical axis, indicating that there is a gradient present within clumps themselves. Moreover, the majority of these clumps change in the direction of increasing age farther from their centers. A handful of the clumps show preferentially an extinction gradient, and for some galaxies (e.g., D13-5) the presence of age gradients is more marked than for others (e.g., G20-2).

a single age line) – see galaxy D13-5, D15-3, G04-1, and G20-2 for examples, (2) clumps whose colour tracks indicate decreasing age with increasing distance from the clump center; these are indicated by steep negative slopes – see galaxy G20-2 for examples, and finally (3) clumps whose colours show large increases in age from the clump center with $\sim$constant extinction (i.e., these tracks cut across many ages lines but no, or few, lines of A_V) in some cases, and with large increases (decreases) in extinction; these are indicated by steep positive (negative) slopes (i.e., these tracks cut across many lines of A_V and many age lines) in other cases. Of the 58 clumps in our sample, the distribution of clumps per scenario is: (1) 7, (2) 10, and (3) 40. Thus, $\sim$70% of the clumps in our sample show colour tracks with increasing ages away from the centers.

To verify that our PSF matching is not falsely producing these colour gradients, we create mock clumps to test our PSF matching procedure. We model clumps with a symmetric 2D Gaussian profile, with sizes matching those of our observed clumps. We convolve each of these to the PSF profile of each HST filter, to simulate observations. We measure the internal clump colour gradients of these simulated clumps, then we perform our PSF-matching and measure the internal clump colours once more. We find that in cases where we create clumps with zero colour gradients, we recover no gradient, and in cases where we create clumps with a given gradient, we are able to recover it as well. Thus, we conclude that our PSF-matching procedure is not producing artificial gradients.

Clumps in the first category, whose colours suggest constant ages and large increases in extinction may correspond to "pseudo-clumps". This may be an indi-

cator that even though we identify these objects as clumps, they may be holes in extinction that create a clumpy light distribution. This was observed in the NIHAO simulation by Buck et al. (2017), where non-clumpy galaxies showed clumpy $U-$band light distributions due to clumpy gas distributions and clumpy star formation events. However, if all clumps that we observe in our DYNAMO sample were the result of this, then we would expect all of their colour tracks to fall in this first category, which is not what we find.

Nearly three-quarters (40) of the clumps we select in these six DYNAMO galaxies lie in the third category: clumps with large increases in age. This trend is particularly well illustrated in galaxies D13-5, and D15-3. This suggests that the evolution of these two colours is driven predominantly by age: the clumps are younger at the centers and older toward the edges, and extinction is not a large contributor to the clump colour evolution. This observation suggests that these clumps are an entity separate from the galaxy disc, with an inner structure whereby star formation is predominantly found in the central regions. These results are interesting because they indicate that clumps observed in high$-z$ galaxies and local analogues likely consist of a combination of "real" physical structures, and "pseudo-clumps" that are a result of clumpy light distributions. The ability to distinguish these would likely be important for simulations of high$-z$ systems, and the colour tracks of clumps could potentially be used as an additional criterion for selecting and distinguishing real clumps in galaxies.

Another possibility is that these clumps are perhaps composed of smaller star forming clusters that follow the cluster pair separation-age difference relation (Efre-

mov and Elmegreen, 1998, de la Fuente Marcos and de la Fuente Marcos, 2009, Grasha et al., 2017). Grasha et al. (2017) show that for eight local galaxies, the age difference between pairs of star forming clusters increases with their separation to the power of $\sim 0.25-0.6$. The authors also find that the maximal scales over which cluster pair separation and age difference are correlated, range from $\sim$ 200 pc -1 kpc. We are unable to resolve any potential smaller clusters within each clump and measure the cluster pair separation-age difference relation (measuring pixel-to-pixel differences is not feasible as the photometric uncertainties are too large to yield meaningful results). It is nonetheless worth noting that these clumps could break up into even smaller structures at higher resolution, which we cannot ascertain with currently available data. However, high-resolution simulations of isolated clumpy, high-z discs do show substructures within giant clumps (see e.g., Ceverino et al., 2012).

3.5.3 Galactocentric Variations of Resolved Clump Properties

Based on the internal colour gradient observation that the majority of clumps appear older in their outskirts and younger at their centers, we compare the "inner" and "outer" clump ages as a function of galactocentric radius, shown in Figure 3.11. Here, we plot the estimated ages of clumps as a function of the clump galactocentric radius, normalized to the effective F467M radius, $R_{eff,f467m}$, in three different ways. We first consider each clump as a whole (left panel), then we split each clump at the radius corresponding to $0.5 \times r_{clump,467}$, to define an "inner" (middle panel) and an

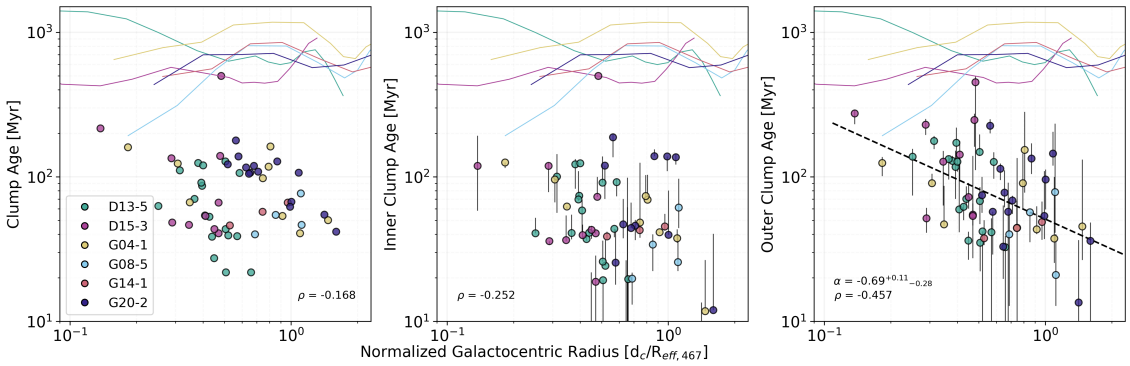

Figure 3.11: Clump ages estimated for the whole clump region from the integrated light within r_{clump} (left), the inner 25% regions (middle), and the outer 75% (right), vs. galactocentric radius, compared to the estimated disc ages (solid coloured lines). Error bars show the spread in ages when shifting the inner and outer clump boundaries by 10%. The strongest correlation is between the outer clump regions and galactocentric radius, which we quantify with the Spearman Rank-Order correlation coefficient, ρ, where we see clump age increasing with decreasing distance. However, the disc profiles are flat in comparison (with the exception of galaxy G08-5), suggesting that the clump age–distance relation is not due to an underlying age trend within the discs themselves. We fit a power law to the outer clump age–distance relation (black dashed line in the right panel) and report the slope of this fit (α). The outlying point in galaxy D15-3, which appears much older than other clumps, is measured as an upper limit in the F225W image.

"outer" (right panel) clump region. These regions, thus, cover the inner 25% and outer 75% of the clump area respectively. In the last panel we also show a fit to the relationship between outer clump age and normalized galactocentric radius using a linear relation in log-log space, which corresponds to a power law in linear space.

For the three panels in Figure 3.11, we measure the clump light in (1) a circular aperture whose radius is r_{clump}, (2) in a circular aperture whose radius is $0.5 \times r_{clump}$, and (3) in an annulus whose inner radius is $0.5 \times r_{clump}$ and whose outer radius is r_{clump} (we check and ensure that the sum of the inner and outer regions is equal to the clump light we measure in the circular aperture of size r_{clump}). Performing this measurement in all three filters, we then calculate both the $225-336$ and the $336-467$ colours of these regions, and simultaneously match them to the `Starburst99` models, as described in Section 3.4.3.1 and done in Figures 3.7 and 3.8. The clumps are separated according to which DYNAMO galaxy they reside in, as indicated by the legend. The error bars on the data points indicate how the spread in estimated ages changes when we shift the boundary between the inner and outer clump by 10%. The downward directed error bars are generally larger than the upper error bars because shrinking the inner clump boundary significantly increases the photometric uncertainties and causes clumps to appear much bluer (as a result of the intrinsic colour gradient).

To compare the clump ages to the discs, we include the solid coloured lines which show the disc age distributions derived from the disc colour profiles, and are the same in all panels. As we show in Figure 3.7, the discs are redder in $336-467$ and thus considerably older than the vast majority of the clumps. We include the

non-parametric Spearman rank correlation coefficient, ρ, in each panel, showing that the most significant correlation is between outer clump age and galactocentric distance. Finally, we also include in the right panel the fitted slope of the outer clump age–distance relation: $\alpha = -0.69^{+0.11}_{-0.28}$, where the uncertainties correspond to 1σ determined from a bootstrap analysis. We compute the mean age and 1σ standard deviation of each panel to further quantify the spread in the data: (left) 90.5 ± 69.1 Myr, (middle) 66.2 ± 70.7 Myr, (right) 96.8 ± 75.3 Myr.

From the left panel of Figure 3.11, we can see that clumps are generally estimated to be $\sim$ a few 100 Myr younger than the galaxy discs, and the "oldest" clumps we see are ~ 250 Myr old. We also do not see any "old" clumps in the outskirts of the galaxies, and we do not see any very "young" clumps close to the centers. We note that we generally observe fewer clumps at the smallest galactocentric radii; however, this may be expected as the infall of clumps closer to the centers of galaxies would take place faster than for clumps farther out. Thus it would be more likely to observe clumps at large galactocentric radii, than at smaller ones. Alternatively, it may also be a geometric effect where we would expect to find fewer clumps in a galaxy if we decrease its size (radius), and therefore its area.

When we break up each clump into an inner and outer region, we see that in general the ages of the inner clumps are younger than the outer clumps by a factor of 2 to 4. Furthermore, outer clump regions in clumps closer to the centers of galaxies tend to be older, while the inner regions of clumps have similar ages regardless of where in the disc the clump is located. In other words, the inner clump ages do not show a trend with galactocentric radius, while the outer clump regions present

a much clearer trend. We can see this well illustrated when comparing the two measures of the age of a clump for a given galaxy. For example in D13-5, the inner clump ages follow a relatively flat distribution with a lot of scatter, while the outer clump ages increase toward smaller galactocentric radii. If clumps keep forming stars in their cores as they migrate through the disc, then young stellar populations will be maintained in these regions and skew the light-weighted ages to younger values. In contrast, the outer regions of clumps show a stronger preference to be older when located closer to the centers of galaxies, and younger at the outskirts. Förster Schreiber et al. (2011) find a steep relation between clump age and distance in their study of clumps in six $z \sim 2$ galaxies (see their Figure 8, bottom panel), with a power-law slope of -2.06 ± 0.63 (slope measured by Genel et al., 2012). In contrast, Guo et al. (2018) find an increasingly steeper clump age–distance relation with decreasing redshift (see their Figure 9): at $z \sim 2-3$ this relation is flat, while at $z \sim 0.5-1$ the slope of the relation becomes ~ -1.5. Similarly, Zanella et al. (2019) find a relatively flat clump age–distance relation for their sample of 53 star forming galaxies at $z \sim 1-3$ (see their Figure 8). However they list as possible explanations for the difference between lower- and higher-redshift results as: (1) signatures of migration might not yet be visible at $z \sim 2$, (2) the improved spatial resolution at lower-redshift may improve the detection of clumps at small galactocentric radii, and (3) measurement uncertainties may "hide" underlying age gradients.

Finally, in Figure 3.12, we plot the age difference between the inner and outer clump regions (middle and right panels of Figure 3.11) as a function of normalized galactocentric distance. Clumps with negative age differences are those with colour

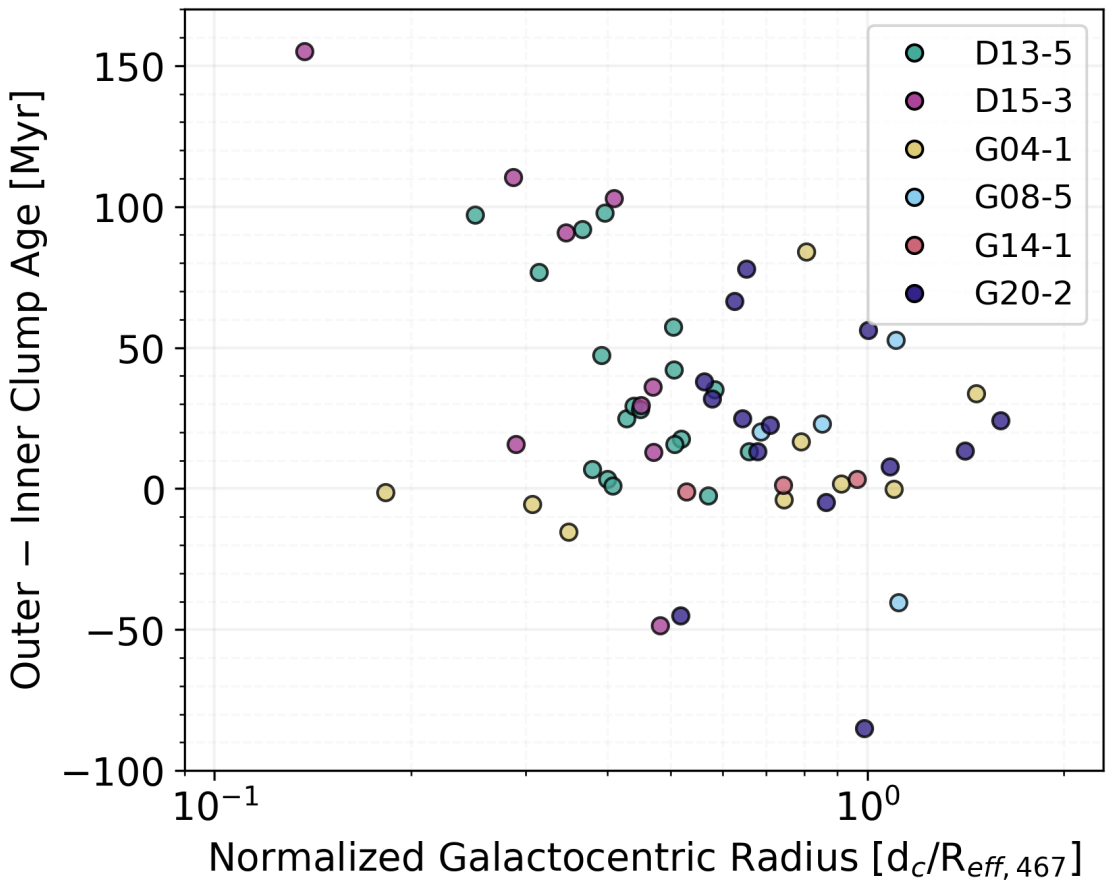

Figure 3.12: The age difference between the outer and inner clump region as a function of normalized galactocentric radius. Negative age differences correspond to clumps whose colour tracks indicate "older" inner clump regions compared to the outer clump regions. In general, the age difference increases with decreasing galactocentric distance, with the innermost clumps showing age differences as large as $\sim$100−150 Myr.

tracks that show decreasing ages with increasing distance from the clump center. For the remaining clumps, we generally observe the smallest age differences for clumps at the largest galactocentric distances, and the largest age differences for the more centrally located clumps. For these, we observe age differences as large as 150 Myr. Dekel et al. (2009) predict that if radiative feedback successfully suppresses star formation in clumps, then the spread in their stellar ages should not exceed $\sim 50-100$ Myr.

3.5.4 Comparison to Hydrodynamic Models

While there is a mixture of results at higher-redshifts, our picture is consistent with the findings of high$-z$ simulations such as those presented in Ceverino et al. (2010, 2012), Bournaud et al. (2014), Mandelker et al. (2017). Ceverino et al. (2010) present results from the first cosmological simulations of three high$-z$, clumpy galaxies that produce disc fragmentation from gas stream driven instabilities. This results in discs with morphologies that are very similar to observed high$-z$ systems, including clumpy star forming rings such as we see in DYNAMO D13-5 (our Figure 3.1; see their Figure 6). The resulting clumps migrate and coalesce with the bulge on timescales of ~ 250 Myr. This timescale is consistent with the outer clump ages of the most centrally located clumps in our sample (see Figure 3.11). Ceverino et al. (2012) build on this by including two additional zoom-in cosmological simulations at $z = 2 - 3$ to study internal support against collapse for 77 clumps. This works includes three clumps analysed at 2 pc resolution, where they find that they frag-

ment into dense subclumps and that resolving these is important for understanding the internal structure of clumps.

Bournaud et al. (2014) identify a population of massive ($\sim 10^8$ $M_\odot$) clumps that remain long-lived in the simulations, meaning that they can be tracked in the simulations for $200 - 500$ Myr, and up to 700 Myr in some cases, which migrate to the centers of their galaxies. These clumps maintain relatively constant masses and star formation rates ($1 - 2$ $M_\odot\,yr^{-1}$), despite outflows ($1 - 2$ $M_\odot\,yr^{-1}$ across a 1 kpc^2 section) and the dynamical loss of older stars ($0.2 - 2$ $M_\odot\,yr^{-1}$), thanks to re-accretion of gas from the surrounding gas-rich discs ($2 - 15$ $M_\odot\,yr^{-1}$). The observational consequence of this is that the apparent ages of clumps are dominated by the light of young stars, and therefore saturate at around 200 Myr, thus clumps can be up to twice as old as the median age of the stars within them. This is consistent with the lack of clumps much older than $\sim$ 200 Myr that we observe, while the tendency of older clumps to be preferentially located towards the centers of galaxies supports the clump migration scenario. Furthermore, if the re-accreted gas falls to the centers of clumps and forms stars there, then this would create clumps with young centers and older outskirts, consistent with the clump age substructures we observe in our sample.

Similar results are found by Mandelker et al. (2017), who also find that the stellar ages of clumps are less than the true lifetime of clumps due to ongoing star formation. In this work, the authors study the properties of high$-z$ galaxies in zoom-in hydro-cosmological simulations with and without radiation pressure feedback. The authors find that even in the case of radiation pressure feedback, clumps

more massive than $10^{8.2}$ $M_\odot$ are able to survive in the disc and migrate to the centers of galaxies, while less massive clumps are considered short-lived (as long as their ages are $\lesssim 20\times$ the clump free-fall timescale; see Mandelker et al., 2017, § 5.1.2 for details). The authors present a comparison of the ages of short-lived clumps, long-lived clumps, and *ex situ* clumps (which are clumps that join the disc after a merger event), as a function of galactocentric radius (their Figure 15, top left panel).

We reproduce these results in Figure 3.13, where the coloured data points represent the long-lived clumps (blue circles), short-lived clumps (yellow diamonds), and *ex situ* clumps (pink squares), while the solid coloured lines with black outlines represent the 50^{th} percentile of the respective three clump populations, binned in the log of the normalized galactocentric distance. We can see from the data points in Figure 3.13 that the scatter is large for all three populations of clumps. Two factors make a direct comparison difficult: (1) the galactocentric distances in Mandelker et al. (2017) are normalized to R_d, the radius that contains 85% of the cold mass within a cylinder of a certain size (see Mandelker et al., 2017, for a more detailed description), and (2) the ages of simulated clumps are measured as the mass-weighted mean stellar age. Neither the cold mass distribution nor the mass-weighted age can be easily measured in observations: the lack of a good handle on the first introduces an uncertainty in the scaling of the x-axis, while the light-weighted stellar ages we observe will be systematically younger than mass-weighted ages. As a result, a direct comparison of the DYNAMO clump age estimates to the simulated clump ages is not meaningful. However, we can compare the slope of the power law fit to the DYNAMO outer clump ages as a function of galactocentric distance, to the slopes

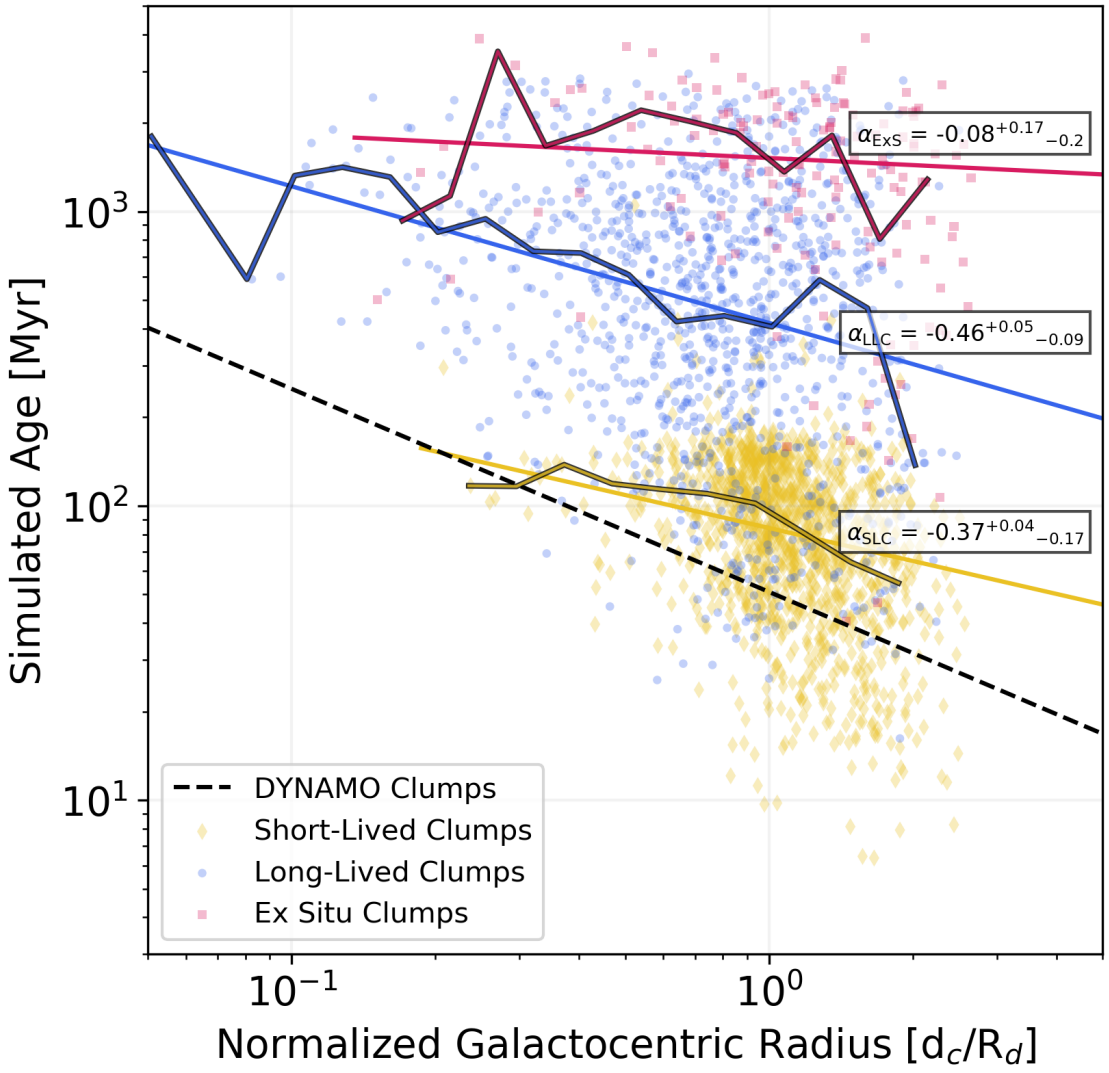

Figure 3.13: Comparison of the short-lived (yellow diamonds), long-lived (blue circles), and *ex situ* (pink squares) clumps of Mandelker et al. (2017). The solid coloured lines with black outlines correspond to the 50^{th} percentile in bins of log normalized galactocentric radius, while the coloured lines with no black outline represent the power law fits to the 50^{th} percentiles. The power law slopes with uncertainties determined through a bootstrap analysis are included in the figure. For reference, the black dashed line is the best power law fit to the outer clump ages which we show in Figure 3.11.

of the power law fits of the three clump populations of Mandelker et al. (2017). To determine the slopes, we fit a power law to the 50^{th} percentile lines; these fits are represented by the coloured lines (no black outline). Finally, we perform a bootstrap analysis to determine the uncertainties of these three fits. The three slopes along with their 1σ uncertainties are shown on the figure. They are: $\alpha_{\rm SLC} = -0.37^{+0.04}_{-0.17}$, $\alpha_{\rm LLC} = -0.46^{+0.05}_{-0.09}$, and $\alpha_{\rm ExS} = -0.08^{+0.17}_{-0.19}$. In comparison, the slope we find for the DYNAMO outer clump ages is: $\alpha = -0.63^{+0.15}_{-0.13}$.

From this analysis, we are able to conclude that the properties of the DYNAMO clumps are distinct from the *ex situ* clumps, and thus that the clumps we observe are likely not *ex situ* clumps. This conclusion is also reported by Huertas-Company et al. (2020). The authors present a new neural networks based method for selecting clumps, which they apply to 9,000 star forming galaxies in CANDELS in the redshift range $z \sim 1 - 3$. Their method yields ∼3,000 clumps in ∼1,500 galaxies. They derive clump properties, including stellar mass, from spectral energy distribution fitting of seven photometric bands, and then construct a clump stellar mass function. The authors apply the same procedure to 35 galaxies from the VELA simulations (Ceverino et al., 2014) and find that, under the same conditions, the cluster stellar mass functions agree well, suggesting an *in situ* origin for clumps in CANDELS.

The slope of the age–distance relations for DYNAMO clumps may be as steep as -0.76 or as shallow as -0.48, which puts it within the upper bound of the long-lived clumps slope (ranges from -0.41 to -0.55). However, the slope of the short-lived clumps ranges from -0.33 to -0.54, thus it is not entirely clear if the

outer clump regions of DYNAMO clumps are more similar to short-lived or long-lived clumps in the high$-z$ simulations of Mandelker et al. (2017). This is a result of the scatter at large galactocentric radii, which drives the large uncertainty toward steeper slopes for both the short-lived and long-lived clumps. We note that in their high resolution cosmological simulations of $z \sim 2$ galaxies, Genel et al. (2012) find a power law slope of -0.57 $\pm$ 0.14 for the relation between clump age and distance, which is in good agreement with our result. However, the authors explain that their age gradient is due to the dominance of "background" stars which are a part of the galaxy discs and not actually gravitationally associated with the clumps. Then, since their galaxy discs themselves have a negative age gradient (older disc stars near the centers of galaxies), the clumps that are at found at smaller galactocentric radii also appear older, despite no evidence of clump migration. Thus they conclude that the clump-distance relation is a consequence of inside-out disc formation. In contrast, the colours we measure for the DYNAMO galaxy discs do not imply such strong negative age gradients, as was also observed in Ceverino et al. (2012) who found a slope of -1.2 for their simulated clump age–distance relation and a slope of only -0.3 for the simulated discs; thus we conclude that the age gradients we observe in the clumps are not driven by the stellar distributions of the discs.

As a final point, we note that the simulated short-lived clumps are not common at very small radii. Thus, despite the uncertainty introduced by the different radius normalization between our work and that of Mandelker et al. (2017), we draw a comparison between the distribution of DYNAMO clumps in galactocentric radius, to the distribution of the short-lived, long-lived, and *ex situ* clumps in Figure 3.14.

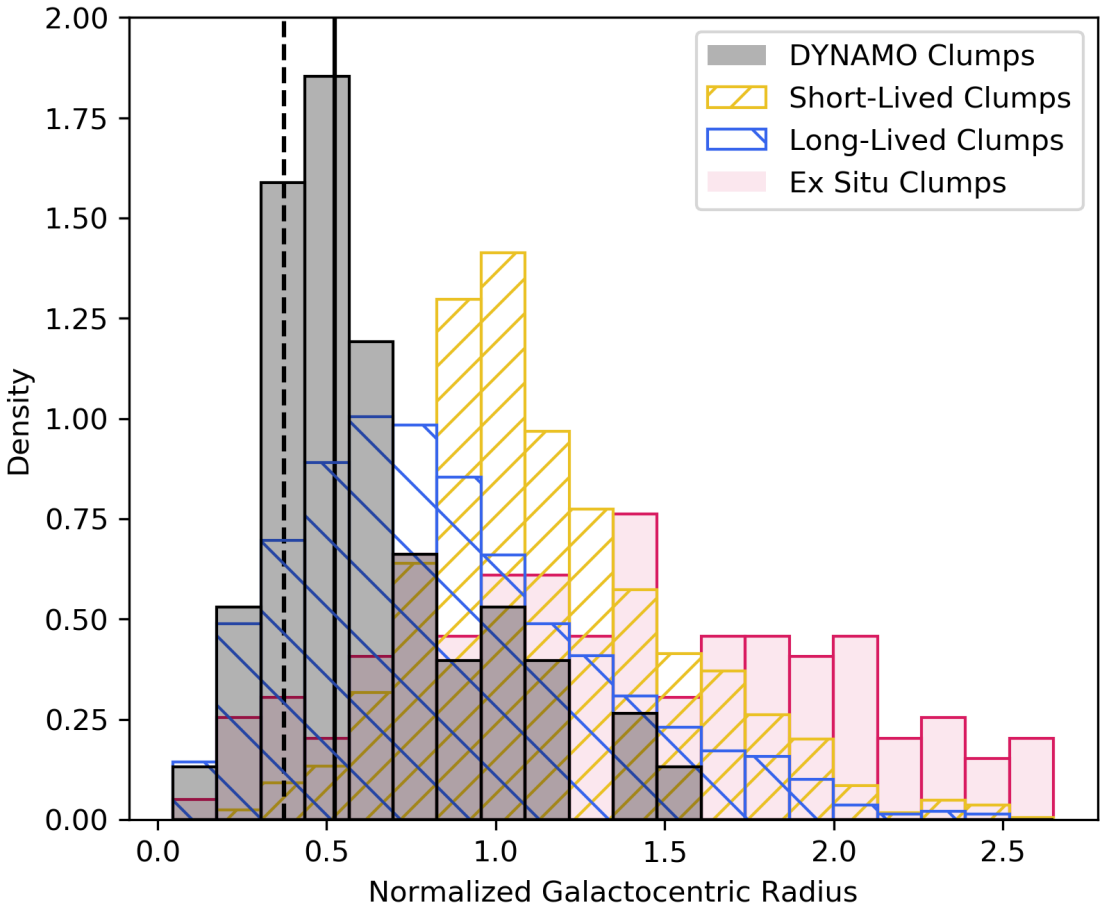

Figure 3.14: Comparison of the distribution of DYNAMO (grey), short-lived (yellow), long-lived clumps (blue), and *ex situ* clumps in terms of normalized galactocentric radius. The DYNAMO clumps are clearly distinct from the short-lived clumps and cluster at radii < 1, as do the long-lived clumps. The median distance of DYNAMO clumps (vertical black solid line) is ~ 0.5 and is ~ 1.1 for the short-lived clumps. The radius normalization of the simulated clumps corresponds to the radius that contains 85% of the cold mass, while we normalize to the 50% light-radius measured in the F467M images. If we choose a larger radius definition as our normalization, the median distance of DYNAMO clumps becomes ~ 0.5 (vertical dashed black line).

We can see that the short-lived clumps cluster at larger galactocentric radii than do the long-lived and DYNAMO clumps. Thus the DYNAMO clumps and short-lived clumps appear as two distinct populations in this figure. In fact, 50% of the simulated short-lived clumps reside within a normalized galactocentric radius of $\sim$1.1, while 50% of the DYNAMO clumps are found within a distance of $\sim$0.5; this implies that a large fraction of our clumps are not short-lived. We use the 50% light-radius in the F467M filter as our normalization for each galaxy; however, if we instead normalize to the 85% light-radius in the F467M filter the peak of the distribution shifts to slightly smaller distances. The vertical black solid line indicates the median galactocentric radius of DYNAMO clumps when normalized to the 50% light-radius, while the vertical, dashed black line indicates the shifted peak when we normalize to the 85% light-radius. This shift represents a change of a factor of 0.15 dex. Thus, we tentatively conclude from these comparisons that the radial distribution of the DYNAMO clumps is more similar to the long-lived clumps than the short-lived clumps identified in the high$-z$ simulations of Mandelker et al. (2017).

3.5.5 Toward a General Picture of Star Formation in Clumps

Putting the results of our HST photometry and colour measurements together, we have a picture which is consistent with clump ages ranging from 10$-$250 Myr, with older appearing clumps preferentially located closer to the centers of their galaxies. We find that more than half of the clumps in our sample have an internal

age gradient, such that stellar population age increases toward the clump edges. We interpret this as a scenario where continuous star formation in the centers of clumps replenishes the populations of massive young stars as the clumps age and move through their galaxy disc. This is consistent with the detailed picture of long-lived clumps from simulations (Ceverino et al., 2010, 2012, Bournaud et al., 2014, Mandelker et al., 2017).

White et al. (submitted) find with AO-enabled K-band imaging from Keck/NIRC2 that the stellar masses of clumps in DYNAMO G04-1, included in this sample, are preferenced toward low masses. The clumps with $M_{star} > 10^8$ $M_\odot$ are located in the center of the galaxy (after accounting for disc subtraction). This is consistent with our picture of long-lived stellar clumps that grow as they migrate to the galaxy center.

The range of ages we find, the trend of increasing age with decreasing galactocentric radius, and the young clump centers are all consistent with high$-z$ simulations that show the existence of long-lived clumps that are able to migrate to the centers of their galaxies. The distribution of our clumps in terms of normalized galactocentric radius is consistent with the long-lived clumps of Mandelker et al. (2017), which further supports this scenario.

Our data are not consistent with predictions that clumps are only a result of extinction gradients (Buck et al., 2017), as we observe that more than half of our clumps have colour tracks that indicate large variations in age with little variation in extinction. Furthermore, we propose that internal clump colour gradients may be potentially used as a discriminator between clumps in mass and clumpy light

distributions, and suggest that observed clumps in high$-z$ samples may consist of a combination of these.

These results point to a depiction of clumps, not as monolithic structures, but as complex objects with substructures that require further study. A comparison of high resolution clump properties and their substructure with high resolution simulations would be very interesting in this regard. Several simulations of gas-rich, clumpy star forming high-redshift galaxies that study the effect of resolution on observed clump properties find significant substructures within clumps (Ceverino et al., 2012, Behrendt et al., 2016, 2019, Faure et al., 2021). The giant clumps that are ubiquitous at $z \sim 1-3$ appear in these simulations to be collections of smaller clumps with masses of 10^{7-8} $M_{\odot}$ and sizes on the order of 100 pc. When matched to the spatial resolution of high-redshift observations, these smaller clumps appear to coalesce into these giant clumps with very well-matched properties including size, mass, and high intrinsic velocity dispersions.

3.6 Conclusions

In this work we use HST observations of six DYNAMO galaxies taken in the F225W, F336W, and F467M filters. We perform aperture photometry and surface brightness photometry on these data, and use the results to measure the integrated and clump$-$resolved $225-336$ and $336-467$ colours of clumps. These colours are sensitive to extinction and age respectively: while the two colours are not independent of each other, changes in extinction result primarily in changes in the $225-336$

colour, and changes in age are reflected primarily in changes in the $336-467$ colour. Our main findings are:

1. The integrated $336-467$ colours of clumps become increasingly redder with decreasing galactocentric radius. This indicates that clumps closer to the centers of galaxies are older than ones farther out. Furthermore, the underlying colour distributions of the galaxy discs are comparatively much flatter than the trends we observe in the clump colours. This implies that contamination from disc light is not the source of the trend we find. This is consistent with the findings of Guo et al. (2018).

2. Comparing the integrated clump colours to outputs from `Starburst99` colours, we find that their colours are consistent with ages between 10 and 250 Myr, and A_V extinction between 0.6 and 2.0. The lack of significantly older clumps is consistent with the simulations of clumps in high$-z$ galaxies from Bournaud et al. (2014), who shows that the ages of clumps saturate at $\sim$250 Myr because the clumps simultaneously experience ongoing star formation and the loss of older stars through dissipation.

3. We analyze the internally resolved colours of clumps and find that for the majority of them the $336-467$ colour is progressively redder toward their edges; based on our stellar population modeling, this is consistent with an age gradient such that age increases from their centers to their edges. Clump centers tend to be fairly young,

and their age does not show a measurable trend with galactocentric distance. The outer regions of clumps, on the other hand, do show a significant trend with galactocentric distance and a tighter correlation than the clump ages from the integrated light. This is likely caused by ongoing star formation in clump centers throughout their lifetime, so we take the age of the stellar population in the outer clumps to be more indicative of the actual age of the clump.

4. We compare the outer ages of DYNAMO clumps to the Mandelker et al. (2017) high$-z$ simulations, by analyzing the slopes of the power law fits of the *ex situ*, short-lived, and long-lived clumps. We determine from this comparison that the DYNAMO clumps are distinct from the *ex situ* clumps. When comparing the distribution of DYNAMO clumps and simulated clumps in terms of galactocentric radius, we find a clear distinction between the short-lived clumps and DYNAMO clumps. The majority of short-lived clumps are found at larger normalized galactocentric radii, while the DYNAMO clumps preferentially cluster a smaller distances, much like the long-lived clumps.

Chapter 4: Linking it Together – Gas and Star Formation in Nearby High$-z$ Analogs

4.1 Overview

Using $\sim 1-2$ kpc scale ALMA observations of CO(3$-$2) and CO(4$-$3) combined with HST observations of Hα, we characterize the molecular gas and star formation properties of nine local analogs of main sequence galaxies at $z \sim 1-3$, drawn from the DYNAMO sample. From the ALMA CO observations, we measure CO(4$-$3)/CO(3$-$2) across the disk of each galaxy and find that the median line ratio of the sample is $r_{43} = 0.54$. Comparing to line ratio constraints in the literature, we conclude that in this regard, DYNAMO galaxies are most similar to main sequence star forming galaxies at $z \sim 2$, and local Luminous Infrared Galaxies (LIRGs). In addition, we measure beam smearing corrected velocity dispersions and relate these to the molecular gas and star formation rate surface densities. Despite being relatively nearby ($z \sim 0.1$), DYNAMO galaxies exhibit high velocity dispersion and surface densities when compared to local star forming samples throughout their disks. This may be attributed to gas flows which could drive the gas surface densities to high values leading to higher star formation rate surface densities. Sim-

ilarly, if inward radial gas flows were present, the release of gravitational potential energy could drive the high velocity dispersions. Finally, comparing the DYNAMO measurements to predictions from star formation theory, we find that if turbulent dissipation is assumed to depend on the angular velocity, then we are unable to reproduce the observed DYNAMO velocity dispersions. To reproduce the observations, the turbulent dissipation would need to depend on a quantity that increases with galactocentric radius.

4.2 Introduction

Disk galaxies across cosmic time and across a range of stellar mass and gas content properties are in some ways strikingly similar. One such similarity is the Kennicutt-Schmidt relation (hereafter KS relation; Kennicutt, 1998a, Kennicutt and Evans, 2012), which ties the surface density of star formation ($\Sigma_{\rm SFR}$) to the surface density of molecular hydrogen gas ($\Sigma_{\rm mol}$) through a power law relation with a slope of $N \sim 1.4$. The KS relation spans several orders of magnitude in both the star formation rate (SFR) and gas surface density, it holds for both normal star forming galaxies and starbursting systems (Kennicutt and De Los Reyes, 2021) at low- and high-redshift (Bouché et al., 2007, Daddi et al., 2010b, Genzel et al., 2010, Tacconi et al., 2013), and appears to persist on $\sim$ 1 kpc scales (e.g., Kennicutt et al., 2007, Leroy et al., 2008, 2013, Momose et al., 2013). The KS relation provides a useful means of scaling the magnitude of star formation in disk galaxies based on the availability of gas. However, alone it does not provide information about the underlying

mechanisms that work to produce the observed relation.

As a result, much theoretical and numerical simulation work has been done to understand the relation between star formation and the ISM. Theories seek to understand this relation through an energy and pressure equilibrium. The gas, stellar, and dark matter potentials that work to collapse the gas are balanced by thermal, turbulent, radiation, and magnetic pressures. However, turbulence is believed to be the primary balancing force. An important question in understanding this equilibrium state is determining what mechanism or mechanisms predominantly drive turbulence in the ISM. Under the theory of self-regulated star formation, momentum injected by stellar feedback is enough to drive the turbulence needed to balance the vertical weight of the ISM (Shetty and Ostriker, 2012, Faucher-Giguère et al., 2013). Alternatively, theories of gas dynamics predict that the accretion-powered release of gravitational potential energy via radial inflows of gas through a galactic disk are the primary drivers of turbulence (Krumholz and Burkhart, 2016) or that both stellar feedback and gas transport are required to explain observations of the velocity dispersion–star formation rate surface density relation (Elmegreen and Burkert, 2010, Klessen and Hennebelle, 2010, Krumholz et al., 2018).

While theoretical studies debate the relative importance of gravitationally-driven turbulence to stellar feedback, there are hydrodynamic simulation studies that suggest large-scale turbulent driving such as might result from gas accretion may be a necessary component of star formation regulation. Bournaud et al. (2010) study the substructure and turbulence of the interstellar medium (ISM) with resolution reaching up to 0.8 pc, by analyzing the power spectrum of the velocity field

components. They find that turbulence on large scales and cloud scales is mainly regulated by gravitational processes, but that stellar feedback is still required to maintain the ISM in a steady state. Similarly, Brucy et al. (2020) perform magnetohydrodynamic simulations in kpc-sized regions of Milky Way-like and high-redshift galaxies to study the effects of stellar feedback and large-scale turbulent driving on the derived KS relation. They find that for Milky Way-like galaxies, stellar feedback alone is enough to reproduce the widely accepted slope of the KS relation of $N \sim 1.4$. However, when considering galaxies with very high gas fractions, as is observed in main sequence star forming $z \sim 1-2$ galaxies, the addition of large-scale turbulent driving is required to reproduce the KS relation. With stellar feedback alone, the simulations of gas-rich galaxies produce a KS relation that is much steeper than observed. Perhaps in agreement with this finding, Orr et al. (2020) find that for Milky Way-like galaxies at $z \sim 0$ in the Feedback in Realistic Environments (FIRE-2; Wetzel et al., 2016, Hopkins et al., 2018) cosmological simulations, stellar feedback is the primary driver of turbulence, while accretion powering is secondary to that. Nonetheless, numerical studies predict the presence of radial inflows of gas on the order of $\sim 1-7\ \mathrm{M_\odot\,yr^{-1}}$ (Fensch and Bournaud, 2021, Trapp et al., 2021).

To attempt to observationally differentiate between turbulence powering mechanisms, we study the molecular gas velocity dispersions (σ_{mol}), molecular gas surface densities (Σ_{mol}), and star formation rate surface densities (Σ_{SFR}) of nine highly turbulent, nearby ($z \sim 0.1$) galaxies from the DYnamics of Newly Assembled Massive Objects (DYNAMO; Green et al., 2014) sample. Galaxies in the DYNAMO sample were selected to have Hα brighter than 10^{42} erg s^{-1} in the SDSS 3″ fiber. Mea-

surements of the gas fractions, ionized gas velocity dispersions, and SFRs of these galaxies indicate they are most consistent with main sequence star forming galaxies at $z \sim 2$ (Green et al., 2014). Furthermore, the star formation rates and stellar masses of DYNAMO galaxies place them on the main sequence of star formation at $z \sim 2$ rather than the local one (Fisher et al., 2019). Their resemblance to high-redshift spirals and proximity allow us to probe the turbulence powering mechanisms in gas-rich, turbulent galaxies at scales that are not yet achievable at $z \sim 2$. Thus, we combine Hα observations from the Hubble Space Telescope with CO(3−2) and CO(4−3) observations from the Atacama Large Millimeter/sub-millimeter Array to study the $\sigma_{\rm mol}$−$\Sigma_{\rm mol}$ and $\sigma_{\rm mol}$−$\Sigma_{\rm SFR}$ relations resolved on $\sim 1-2$ kpc scales, and compare these to results from simulations and expectations from star formation theory.

This paper is structured as follows: §4.3 describes our observations and data reduction, §4.4 describes how we derive our methods for measuring molecular gas surface density, star formation rate surface density, stellar mass surface density, and velocity dispersions, §4.5 and §4.6 describe and discuss our results, and finally we conclude in §4.7.

Throughout this work, we assume ΛCDM cosmology with $\rm H_0 = 69.6\ km\,s^{-1}$, $\Omega_m = 0.286$, and $\Omega_\Lambda = 0.714$ (consistent with the nine years combined WMAP results Hinshaw et al., 2013), and a Kroupa initial mass function (Kroupa, 2001).

4.3 Observations and Data Reduction

The DYnamics for Newly Assembled Massive Objects (DYNAMO) sample of galaxies, was first defined by Green et al. (2014), who selected galaxies from the MPA-JHU Value Added Catalog of the Sloan Digital Sky Survey based on their redshift and Hα emission. The sample consists of 67 galaxies, with half of the galaxies having $L_{H\alpha} > 10^{42}$ erg s^{-1}. DYNAMO galaxies have been well studied, and their SFRs, stellar masses, molecular gas masses, gas fractions, ionized gas velocity dispersions, and Hα extinctions properties have been constrained (Green et al., 2014, Fisher et al., 2014, 2017b,a, Bassett et al., 2017, White et al., 2017, Fisher et al., 2019, Girard et al., 2021, Lenkić et al., 2021).

4.3.1 ALMA CO Observations

We make use of the CO(3−2) and CO(4−3) observations of nine DYNAMO galaxies with the Atacama Large Millimeter/Submillimeter Array (ALMA), associated with project code 2017.1.00239.S. Observations were taken in Band 7 ($275 - 373$ GHz) and Band 8 ($385 - 500$ GHz) between 2018-06-01 and 2018-07-10. The spectral windows were configured with bandwidths of 2.00 GHz and channel widths of 15.625 MHz (128 channels). In addition, we also make use of higher resolution CO(3−2) ALMA observations of three DYNAMO galaxies (G04-1, G08-5, and G14-1) associated with the project code 2019.1.00447S. These observations were taken in Band 7 between 2019-10-09 and 2019-10-10. The spectral windows were configured with bandwidths of 1.875 GHz and channel widths of 7.8125 MHz (240

channels). The data associated with both projects were presented in Girard et al. (2021).

The visibilities were calibrated and flagged by the observatory with the Common Astronomy Software Application (CASA, McMullin et al., 2007) pipeline versions listed in the fourth column of Table 4.1. We imaged each observation using `tclean` in CASA version 6.1.0.188 with parameters `deconvolver='hogbom'`, `weighting='briggs'`, `robust=0.5`, and `restfreq` set to the redshifted frequency of the observed CO line. We cleaned the data until the residuals were consistent with the root-mean-square (rms) noise levels that are listed in the third column of Table 4.1. To derive these thresholds, we consider data cubes with just a shallow clean, mask the emission (see below), and calculate the standard deviation of the masked cubes; i.e., non-line channels. These values are listed in column three in Table 4.1, and we re-clean the data cubes to that rms level. We convolve the final cubes to a circular beam, listed in the second column of Table 4.1, with the CASA `imsmooth` function. At the redshifts of DYNAMO galaxies in our sample, the beam sizes correspond to physical scales of $\sim 1-2$ kpc. Finally, we export all data cubes with the spectral axis in units of velocity, in the local standard of rest frame and adopting the radio convention. We present channel maps of CO(3−2) for DYNAMO G04-1 in Figure 4.1 to show an example of the resulting final data sets, with the circularized beam shown in each panel. The entire set of channel maps of all final data cubes we produce are in Appendix C.1.

We produce moment zero maps (integrated intensity) by first masking each cleaned data cube along both the spatial and spectral axes. To produce our masks,

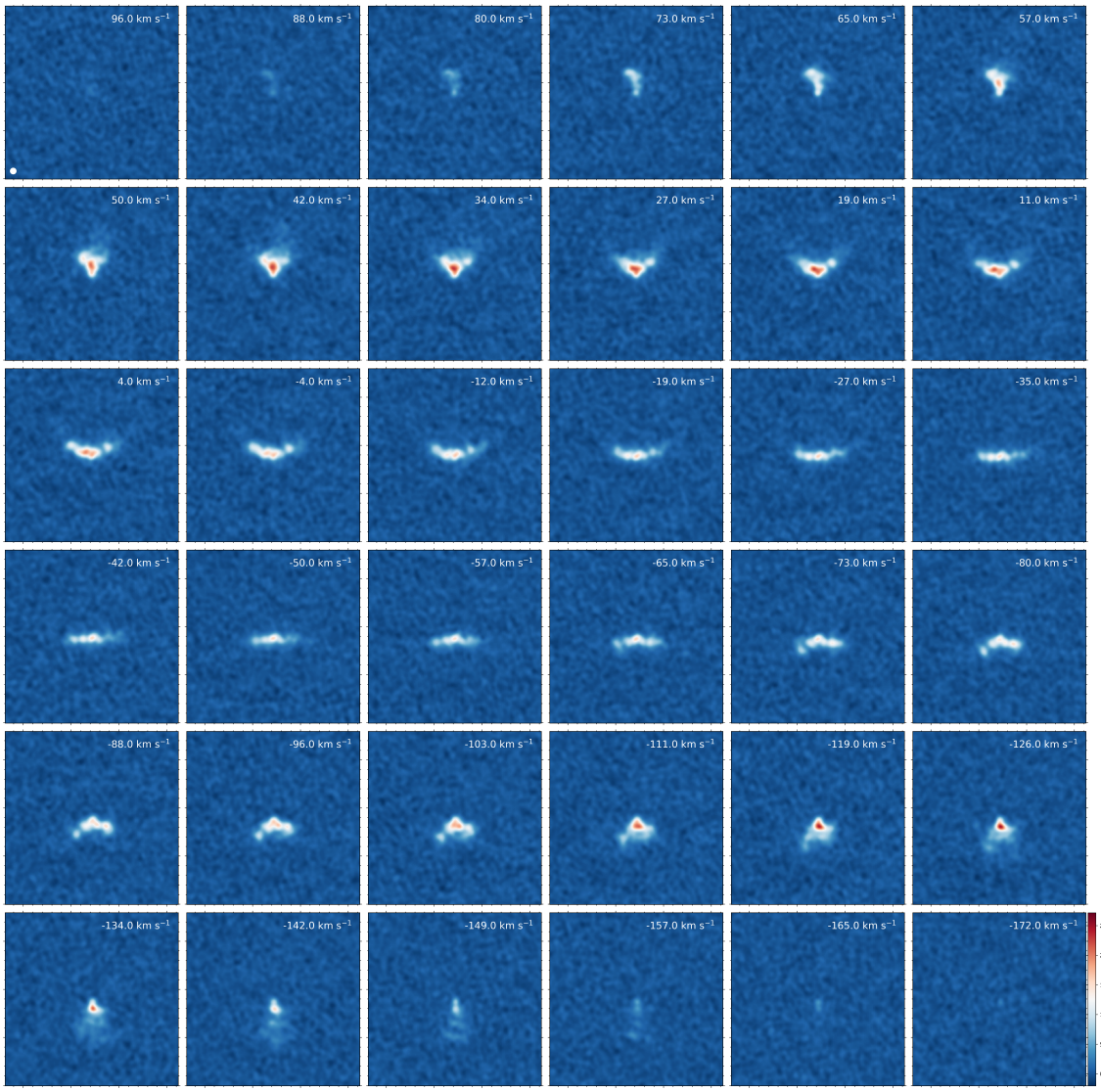

Figure 4.1: Channel maps of CO(3−2) for the galaxy DYNAMO G04-1 in units of mJy beam^{-1}. Each panel is centered at 04h12m19.713s, -05d54m48.62s, and 10.8×10.8″ in size. The velocity range is −172 to 96 km s^{-1} in steps of ∼8 km s^{-1}, as indicated in the top right corners. The circularized beam is shown in white in the bottom left corner of each panel.

Galaxy	CO Trans.	Beam FWHM (arcsec)	rms Noise (mK)	CASA Cal.
C13-1	$3-2$	1.07	11.5	v5.1.1-5
C22-2	$3-2$	1.07	16.0	v5.1.1-5
	$4-3$	0.81	12.5	v5.1.1-5
D13-5	$3-2$	1.10	8.2	v5.1.1-5
	$4-3$	0.79	12.1	v5.1.1-5
D15-3	$4-3$	0.96	10.8	v5.1.1-5
G04-1	$3-2$	0.42	29.1	v5.6.1-8
	$4-3$	0.84	21.5	v5.1.1-5
G08-5	$3-2$	0.40	32.4	v5.6.1-8
G14-1	$3-2$	1.06	3.3	v5.1.1-5
	$4-3$	0.85	6.3	v5.1.1-5
G20-2	$3-2$	1.23	3.7	v5.1.1-5
	$4-3$	0.86	4.8	v5.1.1-5
SDSS J013527.10-103938.6	$3-2$	1.23	5.2	v5.1.1-5
	$4-3$	0.86	4.5	v5.1.1-5

Table 4.1: CO Data Cube Parameters

we first smooth each cleaned data cube to twice the circularized beam full width at half maximum (FWHM). We then compute the rms of the data cube, and mask all pixels that are below 3× the cube rms. For each remaining pixel, we then compute the integrated intensity over the channels that are not masked out. We do this for both the CO(3−2) and CO(4−3) observations. Figure 4.2 presents these moment zero maps in the two rightmost panels. Then, we recompute the rms noise per channel of each cube by determining the rms of all pixels that have values below the 3× rms threshold.

Finally, for the goal of calculating CO(4−3)/CO(3−2) line ratios, we match the pixel scale and resolution of all 2017 CO(4−3) observations to the pixel scale and resolution of the 2017 CO(3−2) observations, where data for both transitions are available. Similarly, we match the pixel scale and resolution of the 2019 CO(3−2) observations to the 2017 CO(4−3) observations, where available. We match the pixel scales using the CASA function `imregrid`, while to match the resolution, we use the CASA `imsmooth` tool to convolve the higher resolution data with a Gaussian kernel to produce the lower resolution Gaussian beam. Finally, we apply the masking of the CO(3−2) observations to the CO(4−3) to produce matching integrated intensity maps. This ensures that the intensities we derive for both lines are integrated over the same velocity ranges.

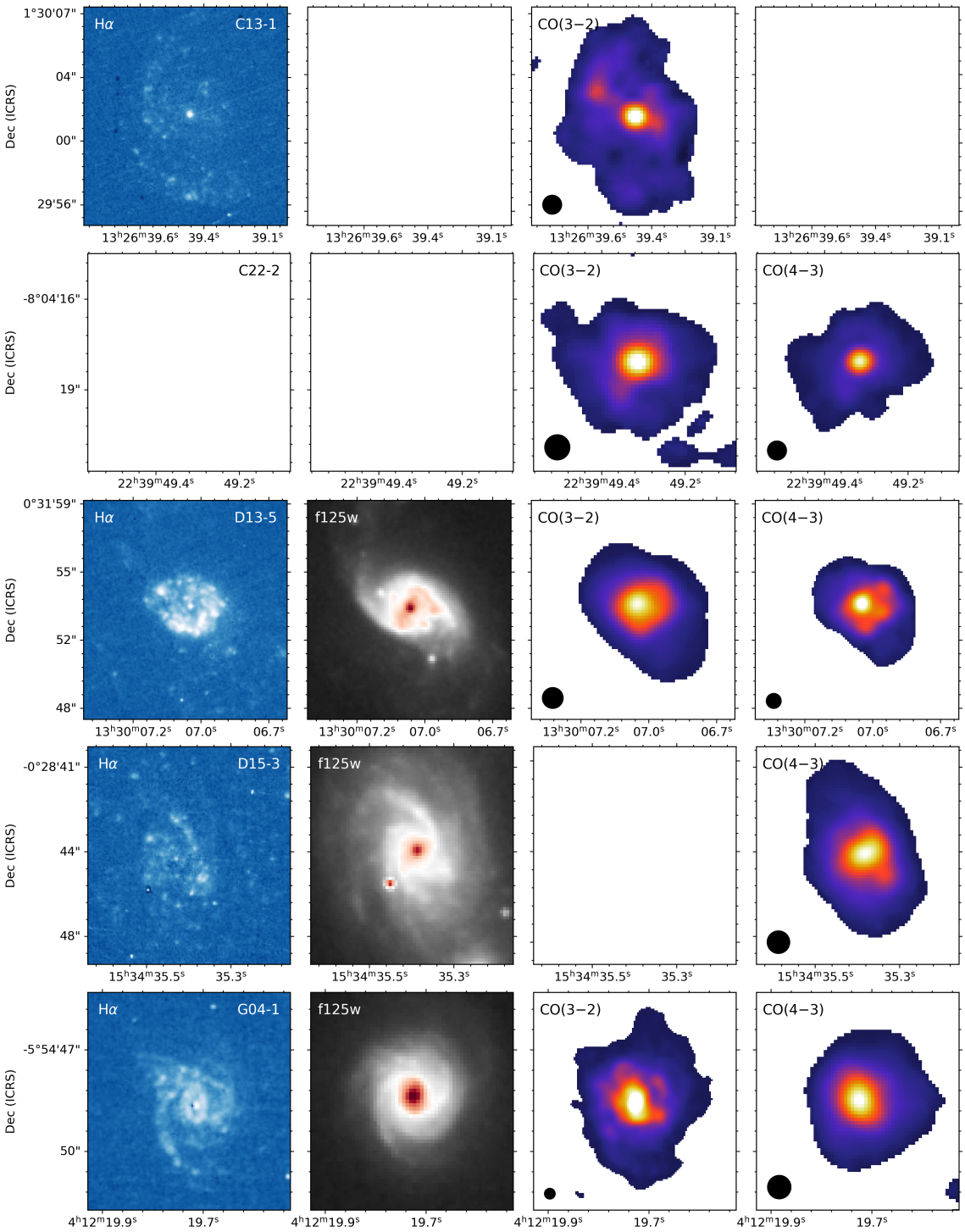
Hα
C13-1
CO(3−2)
C22-2
CO(3−2)
CO(4−3)
Hα
D13-5
f125w
CO(3−2)
CO(4−3)
Hα
D15-3
f125w
CO(4−3)
Hα
G04-1
f125w
CO(3−2)
CO(4−3)
Dec (ICRS)

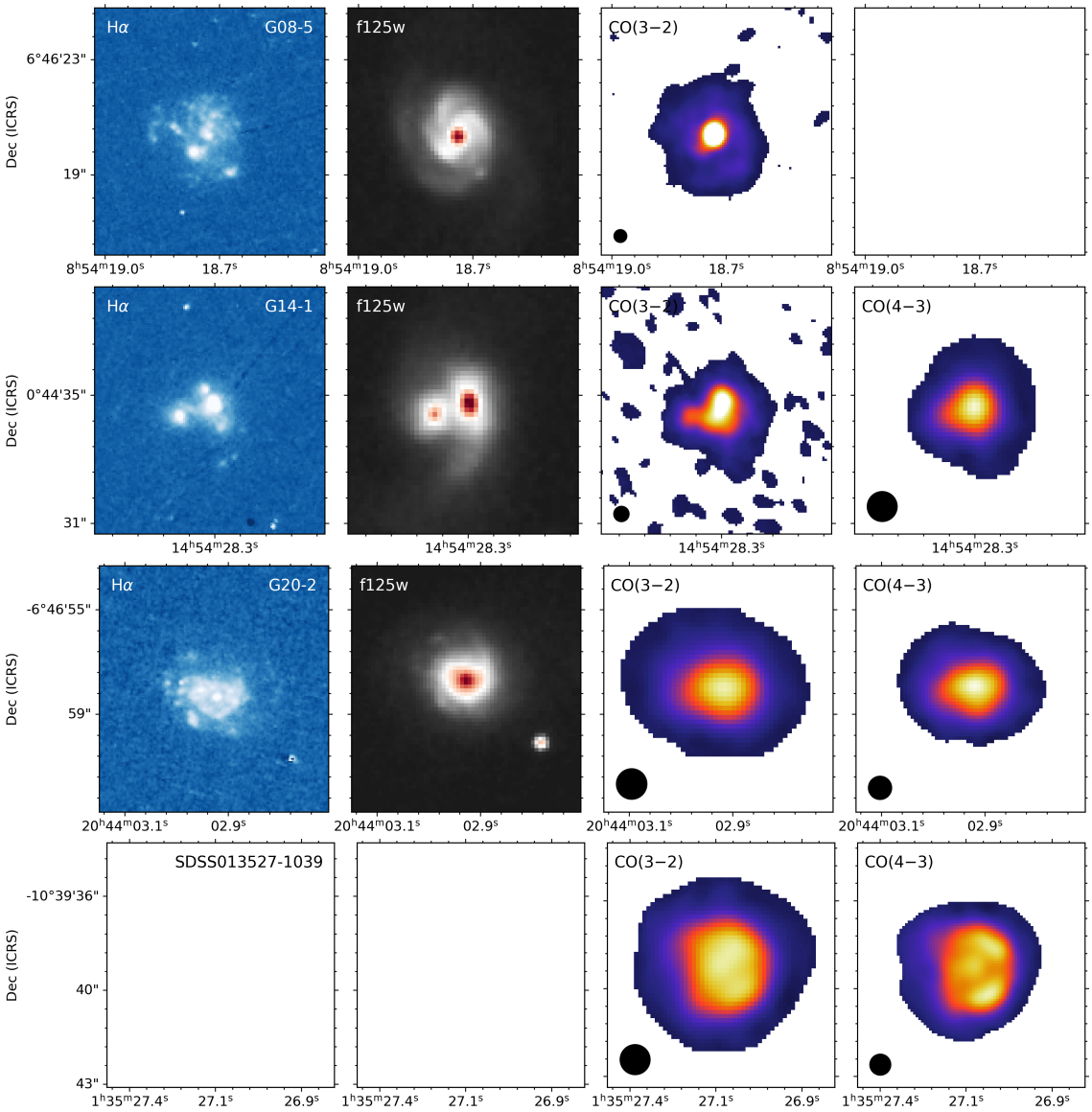

Figure 4.2: Summary of all data sets analyzed in this work for each galaxy in our sample, as indicated in the top right corners of the leftmost panels. The leftmost panels show the continuum subtracted HST Hα data (Fisher et al., 2017b), the second panel show the HST F125W data, the third panels show the CO(3−2) integrated intensity maps, and the rightmost panels show the CO(4−3) integrated intensity maps. Empty panels indicate that data is absent for the given galaxy.

4.3.2 HST Observations

In addition to the ALMA observations of CO in our DYNAMO galaxies, we make use of HST observations of Hα as a tracer of the star formation rate, and HST WFC3/IR F125W observations ($\sim J$ band) as a tracer of the stellar mass (we show these in the two leftmost panels of Figure 4.2). The Hα data were processed and presented in Fisher et al. (2017b), who used HST FR647M continuum maps to produce continuum subtracted Hα maps. We use these continuum subtracted maps in this work. The Hα maps have a pixel scale of $\sim 0.05''$ and a resolution corresponding to physical scales of $\sim 50-200$ pc (Fisher et al., 2017b), while the F125W data have a pixel scale of $\sim 0.12''$. Our ability to make resolved measurements in these DYNAMO galaxies is limited by the resolution of the ALMA data; therefore, we match the pixel scale and resolution of the Hα observations to that of the CO(3−2), where available, and CO(4−3) otherwise. To achieve this, we convolve each Hα observation with a two-dimensional Gaussian function whose FWHM is equal to the circularized beam of the corresponding ALMA observation. Then, we re-project and re-grid the Hα observations to match the WCS information and pixel scale of the CO observations using the Python astropy package `reproject`[1], noting that the reproject functions assume that input images have surface brightness units. Figure 4.2 summarizes the data that we analyze in this work. Blank panels in Figure 4.2 indicate missing data sets for the given galaxy.

[1]https://reproject.readthedocs.io/en/stable/index.html

4.4 Methods

4.4.1 Resolved Measurements

This work aims to investigate the gas and star forming properties of DYNAMO galaxies resolved on a $1-2$ kpc scale. Specifically, the properties we are interested in measuring and studying on these scales are: (1) the molecular gas surface density ($\Sigma_{\rm mol}$) adopting both constant and variable CO-to-H_2 conversion factors ($\alpha_{\rm CO}$) for comparison, (2) the SFR surface density ($\Sigma_{\rm SFR}$), and (3) the molecular gas velocity dispersions (σ_{mol}). Here, we describe our method for extracting these measurements from the data.

For each of our resolution and WCS matched data sets, we define two sets of "grids" of circular, beam-sized apertures: one that is centered on the galaxy, and a second that is offset from the center by $0.5\times$ the beam FWHM in both the x and y directions. This is to ensure that we cover the gaps of the first grid. The measurements we present and consider in our analysis are only those along lines of sight where the signal-to-noise ratio of the integrated CO intensity is greater than five.

4.4.1.1 Molecular Gas Surface Density

We measure the molecular gas surface density from our integrated intensity maps of CO(3−2) in all cases but DYNAMO D15-3, for which no CO(3−2) data were available. In that case, we use the CO(4−3) integrated intensity map. Along

each sight-line, we extract the integrated intensity at the center and calculate the molecular gas surface density from:

$$\Sigma_{mol} = \alpha_{CO} \times r_{J1} \times I_{CO} \ \ [\mathrm{M_\odot\,pc^{-2}}] \tag{4.1}$$

where r_{J1} is the ratio of Rayleigh-Jeans brightness temperature intensities to convert CO(J→J−1) emission to CO(1−0), for which we adopt $r_{31} = 0.67$ and $r_{41} = 0.36$, and I_{CO} is the CO(J→J−1) integrated intensity in units of $\mathrm{K\,km\,s^{-1}}$. In our constant CO-to-H_2 conversion factor case, we adopt α_{CO}= 4.35 $\mathrm{M_\odot\,[K\,km\,s^{-1}\,pc^2]^{-1}}$. We also adopt a variable α_{CO} according to the prescription of Bolatto et al. (2013) (equation 31):

$$\alpha_{CO} \sim 2.9 \times \exp\left(\frac{0.4}{Z'\,\Sigma^{100}_{GMC}}\right) \times \left(\frac{\Sigma_{total}}{100\,\mathrm{M_\odot\,pc{-}2}}\right)^{\gamma} \tag{4.2}$$

4.4.1.2 Star Formation Rate Surface Density

We measure the SFR surface density from our CO-matched Hα observations. We perform aperture photometry along each sight-line to obtain the Hα flux (in electrons per second). We convert these fluxes to units of $\mathrm{erg\,s^{-1}\,cm^{-2}\,\AA^{-1}}$, apply a correction for extinction by relating A_V to $A_{\mathrm{H}\alpha}$ assuming the Cardelli et al. (1989) extinction law, and assuming the A_V measurements from Lenkić et al. (2021). The typical Hα extinction resulting from this is $A_{\mathrm{H}\alpha} \sim 1$ mag. Finally, we calculate Hα luminosities and convert them SFRs using the relation of Hao et al. (2011):

$$\mathrm{SFR}\ [\mathrm{M}_\odot\,\mathrm{yr}^{-1}] = 5.53 \times 10^{-42} \times L_{\mathrm{H}\alpha}\ [\mathrm{erg\,s}^{-1}] \tag{4.3}$$

4.4.1.3 Stellar Mass Surface Density

We measure the stellar mass surface density (Σ_*) from our CO-matched HST F125W observations. We perform aperture photometry as above to extract fluxes and convert to luminosities. To convert the luminosities to stellar mass, we assume a constant mass-to-light ratio, $\Upsilon_{*,f125w} = 0.16$ based on stellar population modelling of six DYNAMO galaxies by Ambachew et al. (in prep).

4.4.1.4 Velocity Dispersion

The data in hand allow us to additionally test theories of star formation, as predicted by theory and simulations. The ALMA CO observations allow us to measure the molecular gas velocity dispersion on $1-2$ kpc scales, and to compare these as a function of molecular gas surface density, which we will show in §4.5.4. Here, we outline our method for measuring molecular gas velocity dispersions, and correcting for beam smearing.

To measure the velocity dispersion, we use the CO(3−2) observations when available, and the CO(4−3) observations otherwise. We begin by creating two overlapping grids of beam regions as described in §4.4.1. Then, for each beam region, we extract the spectrum of the CO line from the central pixel. We fit the line profile with a Gaussian function of the form $f(x) = a \times e^{(x-\mu_o)^2/2\sigma^2}$, where a is the ampli-

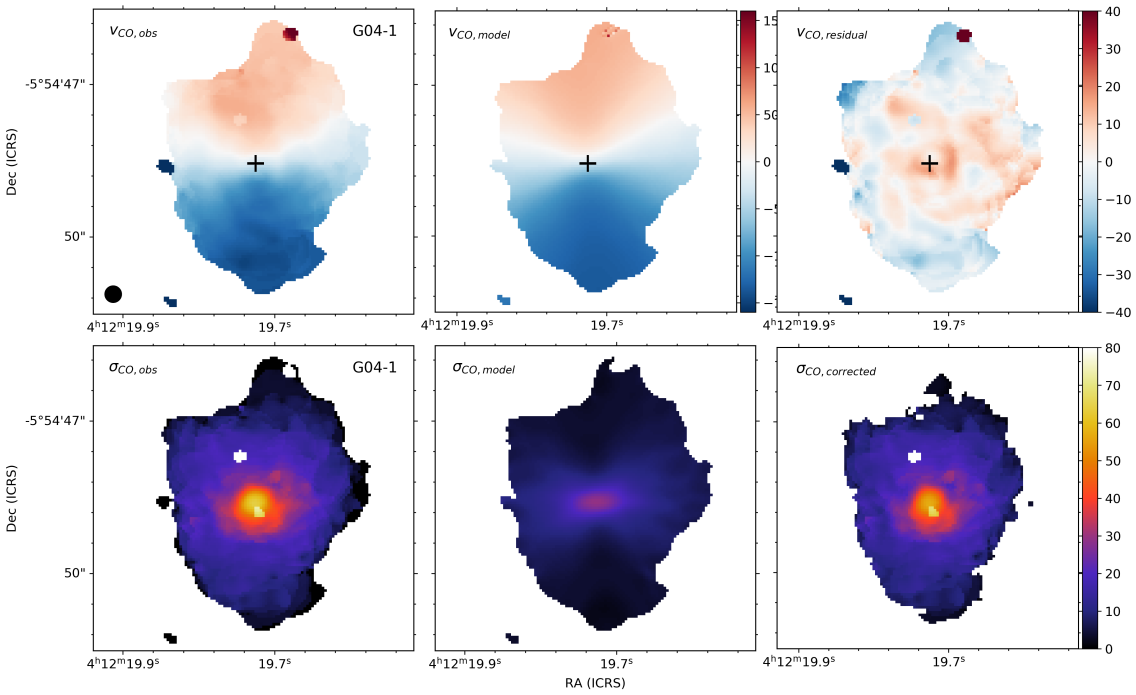

Figure 4.3: Observed and modeled velocity field and velocity dispersion map of DYNAMO G04-1. *Left:* the observed velocity field (top) and velocity dispersion (bottom). *Middle:* the modeled velocity field and velocity dispersion, derived from creating a model data cube by placing the observed velocity in the closest matching channel. *Right:* The velocity field residuals we obtain by subtracting the model velocity field from the observations (top), and the corrected velocity dispersion map obtained by subtracting in quadrature the model velocity dispersion from our measured velocity dispersion. This simulates the effect of beam smearing and corrects for it.

tude of the line, μ_o is its centroid, and σ is its velocity dispersion. We perform our fitting using the PYTHON SCIPY function `curve_fit`. The resulting σ parameters obtained in this way, are our velocity dispersion measurements.

However, beam smearing has a strong effect on measured velocity dispersion, particularly close to the centers of galaxies, and along their minor axes. Furthermore, the effect of beam smearing can be significant even into the disk of the galaxies, if their rotation curves rise slowly. As a result, we apply a beam smearing correction to our measured velocity dispersion using the method outlined in Levy et al. (2018),

which we summarize here for completeness, which involves creating a model cube for the galaxy rotation using its rotation curve parameters. To create our model cubes, we first adopt the arctan model and rotation curve parameters from Girard et al. (2021) to calculate the rotation velocity (v_{rot}) as a function of distance from the center (r):

$$v_{rot} = \frac{2}{\pi} \times V_{rot} \times \arctan\left(\frac{r}{r_t}\right) \tag{4.4}$$

where V_{rot} is the rotation velocity in the flat region of the rotation curve and r_t is the turnover radius of the rotation curve. We then calculate the observed velocity (v_{obs}) from:

$$v_{obs} = v_{rot} \times \sin(i) \times \cos(\theta) \tag{4.5}$$

where i is the inclination, and $\cos(\theta)$ is defined as:

$$\cos(\theta) = \frac{-(x - x_o) \times \sin(PA) - (y - y_o) \times \cos(PA)}{r \times \cos(i)} \tag{4.6}$$

where x_o and y_o are the coordinates of the image center and PA is the galaxy position angle. Finally, r is defined as:

$$r = \sqrt{\frac{(x - x_o)^2 + (y - y_o)^2}{\cos(i)^2}}. \tag{4.7}$$

We create our model cubes by creating an array of zeros with the same size as the actual observed cube, and then calculate v_{obs} at each pixel. We match the

resulting observed velocity to the closest channel, and place a delta function in our model cube at the corresponding pixel and channel, with an amplitude equal to the value (in Jy beam^{-1}) of the same pixel in the same channel in the observed data cube. After performing this for each pixel, we smooth the cube with a Gaussian whose FWHM matches the beam FWHM of the observation. Then, we create a moment 2 (velocity dispersion) map using the PYTHON SPECTRAL-CUBE `linewidth_sigma` function: this is our modeled velocity width due to beam smearing. Finally, we apply the beam smearing correction to the σ values we obtain from our Gaussian fitting, by subtracting in quadrature from each beam region, the model velocity dispersion at the center of the same beam region. In Figure 4.3, we show an example of the final model velocity dispersion map produced in this way for galaxy DYNAMO G04-1.

4.5 Results

4.5.1 CO(4−3)/CO(3−2) Line Ratios

In §4.3.1, we describe our process for matching our CO(4−3) and CO(3−2) observations, and deriving integrated intensity maps. We adopt brightness temperature units, thus our integrated intensity maps have units of K km s^{-1}. To visually determine how the CO(4−3)/CO(3−2) line ratio varies across each galaxy disk, we simply divide our CO(4−3) integrated intensity map by that of the CO(3−2). This is what we present in Figure 4.4, where the color scale indicates the ratio variations across each galaxy disk for which both line transitions were observed, and the black contours indicate line ratio S/N levels starting at S/N = 3 and increasing in units of

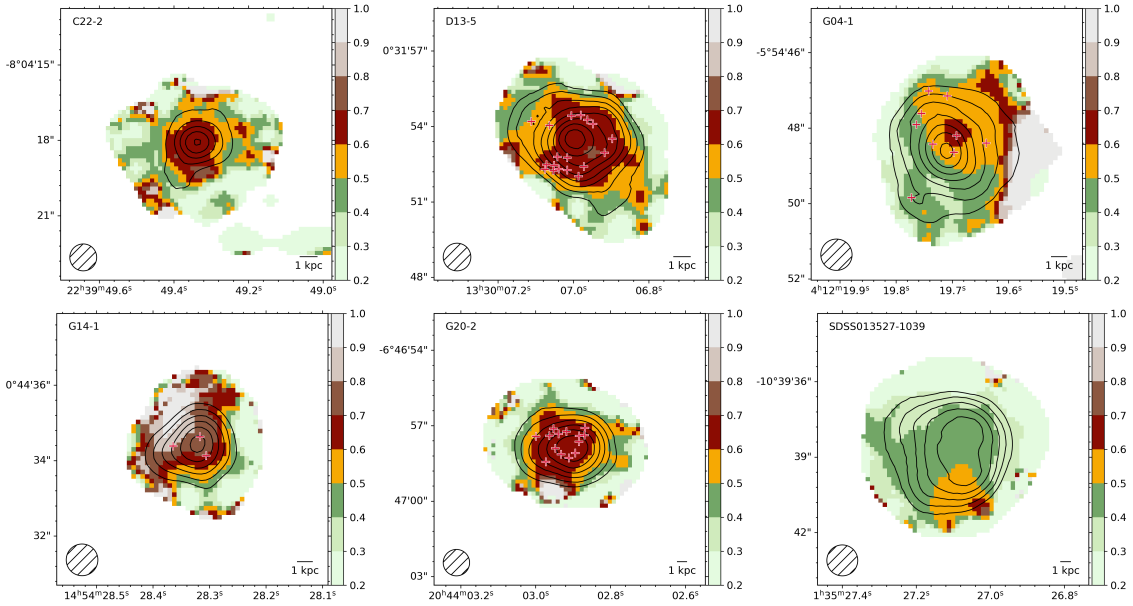

Figure 4.4: CO(4−3)/CO(3−2) line ratios (in brightness temperatures) measured from the pixel scale and resolution matched integrated intensity maps of each transition, integrated over the same velocity ranges. The positions of star forming clumps identified by Lenkić et al. (2021) are included, where available, as crosses. The black contours indicate S/N levels on the line ratios, beginning at 3 and increasing in units of 1. The galaxy name is indicated in the top left corner of each panel, along with the median line ratio across the disk. The black hatched circles in the bottom left corners indicate the circularized beam sizes. Finally, we show a 1 kpc scale bar in the bottom right corners. We see that galaxies generally have fairly constant line ratios within the regions where the uncertainties do not dominate, and that they lie typically around $0.4 - 0.7$. The regions of very high or very low line ratios have S/N < 3; therefore, these are regions of high uncertainty and are thus unreliable.

one. We derive uncertainties for the integrated intensity maps ($\sigma_{\mathrm{J}\rightarrow\mathrm{J}-1}$) by summing in quadrature the rms of every channel over which we integrate and multiplying by the channel width:

$$\sigma_{\mathrm{J}\rightarrow\mathrm{J}-1} = \Delta v \sqrt{\sum_{i}^{N} \mathrm{rms}_i} \tag{4.8}$$

where Δv is the channel width, rms_i is the rms of the i^{th} channel (computed as the standard deviation of all pixels in the channel, excluding those identified as emission by our masking procedure described above), and N is the number of channels included in the integration (considering only channels with emission). We compute this uncertainty at each pixel included in our final integrated intensity maps. To obtain the final uncertainty on the line ratio, we add in quadrature the uncertainties of the CO(4−3) and CO(3−2) integrated intensity maps. From Figure 4.4, we see that the line ratio for galaxies in our sample are fairly constant across the disks, with typical values ranging from $r_{43} \sim 0.4-0.7$ with a typical uncertainty of ~ 0.09. Regions with very low or very high line ratios (regions outside the outermost contours of Figure 4.4) correspond to regions of high uncertainty (of order equal to the measurements), and thus low S/N, and are not reliable.

While we cannot constrain the physical conditions of the gas using a single line ratio, we run models using the non-LTE radiative transfer code RADEX (van der Tak et al., 2007) for varying CO column densities to obtain some insight into the possible physical conditions of the gas. In Figure 4.5, we present the RADEX model for a CO column density of $\mathrm{N(CO)} \sim 10^{17}$ cm^{-2}, where the hatched regions

indicate the typical line ratios we measure in DYNAMO galaxies. We choose this as our fiducial model, assuming that $N(H) \equiv N(HI) + N(H_2) \times 2 \sim 1.9 \times 10^{21}$ cm^{-2} A_V (equation 21 in Bolatto et al., 2013). Then, assuming $A_V \sim 4$ in a molecular cloud, a carbon abundance of C/H $\sim 10^{-4}$, and that all carbon is in CO, then the column density of CO is $N(CO) \sim 10^{-4} \times 1.9 \times 10^{20}$ cm^{-2} $\times$ 4 = 7.6×10^{17} cm^{-2}. Finally, assuming a typical cloud line width of ~ 10 km s^{-1}, we find $N(CO) \sim 7.6 \times 10^{16}$ cm^{-2} per dv = 1 km s^{-1}. We see that for very hot temperatures ($T \gtrsim 150$ K) and higher densities, the J= 3 level de-populates, the emission becomes optically thin, and the CO(4−3)/CO(3−2) line ratio becomes greater than one. We can expect that our line ratios likely correspond to cooler temperatures, $T \lesssim 60$ K and densities of $n_H \sim 10^4$ cm^{-3}. At much lower N(CO) (e.g., $\sim 10^{13}$ cm^{-2}), it becomes much more difficult to produce the line ratios we observe at $T \lesssim 60$ K, and requires $n_H \gtrsim 10^5$ cm^{-3}. Furthermore, in the low N(CO) case, the line ratios surpass unity at $T \gtrsim 80$ K and $n_H \gtrsim 10^4$ cm^{-3}.

Next, we perform $\sim 1 - 2$ kpc sized sightline measurements of the line ratio across the disk of each galaxy, as described in §4.4.1, to characterize the typical line ratio we measure, and the magnitude of the spread. To this end, we construct a kernel density estimate (KDE), which can be read like a histogram, but incorporates the uncertainties of the measurements. We construct the KDE by modeling each beam-averaged line ratio measurement as a one-dimensional Gaussian with centroid corresponding to the measured line ratio, and with width equal to the line ratio uncertainty: $\sigma = \sigma_{43}$. The area of each Gaussian is normalized to unity, then we sum all Gaussians to produce the final KDE. This is what we show in Figure

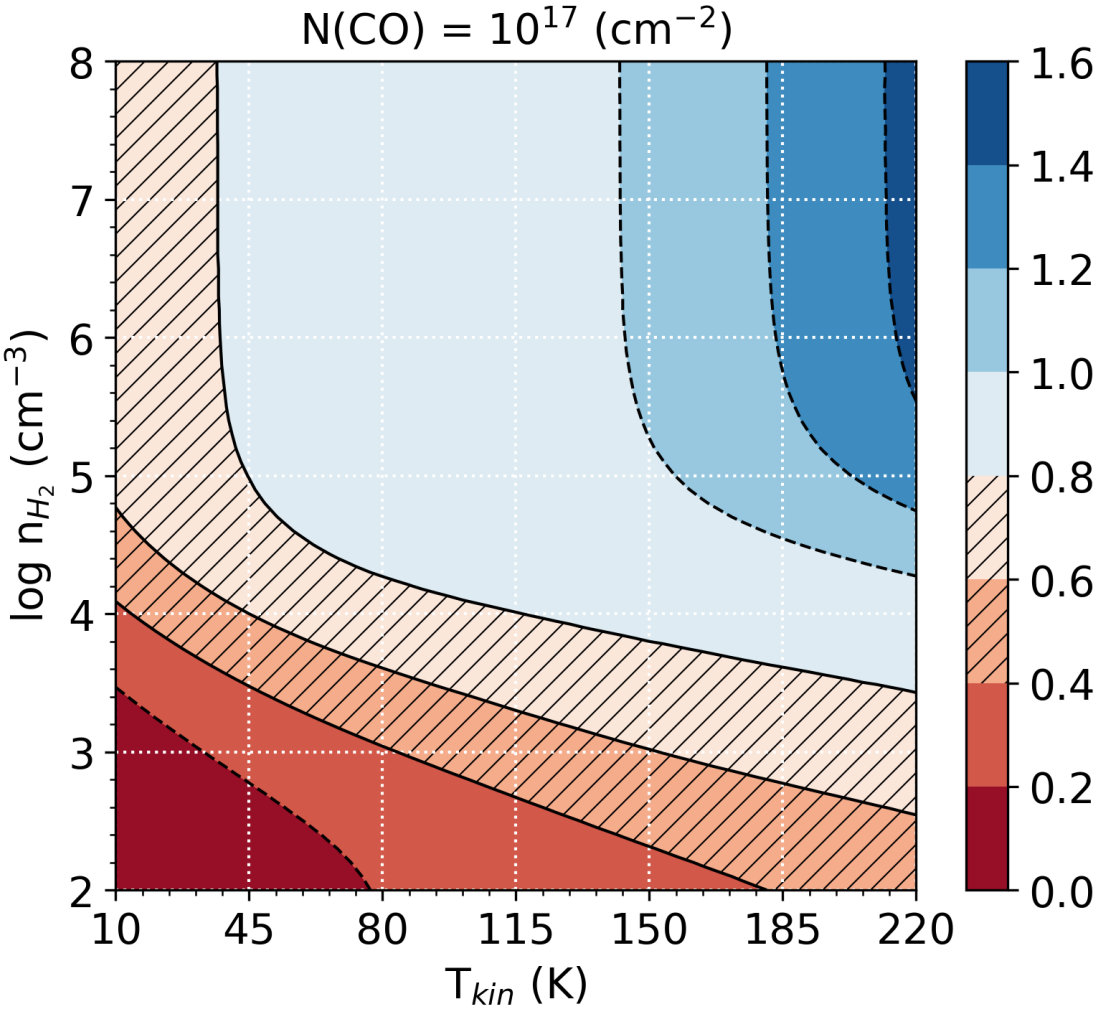

Figure 4.5: Prediction of the CO(4−3)/CO(3−2) line ratio as a function of kinetic temperature and H_2 number density, from the non-LTE radiative transfer code RADEX (van der Tak et al., 2007). Hatched regions indicate the typical line ratios we measure across the disks of DYNAMO galaxies.

4.6. From this analysis, we find that the median line ratio and 1σ uncertainties for DYNAMO galaxies are: $r_{43} = 0.54^{+0.16}_{-0.15}$. These values are taken as the 15.9, 50, and 84.1 percentiles of the cumulative distribution function of the KDE.

For comparison, we compile estimates of the CO(4−3) to CO(3−2) line ratio from the literature and describe them here. Daddi et al. (2015) use IRAM Plateau de Bure Interferometer observations of CO(2−1), CO(3−2), and CO(5−4), and Very Large Array observation of CO(1−0) in three main-sequence star forming disk galaxies at $z = 1.5$ to study their CO excitations. We use their average r_{31} and interpolate their models from their Figure 10 to extract r_{41}, then take the ratio r_{41}/r_{31} to obtain $r_{43} = 0.74 \pm 0.26$, which we include in Figure 4.6 as a black circle.

Henríquez-Brocal et al. (2021) combine NOrthern Extended Millimeter Array observations of [CI](1−0), [CI](2−1), and CO(7−6) with ancillary CO(1−0) and CO(3−2) observations to model the CO spectral line energy distribution (SLED) of Q1700-MD94, a massive main-sequence galaxy at $z \sim 2$, with a one- and two-temperature component model using the non-LTE radiative transfer code RADEX (van der Tak et al., 2007). We interpolate the model curves in their Figure 3 to extract $r_{43} = 0.92 \pm 0.18$ and 0.77 ± 0.15 for the one- and two-component models respectively (taking a 20% uncertainty), and plot these as black and gray squares.

Rosenberg et al. (2015) study the CO SLEDs of 29 (Ultra) Luminous Infrared Galaxies (U/LIRGs) from CO(1−0) through CO(13−12). They classify their objects into three classes based on their excitation level. Where available, we compiled CO(4−3) and CO(3−3) fluxes from their Tables 2 and 3, and divided the resulting ratios by (J^3_u/J^3_l) to convert from units of $\mathrm{W\,m^{-2}}$ to $\mathrm{K\,km\,s}-1$. Finally, we separated

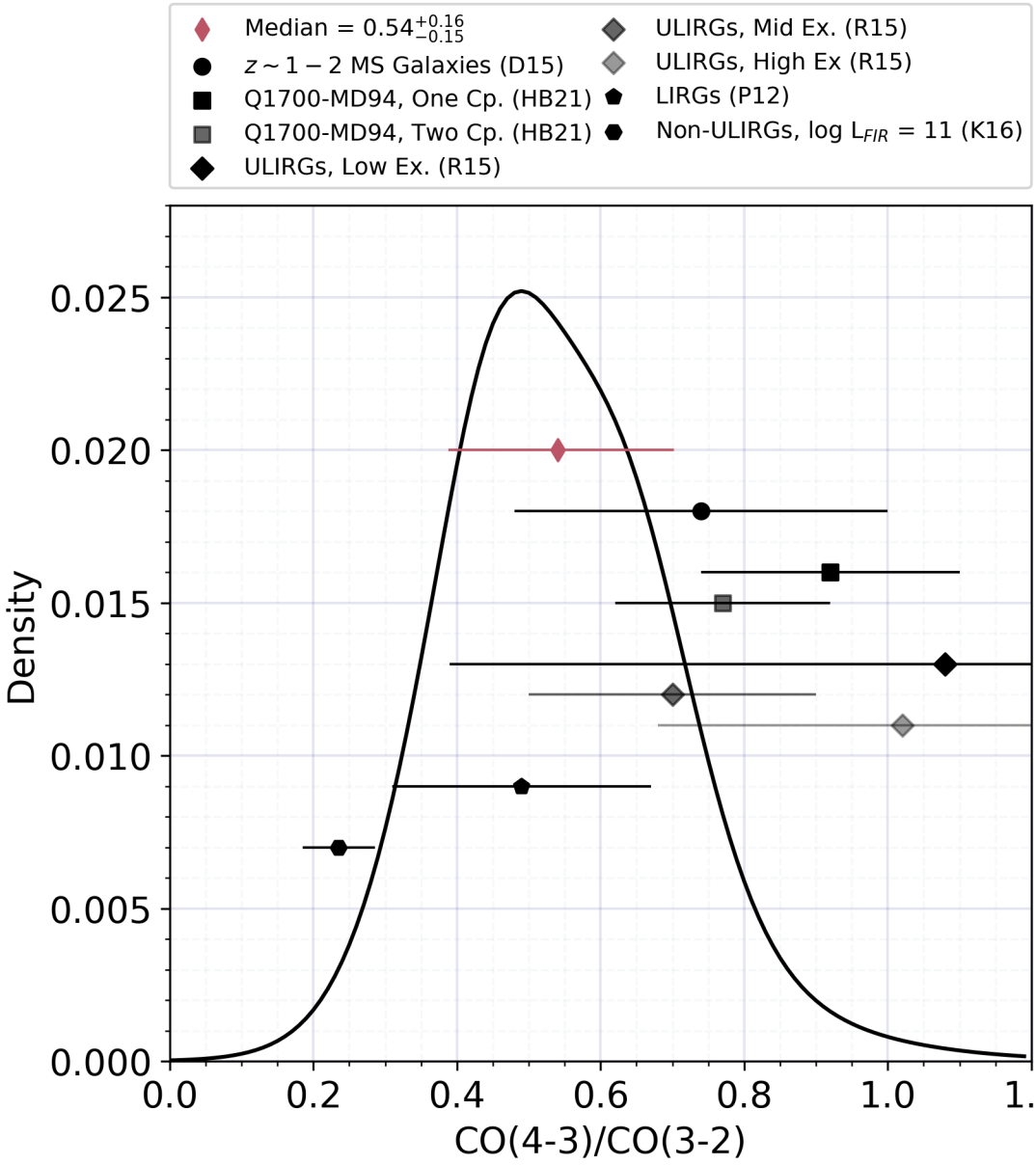

Figure 4.6: Kernel density estimator (KDE) for the resolved CO(4−3)/CO(3−2) line ratio measurements. The KDE can be read as a histogram with measurement uncertainties incorporated. We construct the KDE by modeling each measurement as a Gaussian whose width is the line ratio uncertainty. Summing each individual Gaussian results in the figure shown here. From the cumulative distribution function of this KDE, we infer a median line ratio of $r_{43} = 0.54$. For comparison, we include estimates from the literature: $r_{43} = 0.74 \pm 0.26$ for three $z = 1.5$ main sequence star forming galaxies (black circle; Daddi et al., 2015), $r_{43} = 0.92, 0.77$ for Q1700-MD94, adopting a one- and two-component temperature model respectively (black squares; Henríquez-Brocal et al., 2021), $r_{43} = 1.08, 0.70, 1.02$ for low-, mid-, and high-excitation ULIRGs respectively (black diamonds; Rosenberg et al., 2015), $r_{43} = 0.49 \pm 0.18$ for LIRGs (black pentagon; Papadopoulos et al., 2012), and $r_{43} = 1.32, 0.25$ for ULIRGs and non-(U)LIRGs respectively (black octagons; Kamenetzky et al., 2016).

the galaxies according to their classification, and plot the median line ratio for each class as black and gray diamonds. The error bars represent the standard deviation of line ratios in each class to illustrate their spread.

Papadopoulos et al. (2012) study the CO SLEDs of 70 U/LIRGs; we compile fluxes from their Tables 4 and 5 and adopt the same approach as above for extracting the CO(4−3)/CO(3−2) line ratio, and plot this as a black pentagon.

Finally, Kamenetzky et al. (2016) find a linear relation between L_{FIR} and L'_{CO} for low- to mid-J CO lines and a slightly sub-linear relation for high-J CO lines. We adopt the slope and intercepts of the relations for CO(4−3) and CO(3−2) from their Tables 6 and 7 (for ULIRGs and non-(U)LIRGs respectively), and assume a far-infrared luminosity of 10^{12} for the ULIRG case and 10^{10} for the non-(U)LIRG case to derive the $L_{FIR} - L'_{CO}$ relations. Taking the ratio of these we find $r_{43} = 1.32 \pm 0.26$ and 0.24 ± 0.05 for ULIRGs and non-(U)LIRGs respectively, assuming 20% uncertainty. We plot the resulting non-(U)LIRG line ratio as a black hexagon. We summarize all line ratios we compile from the literature, the median line ratios we measure for each DYNAMO galaxy individually, and the median line ratio for the entire DYNAMO sample studied here in Table 4.2.

This comparison reveals that the CO(4−3)/CO(3−2) line ratio in DYNAMO galaxies is, within the uncertainties, comparable to those measured in the $z = 1.5$ sample of three main sequence galaxies of Daddi et al. (2015), the sample of LIRGs from Papadopoulos et al. (2012), and the $z \sim 2$ main-sequence galaxy G1700-MD94, when assuming a two component temperature model from Henríquez-Brocal et al. (2021). In contrast, the non-U/LIRG line ratio of Kamenetzky et al. (2016) is much

Object(s)	Line Ratio	Reference	Notes
$z = 1.5$ MS Galaxies	0.74 ± 0.26	Daddi et al. (2015)	interpolated
G1700-MD94 one component model	0.92 ± 0.18	Henríquez-Brocal et al. (2021)	interpolated
G1700-MD94 two component model	0.77 ± 0.15	Henríquez-Brocal et al. (2021)	interpolated
ULIRGs low CO excitation	1.08	Rosenberg et al. (2015)	
ULIRGs mid CO excitation	0.70	Rosenberg et al. (2015)	
ULIRGs high CO excitation	1.02	Rosenberg et al. (2015)	
LIRGs	0.49 ± 0.18	Papadopoulos et al. (2012)	
ULIRGs	1.32 ± 0.26	Kamenetzky et al. (2016)	$log(L_{FIR}) = 12$
non-(U)LIRGs	$0.25 \pm 0.0.05$	Kamenetzky et al. (2016)	$log(L_{FIR}) = 10$
C22-2	0.62 ± 0.13	This work	
D13-5	0.57 ± 0.08	This work	
G04-1	0.50 ± 0.08	This work	
G14-1	0.71 ± 0.11	This work	
G20-2	0.61 ± 0.07	This work	
SDSS J013527.10-103938.6	0.44 ± 0.05	This work	
DYNAMO all	$0.54^{+0.16}_{-0.15}$	This work	

Table 4.2: CO(4−3)/CO(3−2) Line Ratios Compiled from the Literature Compared to DYNAMO

lower and inconsistent with what we observe. DYNAMO galaxies lie on the star formation main-sequence at $z \sim 2$ (Fisher et al., 2019), and have gas fractions and velocity dispersions that are more similar to main-sequence galaxies of that epoch than local ones. Therefore, this result is consistent with lines of evidence that indicate DYNAMO galaxies are local analogs of high$-z$ main-sequence systems. Local ULIRG samples have systematically larger line ratios than we observe in DYNAMO, and this too is consistent with previous observations of DYNAMO galaxies. Using *Herschel* PACS+SPIRE observations of nine DYNAMO galaxies, White et al. (2017) found that despite their large FIR luminosities, log $L_{FIR} > 11$, these galaxies have much lower dust temperatures ($\sim$ 30 K) than ULIRGs. Therefore, unlike ULIRGs, the star formation in DYNAMO galaxies is more distributed throughout the disks; thus, colder dust temperatures would be expected and likewise lower CO(4−3)/CO(3−2) line ratios.

4.5.2 Resolved KS-Law

Figure 4.7 shows the resolved measurements of $\Sigma_{\rm SFR}$ versus $\Sigma_{\rm mol}$, where each set of colored data points corresponds to measurements within one DYNAMO galaxy, as indicated by the legend. The left panel assumes a constant $\alpha_{\rm CO}$, while the right panel assumes a variable $\alpha_{\rm CO}$ as prescribed in equation 4.2. The matching colored data points with black outlines in the left panel correspond to the disk averaged $\Sigma_{\rm SFR}$ and $\Sigma_{\rm mol}$ values, measured within the half-light radius of HST F336W images reported in Lenkić et al. (2021). For comparison, we include the measurements of Leroy et al. (2013) who used CO(2−1) HERACLES maps and Hα+24 μm derived SFRs to study the relation between $\Sigma_{\rm mol}$ and $\Sigma_{\rm SFR}$ on 1 kpc scales. We include the results of this work in both panels as black contours which include 50, 68, and 97.5% of the entire data set.

We see that the resolved $\Sigma_{\rm mol}$ and $\Sigma_{\rm SFR}$ measurements in DYNAMO extend those of Leroy et al. (2013) to higher molecular gas and SFR surface densities. We fit our measurements, assuming both the constant and variable $\alpha_{\rm CO}$, with a power law of the form

$$\log \Sigma_{\rm SFR} = N \times \log \Sigma_{\rm mol} + A \tag{4.9}$$

by minimizing the distance between each data point and lines with a given set of parameters N and A. In both cases, we find a sub-linear slope: $N = 0.77$, $A = -2.35$ for the constant $\alpha_{\rm CO}$ case (solid blue line in both panels), and $N = 0.90$,

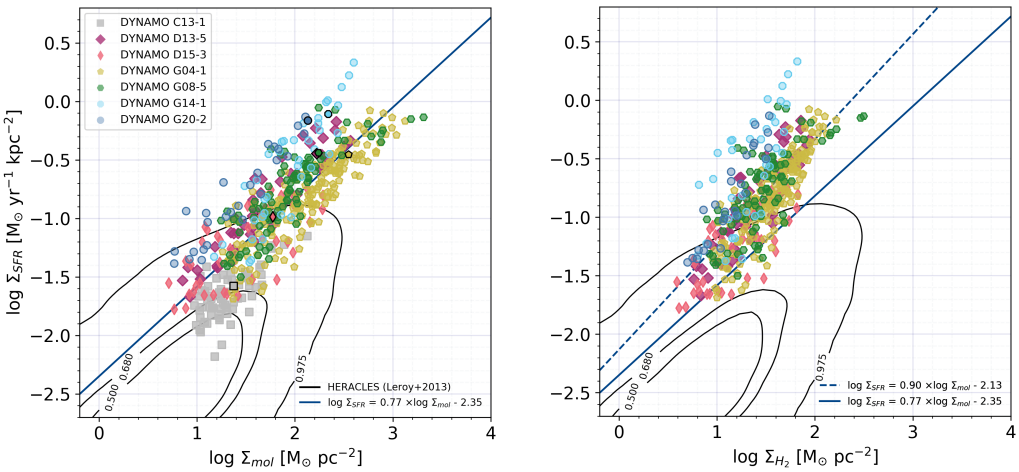

Figure 4.7: The $\Sigma_{\rm SFR}-\Sigma_{\rm mol}$ relation for DYNAMO galaxies, measured in $\sim 1-2$ kpc sightlines (colored data points). The seven colored data points with black outlines are the disk-averaged values of $\Sigma_{\rm SFR}$ and $\Sigma_{\rm mol}$ we measure when adopting the HST F336W half-light radii of Lenkić et al. (2021). We include the 1 kpc scale measurements of Leroy et al. (2013) for 30 nearby disk galaxies, using HERACLES CO(2−1) maps and Hα+24 μm derived SFRs, as black contours which contain 50, 68, and 97.5% of the data.

$A = -2.13$ for the variable $\alpha_{\rm CO}$ case (dashed blue line in the right panel). Leroy et al. (2013) derive $N = 0.80 \pm 0.14$, $A = -2.35 \pm 0.09$ when using only Hα as a SFR tracer and assuming $A_{\rm H\alpha} = 1$ mag (the typical Hα extinction we find as well), and $N = 0.95 \pm 0.15$, $A = -2.40 \pm 0.09$ when using the combination of Hα and 24 μm observations to measure star formation (see their Table 4). Thus, our measurements of the KS relation in DYNAMO galaxies are consistent within the uncertainties with the Leroy et al. (2013) results.

4.5.3 Radial Distribution of Velocity Dispersion

In Figure 4.8, we present the results of our velocity dispersion measurements, corrected for beam smearing as a function of radius as discussed in §4.4.1.4 (black data points), where each panel corresponds to the galaxy indicated in the legend.

The black solid line in each panel is the median velocity dispersion in the disk of all points beyond a radius of 1.5 × the beam FWHM to avoid measurements that are heavily contaminated by beam smearing near the galaxy centers. For comparison and as a check of our beam smearing correction, the Girard et al. (2021) molecular and ionized gas velocity dispersions and uncertainties are included as the black dashed, black dot dashed, and grey shaded regions respectively. The beam FWHM and channel width are represented by the error bars in the top left corner of each panel.

Girard et al. (2021) obtained their velocity dispersion measurements from fitting the ALMA rotation curves using GalPak3D (which accounts for beam smearing Bouché et al., 2015), assuming a flat dispersion model. Beyond the central beam region of each galaxy, our beam smearing correction approach produces velocity dispersion results that are consistent with the results of Girard et al. (2021).

The DYNAMO galaxies in our sample all appear to have higher velocity dispersions in the central beam region than they do in the disk. To assess the significance of this observation, we include as the solid blue lines the median beam smearing correction, measured in annuli of increasing radius from our model dispersion maps (bottom row, middle panel of Figure 4.3). Taking into account the channel width and comparing to the median beam smearing correction, it is possible to say that this may be the case for DYNAMO C13-1 and D13-5, and is very likely to be the case for DYNAMO G04-1, G08-5, and G14-1. These three galaxies are the ones for which we use the higher resolution ALMA observations. This, combined with the rotation curve turnover radius of < 1 kpc, suggest that the enhanced velocity dis-

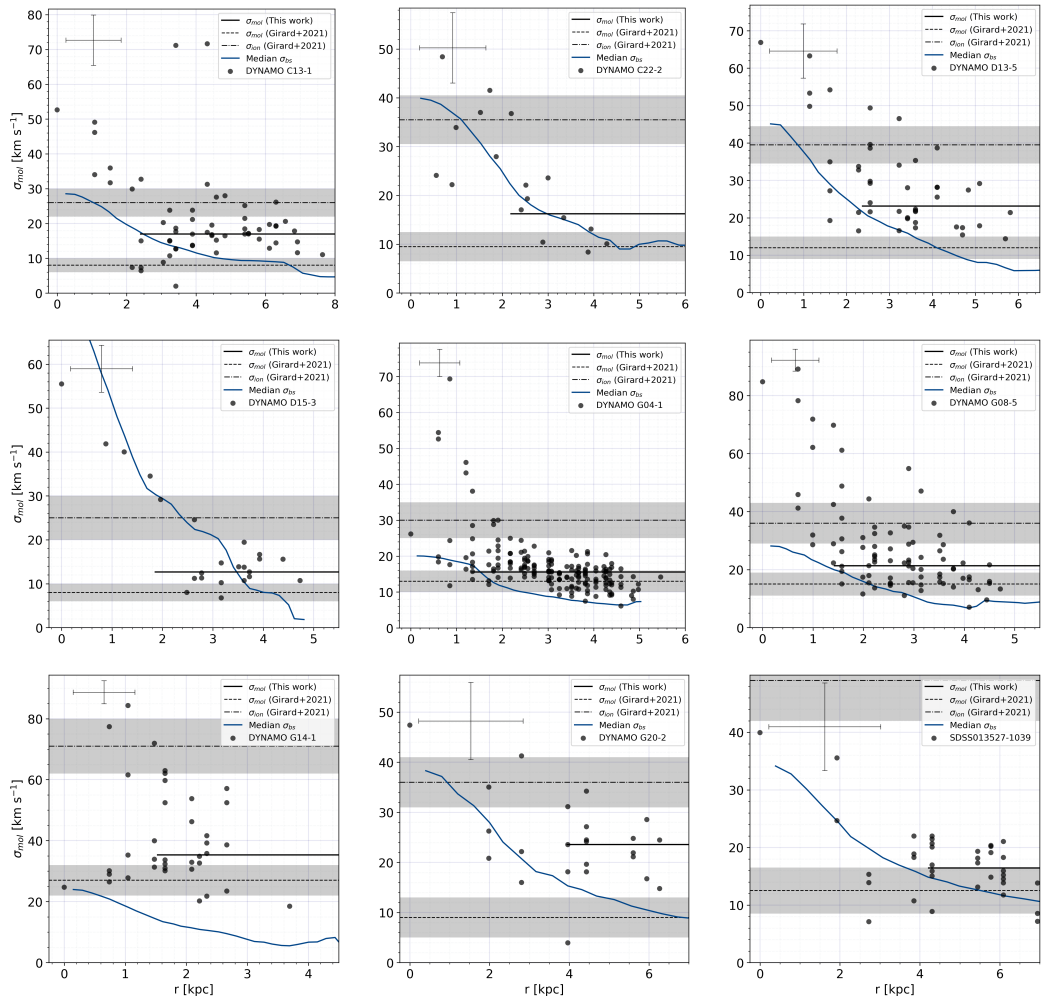

Figure 4.8: Radial distribution of beam smearing corrected velocity dispersion measurements in DYNAMO along beam-sized sightlines (black data points). The black solid line corresponds to the median velocity dispersion in DYNAMO galaxies at radii larger than 1.5 × the beam FWHM. The error bars in the top left corner of each panel indicate the beam FWHM and the channel size of the CO(3−2) observations used to measure velocity dispersions. For comparison, the black dashed and dot-dashed lines mark the molecular gas and ionized gas velocity dispersion respectively from Girard et al. (2021), while the gray shaded region indicates their uncertainties. Our beam smearing corrected velocity dispersions are consistent with those found by Girard et al. (2021). Finally, the blue solid lines are the radial profiles of the median beam smearing corrections we apply to each velocity dispersion measurement. From this, we can see that for DYNAMO G04-1, G08-5, and G14-1, the increase in velocity dispersion towards small radii are likely real and not due to effects of beam smearing.

persions we measure at smaller radii are likely real and not a consequence of beam smearing.

4.5.4 $\sigma_{\rm mol}-\Sigma_{\rm mol}$ and $\sigma_{\rm mol}-\Sigma_{\rm SFR}$ Relations

We now explore the relation between beam smearing corrected molecular gas velocity dispersion, and $\Sigma_{\rm mol}$ and $\Sigma_{\rm SFR}$. Figure 4.9 presents the $\sigma_{\rm mol}-\Sigma_{\rm mol}$ relation in the left panel, and the $\sigma_{\rm mol}-\Sigma_{\rm SFR}$ relation in the right panel, where all measurements are made along $\sim 1-2$ kpc sized lines of sight. DYNAMO data points are separated by galaxy and color coded according to the legend. Measurements of $\sigma_{\rm mol}$, $\Sigma_{\rm mol}$, and $\Sigma_{\rm SFR}$ by Sun et al. (2020) from the PHANGS-ALMA CO(2−1) survey (Leroy et al., 2021), are included as black stars[2] whose sizes are scaled by their inverse galactocentric distance squared. PHANGS-ALMA observed 90 nearby ($d \lesssim 20$ Mpc) galaxies that are on or near the $z = 0$ main-sequence in CO(2−1) at $\sim$ 100 pc resolution, and Sun et al. (2020) present results for 70 of these targets, consisting of 102,778 independent lines of sight. The data we show in Figure 4.9 have been matched to the kpc-scale resolution of our observations (J. Sun, private communication), and only include lines of sight from galaxies with inclinations less than 49° (corresponding to the largest inclination in our sample).

We make several observations from Figure 4.9. First, we note that the results of our $\sigma_{\rm mol}-\Sigma_{\rm mol}$ and $\sigma_{\rm mol}-\Sigma_{\rm SFR}$ relations derived in DYNAMO galaxies are consistent with the kpc-scale measurements of Sun et al. (2020): increasing values of $\Sigma_{\rm mol}$

[2]We caution, however, that the PHANGS-ALMA observations are not corrected for beam smearing.

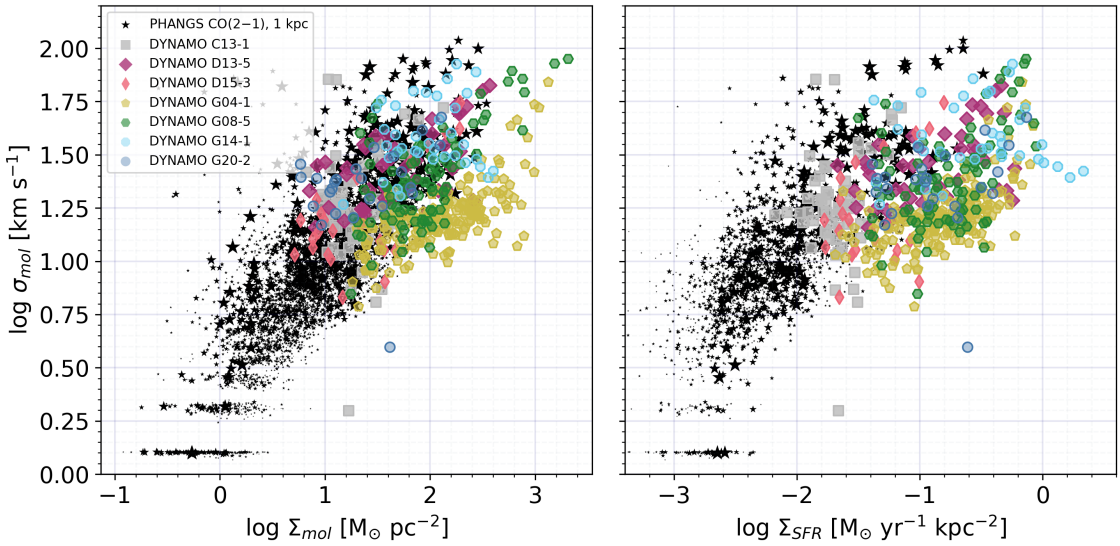

Figure 4.9: Beam smearing corrected molecular gas velocity dispersions as a function of molecular gas surface density (left), and star formation rate surface density (right), for individual $\sim 1-2$ kpc-scale lines of sight in seven DYNAMO galaxies, as indicated by the legend. The black stars (scaled by the inverse galactocentric distance squared of each point) correspond to the PHANGS-ALMA derived measurements of Sun et al. (2020) in 70 nearby galaxies, at a resolution of 1 kpc to match our observations (J. Sun, private communication). Consistent with the PHANGS-ALMA results, velocity dispersions in DYNAMO galaxies increase with $\Sigma_{\rm mol}$ and $\Sigma_{\rm SFR}$, with DYNAMO measurements acting as a high $\Sigma_{\rm mol}$ and $\Sigma_{\rm SFR}$ extension of the PHANGS-ALMA observations. Furthermore, we observe that the molecular gas and SFR surface densities across the entire DYNAMO disks are more similar to the central regions of PHANGS-ALMA galaxies. PHANGS-ALMA velocity dispersions are not corrected for beam smearing; however, we do not expect it to significantly alter the comparison, except in the central regions where the velocity dispersions are highest and most heavily affected by beam smearing. Finally, we also note that the scatter in velocity dispersions within a given DYNAMO galaxy (on average 12.7 km s^{-1}) is in general less than the overall scatter of our full sample ($\sim$ 14.2 km s^{-1}), implying that some property or combination of properties within each galaxy "sets" the velocity dispersion of the molecular gas.

and $\Sigma_{\rm SFR}$ are correlated with larger velocity dispersions. Combining this with our velocity dispersion profiles of Figure 4.8, we can see that these high $\sigma_{\rm mol}$, $\Sigma_{\rm mol}$, and $\Sigma_{\rm SFR}$ are preferentially located at smaller galactocentric radii, as we would expect. We also see that, despite being local galaxies, DYNAMO systems are unlike the PHANGS-ALMA nearby targets in the sense that DYNAMO measurements act as an extension of the $\sigma_{\rm mol}-\Sigma_{\rm mol}$ and $\sigma_{\rm mol}-\Sigma_{\rm SFR}$ relations at high molecular gas and SFR surface density compared to PHANGS-ALMA.

Secondly, when comparing the distribution of DYNAMO measurements with respect to those of PHANGS-ALMA and taking into account the galactocentric distance of each point, we see that even regions within the disks of DYNAMO galaxies are more comparable to the central regions of PHANGS-ALMA galaxies. This is even more clearly illustrated in Figure 2 of Sun et al. (2020), where regions within the central zones of barred galaxies clearly show particularly elevated values of $\sigma_{\rm mol}$ and $\Sigma_{\rm mol}$. Indeed, they find that the central regions of barred galaxies have $\sim 20\times$ higher mass-weighted $\Sigma_{\rm mol}$ than disk regions. In PHANGS-ALMA, this observation is linked to the role of stellar bars driving large inflows of gas into galaxy centers and boosting $\Sigma_{\rm mol}$ to large values.

However, an alternative mechanism would be required to explain the elevated $\Sigma_{\rm mol}$ values in DYNAMO disks. Theoretical work and numerical simulations of high$-z$ galaxies show that cold, smooth streams of gas join the disks of these galaxies at large radii ($\sim 0.1-0.3\times$ the virial radius, or $\sim 10\times$ the stellar scale length; Danovich et al., 2015, Trapp et al., 2021), generating large gas surface densities in these outer regions (Dekel et al., 2009). Furthermore, the radial inflow of this

accreted gas may drive turbulence, and thus velocity dispersion, through loss of gravitational potential energy (Elmegreen and Burkert, 2010, Klessen and Hennebelle, 2010, Krumholz et al., 2018). Similarly, magnetohydrodynamic simulations of local and high$-z$, gas-rich disks (Brucy et al., 2020) show that stellar feedback alone is enough to suppress star formation to levels of the KS law in $z \sim 0$ disks, but is insufficient to do so in high$-z$ systems. For these, large-scale turbulent driving is required. Furthermore, (Brucy et al., 2020) find that the velocity dispersions in these objects are highly anisotropic, with dispersions parallel to the disk planes up to 10$\times$ larger than the vertical dispersions. The nature of the large-scale turbulent driving needed to match high$-z$ disk galaxies to the KS relation is an open question; however, it provides evidence for the need for additional mechanisms.

Finally, we observe that every galaxy in our sample appears to follow "its own" $\sigma_{\rm mol}-\Sigma_{\rm mol}$ and $\sigma_{\rm mol}-\Sigma_{\rm SFR}$ relation. For example, the scatter in velocity dispersion values for DYNAMO G04-1 (taken to be the standard deviation) is ~ 7.8 km s^{-1}, while the scatter for the whole sample is ~ 14.2 km s^{-1}. This implies that galaxy specific properties "set" the velocity dispersions.

4.6 Discussion

4.6.1 Effect of $\Sigma_{\rm SFR}$ on CO(4$-$3)/CO(3$-$2)

The $\sim 1-2$ kpc-scale ALMA observations allow us to investigate how the line ratios we measure are affected by the surface density of star formation. We expect that the CO(4$-$3) transition will be more highly excited in regions of higher

SFR surface densities, because these regions will have larger UV radiation fields, and thus warmer dust temperatures (Narayanan and Krumholz, 2014). To test this, we compare out resolved line ratio measurements to the SFR surface density measurements we make in the same beam regions. Figure 4.10 shows the line ratio as a function of SFR surface density for four galaxies for which all necessary observations were available, as indicated by the legend. For each galaxy, we plot the set of beam measurements as previously described. Though the line ratio uncertainties are large, there is a moderate positive correlation between the line ratios and SFR surface density measurements, as expected. We perform a Spearman Rank Order correlation and find a coefficient of $\rho = 0.614$. In addition, we perform a linear fit of our observed line ratio$-\Sigma_{\rm SFR}$ relation, which we show with the black solid line. In contrast, the black dashed line corresponds to the parameterization of CO line emission intensity as a function of $\Sigma_{\rm SFR}$, derived by Narayanan and Krumholz (2014), in their equation 19:

$$\frac{I_{ij}}{I_{1-0}} = A \times [\log_{10}(\Sigma_{\rm SFR}) - \chi]^B + C \tag{4.10}$$

where I_{ij} is the intensity of the CO($i-j$) transition, A, B, and C are fit parameters, and $\chi = -1.85$. We adopt values for A, B, and C from their Table 3 for CO(3$-$2) and CO(4$-$3) and substitute in our measured values of $\Sigma_{\rm SFR}$. Finally, we take the ratio of the two equations and divide by $J_u^2/J_l^2 = 4^2/3^2$ to convert from Jy to K and produce the line in Figure 4.10.

Overall, our fitted relation suggests a steeper relation between the CO(4$-$3) to

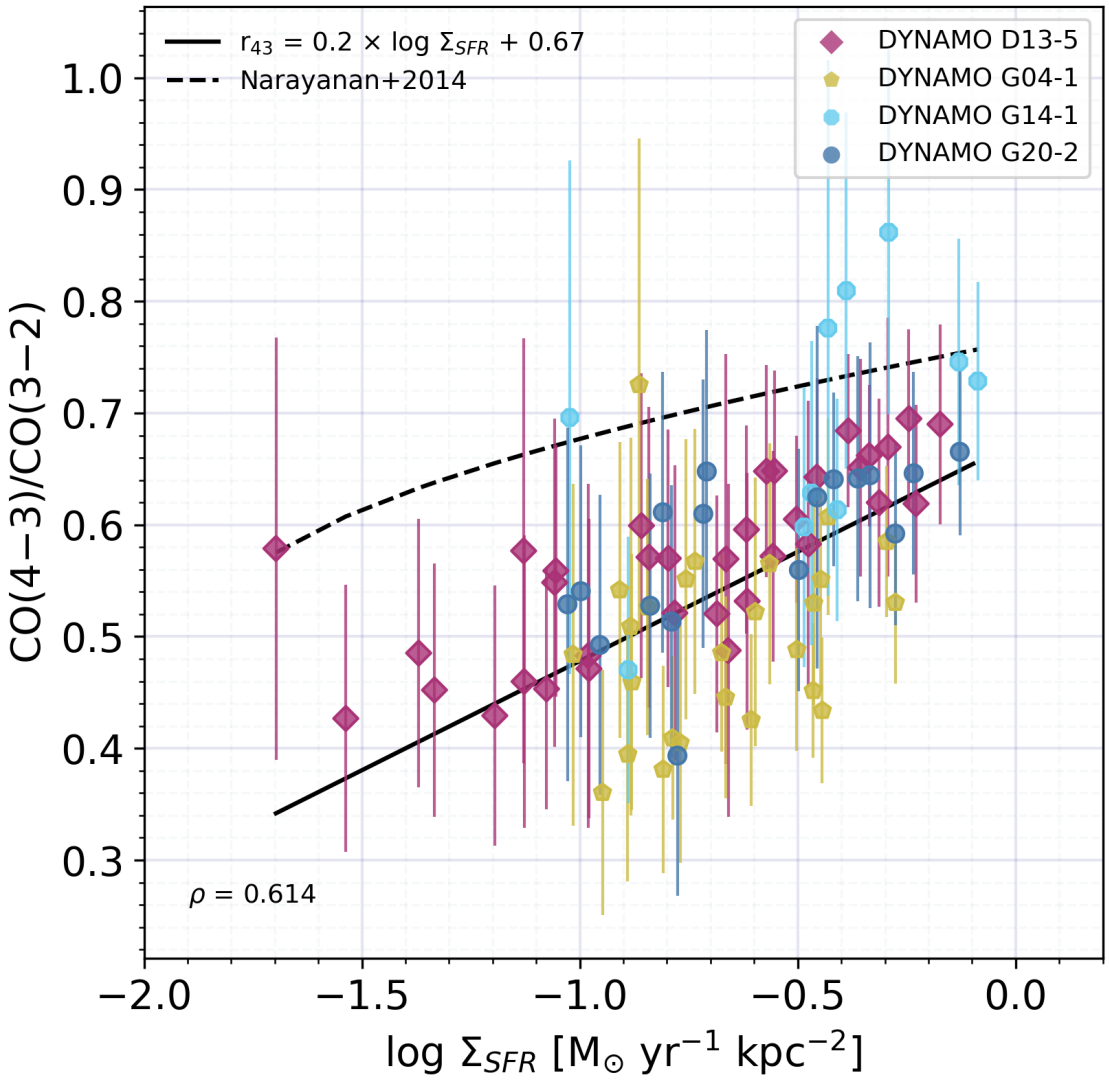

Figure 4.10: CO(4−3)/CO(3−2) line ratio as a function of SFR surface density, measured in beam-sized regions across the disk of each galaxy, indicated by the color and symbol coding in the legend. We present this data for galaxies where observations of both CO transitions and Hα exist. Despite the large uncertainties, there is an indication of an increasing line ratio with increasing SFR surface density trend. This is parameterized by the Spearman's rank-order correlation coefficient of $\rho = 0.614$, suggesting a moderate positive correlation between these two ratios. We present a linear fit to our measurements, presented here as the black solid line. For comparison, we include the predicted line ratio using the relation between CO intensity and $\Sigma_{\rm SFR}$ of Narayanan and Krumholz (2014), presented here as the black dashed line.

CO(3−2) line ratio and $\Sigma_{\rm SFR}$ than is predicted by the parameterization of equation 4.10. At the lowest $\Sigma_{\rm SFR}$ values, equation 4.10 over-estimates our fitted relation by a factor of ~ 1.7, while at the highest $\Sigma_{\rm SFR}$ values, the difference is only a factor of ~ 1.2.

4.6.2 Comparison of $\sigma_{\rm mol}-\Sigma_{\rm mol}$ and $\sigma_{\rm mol}-\Sigma_{\rm SFR}$ to Hydrodynamic Models and Theory

In this section, we further explore the $\sigma_{\rm mol}-\Sigma_{\rm mol}$ and $\sigma_{\rm mol}-\Sigma_{\rm SFR}$ relations by comparing our observational results to results from numerical simulations and predictions from theory. In Figure 4.11, we show the DYNAMO and PHANGS-ALMA measurements previously discussed as shaded red and blue regions respectively, that include 68% of the data; i.e., data points within $\pm1\sigma$ from the median. For PHANGS-ALMA, we further scale the shading by the number of data points within each $\Sigma_{\rm mol}$ bin: the lightest shadings at $\log\Sigma_{\rm mol} > 2$ correspond to fewer than 10 data points (these are upper limits because the PHANGS-ALMA measurements are not corrected for beam smearing), while the darkest shadings at $\log\Sigma_{\rm mol} \sim 1$ corresponds to more than 500 data points (this is also similar for the PHANGS-ALMA $\Sigma_{\rm SFR}$ measurements). Because molecular gas becomes a poor tracer of total gas at $\Sigma_{\rm mol} \lesssim 10$ $\rm M_\odot\,yr^{-1}$, we highlight this region in gray to remind readers of this caveat. Similarly, we add a gray shaded area in the right panel by converting $\Sigma_{\rm mol} = 10$ $\rm M_\odot\,yr^{-1}$ to a SFR surface density by assuming the KS relation of Leroy et al. (2013) for Hα+24 μm derived SFRs. We compare the DYNAMO and

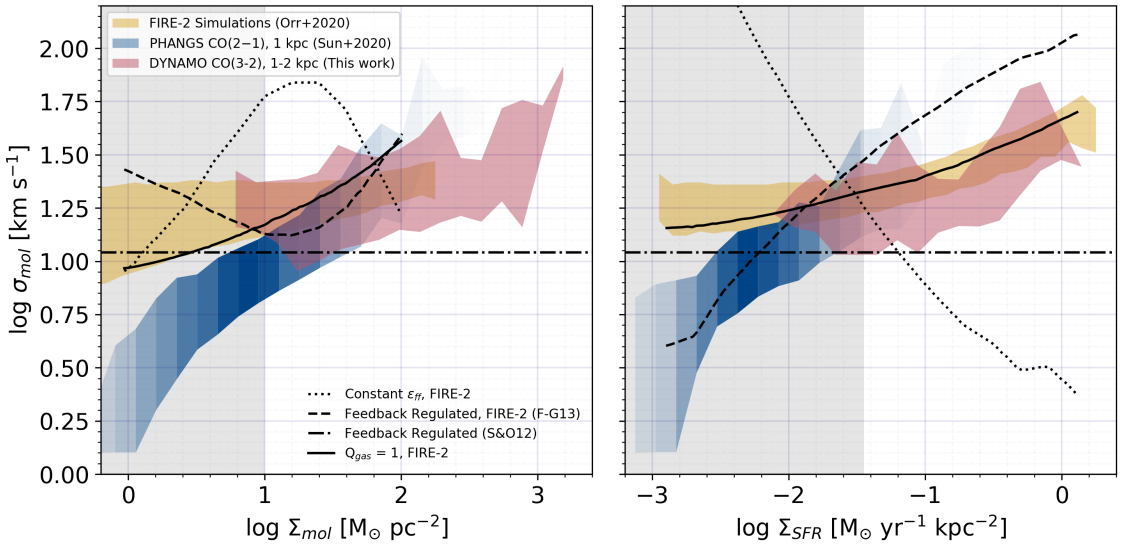

Figure 4.11: Comparison of the $\sigma_{\rm mol}-\Sigma_{\rm mol}$ (left panel) and $\sigma_{\rm mol}-\Sigma_{\rm SFR}$ (right panel) relation observed for DYNAMO galaxies (red shaded region, 68% of data) and the PHANGS-ALMA results (blue shaded region, 68% of data; Sun et al., 2020), to the FIRE-2 simulation results (yellow shaded region, 50% of data; Orr et al., 2020). We shade the PHANGS-ALMA region (which are not corrected for beam smearing) according to the number of data points that are within each bin; the lightest shaded regions have fewer than 10 points, while the darkest regions contain several hundred points. At $\Sigma_{\rm mol} < 10$ M$_\odot$ pc^{-2} (gray shaded region), gas becomes HI dominated and molecular gas becomes a poor tracer of the total gas. Due to a lack of HI data, the discrepancy between the observations and FIRE-2 in this region can be attributed to this effect. At larger $\Sigma_{\rm mol}$ and $\Sigma_{\rm SFR}$ values, the agreement between the observations and FIRE-2 is reasonably good when considering each relation separately. However, taken together, DYNAMO galaxies have much larger $\Sigma_{\rm mol}$ values than FIRE-2, yet comparable $\Sigma_{\rm SFR}$ values, indicating that the depletion times of DYNAMO are not reproduced by the simulations.

PHANGS-ALMA measurements to the results of Orr et al. (2020) who used the cosmological zoom-in simulations from the Latte suite of FIRE-2 (Wetzel et al., 2016, Hopkins et al., 2018) of Milky Way-mass disk galaxies at $z \sim 0$ (yellow shaded region which includes 50% of the simulation data; i.e., $25^{th} - 75^{th}$ percentile), to study the turbulence driving mechanisms. We note, however, that the FIRE-2 simulation measures HI+H_2; therefore this introduces uncertainties when comparing to observations, which consist of only H_2 measurements.

In the high $\Sigma_{\rm mol}$ and $\Sigma_{\rm SFR}$ regime, the scaling of the FIRE-2 results with respect to our DYNAMO measurements are seemingly very good, and both the simulations and observations occupy very similar regions of the $\sigma_{\rm mol}-\Sigma_{\rm mol}$ and $\sigma_{\rm mol}-\Sigma_{\rm SFR}$ parameter space. However, when we compare both relations simultaneously , we see that while both FIRE-2 and DYNAMO extend to $\log\Sigma_{\rm SFR}\sim 0$, DYNAMO galaxies have much higher molecular gas surface densities than the FIRE-2 galaxies. This indicates that the gas depletion times (t_{dep} $=\Sigma_{\rm mol}/\Sigma_{\rm SFR}$) of FIRE-2 galaxies do not reproduce the depletion times we observe in DYNAMO. At the low $\Sigma_{\rm mol}$ and $\Sigma_{\rm SFR}$ regime, FIRE-2 galaxies do not show the large velocity dispersion drop off that is observed in the PHANGS-ALMA galaxies. This can be attributed to the lack of observational HI data, as we can see that much of the PHANGS-ALMA measurements reside in the region where atomic hydrogen is believed to become the dominant tracer of total gas. Because the molecular gas surface densities in DYNAMO galaxies are so high, they are especially well suited for comparison with numerical simulations.

In addition to FIRE-2, we compare our measurements to theoretical predictions of the $\sigma_{\rm mol}-\Sigma_{\rm mol}$ and $\sigma_{\rm mol}-\Sigma_{\rm SFR}$ relations, which are indicated by black lines: (1) the black dotted line shows the expected scaling of $\sigma_{\rm mol}$ when assuming a constant star forming efficiency per free-fall time and the FIRE-2 $\Sigma_{\rm mol}$ and $\Sigma_{\rm SFR}$ measurements (see equation 6 in Orr et al., 2020):

$$\sigma_z \sim \frac{32G}{3\pi}\epsilon_{\rm ff}^2\frac{\Omega\Sigma_{\rm gas}^2\Sigma_{\rm disk}}{\Sigma_{\rm SFR}^2} \tag{4.11}$$

where $\Omega \equiv v_{rot}/R$ is the angular velocity; (2) the black solid line corresponds to the

expected scaling for marginal gas stability and the FIRE-2 $\Sigma_{\rm mol}$ and $\Sigma_{\rm SFR}$ measurements (see equation 4 in Orr et al., 2020):

$$\sigma_z = \frac{\pi G(\Sigma_{\rm gas} + \gamma\Sigma_*)}{\sqrt{2}\Omega}; \tag{4.12}$$

where γ is the fraction of the stellar mass surface density (Σ_*) that resides within the disk scale height, (3) the black dashed line shows the $\sigma_{\rm mol}$ scaling for feedback regulated star formation assuming the FIRE-2 $\Sigma_{\rm mol}$ and $\Sigma_{\rm SFR}$ measurements (see equation 5 in Orr et al., 2020, Faucher-Giguère et al., 2013):

$$\sigma_z \sim \frac{2}{\sqrt{3}}(P/m_*)\frac{\Sigma_{\rm SFR}}{\Omega\Sigma_{\rm gas}}; \tag{4.13}$$

where $P/m*$ is the momentum injection per unit mass, and (4) the black dashed-dotted line is the Shetty and Ostriker (2012) feedback regulated scaling of $\sigma_{\rm mol}$ (see their equation 20) assuming that $f_p = 2$ (which characterizes the magnitude of turbulent dissipation and is defined as the ratio between turbulent pressure and the vertical momentum injected by star formation; $f_p \sim 2$ for weak dissipation and $f_p \sim 1$ for strong dissipation), $\chi = 0$ (which accounts for the gravitational potential due to the bulge relative to the gas self-gravity; see Ostriker and Shetty (2011) for more details), $P/m_* = 3000$ km s^{-1}, and $\epsilon_{\rm ff}(n_0) = 0.005$ (the free-fall efficiency at the disk midplane density):

$$\sigma = 5.5 \text{ km s}^{-1} \frac{f_p}{(1+\chi)^{1/2}} \left(\frac{\epsilon_{\rm ff}(n_0)}{0.005}\right) \left(\frac{P/m_*}{3000 \text{ km s}^{-1}}\right). \tag{4.14}$$

While the marginal gas stability and feedback regulated star formation model of Faucher-Giguère et al. (2013) reasonably match the DYNAMO and PHANGS-ALMA observations, as plotted in Figure 4.11, it is important to note that these model prediction lines were derived in Orr et al. (2020) from the FIRE-2 measured values of $\Sigma_{\rm mol}$ and $\Sigma_{\rm SFR}$. As we note already, the depletion time between FIRE-2 galaxies and DYNAMO are different; therefore, the model predictions may not be comparable to the observations. Furthermore, the marginal gas stability model assumes that the Toomre parameter $Q = 1$, while studies show that $Q < 1$ in DYNAMO galaxies (see White et al., 2017, Girard et al., 2021).

Focusing on the feedback regulated model of equation 4.13, we are able to use our measured $\Sigma_{\rm mol}$, $\Sigma_{\rm SFR}$, and Ω values to verify what velocity dispersion scaling is predicted for DYNAMO. We find from this experiment that the feedback regulated model in equation 4.13 predicts that the velocity dispersion in DYNAMO should scale inversely with $\Sigma_{\rm mol}$ and $\Sigma_{\rm SFR}$, which is contrary to our observations.

To verify that our measurements of $\Sigma_{\rm SFR}$are not biased, we examine our assumption of constant extinction correction in calculating SFRs. If extinction is significantly higher in the centers, we would under-predict the $\Sigma_{\rm SFR}$ and find longer depletion times in these regions. To test this, we plot in the left panel of Figure 4.12 the beam smearing corrected velocity dispersions as a function of the gas depletion time. We note from this that overall, the velocity dispersions we measure are not a strong function of depletion time. There are instances of high $\sigma_{\rm mol}$ values, which we tend to preferentially measure at the centers of our targeted galaxies, that are associated with longer depletion times. This indicates that it is possible our extinc-

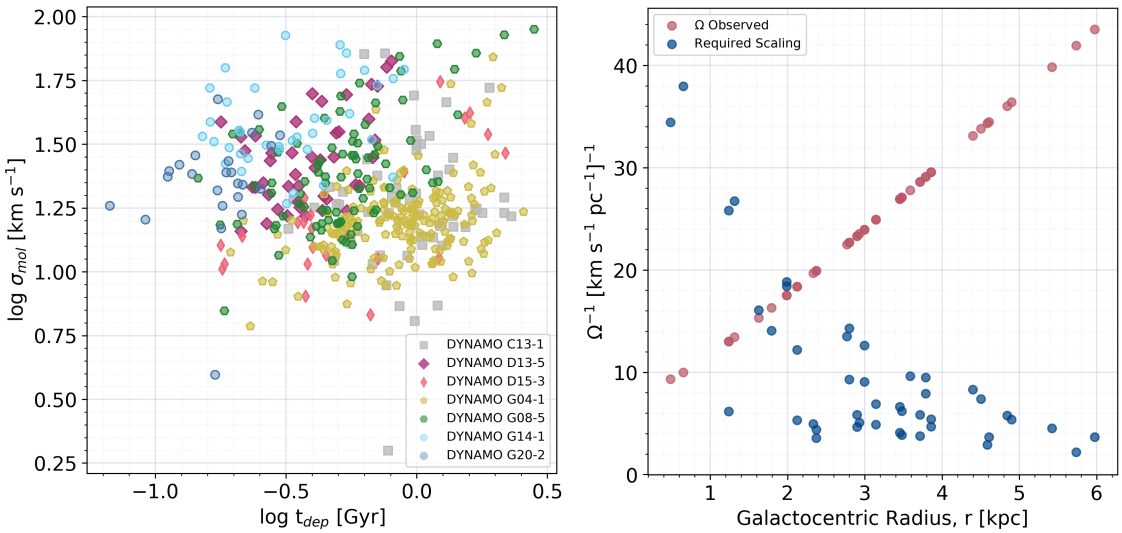

Figure 4.12: *Left*: Beam smearing corrected molecular gas velocity dispersion as a function of the gas depletion time (t_{dep}), measured along individual $\sim 1-2$ kpc sized lines of sight. Despite a few high $\sigma_{\rm mol}$ values with long depletion times, overall there is no strong correlation between $\sigma_{\rm mol}$ and t_{dep}. *Right*: Comparison of the inverse angular velocity of DYNAMO D13-5 (red points), compared to the scaling that would be required in the feedback regulated model of star formation in equation 4.13 to reproduce the observed velocity dispersion measurements.

tion assumptions are affecting the SFRs we measure; however, it does not appear to be a major effect. Indeed, we find that if we fix the depletion time for each line of sight measurement (thus fixing the ratio of $\Sigma_{\rm mol}$ to $\Sigma_{\rm SFR}$ and only varying Ω), then the issue persists. This suggests that our $\Sigma_{\rm SFR}$ measurements are not the primary drivers of the discrepancy between the observed $\sigma_{\rm mol}$ measurements, and $\sigma_{\rm mol}$ values predicted by equation 4.13.

Rather, it is the Ω^{-1} scaling that is largely responsible. The dependence of $\sigma_{\rm mol}$ on Ω in the feedback regulated model comes from the assumption that turbulent momentum decay takes place on a eddy (disk) crossing time. However, this scaling produces a predicted dependence of $\sigma_{\rm mol}$ on $\Sigma_{\rm mol}$ and $\Sigma_{\rm SFR}$ that is opposite to what we observe. Thus, we invert equation 4.13 to solve for the "Ω" scaling that would be

required to reproduce our observed $\sigma_{\rm mol}$ values, and show the result in the right panel of Figure 4.12 for the galaxy DYNAMO D13-5. The red data points correspond to Ω^{-1} derived from the D13-5 rotation curve of Girard et al. (2021). In contrast, the blue data points correspond to the "Ω" value that would produce the velocity dispersions we observe in this galaxy. We see that Ω^{-1} increases with radius, as we would expect, while the turbulent momentum dissipation timescale would need to be related to a quantity that decreases with radius. This is perhaps not a surprising result, since turbulent momentum dissipation might be expected to be related to the microphysics of the gas, while the angular velocity is a large scale galaxy property.

4.7 Conclusions

In this work, we have combined $\sim 1-2$ kpc scale ALMA observations of CO(3−2) and CO(4−3), with HST observations of Hα, to study the KS relation, the CO(4−3)/CO(3−2) line ratio and its dependence on SFR surface density, and the relation between molecular gas velocity dispersion and the surface densities of star formation and molecular gas. We summarize our findings here:

1. DYNAMO galaxies have typical CO(4−3)/CO(3−2) line ratios of $r_{43} = 0.54^{+0.16}_{-0.15}$, which is most consistent with samples of star forming $z \sim 1-2$ main-sequence galaxies and LIRGs (Papadopoulos et al., 2012, Daddi et al., 2015, Henríquez-Brocal et al., 2021).

2. The DYNAMO CO(4−3)/CO(3−2) line ratios are positively correlated with the $\Sigma_{\rm SFR}$ measurements, with a Spearman Rank Order correlation coefficient of $\rho = 0.614$. Our best fit relation between the CO(4−3)/CO(3−2) line ratio and $\Sigma_{\rm SFR}$ is $r_{43} = 0.2 \times \log \Sigma_{\rm SFR} + 0.67$. This relation suggests a steeper relation than predicted by the parameterization of Narayanan and Krumholz (2014); however, the line ratio uncertainties are large.

3. The resolved KS relation in DYNAMO galaxies has a sub-linear slope of $N = 0.77$ when assuming a fixed, Milky Way-like $\alpha_{\rm CO}$ factor. Adopting a variable $\alpha_{\rm CO}$ (equation 31 in Bolatto et al., 2013) results in a slope of $N = 0.90$. These results are consistent with the kpc-scale measurements of the KS relation from the HERACLES CO(2−1) and Hα+24 μm measurements of Leroy et al. (2013).

4. The molecular gas velocity dispersions in DYNAMO galaxies are positively correlated with molecular gas surface density and SFR surface density, consistent with observations in other samples of galaxies (e.g., Sun et al., 2020). Furthermore, we show that the DYNAMO sample extends the range of $\Sigma_{\rm mol}$ and $\Sigma_{\rm SFR}$ conditions probed compared to local samples of star forming galaxies. When predicting the molecular gas velocity dispersions in DYNAMO with theoretical models like the feedback regulated model of star formation, we find that the velocity dispersions should decrease with increasing gas and SFR surface densities. We find that the primary driver of this effect is the assumption that the turbulent momentum dissipation is related to the angular velocity of a galaxy. Angular velocity decreases

outward as a function of galactocentric radius, while to reproduce the observed DYNAMO velocity dispersions, the turbulent momentum dissipation would need to depend on a quantity that behaves in the opposite way and suggest that it is likely driven by gas microphysics.

Chapter 5: Future Work

While the work I have presented in this thesis addresses important questions regarding gas and star formation in galaxies across cosmic time, there remain numerous unanswered ones. In this chapter, I outline some of these questions, and highlight planned and potential future work that will aim to address them.

5.1 The ISM of Clumpy, Turbulent Galaxies

The 158 μm [CII] fine-structure line is an important coolant of the ISM, and is thus a probe of the physical conditions of the ISM. We cannot easily study these conditions in main sequence galaxies at $z \sim 1-2$, the most important epoch of galaxy assembly. We can, however, observe the fine-structure lines in local analogues of main sequence high$-z$ galaxies, like DYNAMO. Observations of DYNAMO exist from facilities such as ALMA, NOEMA, HST, Keck, and Gemini, spanning from the sub-millimeter to the optical/UV, with a gap in the IR.

I am the PI of a SOFIA Cycle 9 observing proposal that has observed [CII] emission and FIR luminosity of seven DYNAMO galaxies with the FIFI-LS and HAWC+ instruments. With these data, I will measure the [CII] line deficits, gas temperatures (which only exist for nine DYNAMO galaxies), and test the suitability

of [CII] as a tracer of star formation, relating these to main sequence galaxies at $z \sim 2$. As galaxies become more luminous and/or compact, the ratio of [CII] line emission to the total FIR luminosity decreases. The [CII]/FIR ratio varies by several orders of magnitude between galaxy types (see Figure 3 in Herrera-Camus et al., 2018a) and with galaxy properties, such as distance from the main sequence and FIR surface brightness (see Figure 5 in Herrera-Camus et al., 2018b). This is observed in local star forming galaxies, galaxies with active galactic nuclei, and high-redshift main sequence objects. DYNAMO galaxies are interesting because their cool dust temperatures and high IR luminosities suggest that they may not have a [CII] deficit. I will test this with my SOFIA observations.

5.2 Large Scale Gas Flows and Clump Scale Gas Kinematics

While the bulk kinematics of galaxies at $z \sim 1-3$ are well studied (see e.g., Wisnioski et al., 2015), the detailed kinematics of gas flows fueling the formation and growth of clumps remain poorly understood. It is widely adopted that the gas is in a state of marginal instability, which has multiple consequences. Krumholz et al. (2018) argue that the instability in gas-rich galaxies should naturally lead to large, non-rotating flows of gas, and that these are responsible for the large gas velocity dispersions in $z > 1$ galaxies. Direct observations of these gas flows in samples of nearby spiral galaxies are rare (Wong et al., 2004, Schmidt et al., 2016), and are otherwise lacking in samples of high$-z$ star forming galaxies, which may be due to the high resolution needed. Secondly, instabilities are thought to be the source of

large clumps (Dekel et al., 2009), yet how clumps dynamically evolve within their galaxies remains uncertain even after a decade of research. Basic concepts, such as the longevity of clumps, remain under debate.

I am the PI of an accepted ALMA Cycle 8 observing proposal that will map the CO(3−2) kinematics and surface brightness in the nearby galaxy DYNAMO D13-5 ($z = 0.0753$) at $\sim 0.2''$ resolution corresponding to a physical scale of ∼280 pc. The goals are to: (1) identify inward mass transport via residuals from velocity models fit to the data, and (2) determine if the clumps are kinematically distinct from the disk and whether they are bound as indicated by their gas virial parameter.

For the first goal, I will use the upcoming $\sim$280 pc observations and existing $\sim$ 1.4 kpc scale observations of this galaxy (presented in Chapter 4) to generate a 2-D model of the velocity field, and then search for significant residuals in the high resolution map. For the second goal, I will use the ALMA observations to measure the gas velocity dispersions and virial parameters of all 18 clumps in D13-5, which will provide a measure of clump longevity and boundness that is independent of the stellar population work I presented in Chapter 4. Because this analysis requires spatial resolution in both kinematics and gas mass sufficient to isolate the individual clumps, the new ALMA observations of D13-5 will provide a completely independent, statistically powerful, assessment of the fundamental nature of clumps in galaxies.

5.3 Feedback from Clumps

Feedback regulated star formation models (e.g., Ostriker et al., 2010) are a standard component of our picture of galaxy evolution. In these theories, newly formed stars and supernovae inject momentum into the ISM which balances it against the inward force of gravity. It is well established at the level of individual supernovae that these explosions carry momentum into the ISM (e.g., Cioffi et al., 1988). At the galaxy wide scale, observations of UV absorption lines indicate that galactic winds are common at $z \sim 1-3$ (e.g., Steidel et al., 2010). However, at intermediate scales, especially in extreme environments like massive star forming clumps, observations are limited. This is because present day facilities cannot adequately resolve these clumpy star forming structures at $z \sim 1-3$. Therefore, it is currently unknown if feedback unbinds clumps before they are able to migrate to the centers of galaxies and contribute to bulge growth, as suggested by theories of instability driven clump formation and migration (Dekel et al., 2009). Determining the ultimate fate of clumps, and the role of feedback, is critical to understanding galaxy evolution in the era of peak star forming activity.

To probe the fate of clumps, I will propose for new observations using the NIRSpec IFU aboard the James Webb Space Telescope (JWST) to map the Paα 1.8751 μm emission line at $\sim$ 150 pc resolution in the DYNAMO galaxy D13-5. Broad-wing emission lines can be used to measure outflows, but in practice this has only been possible for a handful (~ 5) of clumps. The presence of outflowing material causes a fraction of the Paα flux to reside in a blue-shifted broad component. JWST

is the only facility with the spatial resolution and sensitivity required to detect and characterize the properties of the outflowing material, and enable us to study the link between feedback and clump lifetimes. These observations will allow me to: (1) perform the first measurement of the velocity and flux of ionized gas outflows from clumps in a nearby galaxy whose properties are very well-matched to main-sequence, $z \sim 1-3$ galaxies, and (2) determine if clumps are truly bound and rotating structures.

Appendix A: Appendices for Chapter 2

This Appendix includes supplementary material for Chapter 2, including data tables summarizing all candidate CO source properties and their potential counterparts, and Figures showing the detection S/N maps, potential counterparts, and CO line spectra.

A.1 Description of Individual Candidate Sources

Figure 2.5 shows the brightest serendipitous CO sources in the COSMOS, EGS/AEGIS, and GOODS-N fields. The complete set of Figures is available here. The left panels show the signal-to-noise maps at the velocity resolution where each source is detected with the highest SNR. The black contour corresponds to the detection threshold (largest negative SNR). The black box shows the zoom in region for the middle panel images, and the beam is shown in the bottom left corner. The middle panels are HST ACS F814W images where the white contours start at the 3σ level and increase in steps of 0.5σ, the red contour corresponds to the detection threshold, red crosses mark the positions of tentative optical counterparts, and the beam is again shown in the bottom left corner. The size of the red contour appears small in some cases, this is however not a problem since these contours are really

just the peak of the beam over our adopted "threshold". The right panel shows the spectrum of each source extracted at the peak pixel, given unresolved sources. The blue spectrum corresponds to a velocity resolution of $\sim 100\ \mathrm{km\,s^{-1}}$ while the orange spectrum corresponds to the velocity resolution matching that of the left panel. In cases where these two are the same, only the blue lines are shown. The FWHM and redshift of each candidate are added in the top left corners, and the source name (used in Tables A.1 and A.1) and reliability measurement are included in the top right corner.

Table A.1 lists each candidate source, divided according to the three fields (COSMOS, GOODS-N, EGS/AEGIS) with their RA and Dec, central frequency, flux, FWHM, SNR, and their completeness and reliability measures. Table A.1 lists the potential optical counterparts with their IDs, RA and Dec, redshift, and angular separation. Redshifts extracted from the 3D-HST/CANDELS catalogs are photometric redshifts, except where otherwise noted.

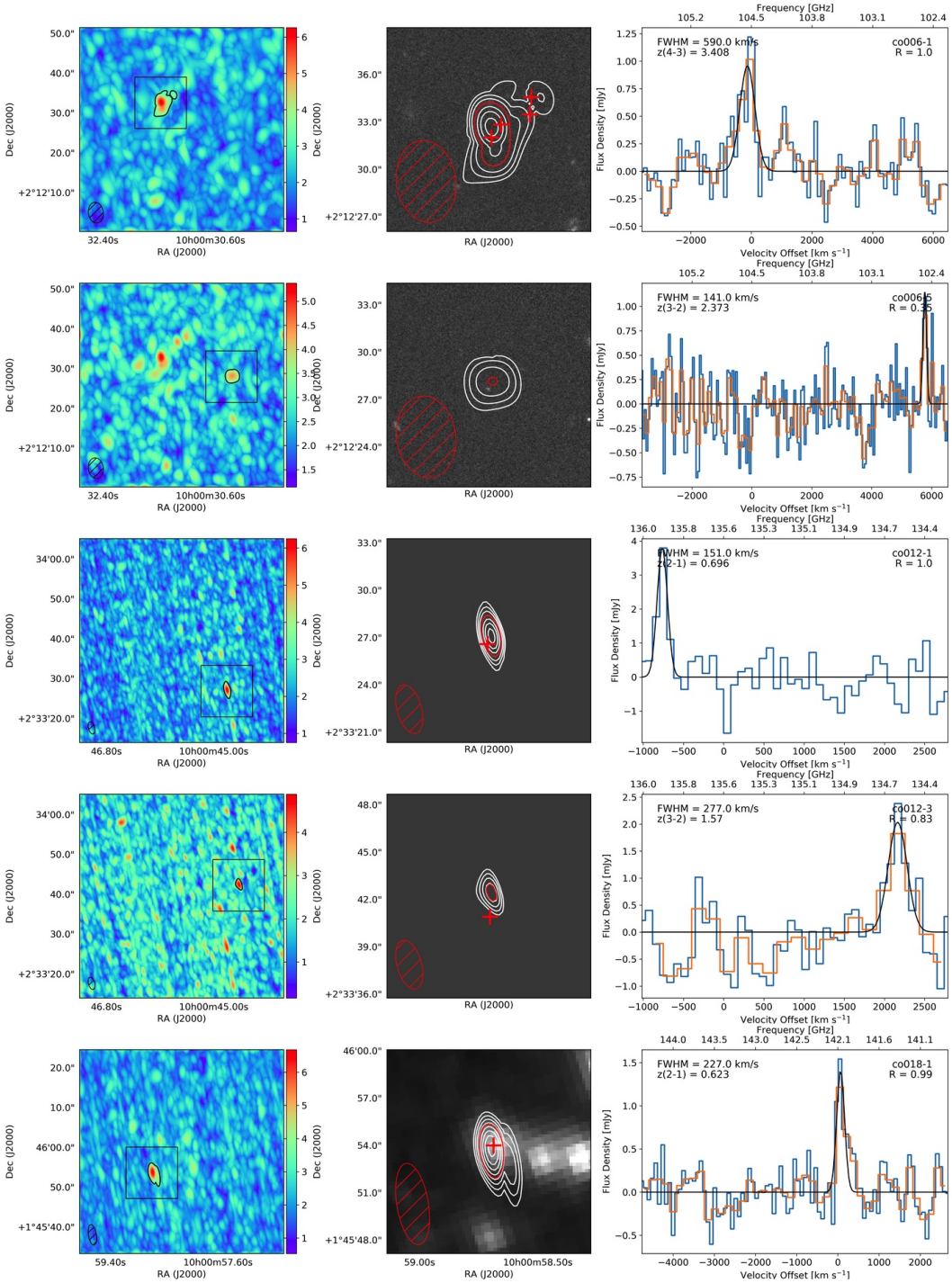
FWHM = 590.0 km/s
z(4-3) = 3.408
co006-1
R = 1.0
FWHM = 141.0 km/s
z(3-2) = 2.373
co006-5
R = 0.35
FWHM = 151.0 km/s
z(2-1) = 0.696
co012-1
R = 1.0
FWHM = 277.0 km/s
z(3-2) = 1.57
co012-3
R = 0.83
FWHM = 227.0 km/s
z(2-1) = 0.623
co018-1
R = 0.99
Frequency [GHz]
Velocity Offset [km s^{-1}]
Flux Density [mJy]
Dec (J2000)
RA (J2000)

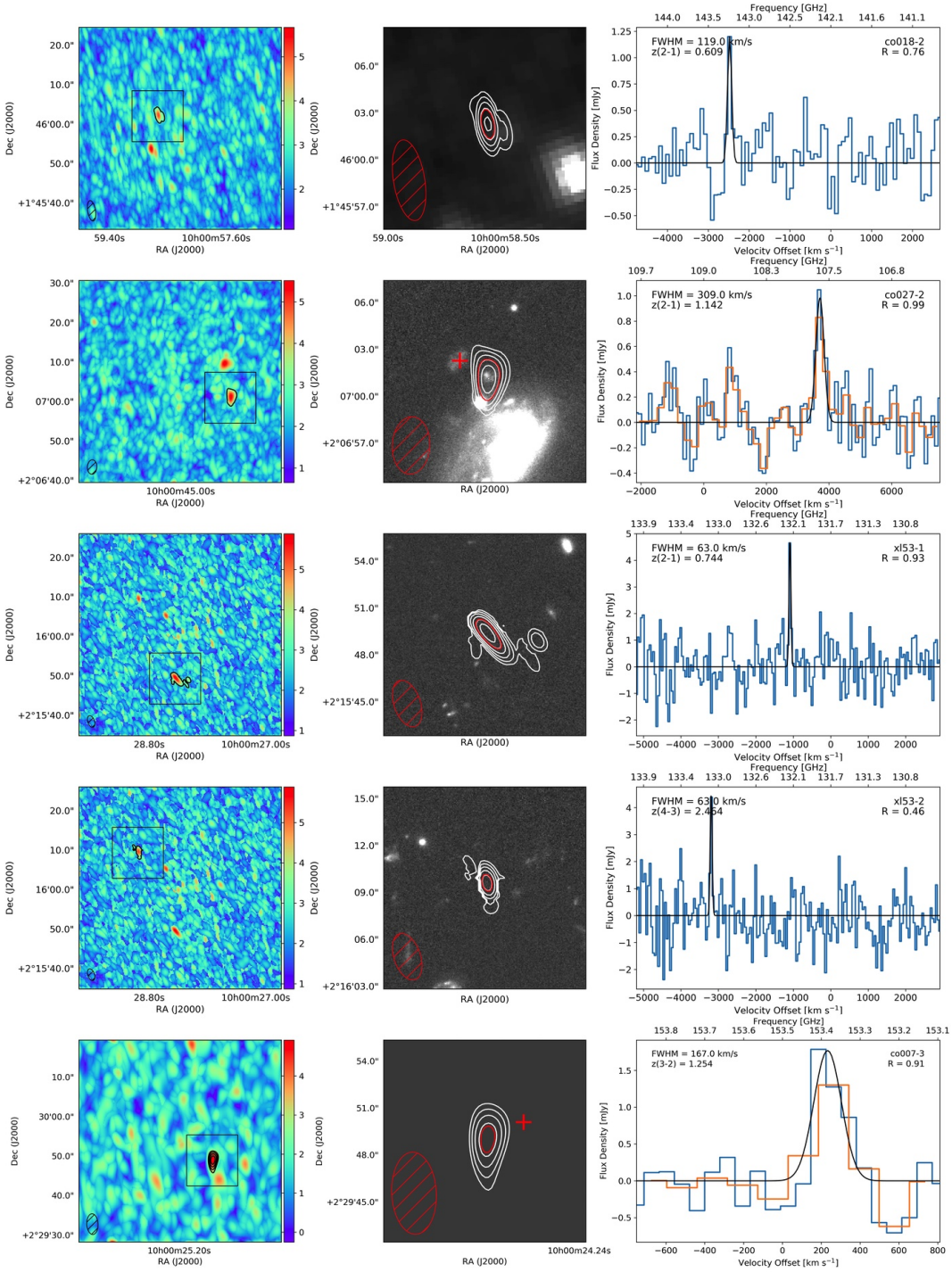
Dec (J2000)
RA (J2000)
Frequency [GHz]
Flux Density [mJy]
Velocity Offset [km s^{-1}]
FWHM = 119.0 km/s
z(2-1) = 0.609
co018-2
R = 0.76
FWHM = 309.0 km/s
z(2-1) = 1.142
co027-2
R = 0.99
FWHM = 63.0 km/s
z(2-1) = 0.744
xl53-1
R = 0.93
FWHM = 6310 km/s
z(4-3) = 2.454
xl53-2
R = 0.46
FWHM = 167.0 km/s
z(3-2) = 1.254
co007-3
R = 0.91

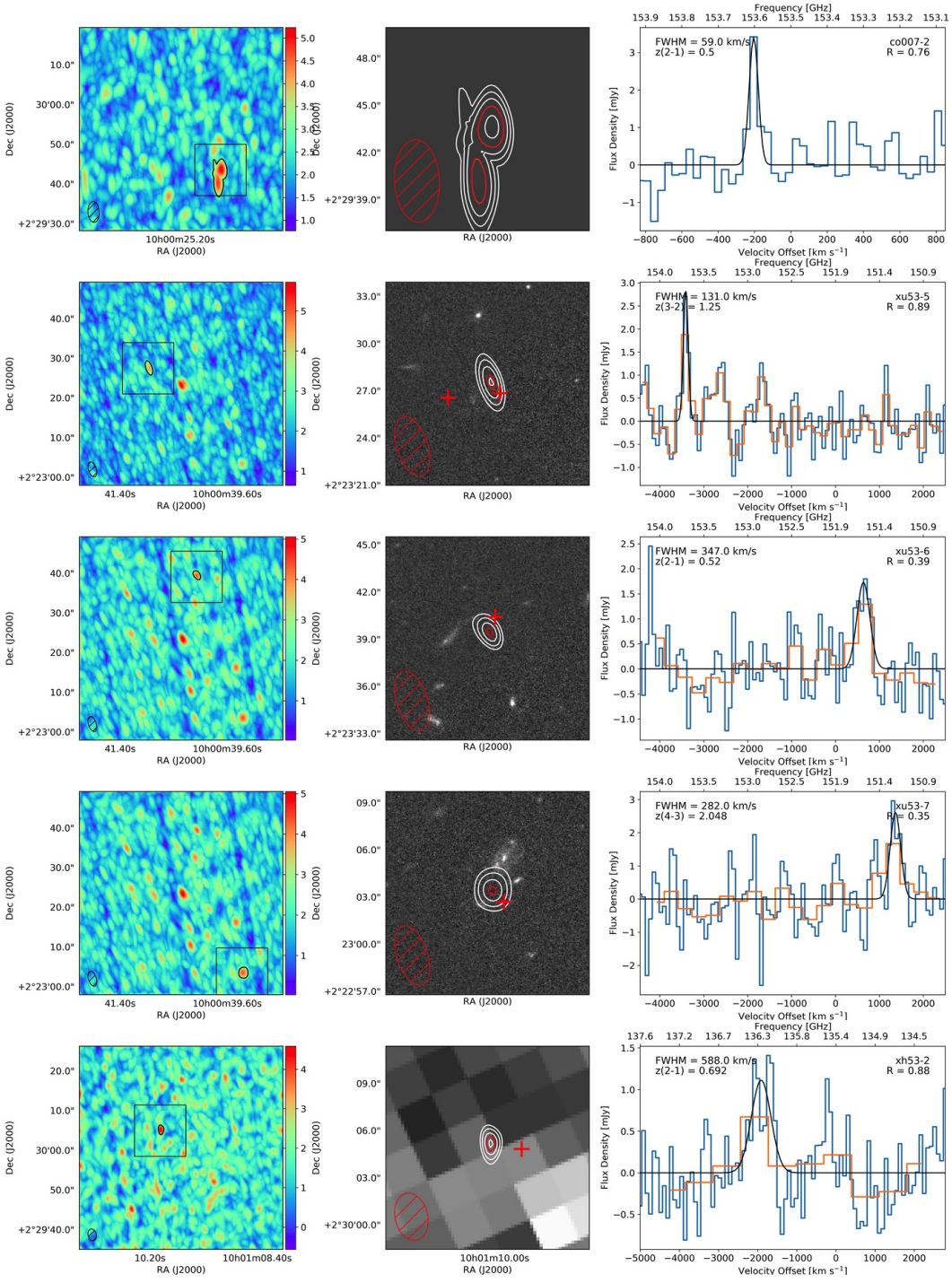
Frequency [GHz]
FWHM = 59.0 km/s
z(2-1) = 0.5
co007-2
R = 0.76
Flux Density [mJy]
Velocity Offset [km s^{-1}]
FWHM = 131.0 km/s
z(3-2) = 1.25
xu53-5
R = 0.89
FWHM = 347.0 km/s
z(2-1) = 0.52
xu53-6
R = 0.39
FWHM = 282.0 km/s
z(4-3) = 2.048
xu53-7
R = 0.35
FWHM = 588.0 km/s
z(2-1) = 0.692
xh53-2
R = 0.88
Dec (J2000)
RA (J2000)

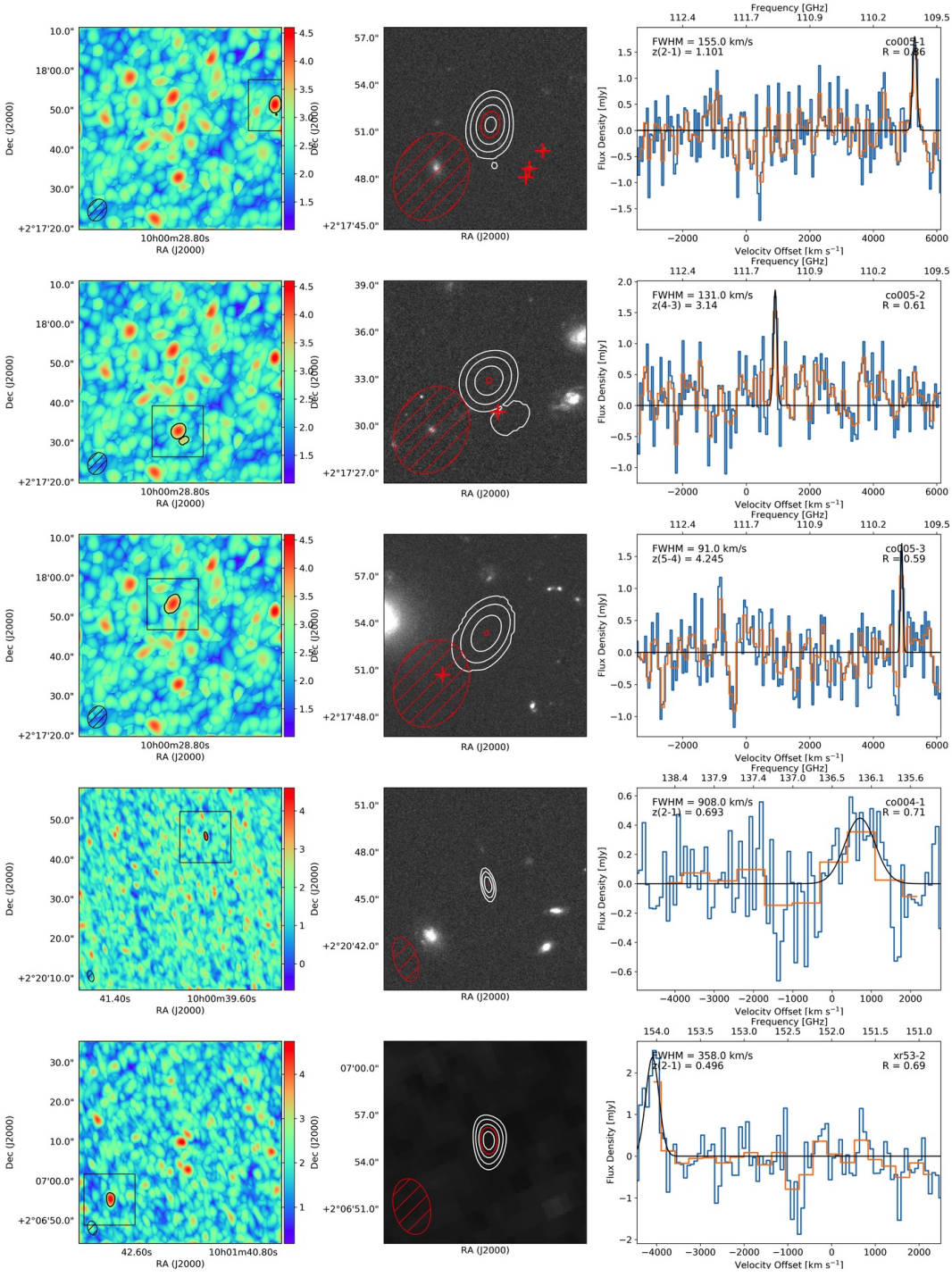
Frequency [GHz]
FWHM = 155.0 km/s
z(2-1) = 1.101
co001-1
R = 0.86
Flux Density [mJy]
Velocity Offset [km s^{-1}]
Dec (J2000)
RA (J2000)
FWHM = 131.0 km/s
z(4-3) = 3.14
co005-2
R = 0.61
FWHM = 91.0 km/s
z(5-4) = 4.245
co005-3
R = 0.59
FWHM = 908.0 km/s
z(2-1) = 0.693
co004-1
R = 0.71
FWHM = 358.0 km/s
z(2-1) = 0.496
xr53-2
R = 0.69

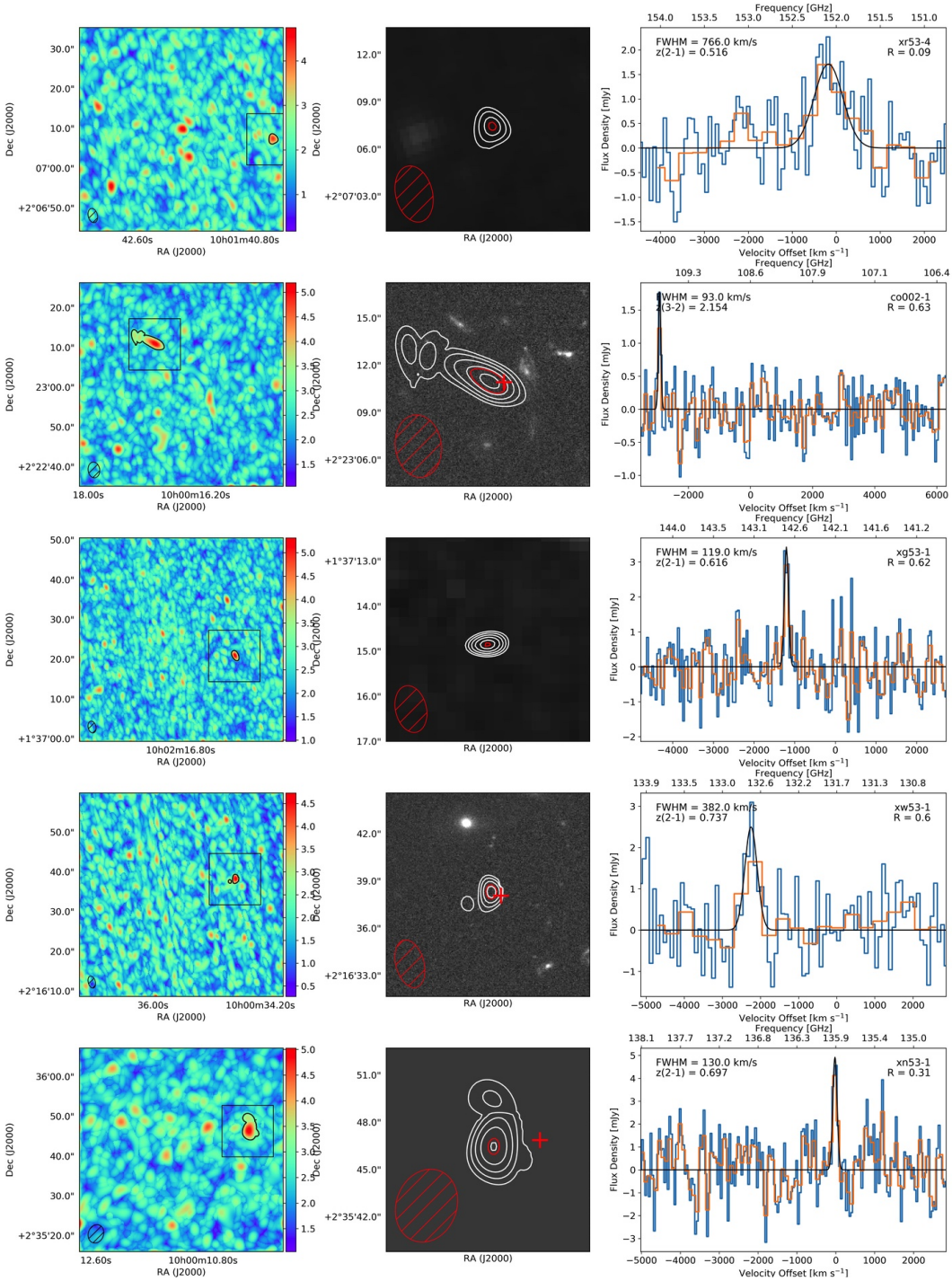
Frequency [GHz]
FWHM = 766.0 km/s
z(2-1) = 0.516
xr53-4
R = 0.09
Flux Density [mJy]
Velocity Offset [km s^{-1}]
FWHM = 93.0 km/s
z(3-2) = 2.154
co002-1
R = 0.63
FWHM = 119.0 km/s
z(2-1) = 0.616
xg53-1
R = 0.62
FWHM = 382.0 km/s
z(2-1) = 0.737
xw53-1
R = 0.6
FWHM = 130.0 km/s
z(2-1) = 0.697
xn53-1
R = 0.31
Dec (J2000)
RA (J2000)

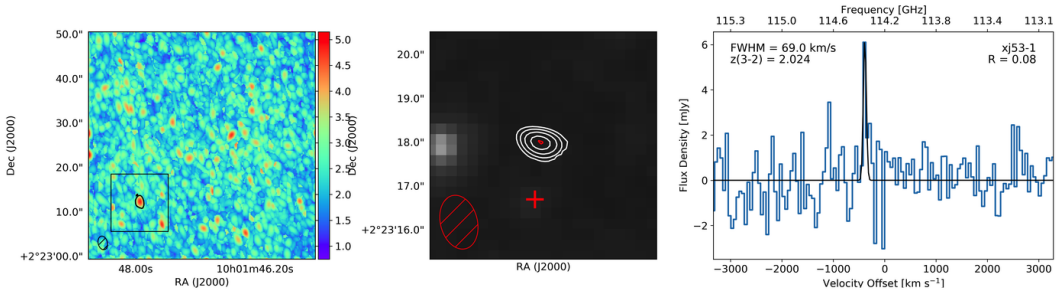

Figure A.1: All candidate CO sources detected in the COSMOS field.

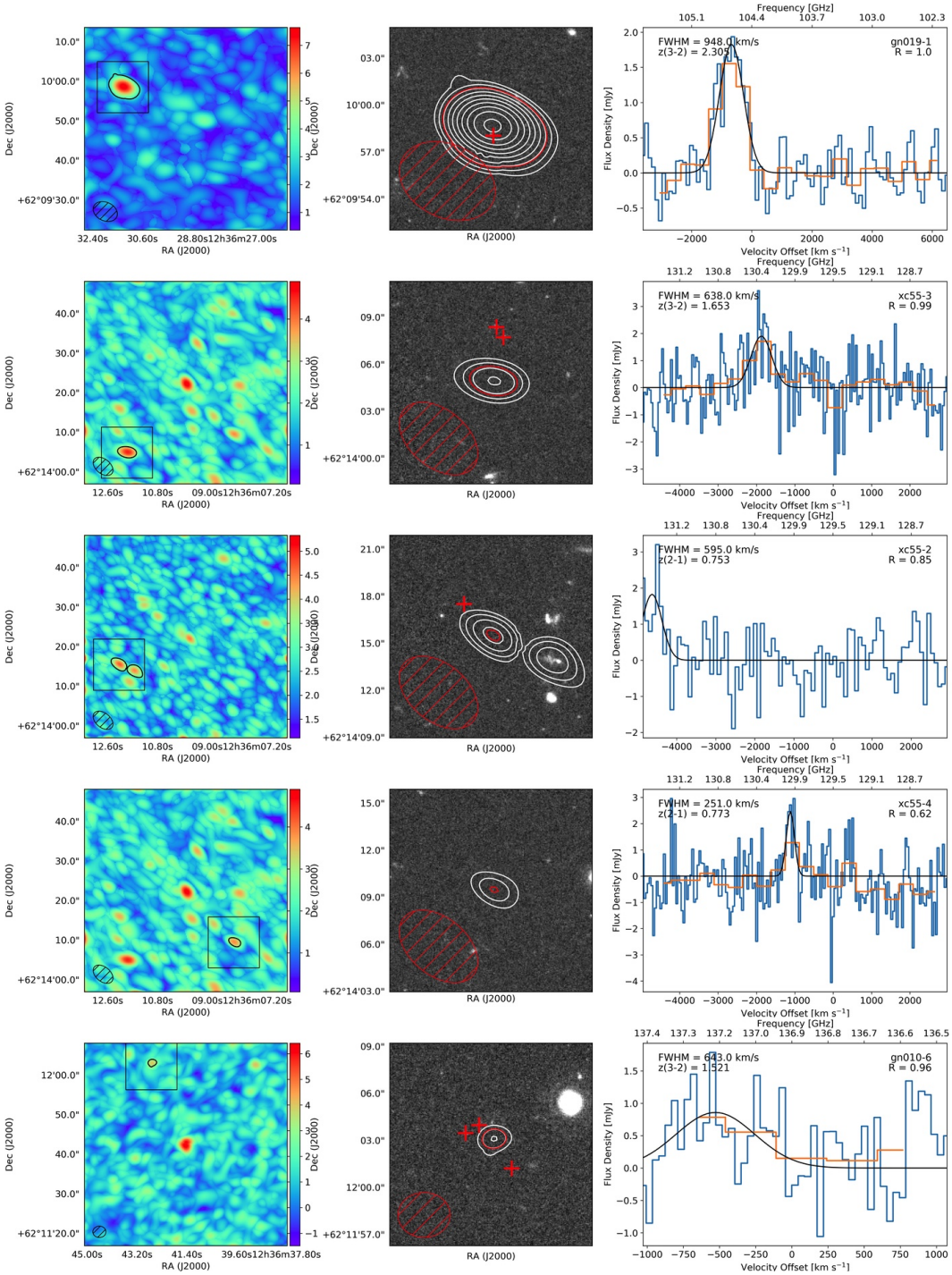
Dec (J2000)
RA (J2000)
Frequency [GHz]
Flux Density [mJy]
Velocity Offset [km s^{-1}]
FWHM = 948.0 km/s
z(3-2) = 2.305
gn019-1
R = 1.0
FWHM = 638.0 km/s
z(3-2) = 1.653
xc55-3
R = 0.99
FWHM = 595.0 km/s
z(2-1) = 0.753
xc55-2
R = 0.85
FWHM = 251.0 km/s
z(2-1) = 0.773
xc55-4
R = 0.62
FWHM = 643.0 km/s
z(3-2) = 1.521
gn010-6
R = 0.96

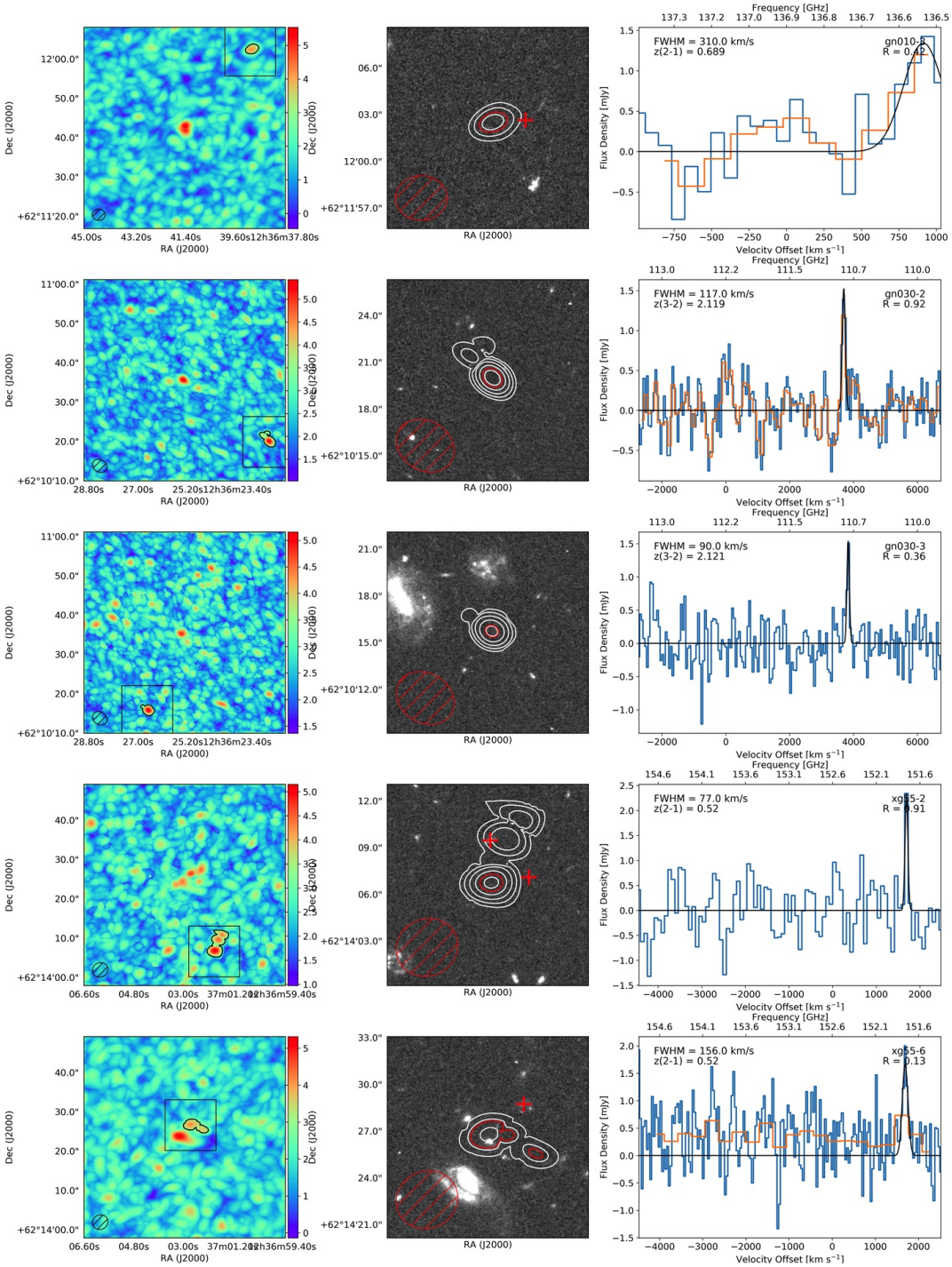
Frequency [GHz]
FWHM = 310.0 km/s
z(2-1) = 0.689
gn010-3
R = 0.42
Flux Density [mJy]
Velocity Offset [km s^{-1}]
FWHM = 117.0 km/s
z(3-2) = 2.119
gn030-2
R = 0.92
FWHM = 90.0 km/s
z(3-2) = 2.121
gn030-3
R = 0.36
FWHM = 77.0 km/s
z(2-1) = 0.52
xg155-2
R = 0.91
FWHM = 156.0 km/s
z(2-1) = 0.52
xg155-6
R = 0.13
RA (J2000)
Dec (J2000)

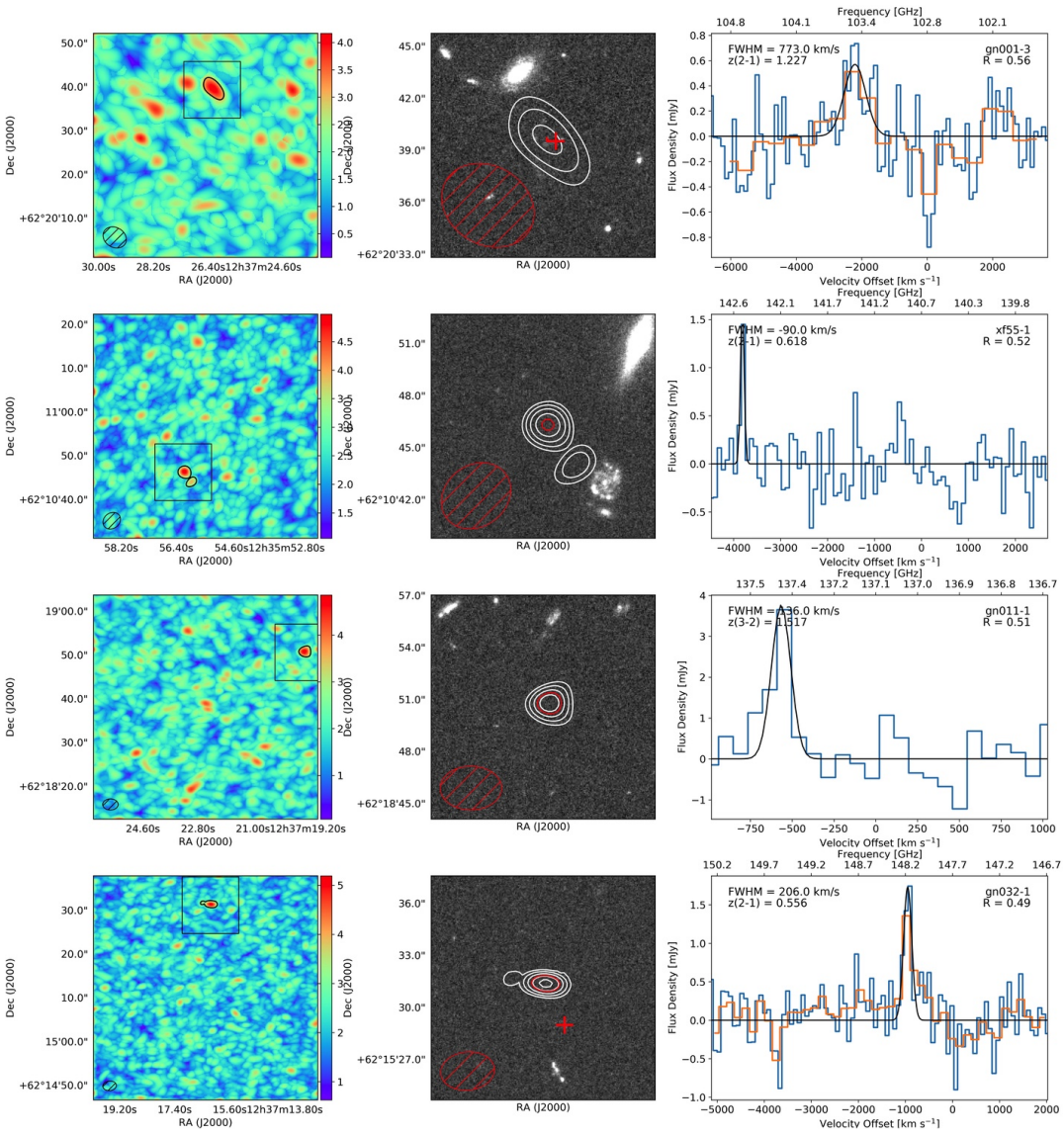
Dec (J2000)
RA (J2000)
Frequency [GHz]
Flux Density [mJy]
Velocity Offset [km s^{-1}]
FWHM = 773.0 km/s
z(2-1) = 1.227
gn001-3
R = 0.56
FWHM = -90.0 km/s
z(2-1) = 0.618
xf55-1
R = 0.52
FWHM = 436.0 km/s
z(3-2) = 1.917
gn011-1
R = 0.51
FWHM = 206.0 km/s
z(2-1) = 0.556
gn032-1
R = 0.49

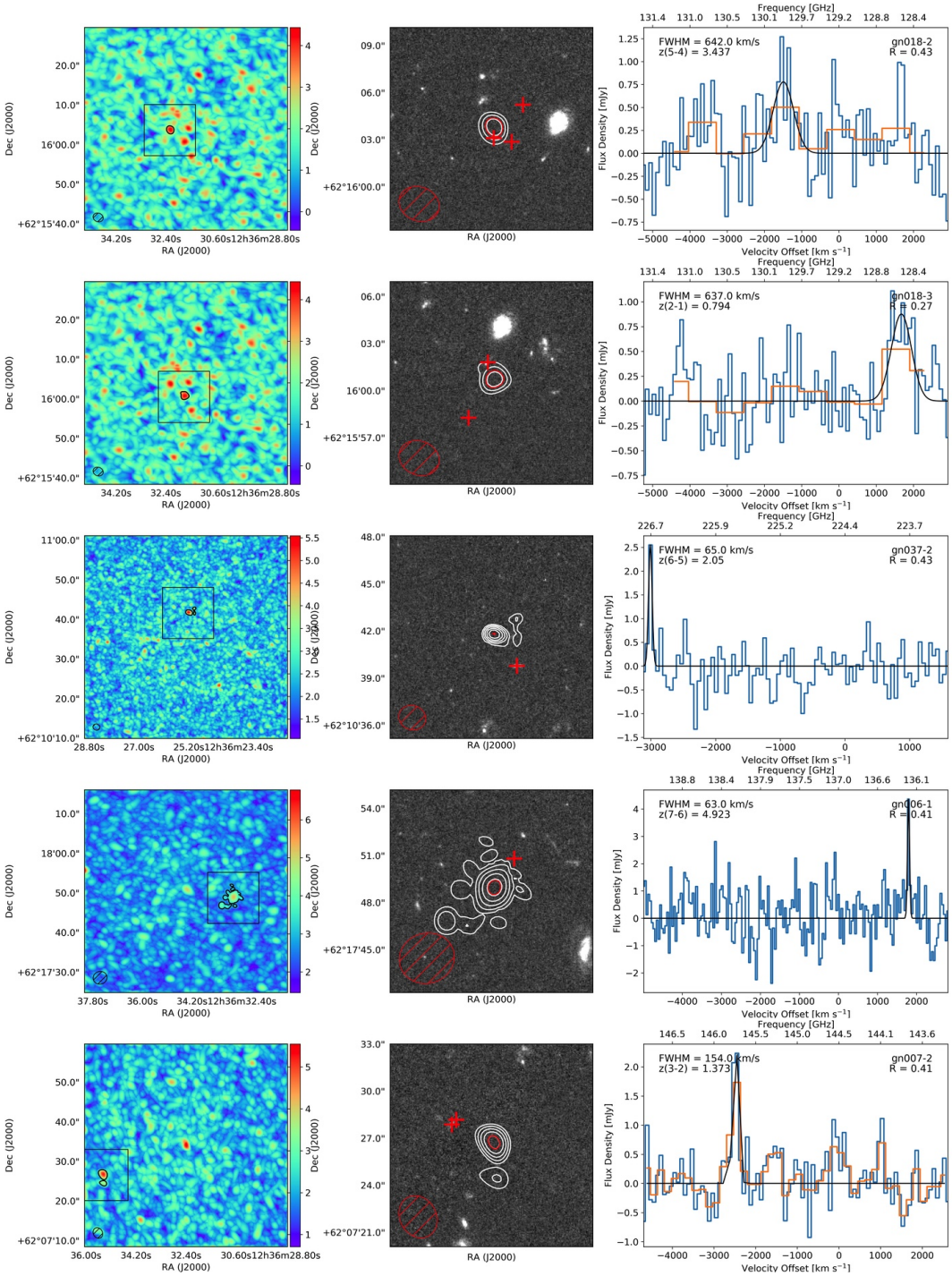
FWHM = 642.0 km/s
z(5-4) = 3.437
gn018-2
R = 0.43
FWHM = 637.0 km/s
z(2-1) = 0.794
gn018-3
R = 0.27
FWHM = 65.0 km/s
z(6-5) = 2.05
gn037-2
R = 0.43
FWHM = 63.0 km/s
z(7-6) = 4.923
gn006-1
R = 0.41
FWHM = 154.0 km/s
z(3-2) = 1.373
gn007-2
R = 0.41
Flux Density [mJy]
Velocity Offset [km s^{-1}]
Frequency [GHz]
RA (J2000)
Dec (J2000)

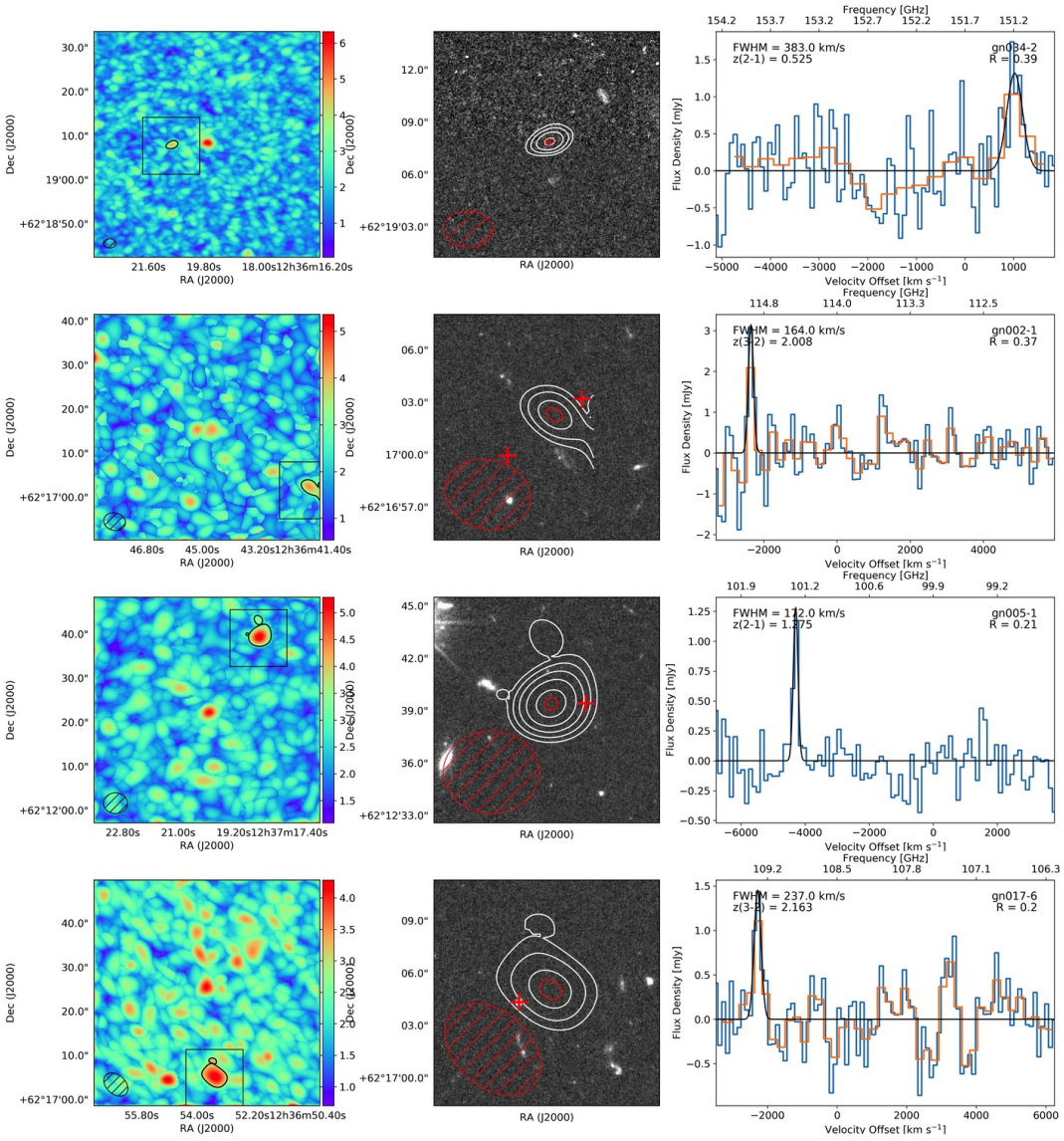
Dec (J2000)
RA (J2000)
Frequency [GHz]
Flux Density [mJy]
Velocity Offset [km s^{-1}]
FWHM = 383.0 km/s
z(2-1) = 0.525
gn034-2
R = 0.39
FWHM = 164.0 km/s
z(3-2) = 2.008
gn002-1
R = 0.37
FWHM = 172.0 km/s
z(2-1) = 1.275
gn005-1
R = 0.21
FWHM = 237.0 km/s
z(3-2) = 2.163
gn017-6
R = 0.2

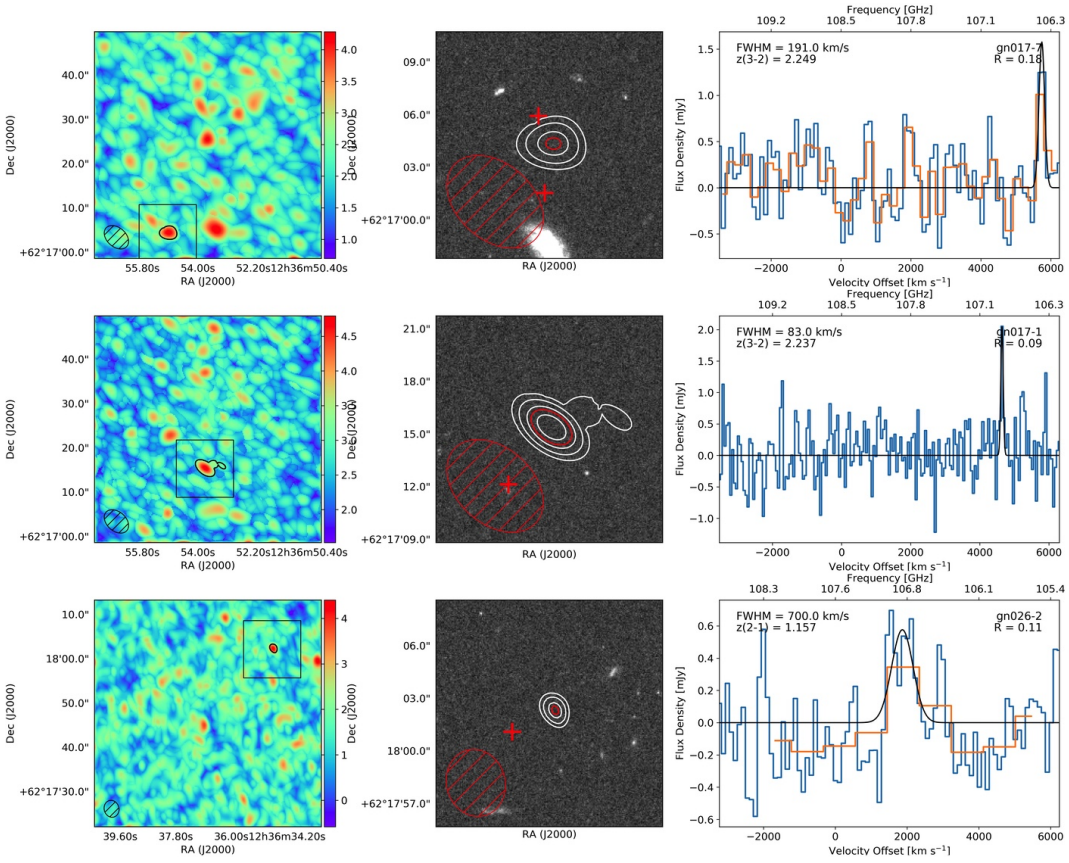

Figure A.2: All candidate CO sources detected in the GOODS-N field.

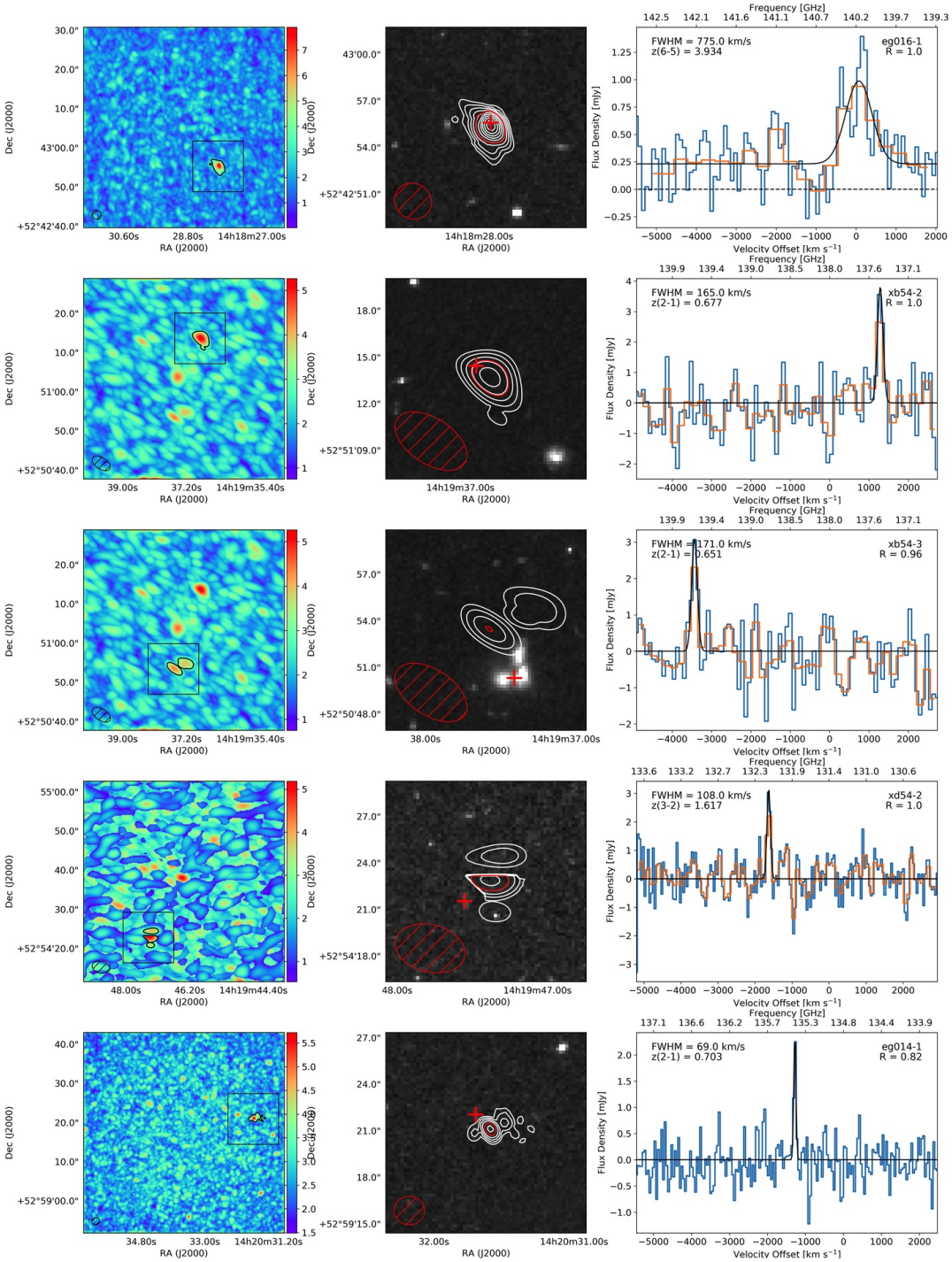
Dec (J2000)
RA (J2000)
Frequency [GHz]
Flux Density [mJy]
Velocity Offset [km s^{-1}]
FWHM = 775.0 km/s
z(6-5) = 3.934
eg016-1
R = 1.0
FWHM = 165.0 km/s
z(2-1) = 0.677
xb54-2
R = 1.0
FWHM = 171.0 km/s
z(2-1) = 0.651
xb54-3
R = 0.96
FWHM = 108.0 km/s
z(3-2) = 1.617
xd54-2
R = 1.0
FWHM = 69.0 km/s
z(2-1) = 0.703
eg014-1
R = 0.82

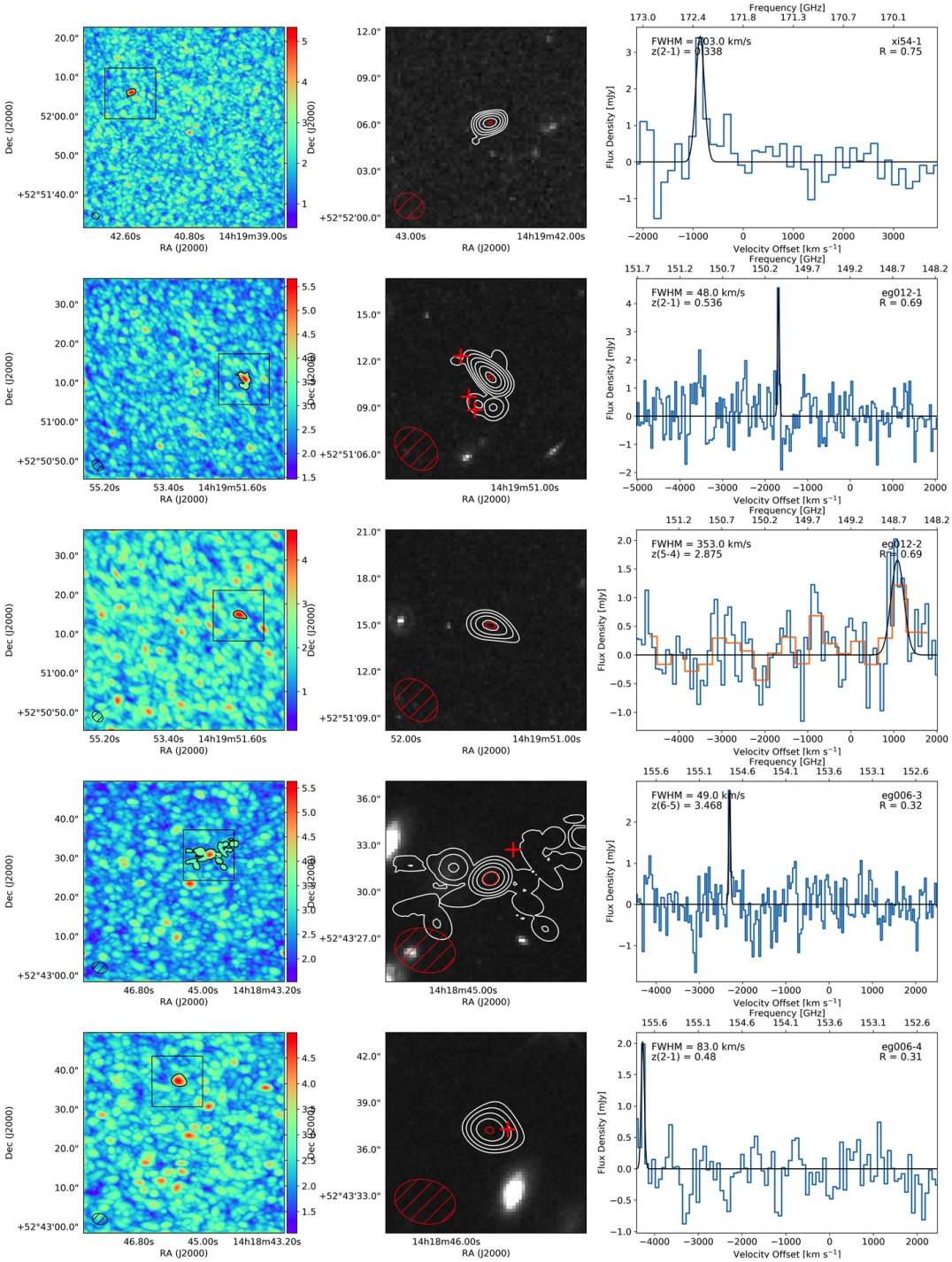
Frequency [GHz]
FWHM = 703.0 km/s
z(2-1) = 0.338
xi54-1
R = 0.75
Flux Density [mJy]
Velocity Offset [km s^{-1}]
FWHM = 48.0 km/s
z(2-1) = 0.536
eg012-1
R = 0.69
FWHM = 353.0 km/s
z(5-4) = 2.875
eg012-2
R = 0.69
FWHM = 49.0 km/s
z(6-5) = 3.468
eg006-3
R = 0.32
FWHM = 83.0 km/s
z(2-1) = 0.48
eg006-4
R = 0.31
Dec (J2000)
RA (J2000)

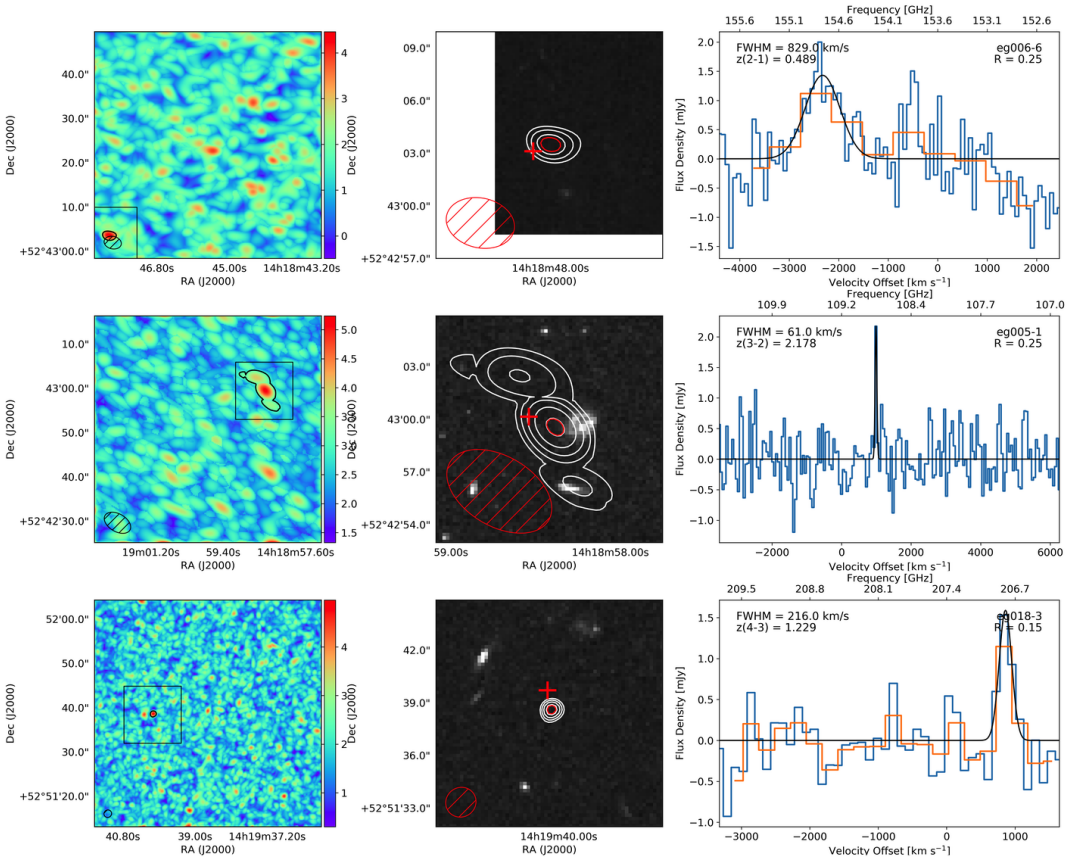

Figure A.3: All candidate CO sources detected in the EGS/AEGIS field.

ID	RA (J2000.0)	Dec (J2000.0)	Frequency (GHz)	Flux (Jy km s^{-1})	FWHM (km s^{-1})	SNR	Comp.	Rel.
co006-1	10h0m31.44	2d12m32.51s	104.582	0.599 ± 0.139	590 ± 104	6.26	0.8209	1.00
co006-5	10h0m30.25	2d12m27.91s	102.524	0.172 ± 0.066	141 ± 41	4.48	0.1973	0.35
co012-1	10h0m44.78	2d33m26.80s	135.900	0.613 ± 0.146	151 ± 27	6.25	0.7720	1.00
co012-3	10h0m44.58	2d33m42.20s	134.577	0.599 ± 0.199	277 ± 69	4.88	0.7510	0.83
co018-1	10h0m58.71	1d45m53.60s	142.039	0.341 ± 0.082	227 ± 41	6.68	0.9219	0.99
co018-2	10h0m58.59	1d46m2.000s	143.244	0.152 ± 0.047	119 ± 27	5.15	0.0968	0.76
co027-2	10h0m44.16	2d07m00.93s	107.631	0.323 ± 0.091	309 ± 66	5.50	0.4237	0.99
xl53-1	10h0m28.36	2d15m49.28s	132.169	0.315 ± 0.091	63 ± 14	5.88	0.0061	0.93
xl53-2	10h0m28.99	2d16m9.28s	133.094	0.304 ± 0.107	63 ± 17	5.38	0.0053	0.46
co007-3	10h0m24.64	2d29m48.88s	153.419	0.315 ± 0.100	167 ± 40	4.92	0.4791	0.91
co007-2	10h0m24.52	2d29m43.48s	153.643	0.216 ± 0.053	59 ± 11	5.23	0.1134	0.76
xu53-5	10h0m40.93	2d23m27.44s	153.676	0.392 ± 0.127	131 ± 32	4.54	0.2351	0.89
xu53-6	10h0m40.11	2d23m39.04s	151.627	0.637 ± 0.226	347 ± 93	4.39	0.2125	0.39
xu53-7	10h0m39.35	2d23m03.24s	151.257	0.782 ± 0.298	282 ± 81	4.37	0.9045	0.35
xh53-2	10h1m10.03	2d30m04.90s	136.249	0.696 ± 0.226	588 ± 144	4.58	0.3127	0.88
co005-1	10h0m27.13	2d17m51.20s	109.715	0.297 ± 0.110	155 ± 43	4.60	0.4130	0.86
co005-2	10h0m28.76	2d17m32.80s	111.352	0.260 ± 0.087	131 ± 33	4.34	0.3219	0.61
co005-3	10h0m28.84	2d17m53.20s	109.868	0.166 ± 0.068	91 ± 28	4.33	0.1388	0.59
co004-1	10h0m39.88	2d20m45.64s	136.209	0.432 ± 0.161	908 ± 255	4.37	0.9414	0.71
xr53-2	10h1m43.05	2d06m55.24s	154.097	0.903 ± 0.228	358 ± 68	4.72	0.0095	0.69
xr53-4	10h1m40.33	2d07m07.24s	152.109	1.395 ± 0.366	766 ± 152	4.33	1.0000	0.09
co002-1	10h0m16.88	2d23m10.77s	109.639	0.177 ± 0.053	93 ± 21	5.20	0.1609	0.63
xg53-1	10h2m15.90	1d37m20.80s	142.676	0.435 ± 0.130	119 ± 27	5.32	0.1321	0.62
xw53-1	10h0m34.62	2d16m38.12s	132.701	1.015 ± 0.339	382 ± 97	4.73	0.6225	0.60
xn53-1	10h0m10.05	2d35m46.24s	135.884	0.678 ± 0.221	130 ± 32	5.03	0.3668	0.31
xj53-1	10h1m47.94	2d23m12.00s	114.346	0.461 ± 0.160	69 ± 18	4.81	0.0150	0.08
gn019-1	12h36m31.31	62d09m58.47s	104.643	1.840 ± 0.247	948 ± 96	7.64	0.9921	1.00
xc55-3	12h36m11.91	62d14m4.80s	130.324	1.289 ± 0.406	638 ± 152	4.56	0.6556	0.99
xc55-2	12h36m12.19	62d14m15.40s	131.516	1.156 ± 0.530	595 ± 232	4.69	0.3219	0.85
xc55-4	12h36m8.04	62d14m9.40s	129.997	0.660 ± 0.267	251 ± 77	3.85	0.4351	0.62
gn010-6	12h36m42.68	62d12m2.73s	137.174	0.587 ± 0.255	642 ± 215	4.04	0.3992	0.96
gn010-3	12h36m39.05	62d12m2.13s	136.516	0.444 ± 0.184	310 ± 107	4.22	0.7280	0.42
gn030-2	12h36m22.27	62d10m19.82s	110.859	0.190 ± 0.056	117 ± 26	5.32	0.1141	0.92
gn030-3	12h36m26.67	62d10m15.62s	110.809	0.148 ± 0.055	90 ± 26	5.16	0.0420	0.36
xg55-2	12h37m1.87	62d14m06.60s	151.712	0.192 ± 0.105	76 ± 38	5.15	0.1196	0.91
xg55-6	12h37m2.73	62d14m26.60s	151.712	0.277 ± 0.111	156 ± 47	4.13	0.1225	0.13
xa55-2	12h36m59.75	62d15m9.80s	132.414	0.286 ± 0.098	28 ± 8	4.95	0.0102	0.62
gn001-3	12h37m26.27	62d20m39.29s	103.518	0.468 ± 0.191	773 ± 238	4.17	0.3312	0.56
xf55-1	12h35m56.17	62d10m46.20s	142.516	0.160 ± 0.173	90 ± 70	4.98	0.0907	0.52
gn011-1	12h37m19.35	62d18m50.56s	137.386	0.543 ± 0.147	136 ± 28	4.85	0.3091	0.51
gn032-1	12h37m16.23	62d15m31.12s	148.202	0.380 ± 0.099	206 ± 41	5.19	0.4593	0.49
gn018-2	12h36m32.26	62d16m03.68s	129.890	0.532 ± 0.225	642 ± 205	4.44	0.2299	0.43
gn018-3	12h36m31.74	62d16m00.48s	128.524	0.595 ± 0.185	637 ± 150	4.35	0.3020	0.27
gn037-2	12h36m25.23	62d10m41.60s	226.683	0.178 ± 0.049	65 ± 14	5.55	0.0113	0.43
gn006-1	12h36m32.72	62d17m48.71s	136.200	0.291 ± 0.091	63 ± 14	5.32	0.0130	0.41
gn007-2	12h36m35.41	62d07m26.53s	145.737	0.431 ± 0.123	154 ± 34	5.29	0.3004	0.41
gn034-2	12h36m20.86	62d19m07.70s	151.152	0.538 ± 0.188	383 ± 101	4.61	0.4066	0.39
gn002-1	12h36m41.56	62d17m01.56s	114.944	0.550 ± 0.158	164 ± 35	4.92	0.4009	0.37
gn021-3	12h36m0.69	62d11m26.18s	142.145	0.303 ± 0.095	58 ± 14	5.40	0.0337	0.37
gn005-1	12h37m18.40	62d12m39.04s	101.340	0.235 ± 0.073	172 ± 42	5.29	0.3657	0.21
gn017-6	12h36m53.43	62d17m04.86s	109.324	0.367 ± 0.132	237 ± 64	4.28	0.2002	0.20
gn017-7	12h36m54.98	62d17m04.26s	106.419	0.320 ± 0.150	191 ± 70	4.27	0.4470	0.18
gn017-1	12h36m53.78	62d17m15.26s	106.817	0.180 ± 0.056	83 ± 19	4.79	0.0950	0.09
gn026-2	12h36m34.68	62d18m02.12s	106.883	0.430 ± 0.168	700 ± 206	4.27	0.3453	0.11
eg016-1	14h18m27.95	52d42m55.28s	140.127	0.635 ± 0.158	791 ± 150	7.90	0.2339	1.00
xb54-2	14h19m36.82	52d51m13.60s	137.437	0.669 ± 0.248	165 ± 47	5.27	0.3905	1.00
xb54-3	14h19m37.57	52d50m53.40s	139.610	0.563 ± 0.207	171 ± 47	4.43	0.2380	0.96
xd54-2	14h19m47.37	52d54m22.80s	132.142	0.365 ± 0.112	108 ± 25	5.19	0.1105	1.00
eg014-1	14h20m31.63	52d59m20.86s	135.400	0.175 ± 0.049	69 ± 15	5.72	0.1315	0.82
xi54-1	14h19m42.46	52d52m05.81s	172.316	0.744 ± 0.182	203 ± 37	5.35	0.2646	0.75
eg012-1	14h19m51.28	52d51m10.86s	150.082	0.241 ± 0.080	48 ± 13	5.67	0.0066	0.69

Continued on next page

ID	RA (J2000.0)	Dec (J2000.0)	Frequency (GHz)	Flux (Jy km s^{-1})	FWHM (km s^{-1})	SNR	Comp.	Rel.
eg012-2	14h19m51.43	52d51m14.66s	148.704	0.622 ± 0.202	353 ± 87	4.69	0.4550	0.69
eg006-3	14h18m44.84	52d43m30.66s	154.766	0.150 ± 0.055	49 ± 14	5.29	0.0419	0.32
eg006-4	14h18m45.72	52d43m37.06s	155.775	0.184 ± 0.099	83 ± 36	5.00	0.0838	0.31
eg006-6	14h18m48.01	52d43m03.46s	154.780	1.262 ± 0.343	829 ± 170	4.46	0.8294	0.25
eg005-1	14h18m58.38	52d42m59.43s	108.805	0.141 ± 0.050	61 ± 18	5.12	0.0537	0.25
eg018-3	14h19m40.06	52d51m38.39s	206.825	0.366 ± 0.122	216 ± 54	4.96	0.8813	0.15

This table lists the properties of all candidate CO sources detected in the PHIBSS2 observations: (1) candidate ID, (2)-(3) RA and Dec of the source, (4) frequency at the line center, (5) integrated flux of the source, (6) FWHM of the source CO line, (7) signal-to-noise ratio of the source, (8) completeness measure of the detection, and (9) reliability of the detection.

Table A.1: Properties of Candidate CO Sources

ID	Counterpart	RA (J2000)	Dec (J2000)	Redshift	CO Redshift	Δr ($''$)	P_a ($''$)
co006-1	COS 2997	10h0m31.43	2d12m32.018s	3.52	3.4084	0.5	0.98
co012-1	COS 33686	10h0m44.79	2d33m26.58s	0.6961[a]	0.6964	0.2	0.99
co012-3	COS 33774	10h0m44.59	2d33m17.67s	0.67	1.5695	1.6	0.70
co018-1	COS 485943	10h0m58.69	1d45m54.00s	0.65	0.6231	0.5	0.98
co027-2	COS 1236431	10h0m44.27	2d7m2.28s	0.95	1.1419	2.1	0.42
co007-3	COS 2345915	10h0m24.48	2d29m50.10s	1.25	1.2539	2.7	0.53
xu53-5	COS 20811	10h0m40.88	2d23m26.84s	1.27	1.2502	1.0	0.89
xu53-6	COS 21168	10h0m40.08	2d23m40.42s	0.67	0.5204	1.5	0.74
xu53-7	COS 20188	10h0m39.28	2d23m2.68s	1.84	2.0481	1.2	0.84
xh53-2	COS 2307212	10h1m9.89	2d30m4.82s	0.67	0.6921	2.2	0.07
co005-1	COS 11546	10h0m26.94	2d17m48.65s	1.15	1.1012	3.8	0.23
co005-1	COS 11595	10h0m26.88	2d17m49.77s	1.34	1.1012	4.0	0.15
co005-1	COS 11549	10h0m26.96	2d17m48.09s	0.94	1.1012	4.0	0.15
co005-2	[Capak2017] 1599172	10h0m28.70	2d17m30.89s	3.11	3.1404	2.1	0.77
co005-3	COS 111603	10h0m29.02	2d17m50.71s	4.26	4.2451	3.7	0.28
co002-1	COS 20413	10h0m16.82	2d23m10.93s	1.85	2.1539	1.0	0.89
xw53-1	COS 09632	10h0m34.57	2d16m38.06s	1.69	1.6058	0.8	0.88
xn53-1	COS 2361883	10h0m9.83	2d35m46.86s	0.73	0.6966	3.4	0.08
gn019-1	GN 05359	12h36m31.29	62d9m58.04s	2.3301[b]	2.3045	0.5	0.99
xc55-3	GN 18914	12h36m11.79	62d14m7.69s	1.99	1.6534, 2.5377	3.0	0.52
xc55-3	GN 18951	12h36m11.86	62d14m8.36s	2.07	0.7690, 1.6534, 2.5377	3.6	0.30
xc55-2	GN 19484	12h36m12.44	62d14m17.49s	3.83	3.3817, 4.2577	2.7	0.61
gn010-6	GN 11844	12h36m42.78	62d12m3.97s	1.70	1.5209	1.5	0.64
gn010-6	GN 11803	12h36m42.91	62d12m3.46s	2.26	1.5209, 2.3610	1.8	0.48
gn010-6	GN 11666	12h36m42.49	62d12m1.21s	1.65	0.6806, 1.5209, 2.3610	2.0	0.36
xg55-2	GN 18857	12h37m1.50	62d14m7.10s	3.01	2.7984	2.7	0.20
xg55-2	GN 19030	12h37m1.85	62d14m9.47s	0.46	0.5196	2.9	0.08
xa55-2	GN 22587	12h36m59.50	62d15m12.37s	0.67	0.7595	3.1	0.32
gn001-3	GN 36945	12h37m26.17	62d20m39.54s	1.00	1.2270	0.8	0.96
gn018-2	GN 25624	12h36m32.24	62d16m3.10s	3.20	3.4366	0.6	0.91
gn018-2	GN 25623	12h36m32.07	62d16m2.86s	0.42	0.7749	1.5	0.42
gn018-3	GN 25587	12h36m31.77	62d16m1.81s	1.46	0.7937	1.3	0.57
gn006-1	[BIO2015] GNDV 6325117508	12h36m32.51	62d17m50.80	4.65	4.9225	1.7	0.59
gn002-1	GN 28898	12h36m41.28	62d17m3.17s	2.31	2.0084	2.6	0.62
gn002-1	GN 28704	12h36m41.89	62d16m59.95s	1.28	1.0056, 2.0084	2.8	0.56
gn005-1	GN 13860	12h37m18.08	62d12m39.43s	1.27	1.2749	2.3	0.69
gn017-6	GN 28920	12h36m53.66	62d17m4.33s	2.28	2.1630	1.7	0.87
gn017-7	GN 29041	12h36m55.07	62d17m5.93s	2.11	2.2494	1.8	0.85
gn017-7	GN 28807	12h36m55.02	62d17m1.54s	0.70	1.1663, 2.2494	2.7	0.67
gn017-1	GN 1308	12h36m54.11	62d17m12.12s	2.52	2.2373	3.9	0.31
gn026-2	GN 31722	12h36m34.99	62d18m1.07s	1.67	1.1569, 2.2353	2.4	0.31
eg016-1	EGS 33606	14h18m27.92	52d42m55.59s	4.16	3.9337	0.4	0.95
xb54-2	EGS 16871	14h19m36.89	52d51m14.44s	0.86	0.6774	1.0	0.93
xb54-3	[Barro2011] 124112	14h19m37.37	52d50m50.32s	0.68	0.6513	3.6	0.15
xd54-2	EGS 21954	14h19m47.52	52d54m21.54s	1.66	1.6168	1.9	0.69
eg014-1	EGS 10403	14h20m31.70	52d59m22.04s	1.74	1.5539	1.4	0.11
eg012-1	EGS 06254	14h19m51.40	2d51m9.70s	2.04	2.0719	1.6	0.55
eg012-1	EGS 06217	14h19m51.36	52d51m8.85s	1.62	1.3040, 2.0719	2.1	0.22
eg012-1	EGS 06392	14h19m51.46	52d51m12.31s	0.94	0.5361, 1.3040	2.2	0.15
eg006-3	EGS 23517	14h18m44.64	52d43m32.71s	3.39	3.4678	2.7	0.16
eg006-4	EGS 23149	14h18m45.56	52d43m37.29s	1.18	0.4799	1.4	0.78
eg006-6	EGS 18930	14h18m48.11	52d43m3.12s	1.4157[b]	1.2341, 1.9787	1.8	0.63
eg005-1	EGS 11013	14h18m58.51	52d43m0.15s	1.80	1.1188, 2.1781	1.4	0.92
eg018-3	EGS 16186	14h19m40.07	52d51m39.71s	1.48	0.6719, 1.2291, 1.7863	1.3	0.02

This table lists the properties of all potential optical counterparts to the candidate CO sources: (1) candidate CO source ID, (2) sesignation of the optical counterpart in the COSMOS, GOODS-N, and EGS/AEGIS catalogs, (3)-(5) RA, DEC, and redshift ("best") of the optical counterpart taken from the COSMOS, GOODS-N, and EGS/AEGIS catalogs, (6) list of redshifts corresponding to the possible CO transitions given the posterior likelihood distributions of the EAZY SED fitting, (7) projected angular separation between candidate source and the potential optical counterpart, and (8) for cases where multiple potential optical counterparts exist, we assign a probability of association that is proportional to the inverse square of the projected angular separation. Redshifts in column (5) with superscript "a" are spectroscopic redshifts, and ones with superscript "b" are grism redshifts.

Table A.2: Properties of Potential Optical Counterparts

A.2 Luminosity Function and Molecular Gas Mass Density Constraints: Tabulated Results

In this appendix, we include the 1σ ranges for each luminosity bin, for every CO luminosity function we measure, as shown in Figure 2.10. Bins are 0.5 dex wide and given in steps of 0.1 dex, therefore every 5th bin is statistically independent. We also include the molecular gas mass density constraint for each redshift bin in tabulated form.

$\log(L'_{CO})$ bin ($K\,km\,s^{-1}\,pc^{-2}$)	$\log\,\Phi$, 1σ ($Mpc^{-3}\,dex^{-1}$)	$\log(L'_{CO})$ bin ($K\,km\,s^{-1}\,pc^{-2}$)	$\log\,\Phi$, 1σ ($Mpc^{-3}\,dex^{-1}$)	$\log(L'_{CO})$ bin ($K\,km\,s^{-1}\,pc^{-2}$)	$\log\,\Phi$, 1σ ($Mpc^{-3}\,dex^{-1}$)
CO(2-1), z $\sim 0.34-0.79$		CO(2-1), z $\sim 1.01-1.27$		CO(3-2), z $\sim 1.22-1.66$	
8.4−8.9	-4.06 , -3.21	9.0−9.5	-3.59 , -2.23	9.0−9.5	-3.00 , -2.34
8.5−9.0	-3.29 , -2.63	9.1−9.6	-3.59 , -2.23	9.1−9.6	-2.99 , -2.44
8.6−9.1	-3.29 , -2.63	9.2−9.7	-3.60 , -2.75	9.2−9.7	-2.99 , -2.44
8.7−9.2	-3.29 , -2.63	9.3−9.8	-3.46 , -2.98	9.3−9.8	-3.00 , -2.52
8.8−9.3	-3.22 , -2.56	9.4−9.9	-3.71 , -3.27	9.4−9.9	-3.74 , -3.19
8.9−9.4	-3.07 , -2.52	9.5−10.0	-3.61 , -3.21	9.5−10.0	-3.79 , -3.24
9.0−9.5	-3.32 , -2.66	9.6−10.1	-3.61 , -3.21	9.6−10.1	-4.05 , -3.50
9.1−9.6	-3.21 , -2.77	9.7−10.2	-3.64 , -3.21	9.7−10.2	-4.05 , -3.50
9.2−9.7	-3.10 , -2.79	9.8−10.3	-3.98 , -3.32	9.8−10.3	-4.19 , -3.54
9.3−9.8	-3.14 , -2.82	9.9−10.4	-4.05 , -2.69	9.9−10.4	-4.37 , -3.71
9.4−9.9	-3.35 , -2.98	–	–	10.0−10.5	-4.84 , -3.98
9.5−10.0	-3.35 , -2.98	–	–	10.1−10.6	-4.84 , -3.48
9.6−10.1	-3.57 , -3.14	–	–	10.2−10.7	-4.84 , -3.48
9.7−10.2	-5.12 , -3.76	–	–	10.3−10.8	-4.84 , -3.48
9.8−10.3	-5.12 , -3.76	–	–	–	–
9.9−10.4	-5.12 , -3.76	–	–	–	–
10.0−10.5	-5.12 , -3.76	–	–	–	–
CO(3-2), z $\sim 2.01-2.31$		CO(4-3), z $\sim 1.03-1.98$		CO(4-3), z $\sim 2.05-2.59$	
9.1−9.6	-3.80,-2.44	8.8−9.3	-8.32,-6.96	9.1−9.6	-2.57,-1.21
9.2−9.7	-3.75,-3.09	8.9−9.4	-8.32,-6.96	9.2−9.7	-2.57,-1.21
9.3−9.8	-3.75,-3.09	9.0−9.5	-8.32,-6.96	9.3−9.8	-2.57,-1.21
9.4−9.9	-3.75,-3.09	9.1−9.6	-8.32,-6.96	9.4−9.9	-2.57,-1.21
9.5−10.0	-3.73,-3.25	9.2−9.7	-5.38,-4.53	9.5−10.0	-2.64,-1.79
9.6−10.1	-4.08,-3.65	9.3−9.8	-5.31,-3.95	9.6−10.1	-4.33,-3.47
9.7−10.2	-4.45,-3.90	9.4−9.9	-5.31,-3.95	9.7−10.2	-4.33,-3.47
9.8−10.3	-4.31,-3.82	9.5−10.0	-5.31,-3.95	9.8−10.3	-4.33,-3.47
9.9−10.4	-4.31,-3.82	9.6−10.1	-5.31,-3.95	9.9−10.4	-4.29,-3.64
10.0−10.5	-4.56,-3.91	9.7−10.2	-5.25,-3.90	10.0−10.5	-4.86,-4.01
10.1−10.6	-4.63,-3.27	9.8−10.3	-5.25,-3.90	10.1−10.6	-4.96,-3.60
10.2−10.7	-4.63,-3.27	9.9−10.4	-5.25,-3.90	10.2−10.7	-4.96,-3.60
10.3−10.8	-4.19,-2.83	10.0−10.5	-5.25,-3.90	10.3−10.8	-4.96,-3.60
10.4−10.9	-4.19,-2.83	10.1−10.6	-5.25,-3.90	–	–
10.5−11.0	-4.19,-2.83	–	–	–	–
10.6−11.1	-4.19,-2.83	–	–	–	–
10.7−11.2	-4.19,-2.83	–	–	–	–
CO(4-3), z $\sim 3.14-3.40$		CO(5-4), z $\sim 3.38-3.44$		CO(5-4), z $\sim 4.25-4.51$	
9.4−9.9	-4.17,-2.81	9.5−10.5	-5.28,-4.43	9.2−10.2	-4.62,-3.77
9.5−10.0	-4.17,-2.81	–	–	–	–
9.6−10.1	-4.17,-2.81	–	–	–	–
9.7−10.2	-4.17,-2.81	–	–	–	–
9.8−10.3	-4.08,-3.22	–	–	–	–
9.9−10.4	-4.48,-3.12	–	–	–	–
10.0−10.5	-4.48,-3.12	–	–	–	–
10.1−10.6	-4.48,-3.12	–	–	–	–
10.2−10.7	-4.48,-3.12	–	–	–	–
CO(6-5), z $\sim 3.47-3.93$					
8.8−9.8	-4.85,-4.0				

This table lists the (x,y) boundaries of the luminosity function bins in Figure 2.10, for each CO transition and redshift range we cover.

Table A.3: Luminosity functions of the observed CO transitions

Redshift	ρ(H2)
0.4799−1.4799	29.31−52.38
1.0056−2.0056	36.55−59.98
2.0084−3.0084	26.27−46.95
3.1404−4.1404	8.22−21.76
4.2451−5.2451	3.83−16.58

This table lists the (x,y) boundaries of the molecular gas mass density bins as a function of redshift in Figure 2.13.

Table A.4: Derived molecular gas mass density evolution constraints

Appendix B: Appendices for Chapter 3

B.1 Clump Properties

Galaxy	ID	RA (J2000)	Dec (J2000)	r_{clump} (pc)	m_{225} (abmag)	m_{336} (abmag))	m_{467} (abmag)
D13-5	1	13:30:06.993	+0:31:54.299	389 ± 14	23.78 ± 0.04	22.55 ± 0.01	21.49 ± 0.03
D13-5	2	13:30:06.976	+0:31:54.115	406 ± 9	23.58 ± 0.03	22.48 ± 0.01	21.42 ± 0.03
D13-5	3	13:30:06.961	+0:31:53.949	336 ± 17	24.38 ± 0.05	23.11 ± 0.02	22.07 ± 0.05
D13-5	4	13:30:07.018	+0:31:54.274	256 ± 7	23.85 ± 0.03	22.91 ± 0.02	22.14 ± 0.04
D13-5	5	13:30:06.910	+0:31:53.361	471 ± 29	24.37 ± 0.10	22.82 ± 0.02	21.53 ± 0.04
D13-5	6	13:30:06.930	+0:31:52.802	285 ± 28	25.24 ± 0.14	23.96 ± 0.06	22.76 ± 0.13
D13-5	7	13:30:07.077	+0:31:53.891	410 ± 22	24.04 ± 0.06	22.85 ± 0.02	21.73 ± 0.06
D13-5	8	13:30:07.125	+0:31:54.052	328 ± 10	22.29 ± 0.01	21.61 ± 0.01	21.27 ± 0.02
D13-5	9	13:30:06.985	+0:31:52.257	397 ± 13	23.41 ± 0.03	22.46 ± 0.02	21.64 ± 0.05
D13-5	10	13:30:07.030	+0:31:52.612	402 ± 37	23.79 ± 0.04	22.54 ± 0.02	21.55 ± 0.04
D13-5	11	13:30:07.056	+0:31:52.641	522 ± 93	22.87 ± 0.02	21.71 ± 0.01	20.67 ± 0.02
D13-5	12	13:30:06.999	+0:31:51.873	362 ± 14	23.83 ± 0.04	22.76 ± 0.02	22.03 ± 0.09
D13-5	13	13:30:07.029	+0:31:52.116	422 ± 11	22.42 ± 0.01	21.60 ± 0.01	20.91 ± 0.02
D13-5	14	13:30:07.064	+0:31:52.308	320 ± 11	22.54 ± 0.01	21.75 ± 0.01	21.18 ± 0.02
D13-5	15	13:30:07.052	+0:31:52.161	622 ± 36	21.20 ± 0.01	20.46 ± 0.004	19.90 ± 0.01
D13-5	16	13:30:07.085	+0:31:52.334	459 ± 19	22.69 ± 0.02	21.74 ± 0.01	21.02 ± 0.02
D13-5	17	13:30:07.066	+0:31:52.096	461 ± 33	21.82 ± 0.01	21.17 ± 0.01	20.78 ± 0.02
D13-5	18	13:30:07.088	+0:31:52.140	371 ± 19	23.24 ± 0.02	22.40 ± 0.01	21.78 ± 0.03
D15-3	1	15:34:35.452	-0:28:45.745	243 ± 6	<28.45	24.62 ± 0.04	21.83 ± 0.03
D15-3	2	15:34:35.405	-0:28:46.004	373 ± 16	24.75 ± 0.07	23.50 ± 0.02	22.29 ± 0.05
D15-3	3	15:34:35.420	-0:28:45.217	572 ± 25	24.31 ± 0.12	22.78 ± 0.02	21.35 ± 0.04
D15-3	4	15:34:35.327	-0:28:45.734	277 ± 9	25.63 ± 0.11	24.56 ± 0.06	23.69 ± 0.59
D15-3	5	15:34:35.449	-0:28:43.476	398 ± 22	24.76 ± 0.08	23.37 ± 0.02	22.43 ± 0.08
D15-3	6	15:34:35.436	-0:28:43.562	435 ± 44	24.38 ± 0.07	23.01 ± 0.02	21.97 ± 0.06
D15-3	7	15:34:35.308	-0:28:45.177	359 ± 13	24.11 ± 0.04	22.90 ± 0.02	22.01 ± 0.05
D15-3	8	15:34:35.293	-0:28:45.235	389 ± 32	23.67 ± 0.03	22.60 ± 0.01	21.88 ± 0.04
D15-3	9	15:34:35.382	-0:28:43.822	920 ± 138	23.98 ± 0.20	22.30 ± 0.04	20.74 ± 0.09
D15-3	10	15:34:35.374	-0:28:42.702	496 ± 31	23.94 ± 0.05	22.53 ± 0.02	21.58 ± 0.05
G04-1	1	4:12:19.650	-5:54:48.543	451 ± 14	23.64 ± 0.03	22.73 ± 0.01	21.57 ± 0.03
G04-1	2	4:12:19.719	-5:54:47.291	321 ± 11	23.73 ± 0.03	22.92 ± 0.02	22.20 ± 0.05
G04-1	3	4:12:19.752	-5:54:47.164	308 ± 9	23.66 ± 0.03	22.94 ± 0.02	22.36 ± 0.05
G04-1	4	4:12:19.703	-5:54:48.345	466 ± 10	22.63 ± 0.02	21.62 ± 0.01	20.41 ± 0.01
G04-1	5	4:12:19.707	-5:54:48.789	487 ± 11	22.49 ± 0.01	21.56 ± 0.01	20.46 ± 0.01
G04-1	6	4:12:19.766	-5:54:47.759	572 ± 39	22.95 ± 0.02	22.01 ± 0.01	20.98 ± 0.02
G04-1	7	4:12:19.745	-5:54:48.567	491 ± 15	22.47 ± 0.01	21.47 ± 0.01	20.52 ± 0.02
G04-1	8	4:12:19.774	-5:54:48.052	366 ± 23	23.80 ± 0.03	22.88 ± 0.02	21.90 ± 0.04
G04-1	9	4:12:19.783	-5:54:49.985	402 ± 11	23.77 ± 0.03	23.21 ± 0.02	22.55 ± 0.06
G08-5	1	8:54:18.797	+6:46:21.327	535 ± 25	22.39 ± 0.01	21.81 ± 0.01	21.20 ± 0.02
G08-5	2	8:54:18.798	+6:46:20.935	583 ± 19	22.68 ± 0.02	22.00 ± 0.01	21.26 ± 0.03
G08-5	3	8:54:18.717	+6:46:19.255	335 ± 9	24.27 ± 0.04	23.54 ± 0.02	22.77 ± 0.06

Continued on next page

Galaxy	ID	RA (J2000)	Dec (J2000)	r_{clump} (pc)	m_{225} (abmag)	m_{336} (abmag))	m_{467} (abmag)
G08-5	4	8:54:18.792	+6:46:19.894	506 ± 35	24.49 ± 0.08	22.81 ± 0.02	21.70 ± 0.03
G14-1	1	14:54:28.329	+0:44:34.584	353 ± 12	21.08 ± 0.01	20.41 ± 0.004	19.82 ± 0.01
G14-1	2	14:54:28.314	+0:44:33.917	455 ± 10	22.75 ± 0.01	22.10 ± 0.01	21.36 ± 0.02
G14-1	3	14:54:28.393	+0:44:34.258	262 ± 5	23.37 ± 0.02	22.39 ± 0.01	21.58 ± 0.02
G20-2	1	20:44:02.885	-6:46:57.221	452 ± 20	22.72 ± 0.01	22.13 ± 0.01	21.22 ± 0.02
G20-2	2	20:44:02.886	-6:46:57.506	537 ± 29	21.82 ± 0.01	21.15 ± 0.01	20.25 ± 0.01
G20-2	3	20:44:02.900	-6:46:57.535	870 ± 173	21.30 ± 0.01	20.55 ± 0.004	19.51 ± 0.01
G20-2	4	20:44:02.901	-6:46:57.766	612 ± 53	21.37 ± 0.01	20.59 ± 0.004	19.51 ± 0.01
G20-2	5	20:44:02.934	-6:46:57.367	363 ± 48	22.71 ± 0.02	21.95 ± 0.01	20.84 ± 0.02
G20-2	6	20:44:02.911	-6:46:58.218	454 ± 41	22.46 ± 0.01	21.72 ± 0.01	20.71 ± 0.02
G20-2	7	20:44:02.955	-6:46:57.455	491 ± 23	21.87 ± 0.01	21.12 ± 0.01	20.17 ± 0.01
G20-2	8	20:44:02.969	-6:46:57.253	425 ± 20	22.43 ± 0.01	21.76 ± 0.01	21.01 ± 0.02
G20-2	9	20:44:02.928	-6:46:58.409	446 ± 25	22.69 ± 0.02	21.90 ± 0.01	20.99 ± 0.02
G20-2	10	20:44:02.949	-6:46:58.266	352 ± 26	22.99 ± 0.02	22.27 ± 0.01	21.40 ± 0.02
G20-2	11	20:44:02.980	-6:46:57.528	669 ± 47	21.62 ± 0.01	20.82 ± 0.01	20.03 ± 0.01
G20-2	12	20:44:02.964	-6:46:58.029	354 ± 42	23.23 ± 0.02	22.35 ± 0.01	21.38 ± 0.03
G20-2	13	20:44:03.016	-6:46:57.556	331 ± 16	23.87 ± 0.03	23.32 ± 0.02	22.77 ± 0.09
G20-2	14	20:44:02.990	-6:46:58.564	401 ± 18	23.02 ± 0.02	22.64 ± 0.01	22.06 ± 0.04

This table lists all measured properties of the DYNAMO clumps: (1) galaxy ID, (2) clump ID, (3)-(4) RA and Dec of the clump, (5) size of the clump, and (6)-(8) results of photometry in all three HST filters with uncertainties.

Table B.1: Properties of HST-DYNAMO Galaxy Clumps

B.2 `Starburst99` Model Comparison

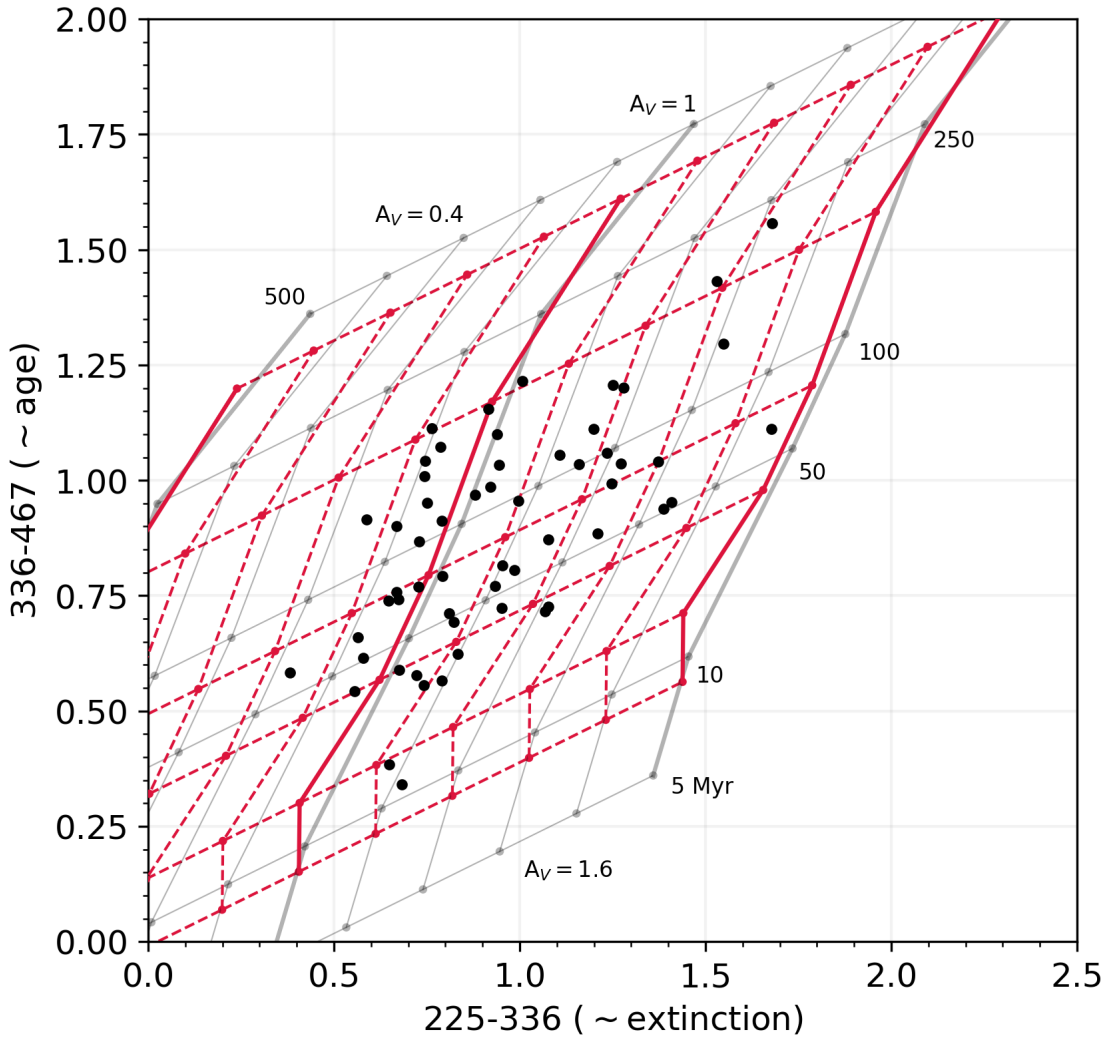

Figure B.1: A comparison of `Starburst99` models: gray lines represent a model with star formation history corresponding to a single burst with solar metallicity, and the red lines represent a model with the same star formation history, but with 40% solar metallicity. We overlay the clump colors we measure as black circles. The effect that assuming a lower metallicity has on the inferred ages and extinction of the DYNAMO clumps is minimal.

Appendix C: Appendices for Chapter 4

C.1 Channel Maps

Here we present CO(3−2) and CO(4−3) channel maps for all ALMA data used in this work. As in Figure 4.1, we show the velocity of each channel in the top right corner of each panel, and we show the circularized beam as a white circle in the bottom left corner of the first panel in each subsequent figure.

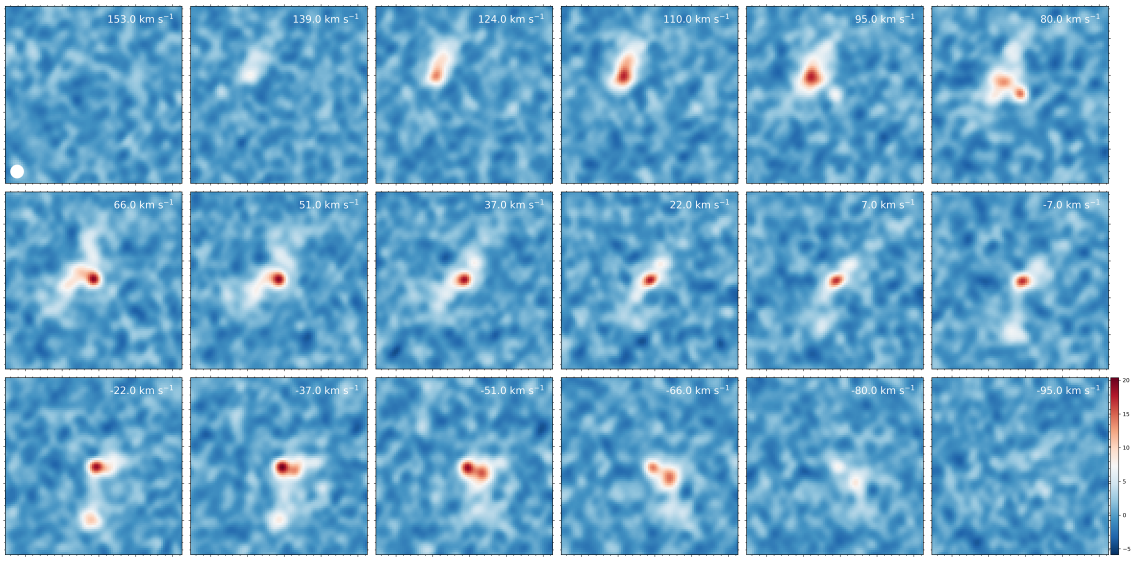

Figure C.1: DYNAMO C13-1 CO(3−2) channel maps. Each panel is centered at 13h26m39.428s, +01d30m01.40s and is 14.4 × 14.4″ in size.

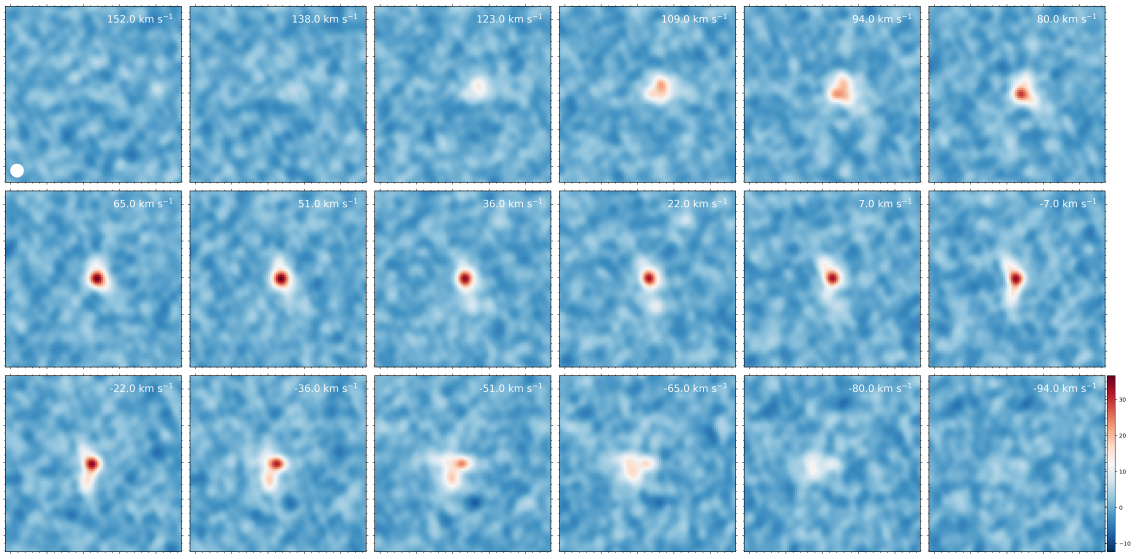

Figure C.2: DYNAMO C22-2 CO(3−2) channel maps. Each panel is centered at 22h39m49.344s, -08d04m18.11s and is 14.4 × 14.4″ in size.

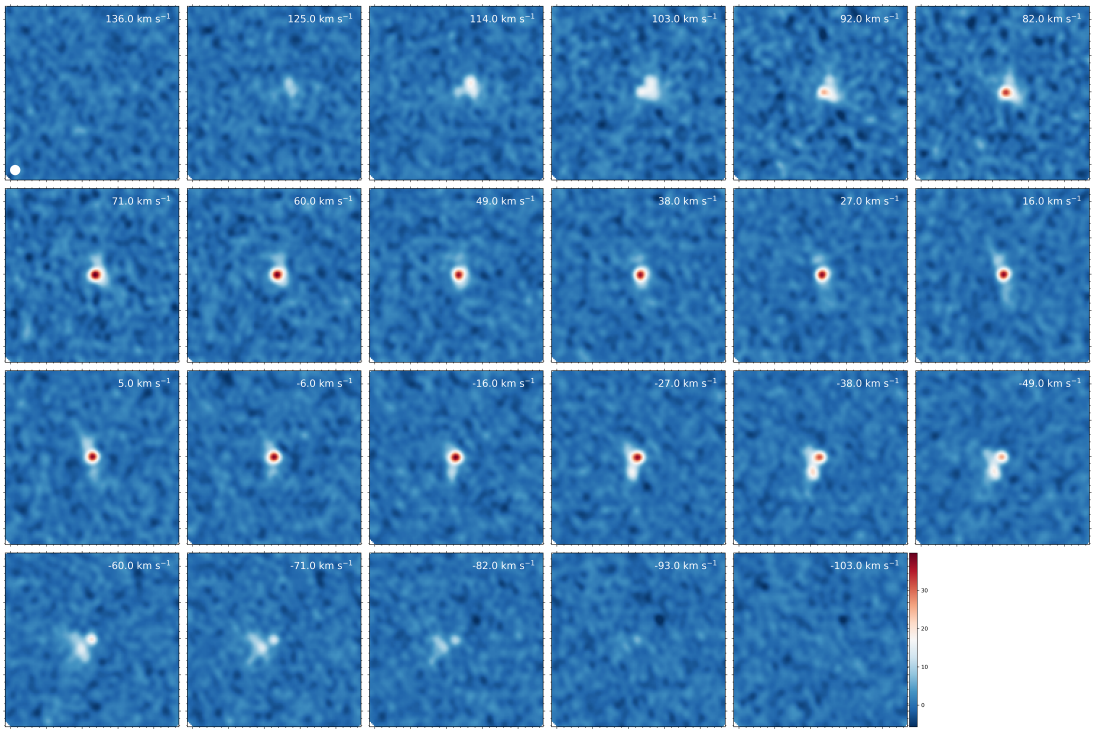

Figure C.3: DYNAMO C22-2 CO(4−3) channel maps. Each panel is centered at 22h39m49.344s, -08d04m18.11s and is 14.4 × 14.4″ in size.

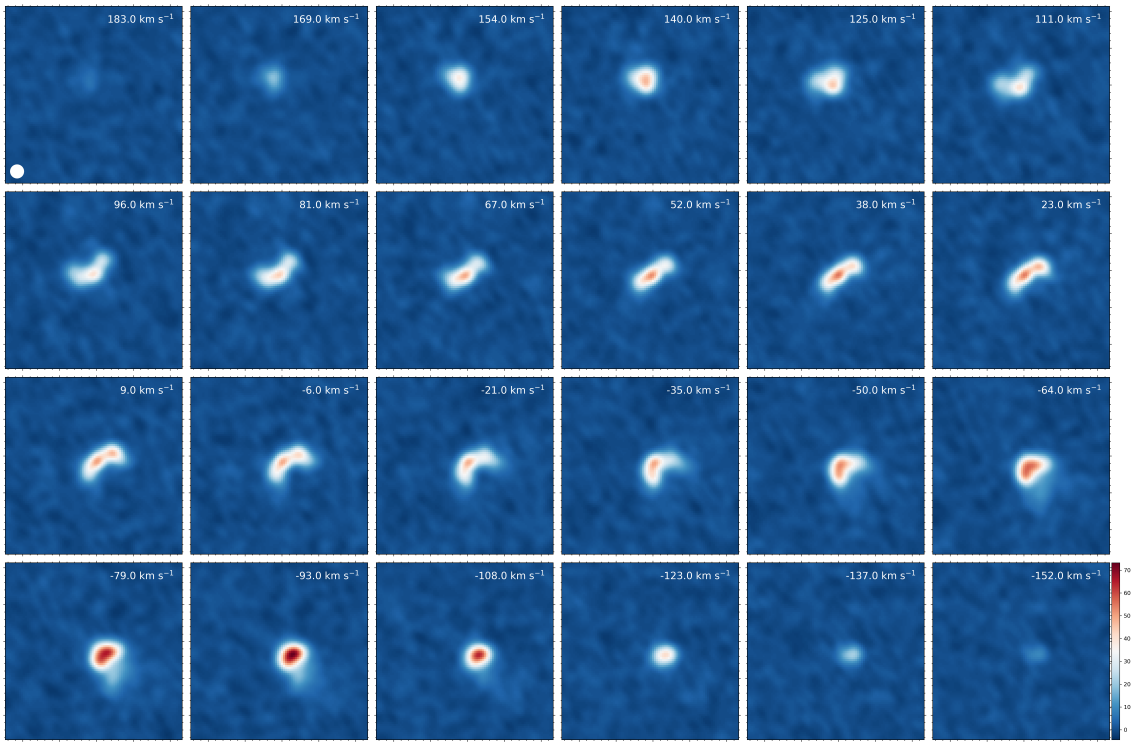

Figure C.4: DYNAMO D13-5 CO(3−2) channel maps. Each panel is centered at 13h30m07.014s, +00d31m53.20s and is 14.4 × 14.4″ in size.

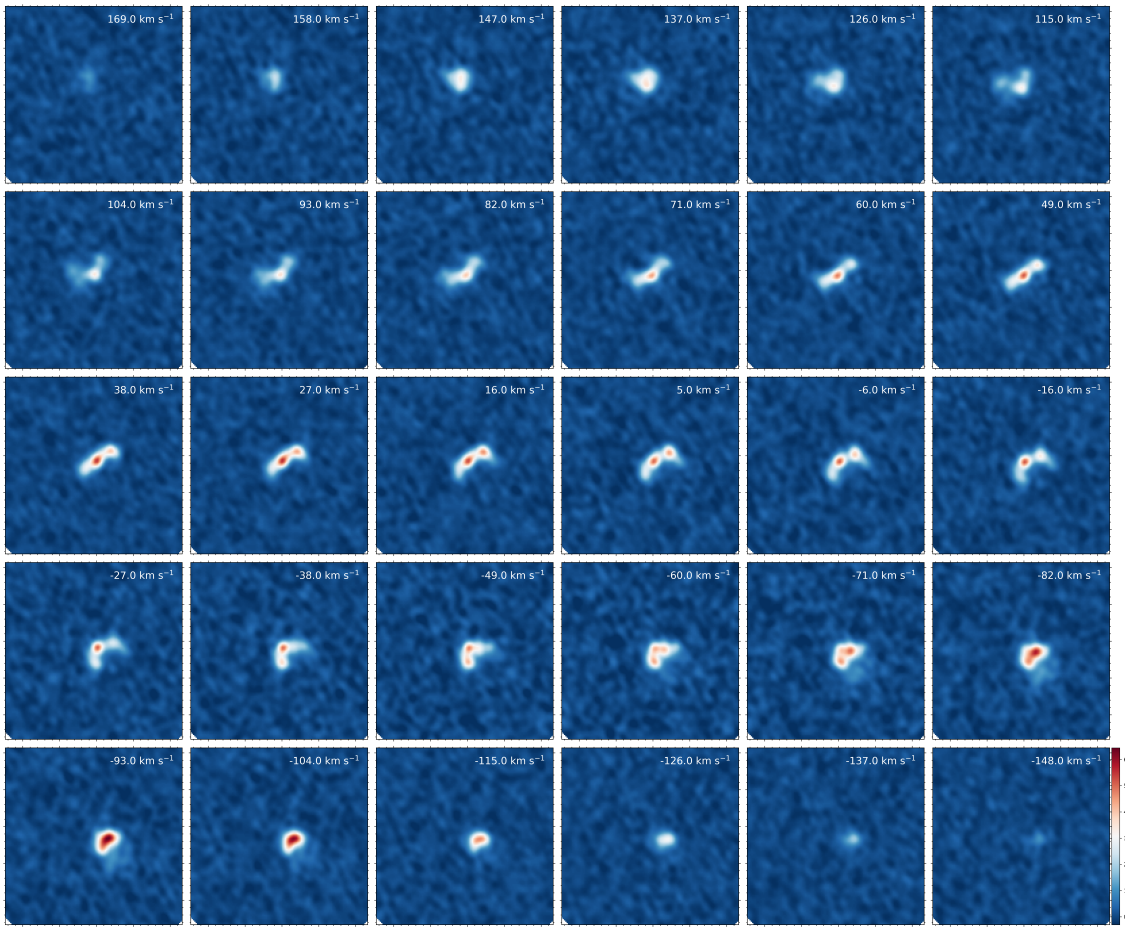

Figure C.5: DYNAMO D13-5 CO(4−3) channel maps. Each panel is centered at 13h30m07.014s, +00d31m53.20s and is 14.4 × 14.4″ in size.

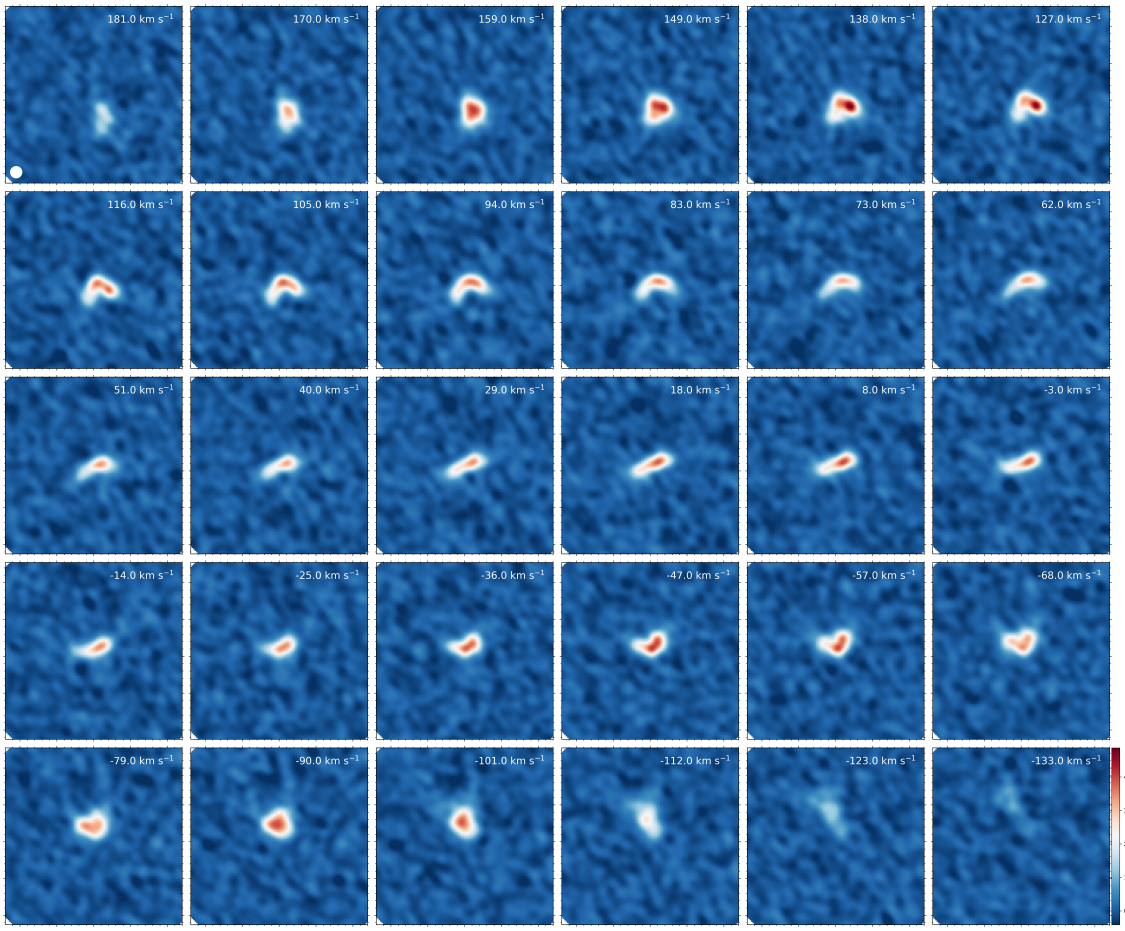

Figure C.6: DYNAMO D15-3 CO(4−3) channel maps. Each panel is centered at 15h34m35.399s, -00d28m44.56s and is 14.4 × 14.4″ in size.

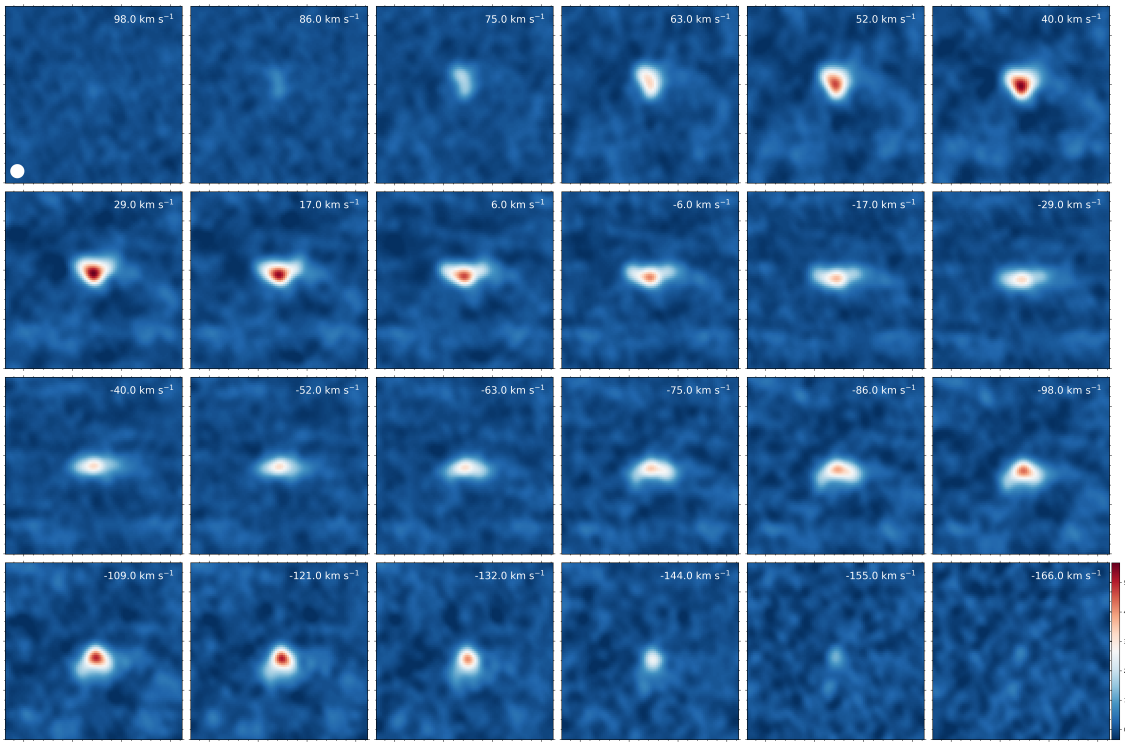

Figure C.7: DYNAMO G04-1 CO(4−3) channel maps. Each panel is centered at 04h12m19.713s, -05d54m48.62s and is 10.8 × 10.8″ in size.

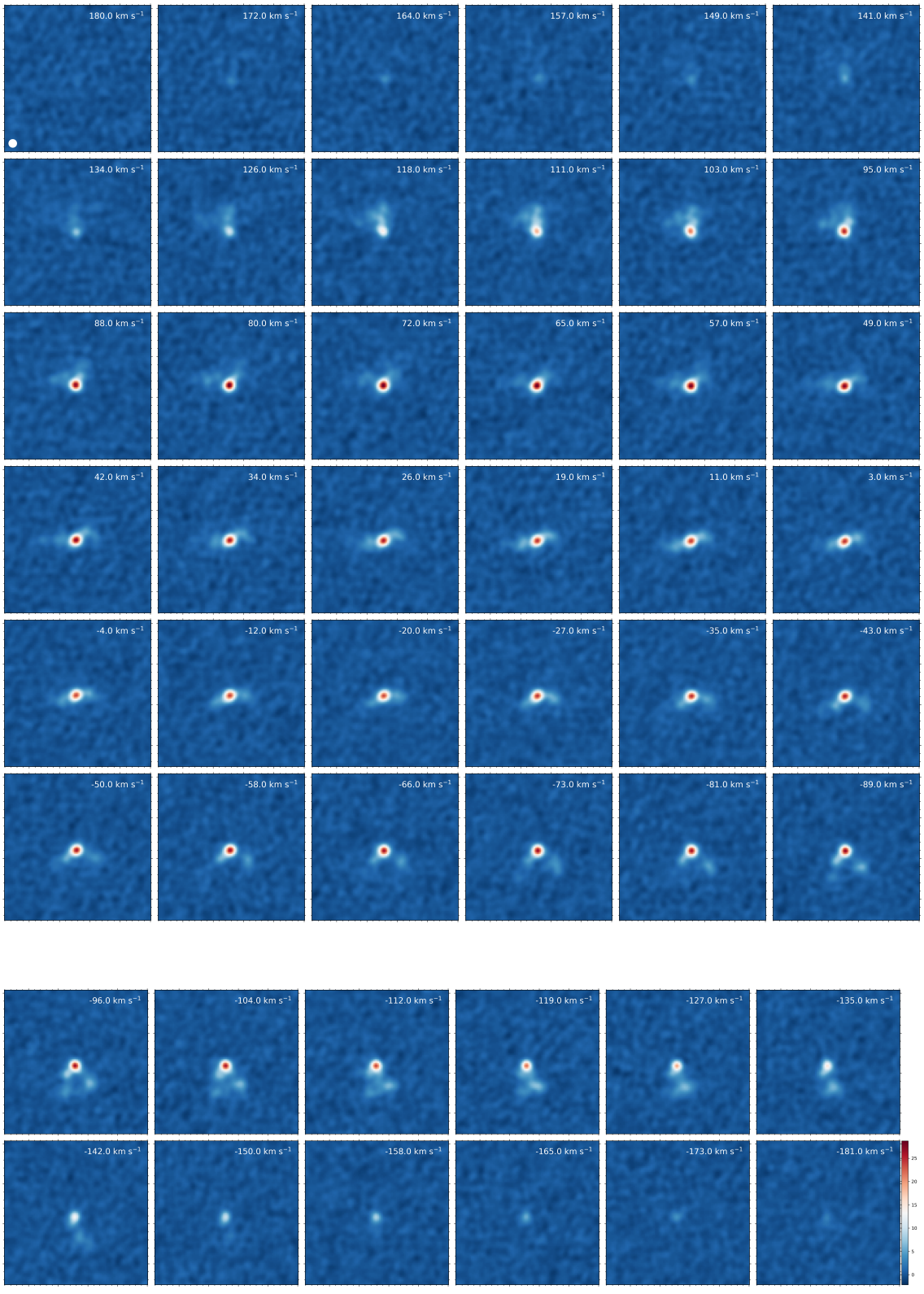

Figure C.8: DYNAMO G08-5 CO(3−2) channel maps. Each panel is centered at 08h54m18.740s, +06d46m20.55s and is 7.2″× 7.2″ in size.

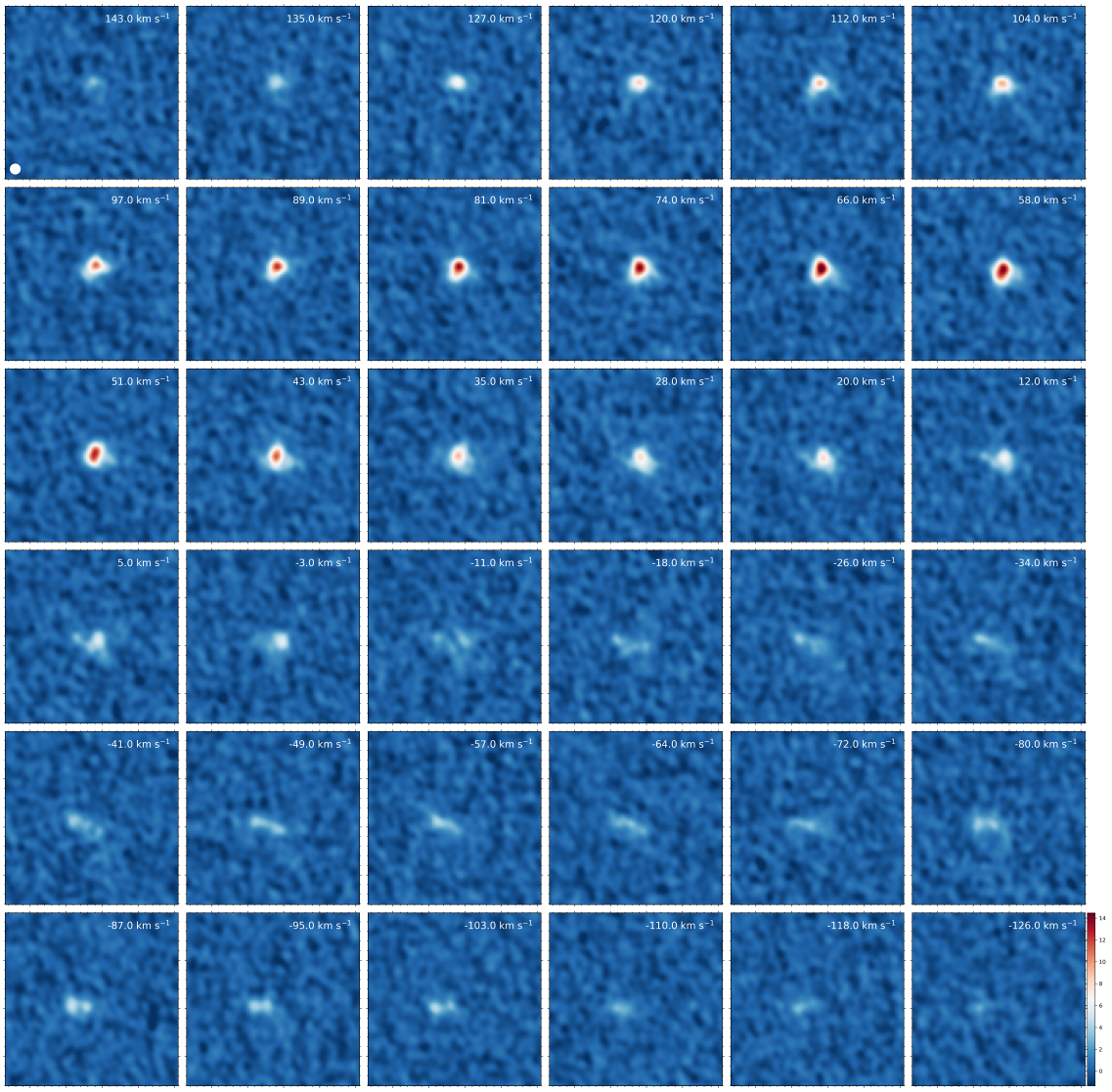

Figure C.9: DYNAMO G14-1 CO(3−2) channel maps. Each panel is centered at 14h54m28.329s, +00d44m34.37s and is $7.2'' \times 7.2''$ in size.

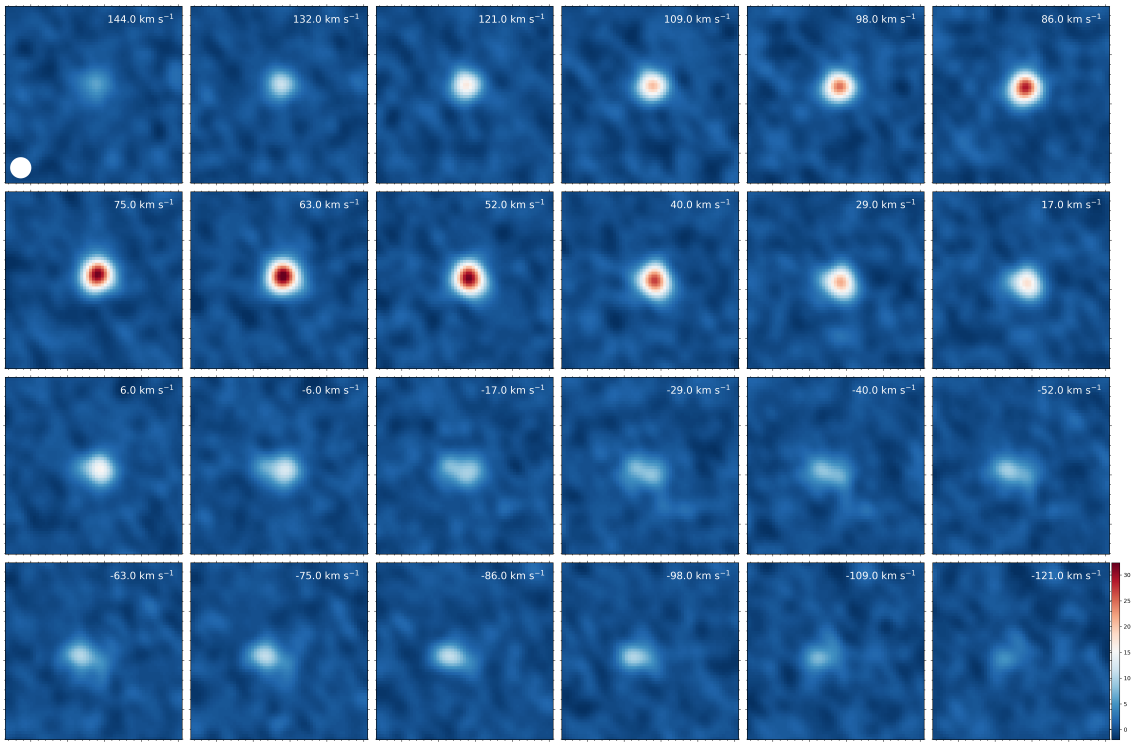

Figure C.10: DYNAMO G14-1 CO(4−3) channel maps. Each panel is centered at 14h54m28.329s, +00d44m34.37s and is 7.2″ × 7.2″ in size.

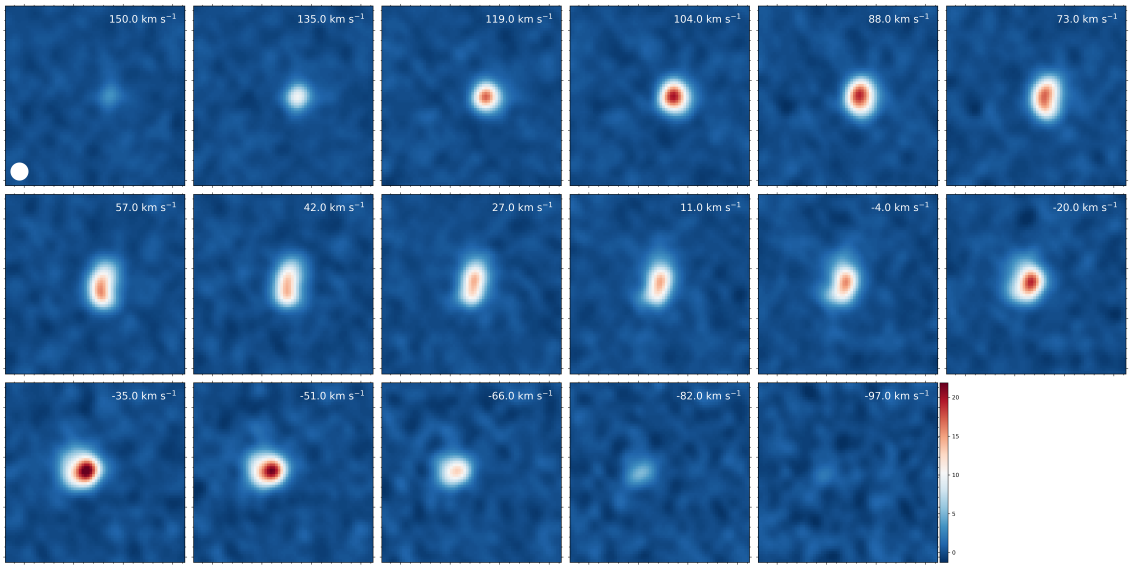

Figure C.11: DYNAMO G20-2 CO(3−2) channel maps. Each panel is centered at 20h44m02.913s, -06d46m57.93s and is 10.8″ × 10.8″ in size.

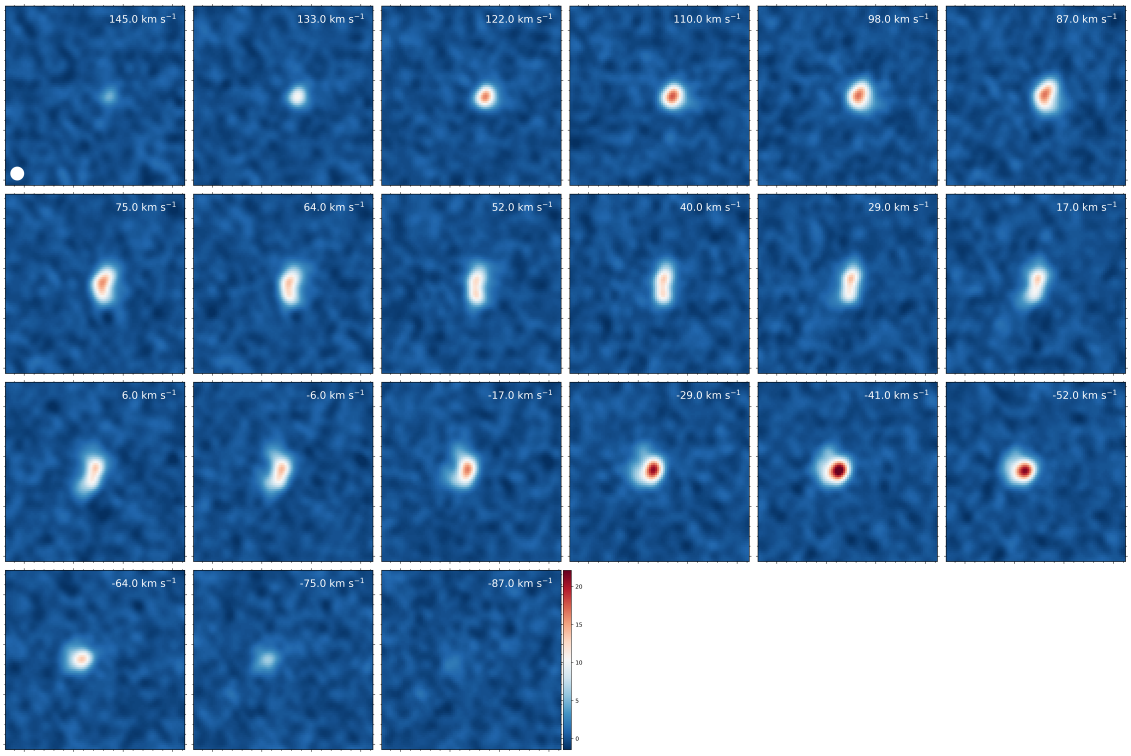

Figure C.12: DYNAMO G20-2 CO(4−3) channel maps. Each panel is centered at 20h44m02.913s, -06d46m57.93s and is 10.8″ × 10.8″ in size.

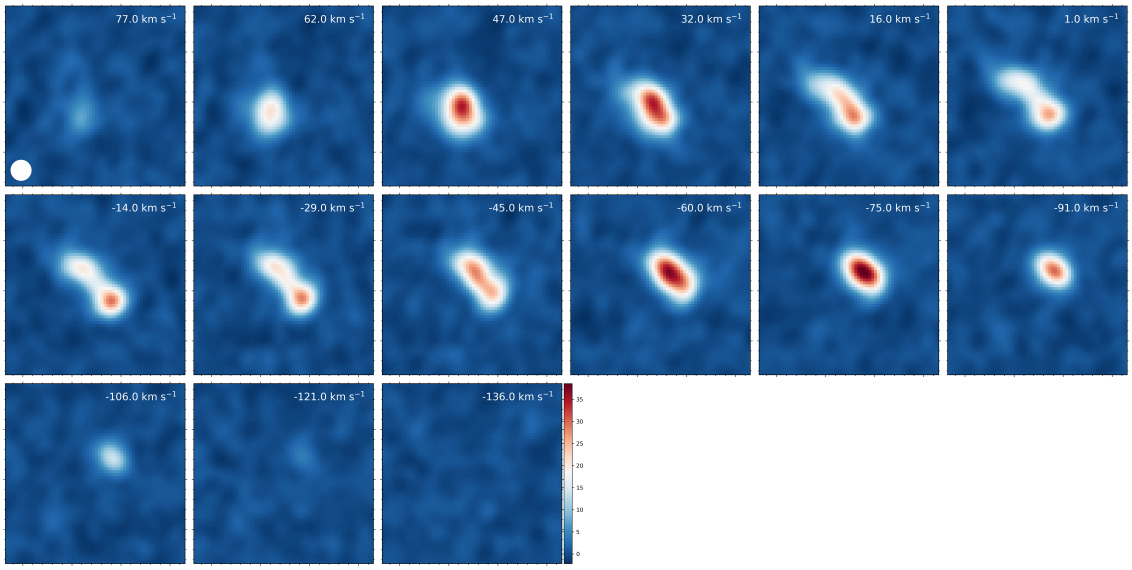

Figure C.13: SDSS J013527.10-103938.6 CO(3−2) channel maps. Each panel is centered at 01h35m27.105s, -10d39m38.64s and is 10.8″ × 10.8″ in size.

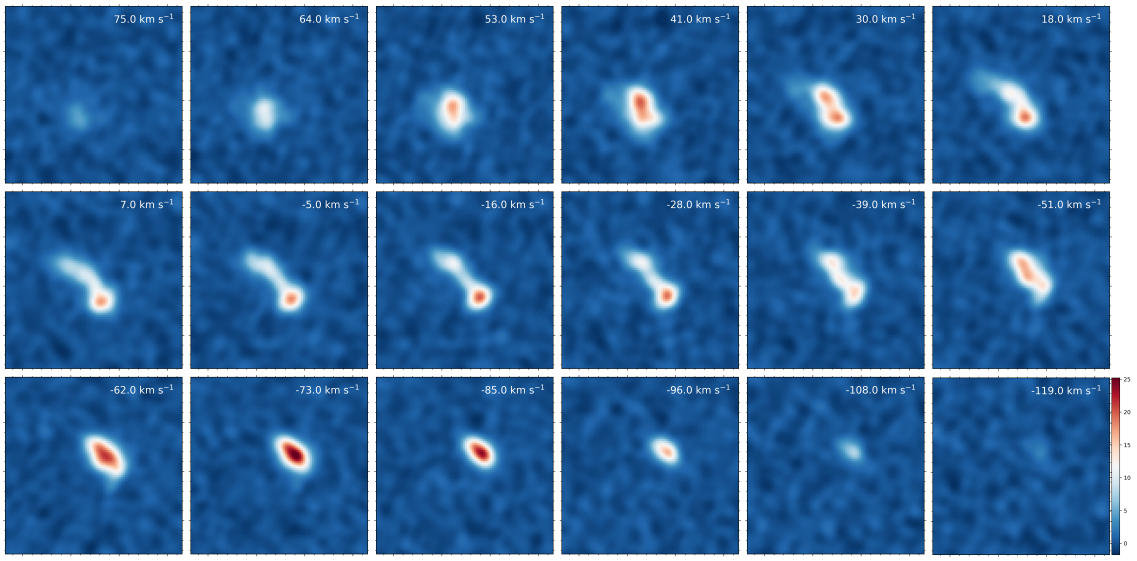

Figure C.14: SDSS J013527.10-103938.6 CO(4−3) channel maps. Each panel is centered at 01h35m27.105s, -10d39m38.64s and is $10.8'' \times 10.8''$ in size.

Appendix D: Facilities and Software

D.1 Facilities

1. ALMA
2. HST/ACS
3. HST/WFC3
4. NOEMA
5. PdBI
6. SDSS
7. Spitzer/IRAC

D.2 Software

1. APLpy (Robitaille and Bressert, 2012)
2. Astropy (Astropy Collaboration et al., 2013, Price-Whelan et al., 2018)
3. CASA (McMullin et al., 2007)
4. corner (Foreman-Mackey, 2016)
5. Cosmological Calculator (Wright, 2006)[1]

[1] http://www.astro.ucla.edu/ wright/CosmoCalc.html

6. cosvar (Driver and Robotham, 2010)[2]
7. MatPlotLib (Hunter, 2007)
8. NumPy (Harris et al., 2020)
9. photutils (Bradley et al., 2020)
10. RADEX (van der Tak et al., 2007)
11. scikit-image (Van der Walt et al., 2014)
12. SciPy (Virtanen et al., 2020)
13. seaborn (Waskom, 2021)
14. Starburst99 (Leitherer et al., 1999)

[2]https://www.rdocumentation.org/packages/celestial/versions/1.4.6/topics/cosvar

Bibliography

Jennifer K. Adelman-McCarthy, Marcel A. Agüeros, Sahar S. Allam, Kurt S. J. Anderson, Scott F. Anderson, James Annis, Neta A. Bahcall, Ivan K. Baldry, J. C. Barentine, Andreas Berlind, Mariangela Bernardi, Michael R. Blanton, William N. Boroski, Howard J. Brewington, Jarle Brinchmann, J. Brinkmann, Robert J. Brunner, Tamás Budavári, Larry N. Carey, Michael A. Carr, Francisco J. Castander, A. J. Connolly, István Csabai, Paul C. Czarapata, Julianne J. Dalcanton, Mamoru Doi, Feng Dong, Daniel J. Eisenstein, Michael L. Evans, Xiaohui Fan, Douglas P. Finkbeiner, Scott D. Friedman, Joshua A. Frieman, Masataka Fukugita, Bruce Gillespie, Karl Glazebrook, Jim Gray, Eva K. Grebel, James E. Gunn, Vijay K. Gurbani, Ernst de Haas, Patrick B. Hall, Frederick H. Harris, Michael Harvanek, Suzanne L. Hawley, Jeffrey Hayes, John S. Hendry, Gregory S. Hennessy, Robert B. Hindsley, Christopher M. Hirata, Craig J. Hogan, David W. Hogg, Donald J. Holmgren, Jon A. Holtzman, Shin-ichi Ichikawa, Željko Ivezić, Sebastian Jester, David E. Johnston, Anders M. Jorgensen, Mario Jurić, Stephen M. Kent, S. J. Kleinman, G. R. Knapp, Alexei Yu. Kniazev, Richard G. Kron, Jurek Krzesinski, Nikolay Kuropatkin, Donald Q. Lamb, Hubert Lampeitl, Brian C. Lee, R. French Leger, Huan Lin, Daniel C. Long, Jon Loveday, Robert H. Lupton, Bruce Margon, David Martínez-Delgado, Rachel Mand elbaum, Takahiko Matsubara, Peregrine M. McGehee, Timothy A. McKay, Avery Meiksin, Jeffrey A. Munn, Reiko Nakajima, Thomas Nash, Jr. Neilsen, Eric H., Heidi Jo Newberg, Peter R. Newman, Robert C. Nichol, Tom Nicinski, Maria Nieto-Santisteban, Atsuko Nitta, William O'Mullane, Sadanori Okamura, Russell Owen, Nikhil Padmanabhan, George Pauls, Jr. Peoples, John, Jeffrey R. Pier, Adrian C. Pope, Dimitri Pourbaix, Thomas R. Quinn, Gordon T. Richards, Michael W. Richmond, Constance M. Rockosi, David J. Schlegel, Donald P. Schneider, Joshua Schroeder, Ryan Scranton, Uroš Seljak, Erin Sheldon, Kazu Shimasaku, J. Allyn Smith, Vernesa Smolčić, Stephanie A. Snedden, Chris Stoughton, Michael A. Strauss, Mark SubbaRao, Alexander S. Szalay, István Szapudi, Paula Szkody, Max Tegmark, Aniruddha R. Thakar, Douglas L. Tucker, Alan Uomoto, Daniel E. Vanden Berk, Jan Vandenberg, Michael S. Vogeley, Wolfgang Voges, Nicole P. Vogt, Lucianne M. Walkowicz, David H. Weinberg, Andrew A. West, Simon D. M. White, Yongzhong Xu, Brian Yanny, D. R. Yocum, Donald G. York, Idit Zehavi, Stefano Zibetti, and Daniel B. Zucker. The Fourth Data Release of the Sloan Digital Sky Survey. *ApJS*, 162(1):38–48, Jan 2006. doi: 10.1086/497917.

G. Aniano, B. T. Draine, K. D. Gordon, and K. Sandstrom. Common-Resolution Convolution Kernels for Space- and Ground-Based Telescopes. *PASP*, 123(908): 1218, Oct 2011. doi: 10.1086/662219.

Astropy Collaboration, T. P. Robitaille, E. J. Tollerud, P. Greenfield, M. Droettboom, E. Bray, T. Aldcroft, M. Davis, A. Ginsburg, A. M. Price-Whelan, W. E. Kerzendorf, A. Conley, N. Crighton, K. Barbary, D. Muna, H. Ferguson, F. Grollier, M. M. Parikh, P. H. Nair, H. M. Unther, C. Deil, J. Woillez, S. Conseil, R. Kramer, J. E. H. Turner, L. Singer, R. Fox, B. A. Weaver, V. Zabalza, Z. I. Edwards, K. Azalee Bostroem, D. J. Burke, A. R. Casey, S. M. Crawford, N. Dencheva, J. Ely, T. Jenness, K. Labrie, P. L. Lim, F. Pierfederici, A. Pontzen, A. Ptak, B. Refsdal, M. Servillat, and O. Streicher. Astropy: A community Python package for astronomy. *A&A*, 558:A33, October 2013. doi: 10.1051/0004-6361/201322068.

Robert Bassett, Karl Glazebrook, David B. Fisher, Emily Wisnioski, Ivana Damjanov, Roberto Abraham, Danail Obreschkow, Andrew W. Green, Elisabete da Cunha, and Peter J. McGregor. Integrated and resolved dust attenuation in clumpy star-forming galaxies at 0.07 < z < 0.14. *MNRAS*, 467(1):239–258, May 2017. doi: 10.1093/mnras/stw2983.

M. Behrendt, A. Burkert, and M. Schartmann. Clusters of Small Clumps Can Explain the Peculiar Properties of Giant Clumps in High-redshift Galaxies. *ApJL*, 819(1):L2, March 2016. doi: 10.3847/2041-8205/819/1/L2.

M. Behrendt, M. Schartmann, and A. Burkert. The possible hierarchical scales of observed clumps in high-redshift disc galaxies. *MNRAS*, 488(1):306–323, September 2019. doi: 10.1093/mnras/stz1717.

Eric F. Bell. Estimating Star Formation Rates from Infrared and Radio Luminosities: The Origin of the Radio-Infrared Correlation. *ApJ*, 586(2):794–813, April 2003. doi: 10.1086/367829.

S. Bhatnagar and T. J. Cornwell. Scale sensitive deconvolution of interferometric images. I. Adaptive Scale Pixel (Asp) decomposition. *A&A*, 426:747–754, November 2004. doi: 10.1051/0004-6361:20040354.

Andrew W. Blain, Ian Smail, R. J. Ivison, J. P. Kneib, and David T. Frayer. Submillimeter galaxies. *PhR*, 369(2):111–176, Oct 2002. doi: 10.1016/S0370-1573(02)00134-5.

A. D. Bolatto, M. Wolfire, and A. K. Leroy. The CO-to-H_2 Conversion Factor. *ARA&A*, 51:207–268, August 2013. doi: 10.1146/annurev-astro-082812-140944.

A. D. Bolatto, S. R. Warren, A. K. Leroy, L. J. Tacconi, N. Bouché, N. M. Förster Schreiber, R. Genzel, M. C. Cooper, D. B. Fisher, F. Combes, S. García-Burillo, A. Burkert, F. Bournaud, A. Weiss, A. Saintonge, S. Wuyts, and A. Sternberg.

High-resolution Imaging of PHIBSS z $\sim$ 2 Main-sequence Galaxies in CO J = 1 $\rightarrow$ 0. *ApJ*, 809:175, August 2015. doi: 10.1088/0004-637X/809/2/175.

N. Bouché, G. Cresci, R. Davies, F. Eisenhauer, N. M. Förster Schreiber, R. Genzel, S. Gillessen, M. Lehnert, D. Lutz, N. Nesvadba, K. L. Shapiro, A. Sternberg, L. J. Tacconi, A. Verma, A. Cimatti, E. Daddi, A. Renzini, D. K. Erb, A. Shapley, and C. C. Steidel. Dynamical Properties of z ~2 Star-forming Galaxies and a Universal Star Formation Relation. *ApJ*, 671(1):303–309, December 2007. doi: 10.1086/522221.

N. Bouché, H. Carfantan, I. Schroetter, L. Michel-Dansac, and T. Contini. GalPak^{3D}: A Bayesian Parametric Tool for Extracting Morphokinematics of Galaxies from 3D Data. *AJ*, 150(3):92, September 2015. doi: 10.1088/0004-6256/150/3/92.

Frédéric Bournaud, Bruce G. Elmegreen, and Debra Meloy Elmegreen. Rapid Formation of Exponential Disks and Bulges at High Redshift from the Dynamical Evolution of Clump-Cluster and Chain Galaxies. *ApJ*, 670(1):237–248, November 2007. doi: 10.1086/522077.

Frédéric Bournaud, Bruce G. Elmegreen, Romain Teyssier, David L. Block, and Ivânio Puerari. ISM properties in hydrodynamic galaxy simulations: turbulence cascades, cloud formation, role of gravity and feedback. *MNRAS*, 409(3):1088–1099, December 2010. doi: 10.1111/j.1365-2966.2010.17370.x.

Frédéric Bournaud, Valentin Perret, Florent Renaud, Avishai Dekel, Bruce G. Elmegreen, Debra M. Elmegreen, Romain Teyssier, Philippe Amram, Emanuele Daddi, Pierre-Alain Duc, David Elbaz, Benoit Epinat, Jared M. Gabor, Stéphanie Juneau, Katarina Kraljic, and Emeric Le Floch'. The Long Lives of Giant Clumps and the Birth of Outflows in Gas-rich Galaxies at High Redshift. *ApJ*, 780(1):57, January 2014. doi: 10.1088/0004-637X/780/1/57.

Rychard Bouwens, Jorge González-López, Manuel Aravena, Roberto Decarli, Mladen Novak, Mauro Stefanon, Fabian Walter, Leindert Boogaard, Chris Carilli, Ugnė Dudzevičiūtė, Ian Smail, Emanuele Daddi, Elisabete da Cunha, Rob Ivison, Themiya Nanayakkara, Paulo Cortes, Pierre Cox, Hanae Inami, Pascal Oesch, Gergö Popping, Dominik Riechers, Paul van der Werf, Axel Weiss, Yoshi Fudamoto, and Jeff Wagg. The ALMA Spectroscopic Survey Large Program: The Infrared Excess of z = 1.5-10 UV-selected Galaxies and the Implied High-redshift Star Formation History. *ApJ*, 902(2):112, October 2020. doi: 10.3847/1538-4357/abb830.

Rychard J. Bouwens, Manuel Aravena, Roberto Decarli, Fabian Walter, Elisabete da Cunha, Ivo Labbé, Franz E. Bauer, Frank Bertoldi, Chris Carilli, Scott Chapman, Emanuele Daddi, Jacqueline Hodge, Rob J. Ivison, Alex Karim, Olivier Le Fevre, Benjamin Magnelli, Kazuaki Ota, Dominik Riechers, Ian R. Smail, Paul van der

Werf, Axel Weiss, Pierre Cox, David Elbaz, Jorge Gonzalez-Lopez, Leopoldo Infante, Pascal Oesch, Jeff Wagg, and Steve Wilkins. ALMA Spectroscopic Survey in the Hubble Ultra Deep Field: The Infrared Excess of UV-Selected z = 2-10 Galaxies as a Function of UV-Continuum Slope and Stellar Mass. *ApJ*, 833(1): 72, December 2016. doi: 10.3847/1538-4357/833/1/72.

Larry Bradley, Brigitta Sipőcz, Thomas Robitaille, Erik Tollerud, Zè Vinícius, Christoph Deil, Kyle Barbary, Tom J Wilson, Ivo Busko, Hans Moritz Günther, Mihai Cara, Simon Conseil, Azalee Bostroem, Michael Droettboom, E. M. Bray, Lars Andersen Bratholm, P. L. Lim, Geert Barentsen, Matt Craig, Sergio Pascual, Gabriel Perren, Johnny Greco, Axel Donath, Miguel de Val-Borro, Wolfgang Kerzendorf, Yoonsoo P. Bach, Benjamin Alan Weaver, Francesco D'Eugenio, Harrison Souchereau, and Leonardo Ferreira. astropy/photutils: 1.0.0, September 2020. URL `https://doi.org/10.5281/zenodo.4044744`.

G. B. Brammer, P. G. van Dokkum, and P. Coppi. EAZY: A Fast, Public Photometric Redshift Code. *ApJ*, 686:1503–1513, October 2008. doi: 10.1086/591786.

G. B. Brammer, P. G. van Dokkum, M. Franx, M. Fumagalli, S. Patel, H.-W. Rix, R. E. Skelton, M. Kriek, E. Nelson, K. B. Schmidt, R. Bezanson, E. da Cunha, D. K. Erb, X. Fan, N. Förster Schreiber, G. D. Illingworth, I. Labbé, J. Leja, B. Lundgren, D. Magee, D. Marchesini, P. McCarthy, I. Momcheva, A. Muzzin, R. Quadri, C. C. Steidel, T. Tal, D. Wake, K. E. Whitaker, and A. Williams. 3D-HST: A Wide-field Grism Spectroscopic Survey with the Hubble Space Telescope. *ApJS*, 200:13, June 2012. doi: 10.1088/0067-0049/200/2/13.

J. Brinchmann, S. Charlot, S. D. M. White, C. Tremonti, G. Kauffmann, T. Heckman, and J. Brinkmann. The physical properties of star-forming galaxies in the low-redshift Universe. *MNRAS*, 351(4):1151–1179, July 2004. doi: 10.1111/j.1365-2966.2004.07881.x.

Noé Brucy, Patrick Hennebelle, Frédéric Bournaud, and Cédric Colling. Large-scale Turbulent Driving Regulates Star Formation in High-redshift Gas-rich Galaxies. *ApJL*, 896(2):L34, June 2020. doi: 10.3847/2041-8213/ab9830.

Tobias Buck, Andrea V. Macciò, Aura Obreja, Aaron A. Dutton, Rosa Domínguez-Tenreiro, and Gian Luigi Granato. NIHAO XIII: Clumpy discs or clumpy light in high-redshift galaxies? *MNRAS*, 468(3):3628–3649, Jul 2017. doi: 10.1093/mnras/stx685.

W. B. Burton, M. A. Gordon, T. M. Bania, and F. J. Lockman. The overall distribution of carbon monoxide in the plane of the Galaxy. *ApJ*, 202:30–49, November 1975. doi: 10.1086/153950.

Jason A. Cardelli, Geoffrey C. Clayton, and John S. Mathis. The Relationship between Infrared, Optical, and Ultraviolet Extinction. *ApJ*, 345:245, Oct 1989. doi: 10.1086/167900.

C. L. Carilli and F. Walter. Cool Gas in High-Redshift Galaxies. *ARA&A*, 51: 105–161, August 2013. doi: 10.1146/annurev-astro-082812-140953.

T. Carleton, M. C. Cooper, A. D. Bolatto, F. Bournaud, F. Combes, J. Freundlich, S. Garcia-Burillo, R. Genzel, R. Neri, L. J. Tacconi, K. M. Sandstrom, B. J. Weiner, and A. Weiss. PHIBSS: exploring the dependence of the CO-H_2 conversion factor on total mass surface density at z<1.5. *MNRAS*, 467:4886–4901, June 2017. doi: 10.1093/mnras/stx390.

Caitlin M. Casey, Desika Narayanan, and Asantha Cooray. Dusty star-forming galaxies at high redshift. *PhR*, 541(2):45–161, Aug 2014. doi: 10.1016/j.physrep.2014.02.009.

Daniel Ceverino, Avishai Dekel, and Frederic Bournaud. High-redshift clumpy discs and bulges in cosmological simulations. *MNRAS*, 404(4):2151–2169, June 2010. doi: 10.1111/j.1365-2966.2010.16433.x.

Daniel Ceverino, Avishai Dekel, Nir Mandelker, Frederic Bournaud, Andreas Burkert, Reinhard Genzel, and Joel Primack. Rotational support of giant clumps in high-z disc galaxies. *MNRAS*, 420(4):3490–3520, March 2012. doi: 10.1111/j.1365-2966.2011.20296.x.

Daniel Ceverino, Anatoly Klypin, Elizabeth S. Klimek, Sebastian Trujillo-Gomez, Christopher W. Churchill, Joel Primack, and Avishai Dekel. Radiative feedback and the low efficiency of galaxy formation in low-mass haloes at high redshift. *MNRAS*, 442(2):1545–1559, August 2014. doi: 10.1093/mnras/stu956.

Denis F. Cioffi, Christopher F. McKee, and Edmund Bertschinger. Dynamics of Radiative Supernova Remnants. *ApJ*, 334:252, November 1988. doi: 10.1086/166834.

B. G. Clark. An efficient implementation of the algorithm 'CLEAN'. *A&A*, 89(3): 377, September 1980.

James J. Condon and Scott M. Ransom. *Essential Radio Astronomy*. 2016.

T. J. Cornwell. Multiscale CLEAN Deconvolution of Radio Synthesis Images. *IEEE Journal of Selected Topics in Signal Processing*, 2(5):793–801, November 2008. doi: 10.1109/JSTSP.2008.2006388.

T. J. Cornwell and K. F. Evans. A simple maximum entropy deconvolution algorithm. *A&A*, 143(1):77–83, February 1985.

Neil H. M. Crighton, Michael T. Murphy, J. Xavier Prochaska, Gábor Worseck, Marc Rafelski, George D. Becker, Sara L. Ellison, Michele Fumagalli, Sebastian Lopez, Avery Meiksin, and John M. O'Meara. The neutral hydrogen cosmological mass density at z = 5. *MNRAS*, 452(1):217–234, September 2015. doi: 10.1093/mnras/stv1182.

E. Daddi, F. Bournaud, F. Walter, H. Dannerbauer, C. L. Carilli, M. Dickinson, D. Elbaz, G. E. Morrison, D. Riechers, M. Onodera, F. Salmi, M. Krips, and D. Stern. Very High Gas Fractions and Extended Gas Reservoirs in z = 1.5 Disk Galaxies. *ApJ*, 713:686–707, April 2010a. doi: 10.1088/0004-637X/713/1/686.

E. Daddi, D. Elbaz, F. Walter, F. Bournaud, F. Salmi, C. Carilli, H. Dannerbauer, M. Dickinson, P. Monaco, and D. Riechers. Different Star Formation Laws for Disks Versus Starbursts at Low and High Redshifts. *ApJL*, 714(1):L118–L122, May 2010b. doi: 10.1088/2041-8205/714/1/L118.

E. Daddi, H. Dannerbauer, D. Liu, M. Aravena, F. Bournaud, F. Walter, D. Riechers, G. Magdis, M. Sargent, M. Béthermin, C. Carilli, A. Cibinel, M. Dickinson, D. Elbaz, Y. Gao, R. Gobat, J. Hodge, and M. Krips. CO excitation of normal star-forming galaxies out to z = 1.5 as regulated by the properties of their interstellar medium. *A&A*, 577:A46, May 2015. doi: 10.1051/0004-6361/201425043.

Mark Danovich, Avishai Dekel, Oliver Hahn, Daniel Ceverino, and Joel Primack. Four phases of angular-momentum buildup in high-z galaxies: from cosmic-web streams through an extended ring to disc and bulge. *MNRAS*, 449(2):2087–2111, May 2015. doi: 10.1093/mnras/stv270.

R. de la Fuente Marcos and C. de la Fuente Marcos. Hierarchical Star Formation in the Milky Way Disk. *ApJ*, 700(1):436–446, July 2009. doi: 10.1088/0004-637X/700/1/436.

Ilse De Looze, Diane Cormier, Vianney Lebouteiller, Suzanne Madden, Maarten Baes, George J. Bendo, Médéric Boquien, Alessandro Boselli, David L. Clements, Luca Cortese, Asantha Cooray, Maud Galametz, Frédéric Galliano, Javier Graciá-Carpio, Kate Isaak, Oskar Ł. Karczewski, Tara J. Parkin, Eric W. Pellegrini, Aurélie Rémy-Ruyer, Luigi Spinoglio, Matthew W. L. Smith, and Eckhard Sturm. The applicability of far-infrared fine-structure lines as star formation rate tracers over wide ranges of metallicities and galaxy types. *A&A*, 568:A62, August 2014. doi: 10.1051/0004-6361/201322489.

R. Decarli, F. Walter, C. Carilli, D. Riechers, P. Cox, R. Neri, M. Aravena, E. Bell, F. Bertoldi, D. Colombo, E. Da Cunha, E. Daddi, M. Dickinson, D. Downes, R. Ellis, L. Lentati, R. Maiolino, K. M. Menten, H.-W. Rix, M. Sargent, D. Stark, B. Weiner, and A. Weiss. A Molecular Line Scan in the Hubble Deep Field North. *ApJ*, 782:78, February 2014. doi: 10.1088/0004-637X/782/2/78.

R. Decarli, F. Walter, M. Aravena, C. Carilli, R. Bouwens, E. da Cunha, E. Daddi, R. J. Ivison, G. Popping, D. Riechers, I. R. Smail, M. Swinbank, A. Weiss, T. Anguita, R. J. Assef, F. E. Bauer, E. F. Bell, F. Bertoldi, S. Chapman, L. Colina, P. C. Cortes, P. Cox, M. Dickinson, D. Elbaz, J. Gónzalez-López, E. Ibar, L. Infante, J. Hodge, A. Karim, O. Le Fevre, B. Magnelli, R. Neri, P. Oesch, K. Ota, H.-W. Rix, M. Sargent, K. Sheth, A. van der Wel, P. van der Werf, and J. Wagg. ALMA Spectroscopic Survey in the Hubble Ultra Deep Field: CO Luminosity

Functions and the Evolution of the Cosmic Density of Molecular Gas. *ApJ*, 833: 69, December 2016. doi: 10.3847/1538-4357/833/1/69.

R. Decarli, C. Carilli, C. Casey, B. Emonts, J. Hodge, K. Kohno, D. Narayanan, D. Riechers, M. Sargent, and F. Walter. Cold Gas in High-z Galaxies: The Molecular Gas Budget. In Eric Murphy, editor, *Science with a Next Generation Very Large Array*, volume 517 of *Astronomical Society of the Pacific Conference Series*, page 565, Dec 2018.

Roberto Decarli, Fabian Walter, Jorge Gónzalez-López, Manuel Aravena, Leindert Boogaard, Chris Carilli, Pierre Cox, Emanuele Daddi, Gergö Popping, Dominik Riechers, Bade Uzgil, Axel Weiss, Roberto J. Assef, Roland Bacon, Franz Erik Bauer, Frank Bertoldi, Rychard Bouwens, Thierry Contini, Paulo C. Cortes, Elisabete da Cunha, Tanio Díaz-Santos, David Elbaz, Hanae Inami, Jacqueline Hodge, Rob Ivison, Olivier Le Fèvre, Benjamin Magnelli, Mladen Novak, Pascal Oesch, Hans-Walter Rix, Mark T. Sargent, Ian Smail, A. Mark Swinbank, Rachel S. Somerville, Paul van der Werf, Jeff Wagg, and Lutz Wisotzki. The ALMA Spectroscopic Survey in the HUDF: CO Luminosity Functions and the Molecular Gas Content of Galaxies through Cosmic History. *ApJ*, 882(2):138, September 2019. doi: 10.3847/1538-4357/ab30fe.

Avishai Dekel, Re'em Sari, and Daniel Ceverino. Formation of Massive Galaxies at High Redshift: Cold Streams, Clumpy Disks, and Compact Spheroids. *ApJ*, 703 (1):785–801, September 2009. doi: 10.1088/0004-637X/703/1/785.

Avishai Dekel, Nir Mandelker, Frederic Bournaud, Daniel Ceverino, Yicheng Guo, and Joel primack. Clump Survival and Migration in VDI Galaxies: an Analytic Model versus Simulations and Observations. *arXiv e-prints*, art. arXiv:2107.13561, July 2021.

D. Downes and P. M. Solomon. Rotating Nuclear Rings and Extreme Starbursts in Ultraluminous Galaxies. *ApJ*, 507(2):615–654, November 1998. doi: 10.1086/306339.

Bruce T. Draine. *Physics of the Interstellar and Intergalactic Medium*. 2011.

S. P. Driver and A. S. G. Robotham. Quantifying cosmic variance. *MNRAS*, 407: 2131–2140, October 2010. doi: 10.1111/j.1365-2966.2010.17028.x.

S. P. Driver, A. S. G. Robotham, L. Kelvin, M. Alpaslan, I. K. Baldry, S. P. Bamford, S. Brough, M. Brown, A. M. Hopkins, J. Liske, J. Loveday, P. Norberg, J. A. Peacock, E. Andrae, J. Bland-Hawthorn, N. Bourne, E. Cameron, M. Colless, C. J. Conselice, S. M. Croom, L. Dunne, C. S. Frenk, Alister W. Graham, M. Gunawardhana, D. T. Hill, D. H. Jones, K. Kuijken, B. Madore, R. C. Nichol, H. R. Parkinson, K. A. Pimbblet, S. Phillipps, C. C. Popescu, M. Prescott, M. Seibert, R. G. Sharp, W. J. Sutherland, E. N. Taylor, D. Thomas, R. J. Tuffs, E. van Kampen, D. Wijesinghe, and S. Wilkins. Galaxy And Mass Assembly (GAMA): the

0.013 ¡ z ¡ 0.1 cosmic spectral energy distribution from 0.1 μm to 1 mm. *MNRAS*, 427(4):3244–3264, December 2012. doi: 10.1111/j.1365-2966.2012.22036.x.

Yuri N. Efremov and Bruce G. Elmegreen. Hierarchical star formation from the time-space distribution of star clusters in the Large Magellanic Cloud. *MNRAS*, 299(2):588–594, September 1998. doi: 10.1046/j.1365-8711.1998.01819.x.

Bruce G. Elmegreen and Andreas Burkert. Accretion-Driven Turbulence and the Transition to Global Instability in Young Galaxy Disks. *ApJ*, 712(1):294–302, March 2010. doi: 10.1088/0004-637X/712/1/294.

Claude-André Faucher-Giguère, Eliot Quataert, and Philip F. Hopkins. Feedback-regulated star formation in molecular clouds and galactic discs. *MNRAS*, 433(3): 1970–1990, August 2013. doi: 10.1093/mnras/stt866.

Baptiste Faure, Frédéric Bournaud, Jérémy Fensch, Emanuele Daddi, Manuel Behrendt, Andreas Burkert, and Johan Richard. Hierarchical fragmentation in high redshift galaxies revealed by hydrodynamical simulations. *MNRAS*, February 2021. doi: 10.1093/mnras/stab272.

Robert Feldmann, Nickolay Y. Gnedin, and Andrey V. Kravtsov. The X-factor in Galaxies. I. Dependence on Environment and Scale. *ApJ*, 747(2):124, March 2012. doi: 10.1088/0004-637X/747/2/124.

Jérémy Fensch and Frédéric Bournaud. The role of gas fraction and feedback in the stability and evolution of galactic discs: implications for cosmological galaxy formation models. *MNRAS*, 505(3):3579–3589, August 2021. doi: 10.1093/mnras/stab1489.

D. B. Fisher, A. D. Bolatto, H. White, K. Glazebrook, R. G. Abraham, and D. Obreschkow. Testing Feedback-regulated Star Formation in Gas-rich, Turbulent Disk Galaxies. *ApJ*, 870(1):46, January 2019. doi: 10.3847/1538-4357/aaee8b.

David B. Fisher, Karl Glazebrook, Alberto Bolatto, Danail Obreschkow, Erin Mentuch Cooper, Emily Wisnioski, Robert Bassett, Roberto G. Abraham, Ivana Damjanov, Andy Green, and Peter McGregor. Extreme Gas Fractions in Clumpy, Turbulent Disk Galaxies at z ~0.1. *ApJL*, 790(2):L30, August 2014. doi: 10.1088/2041-8205/790/2/L30.

David B. Fisher, Karl Glazebrook, Roberto G. Abraham, Ivana Damjanov, Heidi A. White, Danail Obreschkow, Robert Basset, Georgios Bekiaris, Emily Wisnioski, Andy Green, and Alberto D. Bolatto. Connecting Clump Sizes in Turbulent Disk Galaxies to Instability Theory. *ApJL*, 839(1):L5, April 2017a. doi: 10.3847/2041-8213/aa6478.

David B. Fisher, Karl Glazebrook, Ivana Damjanov, Roberto G. Abraham, Danail Obreschkow, Emily Wisnioski, Robert Bassett, Andy Green, and Peter McGregor.

DYNAMO-HST survey: clumps in nearby massive turbulent discs and the effects of clump clustering on kiloparsec scale measurements of clumps. *MNRAS*, 464(1): 491–507, January 2017b. doi: 10.1093/mnras/stw2281.

Daniel Foreman-Mackey. corner.py: Scatterplot matrices in python. *The Journal of Open Source Software*, 1(2):24, jun 2016. doi: 10.21105/joss.00024. URL `https://doi.org/10.21105/joss.00024`.

N. M. Förster Schreiber, R. Genzel, M. D. Lehnert, N. Bouché, A. Verma, D. K. Erb, A. E. Shapley, C. C. Steidel, R. Davies, D. Lutz, N. Nesvadba, L. J. Tacconi, F. Eisenhauer, R. Abuter, A. Gilbert, S. Gillessen, and A. Sternberg. SINFONI Integral Field Spectroscopy of z ~2 UV-selected Galaxies: Rotation Curves and Dynamical Evolution. *ApJ*, 645(2):1062–1075, Jul 2006. doi: 10.1086/504403.

N. M. Förster Schreiber, A. E. Shapley, R. Genzel, N. Bouché, G. Cresci, R. Davies, D. K. Erb, S. Genel, D. Lutz, S. Newman, K. L. Shapiro, C. C. Steidel, A. Sternberg, and L. J. Tacconi. Constraints on the Assembly and Dynamics of Galaxies. II. Properties of Kiloparsec-scale Clumps in Rest-frame Optical Emission of z ~2 Star-forming Galaxies. *ApJ*, 739(1):45, Sep 2011. doi: 10.1088/0004-637X/739/1/45.

J. Freundlich, F. Combes, L. J. Tacconi, R. Genzel, S. Garcia-Burillo, R. Neri, T. Contini, A. Bolatto, S. Lilly, P. Salomé, I. C. Bicalho, J. Boissier, F. Boone, N. Bouché, F. Bournaud, A. Burkert, M. Carollo, M. C. Cooper, P. Cox, C. Feruglio, N. M. Förster Schreiber, S. Juneau, M. Lippa, D. Lutz, T. Naab, A. Renzini, A. Saintonge, A. Sternberg, F. Walter, B. Weiner, A. Weiß, and S. Wuyts. PHIBSS2: survey design and z = 0.5 - 0.8 results. Molecular gas reservoirs during the winding-down of star formation. *A&A*, 622:A105, February 2019. doi: 10.1051/0004-6361/201732223.

N. Gehrels. Confidence limits for small numbers of events in astrophysical data. *ApJ*, 303:336–346, April 1986. doi: 10.1086/164079.

Shy Genel, Thorsten Naab, Reinhard Genzel, Natascha M. Förster Schreiber, Amiel Sternberg, Ludwig Oser, Peter H. Johansson, Romeel Davé, Benjamin D. Oppenheimer, and Andreas Burkert. Short-lived Star-forming Giant Clumps in Cosmological Simulations of z $\approx$ 2 Disks. *ApJ*, 745(1):11, January 2012. doi: 10.1088/0004-637X/745/1/11.

R. Genzel, A. Burkert, N. Bouché, G. Cresci, N. M. Förster Schreiber, A. Shapley, K. Shapiro, L. J. Tacconi, P. Buschkamp, A. Cimatti, E. Daddi, R. Davies, F. Eisenhauer, D. K. Erb, S. Genel, O. Gerhard, E. Hicks, D. Lutz, T. Naab, T. Ott, S. Rabien, A. Renzini, C. C. Steidel, A. Sternberg, and S. J. Lilly. From Rings to Bulges: Evidence for Rapid Secular Galaxy Evolution at z ~2 from Integral Field Spectroscopy in the SINS Survey. *ApJ*, 687(1):59–77, Nov 2008. doi: 10.1086/591840.

R. Genzel, L. J. Tacconi, J. Gracia-Carpio, A. Sternberg, M. C. Cooper, K. Shapiro, A. Bolatto, N. Bouché, F. Bournaud, A. Burkert, F. Combes, J. Comerford, P. Cox, M. Davis, N. M. F. Schreiber, S. Garcia-Burillo, D. Lutz, T. Naab, R. Neri, A. Omont, A. Shapley, and B. Weiner. A study of the gas-star formation relation over cosmic time. *MNRAS*, 407:2091–2108, October 2010. doi: 10.1111/j.1365-2966.2010.16969.x.

R. Genzel, S. Newman, T. Jones, N. M. Förster Schreiber, K. Shapiro, S. Genel, S. J. Lilly, A. Renzini, L. J. Tacconi, N. Bouché, A. Burkert, G. Cresci, P. Buschkamp, C. M. Carollo, D. Ceverino, R. Davies, A. Dekel, F. Eisenhauer, E. Hicks, J. Kurk, D. Lutz, C. Mancini, T. Naab, Y. Peng, A. Sternberg, D. Vergani, and G. Zamorani. The Sins Survey of z ~2 Galaxy Kinematics: Properties of the Giant Star-forming Clumps. *ApJ*, 733(2):101, Jun 2011. doi: 10.1088/0004-637X/733/2/101.

R. Genzel, L. J. Tacconi, F. Combes, A. Bolatto, R. Neri, A. Sternberg, M. C. Cooper, N. Bouché, F. Bournaud, A. Burkert, J. Comerford, P. Cox, M. Davis, N. M. Förster Schreiber, S. Garcia-Burillo, J. Gracia-Carpio, D. Lutz, T. Naab, S. Newman, A. Saintonge, K. Shapiro, A. Shapley, and B. Weiner. The Metallicity Dependence of the CO $\rightarrow$ H_2 Conversion Factor in z ¿= 1 Star-forming Galaxies. *ApJ*, 746(1):69, February 2012. doi: 10.1088/0004-637X/746/1/69.

R. Genzel, L. J. Tacconi, D. Lutz, A. Saintonge, S. Berta, B. Magnelli, F. Combes, S. García-Burillo, R. Neri, A. Bolatto, T. Contini, S. Lilly, J. Boissier, F. Boone, N. Bouché, F. Bournaud, A. Burkert, M. Carollo, L. Colina, M. C. Cooper, P. Cox, C. Feruglio, N. M. Förster Schreiber, J. Freundlich, J. Gracia-Carpio, S. Juneau, K. Kovac, M. Lippa, T. Naab, P. Salome, A. Renzini, A. Sternberg, F. Walter, B. Weiner, A. Weiss, and S. Wuyts. Combined CO and Dust Scaling Relations of Depletion Time and Molecular Gas Fractions with Cosmic Time, Specific Star-formation Rate, and Stellar Mass. *ApJ*, 800:20, February 2015. doi: 10.1088/0004-637X/800/1/20.

Omri Ginzburg, Marc Huertas-Company, Avishai Dekel, Nir Mandelker, Gregory Snyder, Daniel Ceverino, and Joel Primack. The nature of giant clumps in high-z discs: a deep-learning comparison of simulations and observations. *MNRAS*, 501 (1):730–746, February 2021. doi: 10.1093/mnras/staa3778.

M. Girard, D. B. Fisher, A. D. Bolatto, R. Abraham, R. Bassett, K. Glazebrook, R. Herrera-Camus, E. Jiménez, L. Lenkić, and D. Obreschkow. Systematic Difference between Ionized and Molecular Gas Velocity Dispersions in z $\sim$ 1-2 Disks and Local Analogs. *ApJ*, 909(1):12, March 2021. doi: 10.3847/1538-4357/abd5b9.

Jorge González-López, Roberto Decarli, Riccardo Pavesi, Fabian Walter, Manuel Aravena, Chris Carilli, Leindert Boogaard, Gergö Popping, Axel Weiss, Roberto J. Assef, Franz Erik Bauer, Frank Bertoldi, Richard Bouwens, Thierry Contini, Paulo C. Cortes, Pierre Cox, Elisabete da Cunha, Emanuele Daddi, Tanio Díaz-Santos, Hanae Inami, Jacqueline Hodge, Rob Ivison, Olivier Le Fèvre, Benjamin

Magnelli, Pascal Oesch, Dominik Riechers, Hans-Walter Rix, Ian Smail, A. M. Swinbank, Rachel S. Somerville, Bade Uzgil, and Paul van der Werf. The Atacama Large Millimeter/submillimeter Array Spectroscopic Survey in the Hubble Ultra Deep Field: CO Emission Lines and 3 mm Continuum Sources. *ApJ*, 882 (2):139, September 2019. doi: 10.3847/1538-4357/ab3105.

Karl D. Gordon, Charles W. Engelbracht, George H. Rieke, K. A. Misselt, J. D. T. Smith, and Jr. Kennicutt, Robert C. The Behavior of the Aromatic Features in M101 H II Regions: Evidence for Dust Processing. *ApJ*, 682(1):336–354, July 2008. doi: 10.1086/589567.

K. Grasha, B. G. Elmegreen, D. Calzetti, A. Adamo, A. Aloisi, S. N. Bright, D. O. Cook, D. A. Dale, M. Fumagalli, III Gallagher, J. S., D. A. Gouliermis, E. K. Grebel, L. Kahre, H. Kim, M. R. Krumholz, J. C. Lee, M. Messa, J. E. Ryon, and L. Ubeda. Hierarchical Star Formation in Turbulent Media: Evidence from Young Star Clusters. *ApJ*, 842(1):25, June 2017. doi: 10.3847/1538-4357/aa740b.

Andrew W. Green, Karl Glazebrook, Peter J. McGregor, Ivana Damjanov, Emily Wisnioski, Roberto G. Abraham, Matthew Colless, Robert G. Sharp, Robert A. Crain, Gregory B. Poole, and Patrick J. McCarthy. DYNAMO - I. A sample of Hα-luminous galaxies with resolved kinematics. *MNRAS*, 437(2):1070–1095, Jan 2014. doi: 10.1093/mnras/stt1882.

T. R. Greve, F. Bertoldi, I. Smail, R. Neri, S. C. Chapman, A. W. Blain, R. J. Ivison, R. Genzel, A. Omont, P. Cox, L. Tacconi, and J.-P. Kneib. An interferometric CO survey of luminous submillimetre galaxies. *MNRAS*, 359:1165–1183, May 2005. doi: 10.1111/j.1365-2966.2005.08979.x.

Brendan F. Griffen, Alexander P. Ji, Gregory A. Dooley, Facundo A. Gómez, Mark Vogelsberger, Brian W. O'Shea, and Anna Frebel. The Caterpillar Project: A Large Suite of Milky Way Sized Halos. *ApJ*, 818(1):10, February 2016. doi: 10.3847/0004-637X/818/1/10.

S. Guilloteau, J. Delannoy, D. Downes, A. Greve, M. Guelin, R. Lucas, D. Morris, S. J. E. Radford, J. Wink, J. Cernicharo, T. Forveille, S. Garcia-Burillo, R. Neri, J. Blondel, A. Perrigourad, D. Plathner, and M. Torres. The IRAM interferometer on Plateau de Bure. *A&A*, 262:624–633, September 1992.

Yicheng Guo, Mauro Giavalisco, Henry C. Ferguson, Paolo Cassata, and Anton M. Koekemoer. Multi-wavelength View of Kiloparsec-scale Clumps in Star-forming Galaxies at z ~2. *ApJ*, 757(2):120, Oct 2012. doi: 10.1088/0004-637X/757/2/120.

Yicheng Guo, Henry C. Ferguson, Eric F. Bell, David C. Koo, Christopher J. Conselice, Mauro Giavalisco, Susan Kassin, Yu Lu, Ray Lucas, Nir Mandelker, Daniel M. McIntosh, Joel R. Primack, Swara Ravindranath, Guillermo Barro, Daniel Ceverino, Avishai Dekel, Sandra M. Faber, Jerome J. Fang, Anton M. Koekemoer, Kai Noeske, Marc Rafelski, and Amber Straughn. Clumpy Galaxies in

CANDELS. I. The Definition of UV Clumps and the Fraction of Clumpy Galaxies at 0.5 < z < 3. *ApJ*, 800(1):39, Feb 2015. doi: 10.1088/0004-637X/800/1/39.

Yicheng Guo, Marc Rafelski, Eric F. Bell, Christopher J. Conselice, Avishai Dekel, S. M. Faber, Mauro Giavalisco, Anton M. Koekemoer, David C. Koo, Yu Lu, Nir Mandelker, Joel R. Primack, Daniel Ceverino, Duilia F. de Mello, Henry C. Ferguson, Nimish Hathi, Dale Kocevski, Ray A. Lucas, Pablo G. Pérez-González, Swara Ravindranath, Emmaris Soto, Amber Straughn, and Weichen Wang. Clumpy Galaxies in CANDELS. II. Physical Properties of UV-bright Clumps at $0.5 \leq$ z < 3. *ApJ*, 853(2):108, Feb 2018. doi: 10.3847/1538-4357/aaa018.

Cai-Na Hao, Robert C. Kennicutt, Benjamin D. Johnson, Daniela Calzetti, Daniel A. Dale, and John Moustakas. Dust-corrected Star Formation Rates of Galaxies. II. Combinations of Ultraviolet and Infrared Tracers. *ApJ*, 741(2):124, November 2011. doi: 10.1088/0004-637X/741/2/124.

Charles R. Harris, K. Jarrod Millman, Stéfan J. van der Walt, Ralf Gommers, Pauli Virtanen, David Cournapeau, Eric Wieser, Julian Taylor, Sebastian Berg, Nathaniel J. Smith, Robert Kern, Matti Picus, Stephan Hoyer, Marten H. van Kerkwijk, Matthew Brett, Allan Haldane, Jaime Fernández del Río, Mark Wiebe, Pearu Peterson, Pierre Gérard-Marchant, Kevin Sheppard, Tyler Reddy, Warren Weckesser, Hameer Abbasi, Christoph Gohlke, and Travis E. Oliphant. Array programming with NumPy. *Nature*, 585(7825):357–362, September 2020. doi: 10.1038/s41586-020-2649-2. URL `https://doi.org/10.1038/s41586-020-2649-2`.

C. Heiles, L. M. Haffner, and R. J. Reynolds. The Eridanus Superbubble in its Multiwavelength Glory. In A. R. Taylor, T. L. Landecker, and G. Joncas, editors, *New Perspectives on the Interstellar Medium*, volume 168 of *Astronomical Society of the Pacific Conference Series*, page 211, January 1999.

K. Henríquez-Brocal, R. Herrera-Camus, L. Tacconi, R. Genzel, A. Bolatto, S. Bovino, R. Demarco, N. Förster Schreiber, M. Lee, D. Lutz, and M. Rubio. Molecular gas properties of Q1700-MD94: a massive, main-sequence galaxy at $z \approx 2$. *arXiv e-prints*, art. arXiv:2109.01684, September 2021.

R. Herrera-Camus, A. D. Bolatto, M. G. Wolfire, J. D. Smith, K. V. Croxall, R. C. Kennicutt, D. Calzetti, G. Helou, F. Walter, A. K. Leroy, B. Draine, B. R. Brandl, L. Armus, K. M. Sandstrom, D. A. Dale, G. Aniano, S. E. Meidt, M. Boquien, L. K. Hunt, M. Galametz, F. S. Tabatabaei, E. J. Murphy, P. Appleton, H. Roussel, C. Engelbracht, and P. Beirao. [C II] 158 μm Emission as a Star Formation Tracer. *ApJ*, 800(1):1, February 2015. doi: 10.1088/0004-637X/800/1/1.

R. Herrera-Camus, E. Sturm, J. Graciá-Carpio, D. Lutz, A. Contursi, S. Veilleux, J. Fischer, E. González-Alfonso, A. Poglitsch, L. Tacconi, R. Genzel, R. Maiolino, A. Sternberg, R. Davies, and A. Verma. SHINING, A Survey of Far-infrared Lines in Nearby Galaxies. I. Survey Description, Observational Trends, and Line Diagnostics. *ApJ*, 861(2):94, July 2018a. doi: 10.3847/1538-4357/aac0f6.

R. Herrera-Camus, E. Sturm, J. Graciá-Carpio, D. Lutz, A. Contursi, S. Veilleux, J. Fischer, E. González-Alfonso, A. Poglitsch, L. Tacconi, R. Genzel, R. Maiolino, A. Sternberg, R. Davies, and A. Verma. SHINING, A Survey of Far-infrared Lines in Nearby Galaxies. II. Line-deficit Models, AGN Impact, [C II]-SFR Scaling Relations, and Mass-Metallicity Relation in (U)LIRGs. *ApJ*, 861(2):95, July 2018b. doi: 10.3847/1538-4357/aac0f9.

G. Hinshaw, D. Larson, E. Komatsu, D. N. Spergel, C. L. Bennett, J. Dunkley, M. R. Nolta, M. Halpern, R. S. Hill, N. Odegard, L. Page, K. M. Smith, J. L. Weiland, B. Gold, N. Jarosik, A. Kogut, M. Limon, S. S. Meyer, G. S. Tucker, E. Wollack, and E. L. Wright. Nine-year Wilkinson Microwave Anisotropy Probe (WMAP) Observations: Cosmological Parameter Results. *ApJS*, 208(2):19, October 2013. doi: 10.1088/0067-0049/208/2/19.

Andrew M. Hopkins and John F. Beacom. On the Normalization of the Cosmic Star Formation History. *ApJ*, 651(1):142–154, November 2006. doi: 10.1086/506610.

Philip F. Hopkins, Dušan Kereš, José Oñorbe, Claude-André Faucher-Giguère, Eliot Quataert, Norman Murray, and James S. Bullock. Galaxies on FIRE (Feedback In Realistic Environments): stellar feedback explains cosmologically inefficient star formation. *MNRAS*, 445(1):581–603, Nov 2014. doi: 10.1093/mnras/stu1738.

Philip F. Hopkins, Andrew Wetzel, Dušan Kereš, Claude-André Faucher-Giguère, Eliot Quataert, Michael Boylan-Kolchin, Norman Murray, Christopher C. Hayward, Shea Garrison-Kimmel, Cameron Hummels, Robert Feldmann, Paul Torrey, Xiangcheng Ma, Daniel Anglés-Alcázar, Kung-Yi Su, Matthew Orr, Denise Schmitz, Ivanna Escala, Robyn Sanderson, Michael Y. Grudić, Zachary Hafen, Ji-Hoon Kim, Alex Fitts, James S. Bullock, Coral Wheeler, T. K. Chan, Oliver D. Elbert, and Desika Narayanan. FIRE-2 simulations: physics versus numerics in galaxy formation. *MNRAS*, 480(1):800–863, October 2018. doi: 10.1093/mnras/sty1690.

Steve Bruce Howell. *Handbook of CCD Astronomy*, volume 5. 2006.

Marc Huertas-Company, Yicheng Guo, Omri Ginzburg, Christoph T. Lee, Nir Mandelker, Maxwell Metter, Joel R. Primack, Avishai Dekel, Daniel Ceverino, Sandra M. Faber, David C. Koo, Anton Koekemoer, Gregory Snyder, Mauro Giavalisco, and Haowen Zhang. Stellar masses of giant clumps in CANDELS and simulated galaxies using machine learning. *MNRAS*, 499(1):814–835, November 2020. doi: 10.1093/mnras/staa2777.

J. D. Hunter. Matplotlib: A 2d graphics environment. *Computing in Science & Engineering*, 9(3):90–95, 2007. doi: 10.1109/MCSE.2007.55.

A. Immeli, M. Samland, O. Gerhard, and P. Westera. Gas physics, disk fragmentation, and bulge formation in young galaxies. *A&A*, 413:547–561, January 2004. doi: 10.1051/0004-6361:20034282.

J. Kamenetzky, N. Rangwala, J. Glenn, P. R. Maloney, and A. Conley. L$\cdot_{CO}$/L$_{FIR}$ Relations with CO Rotational Ladders of Galaxies Across the Herschel SPIRE Archive. *ApJ*, 829(2):93, October 2016. doi: 10.3847/0004-637X/829/2/93.

Jr. Kennicutt, Robert C. The Global Schmidt Law in Star-forming Galaxies. *ApJ*, 498(2):541–552, May 1998a. doi: 10.1086/305588.

Jr. Kennicutt, Robert C. Star Formation in Galaxies Along the Hubble Sequence. *ARA&A*, 36:189–232, January 1998b. doi: 10.1146/annurev.astro.36.1.189.

Jr. Kennicutt, Robert C. and Mithi A. C. De Los Reyes. Revisiting the Integrated Star Formation Law. II. Starbursts and the Combined Global Schmidt Law. *ApJ*, 908(1):61, February 2021. doi: 10.3847/1538-4357/abd3a2.

Jr. Kennicutt, Robert C., Daniela Calzetti, Fabian Walter, George Helou, David J. Hollenbach, Lee Armus, George Bendo, Daniel A. Dale, Bruce T. Draine, Charles W. Engelbracht, Karl D. Gordon, Moire K. M. Prescott, Michael W. Regan, Michele D. Thornley, Caroline Bot, Elias Brinks, Erwin de Blok, Dulia de Mello, Martin Meyer, John Moustakas, Eric J. Murphy, Kartik Sheth, and J. D. T. Smith. Star Formation in NGC 5194 (M51a). II. The Spatially Resolved Star Formation Law. *ApJ*, 671(1):333–348, December 2007. doi: 10.1086/522300.

Robert C. Kennicutt and Neal J. Evans. Star Formation in the Milky Way and Nearby Galaxies. *ARA&A*, 50:531–608, September 2012. doi: 10.1146/annurev-astro-081811-125610.

S. M. Kent and J. E. Gunn. The dynamics of rich clusters of galaxies. I. The Coma cluster. *AJ*, 87:945–960, Jul 1982. doi: 10.1086/113178.

D. Keres, M. S. Yun, and J. S. Young. CO Luminosity Functions for Far-Infrared- and B-Band-selected Galaxies and the First Estimate for Ω_{HI}+H_2. *ApJ*, 582: 659–667, January 2003. doi: 10.1086/344820.

R. S. Klessen and P. Hennebelle. Accretion-driven turbulence as universal process: galaxies, molecular clouds, and protostellar disks. *A&A*, 520:A17, September 2010. doi: 10.1051/0004-6361/200913780.

Anne Klitsch, Céline Péroux, Martin A. Zwaan, Ian Smail, Dylan Nelson, Gergö Popping, Chian-Chou Chen, Benedikt Diemer, R. J. Ivison, James R. Allison, Sébastien Muller, A. Mark Swinbank, Aleksandra Hamanowicz, Andrew D. Biggs, and Rajeshwari Dutta. ALMACAL - VI. Molecular gas mass density across cosmic time via a blind search for intervening molecular absorbers. *MNRAS*, 490(1): 1220–1230, November 2019. doi: 10.1093/mnras/stz2660.

E. Komatsu, K. M. Smith, J. Dunkley, C. L. Bennett, B. Gold, G. Hinshaw, N. Jarosik, D. Larson, M. R. Nolta, L. Page, D. N. Spergel, M. Halpern, R. S. Hill, A. Kogut, M. Limon, S. S. Meyer, N. Odegard, G. S. Tucker, J. L. Weiland, E. Wollack, and E. L. Wright. Seven-year Wilkinson Microwave Anisotropy

Probe (WMAP) Observations: Cosmological Interpretation. *ApJS*, 192:18, February 2011. doi: 10.1088/0067-0049/192/2/18.

Pavel Kroupa. On the variation of the initial mass function. *MNRAS*, 322(2): 231–246, April 2001. doi: 10.1046/j.1365-8711.2001.04022.x.

Mark R. Krumholz and Blakesley Burkhart. Is turbulence in the interstellar medium driven by feedback or gravity? An observational test. *MNRAS*, 458(2):1671–1677, May 2016. doi: 10.1093/mnras/stw434.

Mark R. Krumholz, Blakesley Burkhart, John C. Forbes, and Roland M. Crocker. A unified model for galactic discs: star formation, turbulence driving, and mass transport. *MNRAS*, 477(2):2716–2740, June 2018. doi: 10.1093/mnras/sty852.

C. D. P. Lagos, C. M. Baugh, C. G. Lacey, A. J. Benson, H.-S. Kim, and C. Power. Cosmic evolution of the atomic and molecular gas contents of galaxies. *MNRAS*, 418:1649–1667, December 2011. doi: 10.1111/j.1365-2966.2011.19583.x.

C. d. P. Lagos, E. Bayet, C. M. Baugh, C. G. Lacey, T. A. Bell, N. Fanidakis, and J. E. Geach. Predictions for the CO emission of galaxies from a coupled simulation of galaxy formation and photon-dominated regions. *MNRAS*, 426: 2142–2165, November 2012. doi: 10.1111/j.1365-2966.2012.21905.x.

Claus Leitherer, Daniel Schaerer, Jeffrey D. Goldader, Rosa M. González Delgado, Carmelle Robert, Denis Foo Kune, Duília F. de Mello, Daniel Devost, and Timothy M. Heckman. Starburst99: Synthesis Models for Galaxies with Active Star Formation. *ApJS*, 123(1):3–40, July 1999. doi: 10.1086/313233.

Laura Lenkić, Alberto D. Bolatto, Natascha M. Förster Schreiber, Linda J. Tacconi, Roberto Neri, Francoise Combes, Fabian Walter, Santiago García-Burillo, Reinhard Genzel, Dieter Lutz, and Michael C. Cooper. Plateau de Bure High-z Blue Sequence Survey 2 (PHIBSS2): Search for Secondary Sources, CO Luminosity Functions in the Field, and the Evolution of Molecular Gas Density through Cosmic Time. *AJ*, 159(5):190, May 2020. doi: 10.3847/1538-3881/ab7458.

Laura Lenkić, Alberto D. Bolatto, Deanne B. Fisher, Karl Glazebrook, Danail Obreschkow, Roberto Abraham, and Liyualem Ambachew. Giant star-forming complexes in high-z main-sequence galaxy analogues: the internal structure of clumps in DYNAMO galaxies. *MNRAS*, 506(3):3916–3934, September 2021. doi: 10.1093/mnras/stab1954.

Adam K. Leroy, Fabian Walter, Elias Brinks, Frank Bigiel, W. J. G. de Blok, Barry Madore, and M. D. Thornley. The Star Formation Efficiency in Nearby Galaxies: Measuring Where Gas Forms Stars Effectively. *AJ*, 136(6):2782–2845, December 2008. doi: 10.1088/0004-6256/136/6/2782.

Adam K. Leroy, Alberto Bolatto, Karl Gordon, Karin Sandstrom, Pierre Gratier, Erik Rosolowsky, Charles W. Engelbracht, Norikazu Mizuno, Edvige Corbelli,

Yasuo Fukui, and Akiko Kawamura. The CO-to-H_2 Conversion Factor from Infrared Dust Emission across the Local Group. *ApJ*, 737(1):12, August 2011. doi: 10.1088/0004-637X/737/1/12.

Adam K. Leroy, Fabian Walter, Karin Sandstrom, Andreas Schruba, Juan-Carlos Munoz-Mateos, Frank Bigiel, Alberto Bolatto, Elias Brinks, W. J. G. de Blok, Sharon Meidt, Hans-Walter Rix, Erik Rosolowsky, Eva Schinnerer, Karl-Friedrich Schuster, and Antonio Usero. Molecular Gas and Star Formation in nearby Disk Galaxies. *AJ*, 146(2):19, August 2013. doi: 10.1088/0004-6256/146/2/19.

Adam K. Leroy, Eva Schinnerer, Annie Hughes, Erik Rosolowsky, Jérôme Pety, Andreas Schruba, Antonio Usero, Guillermo A. Blanc, Mélanie Chevance, Eric Emsellem, Christopher M. Faesi, Cinthya N. Herrera, Daizhong Liu, Sharon E. Meidt, Miguel Querejeta, Toshiki Saito, Karin M. Sandstrom, Jiayi Sun, Thomas G. Williams, Gagandeep S. Anand, Ashley T. Barnes, Erica A. Behrens, Francesco Belfiore, Samantha M. Benincasa, Ivana Bešlić, Frank Bigiel, Alberto D. Bolatto, Jakob S. den Brok, Yixian Cao, Rupali Chandar, Jérémy Chastenet, I-Da Chiang, Enrico Congiu, Daniel A. Dale, Sinan Deger, Cosima Eibensteiner, Oleg V. Egorov, Axel García-Rodríguez, Simon C. O. Glover, Kathryn Grasha, Jonathan D. Henshaw, I-Ting Ho, Amanda A. Kepley, Jaeyeon Kim, Ralf S. Klessen, Kathryn Kreckel, Eric W. Koch, J. M. Diederik Kruijssen, Kirsten L. Larson, Janice C. Lee, Laura A. Lopez, Josh Machado, Ness Mayker, Rebecca McElroy, Eric J. Murphy, Eve C. Ostriker, Hsi-An Pan, Ismael Pessa, Johannes Puschnig, Alessandro Razza, Patricia Sánchez-Blázquez, Francesco Santoro, Amy Sardone, Fabian Scheuermann, Kazimierz Sliwa, Mattia C. Sormani, Sophia K. Stuber, David A. Thilker, Jordan A. Turner, Dyas Utomo, Elizabeth J. Watkins, and Bradley Whitmore. PHANGS-ALMA: Arcsecond CO(2-1) Imaging of Nearby Star-Forming Galaxies. *arXiv e-prints*, art. arXiv:2104.07739, April 2021.

Rebecca C. Levy, Alberto D. Bolatto, Peter Teuben, Sebastián F. Sánchez, Jorge K. Barrera-Ballesteros, Leo Blitz, Dario Colombo, Rubén García-Benito, Rodrigo Herrera-Camus, Bernd Husemann, Veselina Kalinova, Tian Lan, Gigi Y. C. Leung, Damián Mast, Dyas Utomo, Glenn van de Ven, Stuart N. Vogel, and Tony Wong. The EDGE-CALIFA Survey: Molecular and Ionized Gas Kinematics in Nearby Galaxies. *ApJ*, 860(2):92, June 2018. doi: 10.3847/1538-4357/aac2e5.

S. J. Lilly, L. Tresse, F. Hammer, David Crampton, and O. Le Fevre. The Canada-France Redshift Survey. VI. Evolution of the Galaxy Luminosity Function to Z approximately 1. *ApJ*, 455:108, December 1995. doi: 10.1086/176560.

R. C. Livermore, T. A. Jones, J. Richard, R. G. Bower, A. M. Swinbank, T. T. Yuan, A. C. Edge, R. S. Ellis, L. J. Kewley, Ian Smail, K. E. K. Coppin, and H. Ebeling. Resolved spectroscopy of gravitationally lensed galaxies: global dynamics and star-forming clumps on ∼100 pc scales at 1 ¡ z ¡ 4. *MNRAS*, 450(2):1812–1835, June 2015. doi: 10.1093/mnras/stv686.

Federica Loiacono, Roberto Decarli, Carlotta Gruppioni, Margherita Talia, Andrea Cimatti, Gianni Zamorani, Francesca Pozzi, Lin Yan, Brian C. Lemaux, Dominik A. Riechers, Olivier Le Fèvre, Matthieu Bèthermin, Peter Capak, Paolo Cassata, Andreas Faisst, Daniel Schaerer, John D. Silverman, Sandro Bardelli, Médéric Boquien, Sandra Burkutean, Miroslava Dessauges-Zavadsky, Yoshinobu Fudamoto, Seiji Fujimoto, Michele Ginolfi, Nimish P. Hathi, Gareth C. Jones, Yana Khusanova, Anton M. Koekemoer, Guilaine Lagache, Lori M. Lubin, Marcella Massardi, Pascal Oesch, Michael Romano, Livia Vallini, Daniela Vergani, and Elena Zucca. The ALPINE-ALMA [C II] survey. Luminosity function of serendipitous [C II] line emitters at z $\sim$ 5. *A&A*, 646:A76, February 2021. doi: 10.1051/0004-6361/202038607.

P. Madau and M. Dickinson. Cosmic Star-Formation History. *ARA&A*, 52:415–486, August 2014. doi: 10.1146/annurev-astro-081811-125615.

Piero Madau, Henry C. Ferguson, Mark E. Dickinson, Mauro Giavalisco, Charles C. Steidel, and Andrew Fruchter. High-redshift galaxies in the Hubble Deep Field: colour selection and star formation history to z~4. *MNRAS*, 283(4):1388–1404, December 1996. doi: 10.1093/mnras/283.4.1388.

Mahmoud S. Mahmoud, Andrew Ensor, Alain Biem, Bruce G. Elmegreen, and Sergei Gulyaev. Data provenance and management in radio astronomy: A stream computing approach. *CoRR*, abs/1112.2584, 2011. URL `http://arxiv.org/abs/1112.2584`.

Nir Mandelker, Avishai Dekel, Daniel Ceverino, Colin DeGraf, Yicheng Guo, and Joel Primack. Giant clumps in simulated high- z Galaxies: properties, evolution and dependence on feedback. *MNRAS*, 464(1):635–665, January 2017. doi: 10.1093/mnras/stw2358.

Christopher F. McKee and Eve C. Ostriker. Theory of Star Formation. *ARA&A*, 45(1):565–687, September 2007. doi: 10.1146/annurev.astro.45.051806.110602.

J. P. McMullin, B. Waters, D. Schiebel, W. Young, and K. Golap. CASA Architecture and Applications. In R. A. Shaw, F. Hill, and D. J. Bell, editors, *Astronomical Data Analysis Software and Systems XVI*, volume 376 of *Astronomical Society of the Pacific Conference Series*, page 127, October 2007.

S. Mineo, M. Gilfanov, and R. Sunyaev. X-ray emission from star-forming galaxies - I. High-mass X-ray binaries. *MNRAS*, 419(3):2095–2115, January 2012. doi: 10.1111/j.1365-2966.2011.19862.x.

Houjun Mo, Frank C. van den Bosch, and Simon White. *Galaxy Formation and Evolution*. 2010.

I. G. Momcheva, G. B. Brammer, P. G. van Dokkum, R. E. Skelton, K. E. Whitaker, E. J. Nelson, M. Fumagalli, M. V. Maseda, J. Leja, M. Franx, H.-W. Rix, R. Bezanson, E. Da Cunha, C. Dickey, N. M. Förster Schreiber, G. Illingworth,

M. Kriek, I. Labbé, J. Ulf Lange, B. F. Lundgren, D. Magee, D. Marchesini, P. Oesch, C. Pacifici, S. G. Patel, S. Price, T. Tal, D. A. Wake, A. van der Wel, and S. Wuyts. The 3D-HST Survey: Hubble Space Telescope WFC3/G141 Grism Spectra, Redshifts, and Emission Line Measurements for ˜ 100,000 Galaxies. *ApJS*, 225:27, August 2016. doi: 10.3847/0067-0049/225/2/27.

Rieko Momose, Jin Koda, Jr. Kennicutt, Robert C., Fumi Egusa, Daniela Calzetti, Guilin Liu, Jennifer Donovan Meyer, Sachiko K. Okumura, Nick Z. Scoville, Tsuyoshi Sawada, and Nario Kuno. Star Formation on Subkiloparsec Scale Triggered by Non-linear Processes in Nearby Spiral Galaxies. *ApJL*, 772(1):L13, July 2013. doi: 10.1088/2041-8205/772/1/L13.

Ramesh Narayan and Rajaram Nityananda. Maximum entropy image restoration in astronomy. *ARA&A*, 24:127–170, January 1986. doi: 10.1146/annurev.aa.24.090186.001015.

Desika Narayanan and Mark R. Krumholz. A theory for the excitation of CO in star-forming galaxies. *MNRAS*, 442(2):1411–1428, August 2014. doi: 10.1093/mnras/stu834.

Desika Narayanan, Mark R. Krumholz, Eve C. Ostriker, and Lars Hernquist. A general model for the CO-H_2 conversion factor in galaxies with applications to the star formation law. *MNRAS*, 421(4):3127–3146, April 2012. doi: 10.1111/j.1365-2966.2012.20536.x.

Marcel Neeleman, J. Xavier Prochaska, Joseph Ribaudo, Nicolas Lehner, J. Christopher Howk, Marc Rafelski, and Nissim Kanekar. The H I Content of the Universe Over the Past 10 GYRS. *ApJ*, 818(2):113, February 2016. doi: 10.3847/0004-637X/818/2/113.

Masafumi Noguchi. Early Evolution of Disk Galaxies: Formation of Bulges in Clumpy Young Galactic Disks. *ApJ*, 514(1):77–95, March 1999. doi: 10.1086/306932.

D. Obreschkow, I. Heywood, H.-R. Klöckner, and S. Rawlings. A Heuristic Prediction of the Cosmic Evolution of the Co-luminosity Functions. *ApJ*, 702:1321–1335, September 2009. doi: 10.1088/0004-637X/702/2/1321.

Antonija Oklopčić, Philip F. Hopkins, Robert Feldmann, Dušan Kereš, Claude-André Faucher-Giguère, and Norman Murray. Giant clumps in the FIRE simulations: a case study of a massive high-redshift galaxy. *MNRAS*, 465(1):952–969, Feb 2017. doi: 10.1093/mnras/stw2754.

Matthew E. Orr, Christopher C. Hayward, Anne M. Medling, Alexander B. Gurvich, Philip F. Hopkins, Norman Murray, Jorge L. Pineda, Claude-André Faucher-Giguère, Dušan Kereš, Andrew Wetzel, and Kung-Yi Su. Swirls of FIRE: spatially resolved gas velocity dispersions and star formation rates in FIRE-2 disc environments. *MNRAS*, 496(2):1620–1637, August 2020. doi: 10.1093/mnras/staa1619.

Eve C. Ostriker and Rahul Shetty. Maximally Star-forming Galactic Disks. I. Starburst Regulation Via Feedback-driven Turbulence. *ApJ*, 731(1):41, April 2011. doi: 10.1088/0004-637X/731/1/41.

Eve C. Ostriker, Christopher F. McKee, and Adam K. Leroy. Regulation of Star Formation Rates in Multiphase Galactic Disks: A Thermal/Dynamical Equilibrium Model. *ApJ*, 721(2):975–994, October 2010. doi: 10.1088/0004-637X/721/2/975.

Padelis P. Papadopoulos, Paul P. van der Werf, E. M. Xilouris, K. G. Isaak, Yu Gao, and S. Mühle. The molecular gas in luminous infrared galaxies - I. CO lines, extreme physical conditions and their drivers. *MNRAS*, 426(4):2601–2629, November 2012. doi: 10.1111/j.1365-2966.2012.21001.x.

R. Pavesi, C. E. Sharon, D. A. Riechers, J. A. Hodge, R. Decarli, F. Walter, C. L. Carilli, E. Daddi, I. Smail, M. Dickinson, R. J. Ivison, M. Sargent, E. da Cunha, M. Aravena, J. Darling, V. Smolčić, N. Z. Scoville, P. L. Capak, and J. Wagg. The CO Luminosity Density at High-z (COLDz) Survey: A Sensitive, Large-area Blind Search for Low-J CO Emission from Cold Gas in the Early Universe with the Karl G. Jansky Very Large Array. *ApJ*, 864:49, September 2018. doi: 10.3847/1538-4357/aacb79.

W. J. Pearson, L. Wang, P. D. Hurley, K. Małek, V. Buat, D. Burgarella, D. Farrah, S. J. Oliver, D. J. B. Smith, and F. F. S. van der Tak. Main sequence of star forming galaxies beyond the Herschel confusion limit. *A&A*, 615:A146, July 2018. doi: 10.1051/0004-6361/201832821.

G. Popping, J. P. Pérez-Beaupuits, M. Spaans, S. C. Trager, and R. S. Somerville. The nature of the ISM in galaxies during the star-formation activity peak of the Universe. *MNRAS*, 444(2):1301–1317, Oct 2014a. doi: 10.1093/mnras/stu1506.

G. Popping, E. van Kampen, R. Decarli, M. Spaans, R. S. Somerville, and S. C. Trager. Sub-mm emission line deep fields: CO and [C II] luminosity functions out to z = 6. *MNRAS*, 461:93–110, September 2016. doi: 10.1093/mnras/stw1323.

Gergö Popping, Rachel S. Somerville, and Scott C. Trager. Evolution of the atomic and molecular gas content of galaxies. *MNRAS*, 442(3):2398–2418, August 2014b. doi: 10.1093/mnras/stu991.

Gergö Popping, Annalisa Pillepich, Rachel S. Somerville, Roberto Decarli, Fabian Walter, Manuel Aravena, Chris Carilli, Pierre Cox, Dylan Nelson, Dominik Riechers, Axel Weiss, Leindert Boogaard, Richard Bouwens, Thierry Contini, Paulo C. Cortes, Elisabete da Cunha, Emanuele Daddi, Tanio Díaz-Santos, Benedikt Diemer, Jorge González-López, Lars Hernquist, Rob Ivison, Olivier Le Fèvre, Federico Marinacci, Hans-Walter Rix, Mark Swinbank, Mark Vogelsberger, Paul van der Werf, Jeff Wagg, and L. Y. Aaron Yung. The ALMA Spectroscopic Survey in the HUDF: the Molecular Gas Content of Galaxies and Tensions with IllustrisTNG and the Santa Cruz SAM. *ApJ*, 882(2):137, September 2019. doi: 10.3847/1538-4357/ab30f2.

A. M. Price-Whelan, B. M. Sipőcz, H. M. Günther, P. L. Lim, S. M. Crawford, S. Conseil, D. L. Shupe, M. W. Craig, N. Dencheva, A. Ginsburg, J. T. VanderPlas, L. D. Bradley, D. Pérez-Suárez, M. de Val-Borro, (Primary Paper Contributors, T. L. Aldcroft, K. L. Cruz, T. P. Robitaille, E. J. Tollerud, (Astropy Coordination Committee, C. Ardelean, T. Babej, Y. P. Bach, M. Bachetti, A. V. Bakanov, S. P. Bamford, G. Barentsen, P. Barmby, A. Baumbach, K. L. Berry, F. Biscani, M. Boquien, K. A. Bostroem, L. G. Bouma, G. B. Brammer, E. M. Bray, H. Breytenbach, H. Buddelmeijer, D. J. Burke, G. Calderone, J. L. Cano Rodríguez, M. Cara, J. V. M. Cardoso, S. Cheedella, Y. Copin, L. Corrales, D. Crichton, D. D'Avella, C. Deil, É. Depagne, J. P. Dietrich, A. Donath, M. Droettboom, N. Earl, T. Erben, S. Fabbro, L. A. Ferreira, T. Finethy, R. T. Fox, L. H. Garrison, S. L. J. Gibbons, D. A. Goldstein, R. Gommers, J. P. Greco, P. Greenfield, A. M. Groener, F. Grollier, A. Hagen, P. Hirst, D. Homeier, A. J. Horton, G. Hosseinzadeh, L. Hu, J. S. Hunkeler, Ž. Ivezić, A. Jain, T. Jenness, G. Kanarek, S. Kendrew, N. S. Kern, W. E. Kerzendorf, A. Khvalko, J. King, D. Kirkby, A. M. Kulkarni, A. Kumar, A. Lee, D. Lenz, S. P. Littlefair, Z. Ma, D. M. Macleod, M. Mastropietro, C. McCully, S. Montagnac, B. M. Morris, M. Mueller, S. J. Mumford, D. Muna, N. A. Murphy, S. Nelson, G. H. Nguyen, J. P. Ninan, M. Nöthe, S. Ogaz, S. Oh, J. K. Parejko, N. Parley, S. Pascual, R. Patil, A. A. Patil, A. L. Plunkett, J. X. Prochaska, T. Rastogi, V. Reddy Janga, J. Sabater, P. Sakurikar, M. Seifert, L. E. Sherbert, H. Sherwood-Taylor, A. Y. Shih, J. Sick, M. T. Silbiger, S. Singanamalla, L. P. Singer, P. H. Sladen, K. A. Sooley, S. Sornarajah, O. Streicher, P. Teuben, S. W. Thomas, G. R. Tremblay, J. E. H. Turner, V. Terrón, M. H. van Kerkwijk, A. de la Vega, L. L. Watkins, B. A. Weaver, J. B. Whitmore, J. Woillez, V. Zabalza, and (Astropy Contributors. The Astropy Project: Building an Open-science Project and Status of the v2.0 Core Package. *AJ*, 156:123, September 2018. doi: 10.3847/1538-3881/aabc4f.

D. A. Riechers, R. Pavesi, C. E. Sharon, J. A. Hodge, R. Decarli, F. Walter, C. L. Carilli, M. Aravena, E. da Cunha, E. Daddi, M. Dickinson, I. Smail, P. L. Capak, R. J. Ivison, M. Sargent, N. Z. Scoville, and J. Wagg. COLDz: Shape of the CO Luminosity Function at High Redshift and the Cold Gas History of the Universe. *ApJ*, 872:7, February 2019. doi: 10.3847/1538-4357/aafc27.

T. Robitaille and E. Bressert. APLpy: Astronomical Plotting Library in Python. Astrophysics Source Code Library, August 2012.

M. J. F. Rosenberg, P. P. van der Werf, S. Aalto, L. Armus, V. Charmandaris, T. Díaz-Santos, A. S. Evans, J. Fischer, Y. Gao, E. González-Alfonso, T. R. Greve, A. I. Harris, C. Henkel, F. P. Israel, K. G. Isaak, C. Kramer, R. Meijerink, D. A. Naylor, D. B. Sanders, H. A. Smith, M. Spaans, L. Spinoglio, G. J. Stacey, I. Veenendaal, S. Veilleux, F. Walter, A. Weiß, M. C. Wiedner, M. H. D. van der Wiel, and E. M. Xilouris. The Herschel Comprehensive (U)LIRG Emission Survey (HERCULES): CO Ladders, Fine Structure Lines, and Neutral Gas Cooling. *ApJ*, 801(2):72, March 2015. doi: 10.1088/0004-637X/801/2/72.

V. C. Rubin, D. Burstein, W. K. Ford, Jr., and N. Thonnard. Rotation velocities of 16 SA galaxies and a comparison of Sa, Sb, and SC rotation properties. *ApJ*, 289:81–98, February 1985. doi: 10.1086/162866.

Samir Salim, R. Michael Rich, Stéphane Charlot, Jarle Brinchmann, Benjamin D. Johnson, David Schiminovich, Mark Seibert, Ryan Mallery, Timothy M. Heckman, Karl Forster, Peter G. Friedman, D. Christopher Martin, Patrick Morrissey, Susan G. Neff, Todd Small, Ted K. Wyder, Luciana Bianchi, José Donas, Young-Wook Lee, Barry F. Madore, Bruno Milliard, Alex S. Szalay, Barry Y. Welsh, and Sukyoung K. Yi. UV Star Formation Rates in the Local Universe. *ApJS*, 173(2): 267–292, December 2007. doi: 10.1086/519218.

Kevin Schawinski, C. Megan Urry, Brooke D. Simmons, Lucy Fortson, Sugata Kaviraj, William C. Keel, Chris J. Lintott, Karen L. Masters, Robert C. Nichol, Marc Sarzi, Ramin Skibba, Ezequiel Treister, Kyle W. Willett, O. Ivy Wong, and Sukyoung K. Yi. The green valley is a red herring: Galaxy Zoo reveals two evolutionary pathways towards quenching of star formation in early- and late-type galaxies. *MNRAS*, 440(1):889–907, May 2014. doi: 10.1093/mnras/stu327.

P. Schechter. An analytic expression for the luminosity function for galaxies. *ApJ*, 203:297–306, January 1976. doi: 10.1086/154079.

Tobias M. Schmidt, Frank Bigiel, Ralf S. Klessen, and W. J. G. de Blok. Radial gas motions in The H I Nearby Galaxy Survey (THINGS). *MNRAS*, 457(3): 2642–2664, April 2016. doi: 10.1093/mnras/stw011.

Andreas Schruba, Adam K. Leroy, Fabian Walter, Frank Bigiel, Elias Brinks, W. J. G. de Blok, Gaelle Dumas, Carsten Kramer, Erik Rosolowsky, Karin Sandstrom, Karl Schuster, Antonio Usero, Axel Weiss, and Helmut Wiesemeyer. A Molecular Star Formation Law in the Atomic-gas-dominated Regime in Nearby Galaxies. *AJ*, 142(2):37, August 2011. doi: 10.1088/0004-6256/142/2/37.

Karl-Friedrich Schuster. Iram annual report 2014. *IRAM Annu. Rep. https://www.iram-institute.org/medias/uploads/IRAM_2014.pdf*, 2014.

Rahul Shetty and Eve C. Ostriker. Maximally Star-forming Galactic Disks. II. Vertically Resolved Hydrodynamic Simulations of Starburst Regulation. *ApJ*, 754(1):2, July 2012. doi: 10.1088/0004-637X/754/1/2.

Takatoshi Shibuya, Masami Ouchi, Mariko Kubo, and Yuichi Harikane. Morphologies of ~190,000 Galaxies at z = 0-10 Revealed with HST Legacy Data. II. Evolution of Clumpy Galaxies. *ApJ*, 821(2):72, Apr 2016. doi: 10.3847/0004-637X/821/2/72.

R. E. Skelton, K. E. Whitaker, I. G. Momcheva, G. B. Brammer, P. G. van Dokkum, I. Labbé, M. Franx, A. van der Wel, R. Bezanson, E. Da Cunha, M. Fumagalli, N. Förster Schreiber, M. Kriek, J. Leja, B. F. Lundgren, D. Magee, D. Marchesini, M. V. Maseda, E. J. Nelson, P. Oesch, C. Pacifici, S. G. Patel, S. Price, H.-W. Rix,

T. Tal, D. A. Wake, and S. Wuyts. 3D-HST WFC3-selected Photometric Catalogs in the Five CANDELS/3D-HST Fields: Photometry, Photometric Redshifts, and Stellar Masses. *ApJS*, 214:24, October 2014. doi: 10.1088/0067-0049/214/2/24.

P. M. Solomon, N. Z. Scoville, A. A. Penzias, R. W. Wilson, and K. B. Jefferts. Molecular Clouds in the Galactic Center Region: Carbon Monoxide Observations at 2.6 Millimeters. *ApJ*, 178:125–130, November 1972. doi: 10.1086/151772.

P. M. Solomon, D. Downes, S. J. E. Radford, and J. W. Barrett. The Molecular Interstellar Medium in Ultraluminous Infrared Galaxies. *ApJ*, 478:144–161, March 1997. doi: 10.1086/303765.

Emmaris Soto, Duilia F. de Mello, Marc Rafelski, Jonathan P. Gardner, Harry I. Teplitz, Anton M. Koekemoer, Swara Ravindranath, Norman A. Grogin, Claudia Scarlata, Peter Kurczynski, and Eric Gawiser. Physical Properties of Sub-galactic Clumps at $0.5 \leq Z \leq 1.5$ in the UVUDF. *ApJ*, 837(1):6, Mar 2017. doi: 10.3847/1538-4357/aa5da3.

Charles C. Steidel, Dawn K. Erb, Alice E. Shapley, Max Pettini, Naveen Reddy, Milan Bogosavljević, Gwen C. Rudie, and Olivera Rakic. The Structure and Kinematics of the Circumgalactic Medium from Far-ultraviolet Spectra of z ~= 2-3 Galaxies. *ApJ*, 717(1):289–322, July 2010. doi: 10.1088/0004-637X/717/1/289.

M. L. Strandet, A. Weiss, J. D. Vieira, C. de Breuck, J. E. Aguirre, M. Aravena, M. L. N. Ashby, M. Béthermin, C. M. Bradford, J. E. Carlstrom, S. C. Chapman, T. M. Crawford, W. Everett, C. D. Fassnacht, R. M. Furstenau, A. H. Gonzalez, T. R. Greve, B. Gullberg, Y. Hezaveh, J. R. Kamenetzky, K. Litke, J. Ma, M. Malkan, D. P. Marrone, K. M. Menten, E. J. Murphy, A. Nadolski, K. M. Rotermund, J. S. Spilker, A. A. Stark, and N. Welikala. The Redshift Distribution of Dusty Star-forming Galaxies from the SPT Survey. *ApJ*, 822(2):80, May 2016. doi: 10.3847/0004-637X/822/2/80.

Jiayi Sun, Adam K. Leroy, Eva Schinnerer, Annie Hughes, Erik Rosolowsky, Miguel Querejeta, Andreas Schruba, Daizhong Liu, Toshiki Saito, Cinthya N. Herrera, Christopher Faesi, Antonio Usero, Jérôme Pety, J. M. Diederik Kruijssen, Eve C. Ostriker, Frank Bigiel, Guillermo A. Blanc, Alberto D. Bolatto, Médéric Boquien, Mélanie Chevance, Daniel A. Dale, Sinan Deger, Eric Emsellem, Simon C. O. Glover, Kathryn Grasha, Brent Groves, Jonathan Henshaw, Maria J. Jimenez-Donaire, Jenny J. Kim, Ralf S. Klessen, Kathryn Kreckel, Janice C. Lee, Sharon Meidt, Karin Sandstrom, Amy E. Sardone, Dyas Utomo, and Thomas G. Williams. Molecular Gas Properties on Cloud Scales across the Local Star-forming Galaxy Population. *ApJL*, 901(1):L8, September 2020. doi: 10.3847/2041-8213/abb3be.

L. J. Tacconi, R. Genzel, R. Neri, P. Cox, M. C. Cooper, K. Shapiro, A. Bolatto, N. Bouché, F. Bournaud, A. Burkert, F. Combes, J. Comerford, M. Davis, N. M. F. Schreiber, S. Garcia-Burillo, J. Gracia-Carpio, D. Lutz, T. Naab,

A. Omont, A. Shapley, A. Sternberg, and B. Weiner. High molecular gas fractions in normal massive star-forming galaxies in the young Universe. *Nature*, 463: 781–784, February 2010. doi: 10.1038/nature08773.

L. J. Tacconi, R. Neri, R. Genzel, F. Combes, A. Bolatto, M. C. Cooper, S. Wuyts, F. Bournaud, A. Burkert, J. Comerford, P. Cox, M. Davis, N. M. Förster Schreiber, S. García-Burillo, J. Gracia-Carpio, D. Lutz, T. Naab, S. Newman, A. Omont, A. Saintonge, K. Shapiro Griffin, A. Shapley, A. Sternberg, and B. Weiner. Phibss: Molecular Gas Content and Scaling Relations in z ˜ 1-3 Massive, Main-sequence Star-forming Galaxies. *ApJ*, 768:74, May 2013. doi: 10.1088/0004-637X/768/1/74.

L. J. Tacconi, R. Genzel, A. Saintonge, F. Combes, S. García-Burillo, R. Neri, A. Bolatto, T. Contini, N. M. Förster Schreiber, S. Lilly, D. Lutz, S. Wuyts, G. Accurso, J. Boissier, F. Boone, N. Bouché, F. Bournaud, A. Burkert, M. Carollo, M. Cooper, P. Cox, C. Feruglio, J. Freundlich, R. Herrera-Camus, S. Juneau, M. Lippa, T. Naab, A. Renzini, P. Salome, A. Sternberg, K. Tadaki, H. Übler, F. Walter, B. Weiner, and A. Weiss. PHIBSS: Unified Scaling Relations of Gas Depletion Time and Molecular Gas Fractions. *ApJ*, 853:179, February 2018. doi: 10.3847/1538-4357/aaa4b4.

Linda J. Tacconi and Judith S. Young. The CO Contents of Dwarf Irregular Galaxies. *ApJ*, 322:681, November 1987. doi: 10.1086/165763.

A. Richard Thompson, James M. Moran, and Jr. Swenson, George W. *Interferometry and Synthesis in Radio Astronomy, 3rd Edition*. 2017. doi: 10.1007/978-3-319-44431-4.

A. G. G. M. Tielens. *The Physics and Chemistry of the Interstellar Medium*. 2005.

Cameron Trapp, Dusan Keres, T. K. Chan, Ivanna Escala, Cameron Hummels, Philip F. Hopkins, Claude-Andre Faucher-Giguere, Norman Murray, Eliot Quataert, and Andrew Wetzel. Gas infall and radial transport in cosmological simulations of Milky Way-mass disks. *arXiv e-prints*, art. arXiv:2105.11472, May 2021.

Christy A. Tremonti, Timothy M. Heckman, Guinevere Kauffmann, Jarle Brinchmann, Stéphane Charlot, Simon D. M. White, Mark Seibert, Eric W. Peng, David J. Schlegel, Alan Uomoto, Masataka Fukugita, and Jon Brinkmann. The Origin of the Mass-Metallicity Relation: Insights from 53,000 Star-forming Galaxies in the Sloan Digital Sky Survey. *ApJ*, 613(2):898–913, October 2004. doi: 10.1086/423264.

L. Vallini, C. Gruppioni, F. Pozzi, C. Vignali, and G. Zamorani. CO luminosity function from Herschel-selected galaxies and the contribution of AGN. *MNRAS*, 456:L40–L44, February 2016. doi: 10.1093/mnrasl/slv173.

F. F. S. van der Tak, J. H. Black, F. L. Schöier, D. J. Jansen, and E. F. van Dishoeck. A computer program for fast non-LTE analysis of interstellar line spectra. With diagnostic plots to interpret observed line intensity ratios. *A&A*, 468(2):627–635, June 2007. doi: 10.1051/0004-6361:20066820.

Stéfan van der Walt, Johannes L. Schönberger, Juan Nunez-Iglesias, François Boulogne, Joshua D. Warner, Neil Yager, Emmanuelle Gouillart, Tony Yu, and the scikit-image contributors. scikit-image: image processing in Python. *PeerJ*, 2:e453, 6 2014. ISSN 2167-8359. doi: 10.7717/peerj.453. URL `https://doi.org/10.7717/peerj.453`.

Stefan Van der Walt, Johannes L Schönberger, Juan Nunez-Iglesias, François Boulogne, Joshua D Warner, Neil Yager, Emmanuelle Gouillart, and Tony Yu. scikit-image: image processing in python. *PeerJ*, 2:e453, 2014.

Frances Verter. Systematic Properties of CO Emission from Galaxies. I. Luminosity Function. *ApJS*, 65:555, December 1987. doi: 10.1086/191236.

Frances Verter. The CO Luminosity Function of Galaxies. *ApJ*, 375:95, July 1991. doi: 10.1086/170172.

Pauli Virtanen, Ralf Gommers, Travis E. Oliphant, Matt Haberland, Tyler Reddy, David Cournapeau, Evgeni Burovski, Pearu Peterson, Warren Weckesser, Jonathan Bright, Stéfan J. van der Walt, Matthew Brett, Joshua Wilson, K. Jarrod Millman, Nikolay Mayorov, Andrew R. J. Nelson, Eric Jones, Robert Kern, Eric Larson, C J Carey, İlhan Polat, Yu Feng, Eric W. Moore, Jake VanderPlas, Denis Laxalde, Josef Perktold, Robert Cimrman, Ian Henriksen, E. A. Quintero, Charles R. Harris, Anne M. Archibald, Antônio H. Ribeiro, Fabian Pedregosa, Paul van Mulbregt, and SciPy 1.0 Contributors. SciPy 1.0: Fundamental Algorithms for Scientific Computing in Python. *Nature Methods*, 17:261–272, 2020. doi: 10.1038/s41592-019-0686-2.

F. Walter, R. Decarli, M. Sargent, C. Carilli, M. Dickinson, D. Riechers, R. Ellis, D. Stark, B. Weiner, M. Aravena, E. Bell, F. Bertoldi, P. Cox, E. Da Cunha, E. Daddi, D. Downes, L. Lentati, R. Maiolino, K. M. Menten, R. Neri, H.-W. Rix, and A. Weiss. A Molecular Line Scan in the Hubble Deep Field North: Constraints on the CO Luminosity Function and the Cosmic H_2 Density. *ApJ*, 782:79, February 2014. doi: 10.1088/0004-637X/782/2/79.

F. Walter, R. Decarli, M. Aravena, C. Carilli, R. Bouwens, E. da Cunha, E. Daddi, R. J. Ivison, D. Riechers, I. Smail, M. Swinbank, A. Weiss, T. Anguita, R. Assef, R. Bacon, F. Bauer, E. F. Bell, F. Bertoldi, S. Chapman, L. Colina, P. C. Cortes, P. Cox, M. Dickinson, D. Elbaz, J. Gónzalez-López, E. Ibar, H. Inami, L. Infante, J. Hodge, A. Karim, O. Le Fevre, B. Magnelli, R. Neri, P. Oesch, K. Ota, G. Popping, H.-W. Rix, M. Sargent, K. Sheth, A. van der Wel, P. van der Werf, and J. Wagg. ALMA Spectroscopic Survey in the Hubble Ultra Deep Field: Survey Description. *ApJ*, 833:67, December 2016. doi: 10.3847/1538-4357/833/1/67.

Fabian Walter, Chris Carilli, Roberto Decarli, Dominik Riechers, Manuel Aravena, Franz Erik Bauer, Frank Bertoldi, Alberto Bolatto, Leindert Boogaard, Rychard Bouwens, Denis Burgarella, Caitlin Casey, Asantha Cooray, Paolo Cortes, Pierre Cox, Emanuele Daddi, Jeremy Darling, Bjorn Emonts, Jorge Gonzalez Lopez, Jacqueline Hodge, Hanae Inami, Rob Ivison, Ely Kovetz, Olivier Le Fevre, Benjamin Magnelli, Dan Marrone, Eric Murphy, Desika Narayanan, Mladen Novak, Pascal Oesch, Riccardo Pavesi, Tanio Diaz Santos, Mark Sargent, Douglas Scott, Nick Scoville, Gordon Stacey, Jeff Wagg, Paul van der Werf, Bade Uzgil, Axel Weiss, and Min Yun. The evolution of the cosmic molecular gas density, 2019.

Fabian Walter, Chris Carilli, Marcel Neeleman, Roberto Decarli, Gergö Popping, Rachel S. Somerville, Manuel Aravena, Frank Bertoldi, Leindert Boogaard, Pierre Cox, Elisabete da Cunha, Benjamin Magnelli, Danail Obreschkow, Dominik Riechers, Hans-Walter Rix, Ian Smail, Axel Weiss, Roberto J. Assef, Franz Bauer, Rychard Bouwens, Thierry Contini, Paulo C. Cortes, Emanuele Daddi, Tanio Diaz-Santos, Jorge González-López, Joseph Hennawi, Jacqueline A. Hodge, Hanae Inami, Rob Ivison, Pascal Oesch, Mark Sargent, Paul van der Werf, Jeff Wagg, and L. Y. Aaron Yung. The Evolution of the Baryons Associated with Galaxies Averaged over Cosmic Time and Space. *ApJ*, 902(2):111, October 2020. doi: 10.3847/1538-4357/abb82e.

Liang Wang, Aaron A. Dutton, Gregory S. Stinson, Andrea V. Macciò, Camilla Penzo, Xi Kang, Ben W. Keller, and James Wadsley. NIHAO project - I. Reproducing the inefficiency of galaxy formation across cosmic time with a large sample of cosmological hydrodynamical simulations. *MNRAS*, 454(1):83–94, Nov 2015. doi: 10.1093/mnras/stv1937.

Michael L. Waskom. seaborn: statistical data visualization. *Journal of Open Source Software*, 6(60):3021, 2021. doi: 10.21105/joss.03021. URL `https://doi.org/10.21105/joss.03021`.

Andrew R. Wetzel, Philip F. Hopkins, Ji-hoon Kim, Claude-André Faucher-Giguère, Dušan Kereš, and Eliot Quataert. Reconciling Dwarf Galaxies with ΛCDM Cosmology: Simulating a Realistic Population of Satellites around a Milky Way-mass Galaxy. *ApJL*, 827(2):L23, August 2016. doi: 10.3847/2041-8205/827/2/L23.

K. E. Whitaker, A. Pope, R. Cybulski, C. M. Casey, G. Popping, and M. S. Yun. The Constant Average Relationship between Dust-obscured Star Formation and Stellar Mass from z = 0 to z = 2.5. *ApJ*, 850:208, December 2017. doi: 10.3847/1538-4357/aa94ce.

Heidi A. White, David B. Fisher, Norman Murray, Karl Glazebrook, Roberto G. Abraham, Alberto D. Bolatto, Andrew W. Green, Erin Mentuch Cooper, and Danail Obreschkow. Gas Content and Kinematics in Clumpy, Turbulent Star-forming Disks. *ApJ*, 846(1):35, September 2017. doi: 10.3847/1538-4357/aa7fbf.

R. W. Wilson, K. B. Jefferts, and A. A. Penzias. Carbon Monoxide in the Orion Nebula. *ApJL*, 161:L43, July 1970. doi: 10.1086/180567.

W. J. Wilson, P. R. Schwartz, E. E. Epstein, W. A. Johnson, R. D. Etcheverry, T. T. Mori, G. G. Berry, and H. B. Dyson. Observations of Galactic Carbon Monoxide Emission at 2.6 Millimeters. *ApJ*, 191:357–374, July 1974. doi: 10.1086/152974.

E. Wisnioski, N. M. Förster Schreiber, S. Wuyts, E. Wuyts, K. Bandara, D. Wilman, R. Genzel, R. Bender, R. Davies, M. Fossati, P. Lang, J. T. Mendel, A. Beifiori, G. Brammer, J. Chan, M. Fabricius, Y. Fudamoto, S. Kulkarni, J. Kurk, D. Lutz, E. J. Nelson, I. Momcheva, D. Rosario, R. Saglia, S. Seitz, L. J. Tacconi, and P. G. van Dokkum. The KMOS^{3D} Survey: Design, First Results, and the Evolution of Galaxy Kinematics from 0.7 ¡= z ¡= 2.7. *ApJ*, 799(2):209, February 2015. doi: 10.1088/0004-637X/799/2/209.

Tony Wong, Leo Blitz, and Albert Bosma. A Search for Kinematic Evidence of Radial Gas Flows in Spiral Galaxies. *ApJ*, 605(1):183–204, April 2004. doi: 10.1086/382215.

E. L. Wright. A Cosmology Calculator for the World Wide Web. *PASP*, 118(850): 1711–1715, December 2006. doi: 10.1086/510102.

Stijn Wuyts, Natascha M. Förster Schreiber, Dieter Lutz, Raanan Nordon, Stefano Berta, Bruno Altieri, Paola Andreani, Hervé Aussel, Angel Bongiovanni, Jordi Cepa, Andrea Cimatti, Emanuele Daddi, David Elbaz, Reinhard Genzel, Anton M. Koekemoer, Benjamin Magnelli, Roberto Maiolino, Elizabeth J. McGrath, Ana Pérez García, Albrecht Poglitsch, Paola Popesso, Francesca Pozzi, Miguel Sanchez-Portal, Eckhard Sturm, Linda Tacconi, and Ivan Valtchanov. On Star Formation Rates and Star Formation Histories of Galaxies Out to z ˜3. *ApJ*, 738(1):106, Sep 2011. doi: 10.1088/0004-637X/738/1/106.

Stijn Wuyts, Natascha M. Förster Schreiber, Reinhard Genzel, Yicheng Guo, Guillermo Barro, Eric F. Bell, Avishai Dekel, Sandra M. Faber, Henry C. Ferguson, Mauro Giavalisco, Norman A. Grogin, Nimish P. Hathi, Kuang-Han Huang, Dale D. Kocevski, Anton M. Koekemoer, David C. Koo, Jennifer Lotz, Dieter Lutz, Elizabeth McGrath, Jeffrey A. Newman, David Rosario, Amelie Saintonge, Linda J. Tacconi, Benjamin J. Weiner, and Arjen van der Wel. Smooth(er) Stellar Mass Maps in CANDELS: Constraints on the Longevity of Clumps in High-redshift Star-forming Galaxies. *ApJ*, 753(2):114, Jul 2012. doi: 10.1088/0004-637X/753/2/114.

Stijn Wuyts, Natascha M. Förster Schreiber, Erica J. Nelson, Pieter G. van Dokkum, Gabe Brammer, Yu-Yen Chang, Sandra M. Faber, Henry C. Ferguson, Marijn Franx, Mattia Fumagalli, Reinhard Genzel, Norman A. Grogin, Dale D. Kocevski, Anton M. Koekemoer, Britt Lundgren, Dieter Lutz, Elizabeth J. McGrath, Ivelina Momcheva, David Rosario, Rosalind E. Skelton, Linda J. Tacconi, Arjen van der Wel, and Katherine E. Whitaker. A CANDELS-3D-HST synergy: Resolved Star Formation Patterns at 0.7 ¡ z ¡ 1.5. *ApJ*, 779(2):135, December 2013. doi: 10.1088/0004-637X/779/2/135.

J. S. Young, S. Xie, L. Tacconi, P. Knezek, P. Viscuso, L. Tacconi-Garman, N. Scoville, S. Schneider, F. P. Schloerb, S. Lord, A. Lesser, J. Kenney, Y.-L. Huang, N. Devereux, M. Claussen, J. Case, J. Carpenter, M. Berry, and L. Allen. The FCRAO Extragalactic CO Survey. I. The Data. *ApJS*, 98:219, May 1995. doi: 10.1086/192159.

A. Zanella, E. Le Floc'h, C. M. Harrison, E. Daddi, E. Bernhard, R. Gobat, V. Strazzullo, F. Valentino, A. Cibinel, J. Sánchez Almeida, M. Kohandel, J. Fensch, M. Behrendt, A. Burkert, M. Onodera, F. Bournaud, and J. Scholtz. A contribution of star-forming clumps and accreting satellites to the mass assembly of z $\sim$ 2 galaxies. *MNRAS*, 489(2):2792–2818, October 2019. doi: 10.1093/mnras/stz2099.